In situ Lorentz microscopy and electron holography in magnetic nanostructures

Luis Alfredo Rodríguez González

▶ **To cite this version:**

Luis Alfredo Rodríguez González. In situ Lorentz microscopy and electron holography in magnetic nanostructures. Materials Science [cond-mat.mtrl-sci]. Université Toulouse III Paul Sabatier (UT3 Paul Sabatier); Universidad de Zaragoza, 2014. English. NNT : 2014TOU30228 . tel-01789430

HAL Id: tel-01789430
https://theses.hal.science/tel-01789430

Submitted on 10 May 2018

HAL is a multi-disciplinary open access archive for the deposit and dissemination of scientific research documents, whether they are published or not. The documents may come from teaching and research institutions in France or abroad, or from public or private research centers.

L'archive ouverte pluridisciplinaire **HAL**, est destinée au dépôt et à la diffusion de documents scientifiques de niveau recherche, publiés ou non, émanant des établissements d'enseignement et de recherche français ou étrangers, des laboratoires publics ou privés.

Université de Toulouse

THÈSE

En vue de l'obtention du

DOCTORAT DE L'UNIVERSITÉ DE TOULOUSE

Délivré par :
Université Toulouse III Paul Sabatier (UT3 Paul Sabatier)

Discipline ou spécialité :

Nano-physique

Présentée et soutenue par :
Luis Alfredo Rodríguez González

le : mercredi 17 décembre 2014

Titre :

IN SITU LORENTZ MICROSCOPY AND ELECTRON HOLOGRAPHY
IN MAGNETIC NANOSTRUCTURES

Ecole doctorale :
Sciences de la Matière (SDM)

Unité de recherche :
Centre d'Élaboration de Matériaux et d'Études Structurales (CEMES-CNRS)

Directeur(s) de Thèse :
Dr. Etienne Snoeck, Directeur de Recherche au CNRS-CEMES (France)
Dr. César Magén Dominguez, Researcher ARAID, INA-UNIZAR (Espagne)

Rapporteurs :
Dr. Agustina Asenjo Barahona, Científico Titular au CSIC (Espagne)
Dr. Francisco Rivadulla Fernández, Professeur à l'Universidad de Santiago de Compostela - (Espagne)

Membre(s) du jury :

Dr. Jose Maria de Teresa, Profesor de Investigación au CSIC (Espagne)
Dr. Michel Goiran, Professeur à l'Université Paul Sabatier - LNCMI-CNRS (France)
Dr. Christophe Gatel, Maitre de Conférence à l'Université Paul Sabatier, Membre Junior de l'Institut Universitaire de France - CEMES-CNRS (France)

IN-SITU LORENTZ MICROSCOPY AND ELECTRON HOLOGRAPHY IN MAGNETIC NANOSTRUCTURES

Departamento de Física de la Materia Condensada
Laboratorio de Microscopías Avanzadas (LMA)
Instituto de Nanociencia de Aragón (INA)
Universidad de Zaragoza

Centre d'Élaboration de Matériaux et d'Études Structurales - Centre Nationale de la Recherche Scientifique (CEMES-CNRS)
Université Paul Sabatier

Doctoral Thesis

In situ Lorentz Microscopy and Electron Holography in Magnetic Nanostructures

Luis Alfredo Rodríguez González

Zaragoza, November 2014

Thesis Directors:
César Magén Dominguez
Etienne Snoeck

Dedicado a Dios,
mis Padres y Hermanos,
y a mi esposa Lorena Marín

Abstract

In this Thesis, we have developed quantitative and qualitative studies of the magnetic states of different ferromagnetic nanostructures by *in situ* Lorentz Microscopy (LM) and Electron Holography (EH) experiments under the application of magnetic fields or at low temperature (100 K). A detailed investigation was performed in three different ferromagnetic nanostructures: L-shape cobalt and $Co_{50}Fe_{50}$ nanowires grown by Focused Electron Beam Induced Deposition (FEBID) and Electron Beam Lithography (EBL) techniques, respectively; square cobalt antidot arrays fabricated by the combination of sputtering and Focused Ion Beam (FIB) techniques; and epitaxially strained $La_{2/3}Ca_{1/3}MnO_3$ (LCMO) thin films grown by Pulsed Laser Deposition (PLD). In addition, the traditional method to perform *in situ* LM and EH experiments with the application of controlled magnetic fields through the objective lens has been optimized. We have built the mathematical description that permits the total control of the in-plane component of the magnetic field produced by the objective lens. Such in-plane magnetic field was widely employed to perform magnetization reversal studies in the magnetic nanowires and antidot arrays.

In the ferromagnetic nanowires, we have realized a quantitative study of the reversal magnetization process through the manipulation of single domain walls (DWs). In the case of the L-shape Co nanowires, the DW nucleation process has been correlated with the lateral dimensions and thickness of the nanostructure. For a particular series of 500-nm-wide cobalt nanowires, we detected a progressive variation of the magnetic configuration of the nucleated DW with the increase of the thickness. These configurational changes produced important effects in the thickness dependence of the nucleation field (H_C), such as a maximum value just in the crossover between an asymmetry transversal wall and asymmetry vortex wall. In the case of the notched L-shape $Co_{50}Fe_{50}$ nanowires, *in situ* LM experiments allowed evaluating the pinning/depinning quality of a single DW by an increasing magnetic field. For such evaluation, series of notches arranged along one branch of the L-shape nanowire were

fabricated. We found that a series of curved notches presented the best pinning/depinning behavior.

In the cobalt antidots arrays (holes of 55 nm diameter), the remanent magnetic states for different antidot periodicities (p) were explored. For the magnetic analysis of antidot arrays with small periodicities ($p \leq 160$ nm), a low-frequency filtered method was implemented to enhance the magnetic contrasts observed inside the array through Fresnel-mode LM. In antidot arrays with $116 \leq p \leq 160$ nm, we found that the magnetic structure is mainly composed by extended superdomains and unit-cell-wide confined superdomains called magnetic chains. Magnetization reversal LM experiments in an antidot array with $p = 160$ nm showed that the magnetization switching occurs by the nucleation and propagation of superdomain walls (SDWs), and a clear differences were observed as a function of the magnetic field orientation: while the magnetization switching by the application of magnetic fields transversal to the antidot rows occurs by the simultaneous nucleation and propagation of horizontal and vertical (SDWs), the switching process under magnetic fields parallel to the horizontal antidot rows takes place in two stages: the system first nucleates and propagates horizontal SDWs, and then nucleates and propagates vertical SDWs.

Finally, we achieved the direct visualization of the magnetic configuration of strained LCMO thin films at 100 K using a cryogenic TEM holder, which allowed observing the effects of the substrate-induced strain on the magnetic properties of the films. While LCMO thin films grown on an $SrTiO_3$ substrate (tensile induced strain) present a magnetic phase separation effect with a non ferromagnetic layer at the surface of the film, LCMO thin films grown on $LaAlO_3$ (compressive strain) present an out-of-plane magnetocrystalline anisotropy. These anomalous behaviors were contrasted with macroscopic magnetic measurements finding that they account for an apparent reduction of the saturation magnetization. The evidence of an exchange bias effect and theoretical calculation allowed concluding that the non-ferromagnetic layer has an antiferromagnetic ordering.

Resumen

En esta Tesis, hemos desarrollado estudios cualitativos y cuantitativos de los estados magnéticos de diferentes nanoestructuras ferromagnéticas mediante experimentos *in situ* de Microscopia Lorentz (LM) y Holografia Electrónica (EH) con la aplicación de campos magnéticos o trabajando a bajas temperaturas (100 K). Se ha realizado una investigación detallada en tres diferentes nanoestructuras ferromagnéticas: (*1*) nanohilos de Cobalto y $Co_{50}Fe_{50}$ en forma de "L", crecidos respectivamente por técnicas de deposición inducida por haz de electrones focalizados (FEBID) y litografía por haz de electrones (EBL); (*2*) redes cuadradas de *antidots* de cobalto fabricadas combinando técnicas de *sputtering* y litografía por haz de iones focalizado (FIB); y (*3*) láminas delgadas epitaxiales de $La_{2/3}Ca_{1/3}MnO_3$ (LCMO) crecidas por la técnica de deposición por laser pulsado (PLD). Además se ha optimizado el método tradicional para realizar experimentos *in situ* de LM y EH con la aplicación de campos magnéticos a través de la lente objetivo. En esta optimización, hemos elaborado una descripción matemática que permite el control total de la componente en el plano de la muestra del campo magnético producido por la lente objetivo. Esta componente en el plano se ha usado ampliamente para desarrollar los diferentes estudios de la inversión de la imanación en los hilos y matrices de antidots ferromagnéticos que se presentan a continuación.

En el caso de los nanohilos magnéticos, se ha realizado un estudio cuantitativo de los procesos de inversión de la imanación a través de la manipulación de paredes de dominio (DW) individuales. En el caso de nanohilos de Co en forma de "L", se han estudiado los procesos de nucleación de DW en función de las dimensiones laterales de la nanoestructura y de su espesor. Para una serie particular de nanohilos de Co de 500 nm de anchura, se detectó una variación progresiva de la configuración magnética de las DW nucleadas al aumentar el espesor. Estos cambios de configuración produjeron efectos importantes en la dependencia del campo coercitivo (H_C) con el espesor tales como un valor máximo de H_C justo en la transición entre una pared transversal

asimétrica y una pared tipo vórtice asimétrica. En el caso de los nanohilos de $Co_{50}Fe_{50}$ con nanoconstricciones también con forma de L, experimentos *in situ* de LM han permitido evaluar la calidad del anclaje/desanclaje de DW individuales al incrementar el campo magnético. Para esta evaluación, se fabricaron series de nanoconstricciones dispuestas a lo largo de uno de los brazos del nanohilo, donde se ha analizado cuál es la serie de muescas que presenta un mejor comportamiento de anclaje/desanclaje.

También se han estudiado los estados magnéticos remanentes de redes antidots de cobalto con agujeros de 55 nm de diámetro y diferentes periodicidades (p). Para la exploración de las propiedades magnéticas de redes de antidots con periodicidades bajas ($p \leq 160$ nm), se ha implementado un método de filtrado a bajas frecuencias para aumentar los contrastes magnéticos observado dentro de las redes a través de LM en modo Fresnel. En redes de antidots con $116 \leq p \leq 160$ nm, se encontró que la estructura magnética se compone principalmente de superdominios magnéticos y cadenas magnéticas con una anchura de una celda unidad. Experimentos de inversión de la imanación a través de LM en el arreglo de antidots de 160 nm de periodicidad han demostrado que tal inversión ocurre por la nucleación y propagación de paredes de superdominio magnéticas (SDWs), y se ha observado una clara diferencia en función de la orientación del campo magnético aplicado: mientras ésta ocurre por la nucleación y propagación simultanea de SDWs cuando se aplica campos magnéticos transversales a las columnas de antidots, campos magnéticos paralelos a las columnas de antidots producen un inversión de la imanación en dos etapas: el sistema primero nuclea y propaga SDWs horizontales, para luego nuclear y propagar SDWs verticales.

Finalmente, la visualización directa de la configuración magnética de láminas delgadas tensionadas de LCMO a baja temperatura nos ha permitido analizar los efectos de la tensión epitaxial inducida por el sustrato en las propiedades magnéticas de las láminas. Mientras las láminas crecidas sobre sustratos de $SrTiO_3$ (tensión expansiva) presentan un efecto de segregación de fase magnética donde una capa no ferromagnética se forma en la superficie de la manganita, láminas de LCMO crecidas sobre sustratos de $LaAlO_3$ (tensión compresiva) exhiben una anisotropía magnetocristalina fuera del

plano del sustrato. Estos comportamientos anómalos se han contrastado con medidas macroscópicas de imanación encontrando que dan buena cuenta de la aparente reducción de la imanación de saturación y de la forma de los ciclos de histéresis. Medidas adicionales en las que se ha observado el fenómeno de *exchange bias*, así como cálculos teóricos han permitido concluir que la capa superficial no ferromagnética tiene un ordenamiento antiferromagnético.

Résumé

L'objectif général de la thèse vise à développer des mesures quantitatives des configurations magnétiques locales dans des matériaux nanostructurés par des études *in-situ* en microscopie de Lorentz (LM) et holographie électronique (EH) sous l'application de champs magnétiques extérieurs et à basse température (100 K). Ce travail fait partie d'une collaboration entre les deux groupes de recherche du LMA -INA et du CEMES–CNRS.

Dans la première partie de ma thèse, je me suis attaché au développement d'une procédure d'expérience *in-situ* en LM et EH permettant de contrôler le champ magnétique appliqué dans le plan de l'objet étudié en utilisant le champ magnétique produit par la lentille objectif. Ceci est réalisé en adaptant l'excitation de la lentille objectif et en ajustant l'orientation de l'objet plongé dans ce champ pour contrôler l'intensité et la direction du champ appliqué. J'ai évalué les performances et les limitations de cette procédure d'application d'un champ *in-situ* en MET au travers de deux études : 1/ le contrôle de la position des parois de domaine magnétiques (DW) dans un nano-anneau de Co déposé par FEBID, 2/ l'étude de l'effet de la composante magnétique hors-plan sur la mesure du champ coercitif des films minces monocristallins de manganite et d'un nanofil polycristallin de Co.

Dans une deuxième partie, j'ai utilisé cette méthode de pour étudier les processus de nucléation et propagation de DWs dans les nanofils de Co en forme de « L ». Nous avons étudié les configurations de DWs et leurs champs de nucléation et de propagation pour différentes épaisseurs de nanofils. Pour une largeur donnée de nanofils (500 nm), nous avons trouvé que pour des épaisseurs $t < 13$ nm le DW est une paroi *transverse* alors que pour des épaisseurs $t > 13$ nm elle est de configuration *vortex*. En outre, c'est à cette transition que la paroi est la plus mobile et que la différence entre les champs de nucléation et propagation est la plus grande offrant la possibilité de manipuler facilement cette paroi et d'envisager des applications dans le domaine de l'enregistrement magnétique. J'ai également étudié localement *in-situ* les processus de

piégeage/dé-piégeage de DWs dans des nanofils de $Co_{50}Fe_{50}$ sur lesquels ont été gravé des nanoconstrictions de diverses formes.

Dans une troisième partie, nous avons étudié les configurations magnétiques dans des réseaux d'antidots ferromagnétiques fabriqués à partir d'une couche mince de cobalt. Nous avons tout d'abord étudié l'effet de la géométrie du système (périodicité des réseaux, tailles des trous) sur les configurations magnétiques à rémanence. Pour périodicités $p \leq 160$ nm, nous avons observé la formation de « superdomaines » magnétiques. Pour améliorer la visualisation de ces superdomaines par LM, j'ai développé une méthode de filtrage de Fourier de basse fréquence. J'ai ensuite mené des études *in-situ* en LM en effectuant des cycles d'hystérésis avec un champ appliqué parallèlement aux rangées d'antidots puis dans la diagonale des réseaux. Nous avons mis en évidence des modes de propagation de DWs et des mécanismes de renversement d'aimantation distincts.

La quatrième partie de ma thèse est consacrée au développement d'études LM et EH *in-situ* à basse température pour étudier les effets de contraintes épitaxiales sur les propriétés magnétiques de couches minces épitaxiales de manganites : $La_{2/3}Ca_{1/3}MnO_3$ (LCMO). Nos études à basse température sur diverses couches de LCMO épitaxiées sur différents substrats ($SrTiO_3$, LaSr,$AlTaO_3$ and $LaAlO_3$) ont permis pour la première fois une caractérisation directe de l'aimantation locale dans les couches minces épitaxiées de LCMO. Nous avons mis en évidence la formation d'une couche non ferromagnétique à la surface du film mince de LCMO dépendant de l'état de contrainte (en compression) de la couche; la variation de l'anisotropie magnétocristalline variant avec la contrainte épitaxiale lorsque le film est en tension; la disparition de la couche non ferromagnétique lorsque que la couche de LCMO contrainte relaxe par traitement thermique. Tous ces résultats expérimentaux ont été confortés par des mesures macroscopiques complémentaires que nous avons menées par magnetometry SQUID et par des simulations théoriques prenant en compte les effets de contraintes sur les propriétés magnétiques dans ces couches d'oxydes

Index

Acronym list

2VW: Double Vortex Wall.
AFM: Antiferromagnetic.
ATW: Asymmetric Transversal Wall.
AVW: Asymmetric Vortex Wall.
C-FEG: Cold Field Emission Gun.
CNW: Curved Notch Wire.
CTEM: Conventional TEM.
DFT: Density Functional Theory.
DPC: Differential Phase Contrast.
DW: Domain Wall.
EA: Easy Axis.
EBL: Electron Beam Lithography.
EELS: Electron Energy Loss Spectroscopy.
EH: Electron Holography.
FC: Field Cooling.
FEBID: Focused Electron Beam Induced Deposition.
FFT: Fast Fourier Transform.
FFT^{-1}: Inverse Fast Fourier Transform.
FIB: Focused Ion Beam.
FIBID: Focused Ion Beam Induced Deposition.
FM: Ferromagnetic.
GGA-PBE: Generalized Gradient Approximation – Perdew-Burke-Ernzerhof.
GIS: Gas-Injection-System.
GMR/TMR: Giant magnetoresistance/Tunnel magnetoresistance.
GPA: Geometry Phase Analysis.
GPU: Graphical Processor Unit.
HA: Hard Axis.
HAADF: High Angle Annular Dark Field.
HRTEM: High Resolution Transmission Electron Microscopy.
LCMO: $La_{2/3}Ca_{1/3}MnO_{3.}$
LE-SDW: Low-Energy Superdomain Wall.
LF: Lorentz Force.
LLG: Landau-Lifshitz-Gilbert.
LM: Lorentz Microscopy.
LMIS: Liquid-Metal Ion Source.
LSMO: $La_{2/3}Sr_{1/3}MnO_{3.}$
MBE: Molecular Beam Epitaxy.
MC: Magnetic Chain.
MEMS: Micro-ElectroMechanical System.
MFM: Magnetic Force Microscopy.
MOKE: Magneto-Optical Kerr Effect.
MRAM: Magnetoresistive Random-Access Memory.
MTJ: Magnetic Tunnel Junction.
M-XTM: Magnetic X-ray Transmission Microscopy.
NFL/R: Non ferromagnetic layer/region.

NW: Nanowire.

OL: Objective lens.

OOMMF: Object Oriented MicroMagnetic Framework.

RKKY: Ruderman-Kittel-Kasuya-Yoshida.

RNW: Rectangular Notch Wire.

SD: Superdomain.

SDW: Superdomain Wall.

SEM: Scanning Electron Microscopy.

SEMPA: Scanning Electron Microscopy with Polarization Analysis.

S-FEG: Schottky Field Emission Gun.

SIMS: Secondary Ion Mass Spectroscopy.

SPLEEM: Spin-Polarized Low-Energy Electron Microscopy.

SP-STM: Spin-Polarized Scanning Electron Microscopy.

SQUID: Superconducting Quantum Interference Device.

STEM: Scanning Transmission Electron Microscopy.

STXM: Scanning Transmission X-ray Microscopy.

TEM: Transmission Electron Microscopy/Microscope.

TIE: Transport of Intensity Equation.

TNW: Triangular Notch Wire.

TW: Transversal Wall.

VW: Vortex Wall.

XEDS: X-ray Energy-Dispersive Spectroscopy.

XFEG: High brightness Field Emission Gun.

XMCD-PEEM: X-ray Magnetic Circular Dichroism – PhotoElectron Emission Microscopy.

XRD: X-Ray Diffraction.

ZFC: Zero Field Cooling.

Chapter 1

Introduction

1.1. Magnetism: a brief history and its importance

Just take a glance around us to realize that Magnetism plays a crucial role in our modern life. Most of the technological devices of daily use are based on or contain magnetic materials: TVs, cell phones, computer hard disks, credit cards, speakers, electric motors, sensors… the list would be never-ending. More than 2500 years have passed since the man discovered the first magnetic material, the magnetite (Fe_3O_4), and the human wasted no time in exploiting its attractive properties.

Historically, the first practical application of Magnetism was documented in China, between 221-206 BC, with the invention of the "*south pointer*". This ancestor of the compass was a lodestone carved with a spoon shape that rotated on a surface to align its handle, magically, with the Earth's magnetic field. Considered of divine nature, the south pointer was initially a tool to predict the fortunate location for burials sites, harmonic building construction and even decision-making in Chinese culture (nowadays it is used as part of *feng shui*), but then hunters began to use it as a tool that prevented them from getting lost in their journeys. More than 14 centuries passed before the Chinese started to fabricate compasses for navigation purpose for military orienteering (1040-1044 AC) and maritime navigation (1111-1117 AC).

At the beginning of the 17th century, William Gilbert wrote in his book "*De Magnete*" the first truly scientific study of Magnetism known to that date, giving explanation of some magnetic phenomena formerly attributed to superstition. He investigated the properties of iron magnets and lodestones, and formed a clear picture of the Earth's

magnetic field. In 1743, Daniel Bernoulli invented one of the most iconic symbols of Magnetism: the horseshoe magnet. The idea arose as an attempt to solve the problem of building a reasonably compact magnet that did not destroy itself in its own demagnetizing field. The greatest advances in the understanding of the magnetic phenomenology were achieved in the 19th century. The works of Hans Christian Ørsted, André-Marie Ampère and Dominique François Jean Arago in 1820 demonstrated the relationship between electricity and magnetism, while Michael Faraday discovered in 1845 the connection between magnetism and light (magneto-optic Faraday effect). These discoveries inspired them to develop the key principles of future technologies as revolutionary as the electromagnetic telegram (proposed by Ampère) and an electric motor (proposed by Faraday). All these experimental works, together with other works in the field of electricity, inspired James Clerk Maxwell to formulate a unified theory of electricity, magnetism and light in 1864, which was subsequently summarized in the four famous equations known as *the Maxwell's equations*. The Revolution of the Magnetism started! This boosted a fast development of electromagnetic energy converters (motors and generators), electromagnetic propagation devices (radios, televisions, antennas, radars), and helped to develop new groundbreaking theories… such as the Theory of the Relativity [1]. The 20th century progresses on Magnetism were focused on the understanding of its microscopic origin. In 1907 Pierre Weiss gave a successful explanation of the loss of ferromagnetism above the Curie point through the molecular field theory. He also theorized that magnetic materials were composed by numerous microscopic magnets ("*domains*"), randomly oriented in a virgin ferromagnet that were reoriented along the external field when the system was magnetized. Later on, the discovery of the spin of the electron by George Uhlenbeck and Samuel Goudsmit in 1925 paved the way to Werner Heisenberg, who postulated in 1929 the quantum-mechanical origin of ferromagnetism through a Hamiltonian that represents the exchange interaction between two neighboring atomic spins. The advances in the understanding of Magnetism at the atomic scale allowed the development of important methods such as the magnetic resonance (in the 1940s and 1950s) and the introduction of powerful spectroscopic and diffraction techniques that permitted the determination of the magnetic and electronic structure of solids. In addition to traditional

electromagnetic and electromechanical devices, ferromagnets were used in the second half of the 20th century as data storage media. From credit cards to magnetic recording tapes and hard disk drives, the multidomain nature of magnetic materials is still currently exploited to satisfy the demand for ever-increasing data storage density, currently approaching 1 Tbit/inch^2 [2]. Nowadays, new trends on applied Magnetism aim at manipulating the spin transport electronics (Spintronics) in order to improve the performance of devices purely based on charge transport. This includes devices to read, write and store data, such as Giant Magnetoresistance (GMR) and Tunnel Magnetoresistance (TMR) read heads, magnetoresistive random-access memories (MRAMs) and racetrack memories, but also magnetic sensors and magnetic logic circuits [3]. In the last decade novel, even more ambitious and unexpected applications of Spintronics have been envisaged as a potential alternative to semiconductor electronics based on spin-only transport due to Rashba-type spin-orbit coupling [4,5], or in energy harvesting based on the use of temperature gradients to produce spin currents in the so-called spin-Seebeck effect [6].

1.2. Fundaments of Magnetism

1.2.1. Quantum origin of magnetic order

The magnetism has its origin in the magnetic moment of the atoms produced by the angular momenta of its constituent electrons. Each atomic electron presents two types of angular momenta: an *orbital moment, L*, associated to the orbital motion of the electron around the nucleus, and a *spin momentum*, *S*, which is intrinsic to its nature, see Figure 1.1. Most of the atoms are composed by several electrons, and their individual orbital angular moments couple to produce a total orbital angular momentum of $\mathbf{L} = \sum_i \mathbf{l}_i$. The same occurs with the spin angular moment, so $\mathbf{S} = \sum_i \mathbf{s}_i$. Thus, the electronic magnetic moment, $\boldsymbol{\mu}$, associated to each total atomic angular momenta can be expressed as:

$$\mathbf{m}_L = -\mu_B \mathbf{L} \qquad \text{(Eq. 1.1)}$$

$$\mathbf{m}_S = -2\mu_B \mathbf{S} \qquad \text{(Eq. 1.2)}$$

where μ_B is the *Bohr magneton*, a physical constant depending on the electron charge, e, electron rest mass, m, and reduced Planck constant, $\hbar$, [$\mu_B = e\hbar/(2m) = 9.274\times10^{-24}$ J/T].

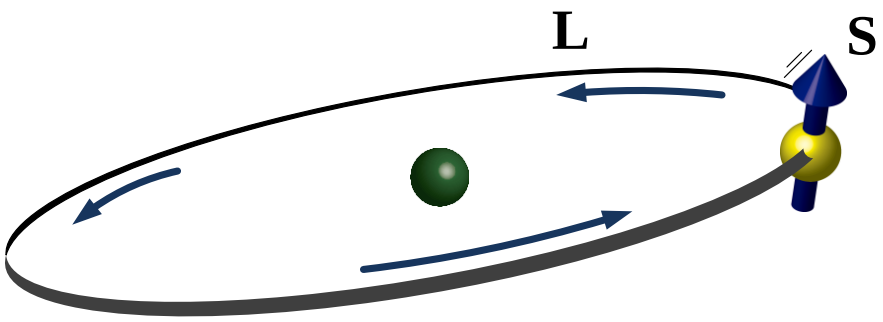

Figure 1.1. Sketch representative of the two angular momenta associated to the electron: orbital (**L**) and spin (**S**) angular momentum. Green and yellow balls ideally represent the electron and nucleus respectively.

Thus, the total magnetic moment in the atom is then given by

$$\mathbf{m} = -\mu_B(\mathbf{L} + 2\mathbf{S}) \qquad \text{(Eq. 1.3)}$$

According to the Pauli exclusion principle [7] and the Hund's rules [8], atoms with "closed electronic shells" (their orbitals fully occupied) have a net magnetic moment equal to zero because, in each shell, the electrons are paired: there are as many electrons orbiting or spinning in one direction as in the opposite direction, so the net magnetic moment in each shell is zero. Atoms with "partially filled electronic shells" have however unpaired electrons, usually in the outermost shell, that contribute to produce a net *atomic magnetic moment* different to zero. Thus, unpaired electrons in the atomic

shells produce the magnetic response of the materials. This atomic magnetic moment will be equal to

$$\mathbf{m}_J = -g_J \mu_B \mathbf{J} \qquad \text{(Eq. 1.4)}$$

where **J** is the total electronic angular momentum of the unpaired electrons and g_J is called the Landé *g*-factor, which is related with the different total quantum numbers *L*, *S*, and *J*

$$g_J = 1 + \frac{J(J+1) + S(S+1) - L(L+1)}{2J(J+1)} \qquad \text{(Eq. 1.5)}$$

Even if Equation 1.4 considers both orbital and spin angular momenta of the atom, the largest contribution to the total magnetic moment is due to the spin, which is 10 times stronger that the orbital angular momentum, for instance, in the ferromagnetic elements Fe, Co and Ni [9]. In an arrangement of atoms (e.g., a crystal lattice), the atomic magnetic moments of neighboring atoms interact with each other through a quantum phenomenon known as *exchange interaction*. Proposed for first time by Heisenberg in 1928 [10], two atoms with unpaired electrons of spins $\mathbf{S}_i$ and $\mathbf{S}_j$ interact with an energy

$$\varepsilon = -2J_{ij}\mathbf{S}_i \cdot \mathbf{S}_j \qquad \text{(Eq. 1.6)}$$

where J_{ij} is the exchange constant. If $J_{ij} > 0$, the energy is lowest when $\mathbf{S}_i$ is parallel to $\mathbf{S}_j$, while $J_{ij} < 0$, an antiparallel alignment of the spins will minimize the energy. Thus, the type of exchange interaction defines the type of magnetism: in absence of an external magnetic field, a parallel alignment of spins produces a long-range *ferromagnetic* (*FM*) order, while an antiparallel alignment of neighboring spins induces an *antiferromagnetic* (*AFM*) order.

1.2.2. Fundaments of ferromagnetism

Ferromagnetism is a term used to refer to a material with a strongly magnetic behavior like permanent magnets. Historically, these ferromagnetic materials were the first magnetic materials discovered and, for this reason, the term "*magnetic materials"* has been traditionally assigned to them. From a macroscopic point of view, a microscopic ferromagnetic order induces a *spontaneous magnetization* at zero applied magnetic field, where the magnetization (**M**) is defined as the magnetic moment density per volume unit. The existence of a net magnetization produces around the material a magnetic induction field, which results in the strong attractive or repulsive force that magnetic materials exert on other ferrous materials. The first theory explaining such spontaneous magnetization was postulated by P. Weiss in 1907 [11]. He considered that, in the site of each spin, there is an effective field produced by the interaction with the neighboring spins. Thus, effective induction field, **B**, that one spins feels is

$$\mathbf{B} = \lambda_W \mathbf{M} \qquad \text{(Eq. 1.7)}$$

where **M** is the total magnetization of the system and λ_W is the mean field parameter that represents the strength of the interaction (*Weiss constant*). These ordered spin states could be altered by the temperature. When the temperature of the system increases, the thermal agitation introduced in the ensemble destroys such long-range spin order. Above a critical temperature, called Curie temperature (T_C), the thermal excitation dominates and their magnetic moments are randomly oriented, producing a *paramagnetic* state. Thus, Curie temperature and spontaneous magnetization are two characteristic parameters of ferromagnetic materials.

Another important feature of ferromagnetic materials is the fact that, even if the exchange interaction is strong enough to align all spins in the same direction at microscopic scale, this state cannot be preserved macroscopically unless an external magnetic field is applied. In a micromagnetic scale, not only the exchange interaction and thermal excitation contributes to the internal energy of the system, there are other

energy contributions related to additional factors such as the crystal structure, the shape, the external magnetic field, stress and magnetostriction.

1.2.3. Micromagnetic energy

The equilibrium state of a ferromagnetic material is determined by the minimization of the total "magnetic" Gibbs free energy of the system. This is composed by the sum of several energy contributions

$$\varepsilon_{tot} = \varepsilon_{ex} + \varepsilon_a + \varepsilon_d + \varepsilon_Z + \varepsilon_{stress} + \varepsilon_{ms} \qquad \text{(Eq. 1.8)}$$

where the first three terms are intrinsic to the ferromagnetic material: exchange (ε_{ex}), magnetocrystalline anisotropy (ε_a) and demagnetizing (ε_d) energies. The fourth energy is associated to the response of the material to the application of an external magnetic field, the Zeeman energy (ε_Z). The last two energy terms are related to applied stress and magnetostriction, and their contribution to the total energy is very small, so that they are usually neglected. More in detail, each energy contribution acts in the system as follow:

Exchange energy: It is caused by the exchange coupling between the spins to tend to line them up in the same direction. The exchange energy can be expressed as an integral overall volume, *V*,

$$\varepsilon_{ex} = \int A\left(\frac{\nabla \mathbf{M}}{M_S}\right)^2 dV \qquad \text{(Eq. 1.9)}$$

where ∇ is the gradient operator applied to the magnetization vector and *A* is the exchange constant. This energy tends to favor that the spins are always parallel between them. The Heisenberg model used to deduce Equation 1.9 describes suitably the direct exchange interaction between two ions; other models such superexchange [12,13] (in oxides) or Ruderman-Kittel-Kasuya-

Yoshida (RKKY) [14–16] (in metals) are used to describe indirect exchange interactions.

Magnetocrystalline energy: This energy contribution reflects the interaction of the magnetization with the crystal lattice. It is associated to the Coulomb interaction between the electrons of a magnetic ion and the surrounding ions in a crystal. The coordination and symmetry of the crystal environment affect the spatial distribution and population of the orbitals of the magnetic ions and, through the spin-orbit coupling, this causes a preferred orientation of the magnetization with respect to the crystal. Thus, this *magnetization easy axis* depends on the crystal structure of the magnetic material. In the case of *uniaxial anisotropy* (only one preferential magnetization direction), the first term of the magnetocrystalline anisotropy is

$$\varepsilon_{aUni} = -\int K \sin^2(\theta) dV \qquad \text{(Eq. 1.10)}$$

where θ is the angle between the easy axis and the magnetization, and K the anisotropy constant. However, in *cubic crystals* (with more than one preferential magnetization direction allowed by symmetry)

$$\frac{\varepsilon_{aCub}}{V} = K_0 + K_1(\alpha_1^2\alpha_2^2 + \alpha_2^2\alpha_3^2 + \alpha_1^2\alpha_3^2) \qquad \text{(Eq. 1.11)}$$

where K_0 and K_1 are anisotropy constants and the α_s (s = 1, 2 and 3) are direction cosines, i.e., the cosines of the angle between the magnetization and the crystal axis.

Demagnetizing energy (or magnetostic energy): The demagnetizing energy is also an anisotropy term related to the geometry of the nanostructure (also called *shape anisotropy*). It could be expressed as

$$\varepsilon_d = -\frac{1}{2}\int \mathbf{M} \cdot \mathbf{H}_d \, dV \qquad \text{(Eq. 1.12)}$$

where $\mathbf{H}_d$ is the *demagnetizing field*, which depends on the magnetic configuration of the system, which in turn depends on the shape of the magnetic material. If the magnetization of the specimen is oriented in one direction (for instance, by means a strong magnetic field), "magnetic free poles" appear producing a magnetic field directed opposite to the magnetization. Its intensity is proportional to the magnetic free pole density and the shape of the specimen

$$H_d = -\frac{1}{\mu_0} NM \qquad \text{(Eq. 1.13)}$$

where μ_0 is the magnetic permeability, M is the magnitude of the magnetization and N is the *demagnetizing factor*, which depends only on the shape of the specimen. The demagnetizing or stray field has important implications in ferromagnetic materials: it is the magnetic field produced by permanent magnet and, at the same time, induces the formation of *"magnetic domains"*.

Zeeman energy: This is the energy contribution of a magnetic material embedded in an external magnetic field, **H**. Similar to the demagnetization energy, Zeeman energy is expressed as

$$\varepsilon_Z = -\int \mathbf{M} \cdot \mathbf{H} dV \qquad \text{(Eq. 1.14)}$$

The Zeeman energy favors the alignment of the spins parallel to the external magnetic field. If it is very strong, the total energy of the system is minimized by reaching its maximum magnetization, which is the same magnetization of each magnetic domain. In this condition, a ferromagnetic system is *saturated*.

Thus, the final stationary micromagnetic state of a magnetic body minimizes the total magnetic energy of the system, i.e., the sum of the different energy terms of the equation 1.8. If we consider an equilibrium state free of external magnetic fields (ε_Z = 0), with a temperature sufficiently low that the thermal energy can be neglected (i.e., $T << T_C$), a saturation magnetization condition along the easy magnetization direction

will minimize both exchange and magnetocrystalline energies. However, this configuration will induce the appearance of positive and negative magnetic charges at the surfaces, producing a large demagnetizing field. To decrease the demagnetizing energy, the local magnetization close to the magnetic charges tends to rotate, orientating parallel to the surface edge. This effect favors the minimization of the ε_d by the reduction of the stray field, but disfavors ε_{ex} and/or ε_a. The best solution found by the system is to break into small regions where the magnitude of the magnetization is the same in each point, but their direction is different with respect to the neighboring regions. Thus the competition of the different terms of micromagnetic energy produces *magnetic domains* in a ferromagnetic material, see Figure 1.2. The shape and size of each domain, as well as the magnetic configuration of all magnetic domains in ferromagnets, depend on the precise balance between these terms, which is determined by the magnetic parameters of the material (exchange constant, A; anisotropy constant, K, saturation magnetization, M_S), the shape of the structure (demagnetizing factor, N) and the magnetic history.

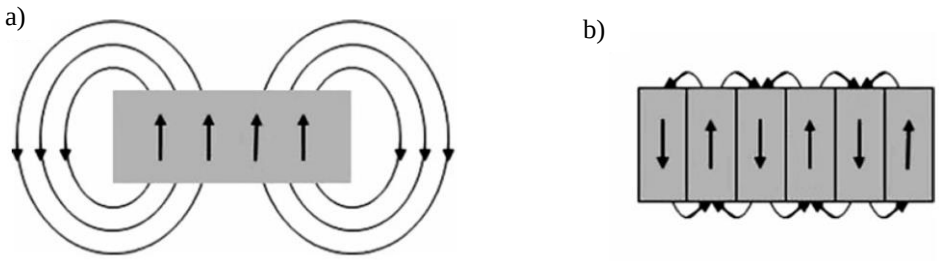

Figure 1.2. Formation of magnetic domains: (a) alignment of the magnetization results in an intensive stray field (large magnetostatic energy); (b) division into small magnetic domains permits the reduction of the magnetostatic energy. Image extracted to Ref. [9].

1.2.4. Micromagnetic Simulation

Magnetic states in a ferromagnetic can be perfectly simulated by the Landau-Lifshitz-Gilbert (LLG) equation [17,18], which defines the time evolution of the magnetization under a local effective magnetic field $\mathbf{H}_{eff}$. Such magnetization equation of motion is usually expressed as

$$\frac{d\mathbf{M}}{dt} = -\gamma\mathbf{M} \times \mathbf{H}_{eff} - \frac{\gamma\alpha}{M_S}\mathbf{M} \times (\mathbf{M} \times \mathbf{H}_{eff}) \qquad \text{(Eq. 1.15)}$$

where $\mathbf{H}_{eff}$, γ and α are the effective field, gyromagnetic ratio and damping parameter, respectively. According to Brown´s theory [19], the effective field can be expressed as a functional derivative of the average energy density, E, as a function of the magnetization:

$$\mathbf{H}_{eff} = -\frac{1}{\mu_0}\frac{\partial E_{tot}}{\partial \mathbf{M}} \qquad \text{(Eq. 1.16)}$$

where $\varepsilon_{tot} = \int_V (E_{tot})\, dV$. This means that E_{tot} will correspond to the sum of the all integrands of Equations 1.9, 1.10, 1.11, 1.12 and 1.14. This effective field exerts a torque on the magnetization vector of each "*magnetic unit cell*" that induces a precession movement, which is described by the first term of Equation 1.15. The magnetization is reoriented toward the effective field following a damping process as a function of time, which is described by the second term of Equation 1.15. There are very few situations where the LLG equation can be solved analytically; in general we need to use numerical methods for its solution. In addition, Equation 1.15 is only valid assuming that: (*i*) magnetization is a continuous function of the position, $\mathbf{M} = \mathbf{M}(\mathbf{r})$; (*ii*) magnetization modulus is constant in every point and equal to the saturation magnetization, $|\mathbf{M}| = M_S$.

There are several micromagnetic simulation packages available to solve the LLG equation such as Nmag [20], Mumax3 [21], MicroMagnum [22] and OOMMF [23] among others, being the last one the most commonly used. However, all micromagnetic

simulations of this Thesis have been carried using the GPMagnet software package [24]. This software performs highly efficient micromagnetic simulations thanks to the use of standard code running in a Graphical Processor Unit (GPU), taking advantage of its potential to make parallel calculations. For instance, in comparison with classical OOMMF package, the computational time of GPMagnet is reduced by two orders of magnitude. The aim of the simulation is to minimize the total energy of the magnetic system, which is usually subdivided in a rectangular mesh of prisms, called *magnetic unit cell*, with lateral sizes preferably less than the characteristic exchange length, $l_{ex} = (2A/\mu_0 M_S^2)^{1/2}$, of each magnetic material (in most ferromagnets l_{ex} has a value of 2-6 nm [25]). The simulation starts from an initial magnetization state that can be stimulated with an external magnetic field. Generally, such initial magnetization conditions does not represent the magnetic state with minimum energy, so the simulation runs iteratively to minimize the energy until a given convergence criteria is satisfied, which could be either a maximum numbers of iterations or that the variation of the magnetization of the system with the time reaches a certain minimum value. The final magnetic configuration is considered the equilibrium state for a given external magnetic field. The solution of the Equation 1.15 allows calculating the magnetization direction distribution through the dynamic evolution of the system. However, if we are only interested in determining the magnetization distribution at equilibrium (static method), it is sufficient to solve the equilibrium equation

$$\mathbf{M} \times \mathbf{H}_{eff} = 0 \qquad \text{(Eq. 1.17)}$$

1.3. Objectives and outline of the Thesis

The aim of this Thesis is the development of qualitative and quantitative studies of the local magnetic states of different ferromagnetic nanostructures such as Co and $Co_{50}Fe_{50}$ nanowires, Co antidot arrays and epitaxially strained $La_{2/3}Ca_{1/3}MnO_3$ (LCMO) thin films by *in situ* Lorentz Microscopy (LM) and Electron Holography (EH) experiments under the application of magnetic fields and working at low temperature

(100 K). For the development of *in situ* experiments with magnetic field, we have improved and generalized the traditional method where a controlled magnetic field is applied with the objective lens of the microscope, in a perpendicular direction of the sample plane. By a predictable double-tilt rotation of the sample, we have achieved a perfect control of the in-plane component of the magnetic field. Such magnetic field has been subsequently employed to perform magnetization reversal studies in different nanoscale ferromagnets, such as magnetic nanowires and antidot arrays. On the other hand, the use of a special TEM holder that cools down the sample to 100 K and reaches the ferromagnetic state of LCMO manganite has allowed us studying the effect of the substrate-induced strain in the magnetic properties of epitaxial LCMO manganite thin films.

This Thesis work has been structured in the present introduction (*Chapter 1*) followed by 6 chapters:

In *Chapter 2* titled "*Experimental Techniques*", we describe the main experimental techniques employed for the fabrication and characterization of the magnetic nanostructures investigated. Most of *Chapter 2* is dedicated to a detailed description of the two main magnetic TEM characterization techniques: Lorentz microscopy and Electron Holography. In addition, we present the fundaments of the DualBeam Focus Ion/Electron Beam equipment, which is used to fabricate most of the nanostructures.

In *Chapter 3* titled "*In situ TEM characterization of magnetic nanostructures under external magnetic field"*, we present the mathematical basis of the quantitative control of the in-plane magnetic field applied by the objective lens that allowed us improving the *in situ* LM and EH experiments. The validation of the calculation, as well as the effect of the unavoidable out-of-plane component of the magnetic field is evaluated through experimental measurements on different magnetic nanostructures grown by Focused Electron Beam Induced Deposition (FEBID). Finally, we show how local hysteresis loops can be reconstructed in magnetic nanostructures with high shape anisotropy with high accuracy, illustrating the method on a Fe-based Magnetic Tunnel Junction (MTJ) heterostructure.

Chapter 4 "*Domain wall manipulation in Co and notched $Co_{50}Fe_{50}$ nanowires"* is devoted to the quantitative studies of domain wall (DW) manipulation in L-shape Co and ($Co_{50}Fe_{50}$) magnetic nanowires by *in situ* LM experiments. In the Co nanowires we study the DW nucleation processes and the dependence of the DW nature with the nanowire lateral dimensions, while in the $Co_{50}Fe_{50}$ nanowires we evaluate the efficiency of the field-driven propagation of DWs through sets of notches of different geometries.

In *Chapter 5* titled "*High-resolution imaging of remanent state and magnetization reversal processes in high-density cobalt antidot arrays"*, we present the qualitative and quantitative studies of the remanent magnetic states of square cobalt antidot arrays of different periodicities. A high-density antidot array with a periodicity of 160 nm has been selected to study the magnetization reversal processes of this system through the nucleation and propagation of magnetic superdomains upon the application of a magnetic field along the easy and hard magnetization axes of the antidot array.

Chapter 6 titled "*Strain-induced effects on the magnetic properties of epitaxial $La_{2/3}Ca_{1/3}MnO_3$ thin films"* explores the potential of low temperature EH experiments by probing locally the changes in the magnetic configuration of strained LCMO thin films and the appearance of a non-ferromagnetic layer (NFL) at the surface. These experiments are combined with additional macro- and microscopic experimental techniques and first-principles calculations to understand the origin of this NFL.

Finally, in the *Chapter 7*, we summarize the main conclusions of this Thesis and draw new perspectives in this area.

References

[1] Lowther D A and Freeman E M 2008 The application of the research work of James Clerk Maxwell in electromagnetics to industrial frequency problems. *Philos. Trans. A. Math. Phys. Eng. Sci.* **366** 1807–20

[2] Terris B D, Thomson T and Hu G 2006 Patterned media for future magnetic data storage *Microsyst. Technol.* **13** 189–96

[3] Wolf S A, Awschalom D D, Buhrman R A, Daughton J M, Von Molnár S, Roukes M L, Chtchelkanova A Y and Treger D M 2001 Spintronics: a spin-based electronics vision for the future. *Science* **294** 1488–95

[4] Awschalom D and Samarth N 2009 Spintronics without magnetism *Physics (College. Park. Md).* **2** 50

[5] Picozzi S 2014 Ferroelectric Rashba semiconductors as a novel class of multifunctional materials *Front. Phys.* **2** 1–5

[6] Uchida K, Takahashi S, Harii K, Ieda J, Koshibae W, Ando K, Maekawa S and Saitoh E 2008 Observation of the spin Seebeck effect. *Nature* **455** 778–81

[7] Pauli W 1925 Über den Zusammenhang des Abschlusses der Elektronengruppen im Atom mit der Komplexstruktur der Spektren *Zeitschrift für Phys.* **31** 765–83

[8] Hund F 1927 *Linienspektren und Periodisches System der Elemente* (Vienna: Springer Vienna)

[9] Stefanita C-G 2012 *Magnetism* (Berlin, Heidelberg: Springer Berlin Heidelberg)

[10] Heisenberg W 1928 Zur Theorie des Ferromagnetismus *Zeitschrift für Phys.* **49** 619–36

[11] Weiss P 1907 L'hypothèse du champ moléculaire et la propriété ferromagnétique *J. Phys. Théorique Appliquée* **6** 661–90

[12] Kramers H A 1934 L'interaction Entre les Atomes Magnétogènes dans un Cristal Paramagnétique *Physica* **1** 182–92

[13] Anderson P 1950 Antiferromagnetism. Theory of Superexchange Interaction *Phys. Rev.* **79** 350–6

[14] Ruderman M A and Kittel C 1954 Indirect Exchange Coupling of Nuclear Magnetic Moments by Conduction Electrons *Phys. Rev.* **96** 99–102

[15] Kasuya T 1956 A Theory of Metallic Ferro- and Antiferromagnetism on Zener's Model *Prog. Theor. Phys.* **16** 45–57

[16] Yosida K 1957 Magnetic Properties of Cu-Mn Alloys *Phys. Rev.* **106** 893–8

[17] Landau L and Lifshits E 1935 On the theory of the dispersion of magnetic permeability in ferromagnetic bodies *Phys. Zeitsch. der Sow.* **8** 153–69

[18] Gilbert T L 1955 A Lagrangian formulation of the gyromagnetic equation of the magnetic field *Phys. Rev.* **100** 1243

[19] Brown W F 1963 *Micromagnetics* (Michigan, USA: Interscience Publishers)

[20] Fischbacher T, Franchin M, Bordignon G and Fangohr H 2007 A Systematic Approach to Multiphysics Extensions of Finite-Element-Based Micromagnetic Simulations: Nmag *IEEE Trans. Magn.* **43** 2896–8

[21] Vansteenkiste A, Leliaert J, Dvornik M, Helsen M, Garcia-Sanchez F and Van Waeyenberge B 2014 The design and verification of MuMax3 *AIP Adv.* **4** 107133

[22] Abert C, Exl L, Bruckner F, Drews A and Suess D 2013 magnum.fe: A micromagnetic finite-element simulation code based on FEniCS *J. Magn. Magn. Mater.* **345** 29–35

[23] Donahue M J and Porter D G 2012 OOMMF User's Guide, Version 1.0, NISTIR 6376, National Institute of Standards and Technology

[24] Lopez-Diaz L, Aurelio D, Torres L, Martinez E, Hernandez-Lopez M A, Gomez J, Alejos O, Carpentieri M, Finocchio G and Consolo G 2012 Micromagnetic simulations using Graphics Processing Units *J. Phys. D. Appl. Phys.* **45** 323001

[25] Coey J M D 2010 *Magnetism and Magnetic Materials* (Cambridge University Press)

Chapter 2

Experimental Techniques

2.1. TEM magnetic imaging

2.1.1. Introduction

The study of the magnetic properties of nanoscale ferromagnets requires the combination of macroscopic characterization techniques, which provide magnetic information averaged over large length scales, with local techniques capable of probing magnetic properties with high spatial resolution and sensitivity. Among the latter, magnetic imaging techniques permit a direct study of the magnetic configurations, particularly magnetic domain structures, at the submicron scale. The possibility of imaging ferromagnetic order, together with the improvement of the computational time of micromagnetic simulations, has significantly contributed to the understanding of the magnetic phenomena that has enabled the latest technological applications in the field of Nanomagnetism and Spintronics [1–3]. Today, there are a substantial number of magnetic imaging techniques. Among the most popular, we can list the Kerr microscopy based in the magneto-optical Kerr effect (MOKE); the scanning electron microscopy with polarization analysis (SEMPA); the spin-polarized low-energy electron microscopy (SPLEEM); synchrotron radiation-based techniques such as x-ray magnetic circular dichroism, photoelectron emission microscopy (XMCD-PEEM) and magnetic x-ray transmission microscopy (M-XTM); the scanning probe techniques such as magnetic force microscopy (MFM) and spin-polarized scanning tunneling microscopy (SP-STM); and TEM-based techniques such as Lorentz microscopy (LM) and electron holography (EH) [4–7]. All these experimental methods offer a wide range of possibilities to study micromagnetic phenomena in different setups, as can be seen in

the comparative list of their main features presented in Table 2.1. Altogether they provide a spatial resolution ranging from microns to few angstroms, time resolution down to nanoseconds, a high sensitivity to detect small changes of the local magnetization, probing the surface or the volume properties, and sufficient versatility to enable the application of multiple external stimuli (temperature, electromagnetic fields, etc.). None of these techniques covers all these possibilities, and they are therefore complementary.

Table 1.1. Summary of the main features of the most relevant magnetic imaging techniques

Technique	Best spatial resolution	Image acquisition time	Type of imaging	Type of depth information	Information depth
XMCD-PEEM	300 nm	0.03 - 10 s	parallel	surface	< 5 nm
Kerr Microscopy	200 nm	10^{-8} to 1 s	parallel - scanning	surface	< 20 nm
MFM	40 nm	5 - 30 min	scanning	surface	< 2 μm
M-XTM	30 nm	3 s	parallel - scanning	volume	< 200 nm
SEMPA	20 nm	1 - 100 min	scanning	surface	< 0.5 nm
SPLEEM	10 nm	1 s	parallel	surface	< 1 nm
Lorentz Microscopy	10 nm	0.04 - 30 s	parallel	volume	< 100 nm
Electron Holography	1-2 nm	0.5 - 10 s	parallel	volume	< 100 nm
SP-STM	lateral (0.2 Å); vertical (0.01 Å)	30 s – 30 min	scanning	surface	< 0.2nm

From Table 2.1, we could classify the methods of magnetic imaging following different criteria that determines their range of application in terms of (spatial and time) resolution and sensitivity:

- The acquisition method: the image can be recorded using either a parallel acquisition of the signal in every point of the image simultaneously (e.g.

XMCD-PEEM, LM), or a serial acquisition in which a fine probe is scanned across the sample (e.g. MFM, SP-STM).

- The probe-specimen interaction on which the magnetic contrast is based: the Lorentz force experienced by electrons in the magnetic field of the sample (e.g. LM); the magnetic force on a magnetic tip caused by a stray field gradient (e.g. MFM); and magneto-optic coupling between photons and the magnetization of the material (e.g. Kerr microscopy); the Aharonov-Bohm effect in EH.

- The depth sensitivity, directly related to the probe-specimen interaction, determines whether the technique is sensitive only to the sample surface (e.g. MOKE, SPLEEM) or to the whole volume of the specimen such as in transmission techniques (e.g. M-XTM, LM and EH).

For the study of the local magnetic states, one of the most important requests is the achievable spatial resolution. This makes the TEM-based techniques very powerful tools that provide quantitative magnetic information of the volume of the sample with flexibility to apply external biases (magnetic and electric fields, injection of electrical current, changes in temperature, stress, light…) with a spatial resolution of few nanometers. The latter is only surpassed by SP-STM, whose spatial resolution goes down to atomic scale. To achieve the goals of the current "Nanotechnology revolution" – to understand and control matter at the nanoscale for industrial and technological application that benefit the society – magnetic TEM imaging techniques have become an indispensable instrument for the development of magnetic-based nanodevices.

Historically, the first attempts to study magnetic materials by TEM were to correlate the microstructure with the magnetic domain configuration measured by other techniques. For example, in 1958, Livingston explored the shape, size and distribution of ferromagnetic Co precipitates in relation with their magnetic characteristics [8,9]. A year before (1957), Mayer established the first method to observe the magnetism adapting an electron mirror microscope to observe artificial magnetic domain patterns produced by an array of linear magnetic stray fields and the magnetic contrasts of

ferromagnetic barium and nickel ferrite films [10]. In 1959, M. E. Hale and collaborators developed the first methods to image domain patterns in ferromagnetic thin films through defocused TEM imaging [11] and, thanks to the use of an off-centered objective diaphragm, to image magnetic domains [12]. These established the basis of LM in Fresnel and Foucault mode, respectively. In the 1970s and 1980s, other TEM-based magnetic techniques such as phase contrast microscopy [13–16] and off-axis EH (in the following, simply EH) [17,18] were developed. In these methods the magnetic information was obtained by retrieving the phase of the electron wave, although the electron beam phase shift measurements with sufficiently sensitivity had to wait for the development of high coherence electron sources which were available in commercial microscopes in the 90's. The basic principle of EH is based on an original ideal proposed by Gabor [19], in 1949 to overcome the resolution-limiting spherical aberration of the objective lens. He proposed to perform an interferometric experiment in TEM by overlapping the exit electron wave that interacts with the object with an unperturbed electron wave that passes entirely through the vacuum (reference wave), allowing extracting the full information of the exit electron wave (amplitude and phase). Thus EH can be used to measure the phase shift of the electron wave that has interacted with a magnetic field and therefore to measure this magnetic induction (see section 2.3).

The most common magnetic TEM imaging techniques are LM in Fresnel mode and EH, which are the ones used in this Thesis. In the following, we will describe the image formation processes in TEM, showing how LM and EH solve one of the big challenges of TEM imaging: the retrieval of the phase shift of the electron wavefunction, which is usually lost in a conventional TEM imaging process.

2.1.2 Image formation in TEM

The overall process of the image formation in TEM can be summarized in six steps, which follow the electron wave trajectory:

1- Creation and acceleration of an electron beam from an electron source

2- Illumination of the specimen with the (coherent) electron probe.

3- Scattering of the electron wave by the specimen,

4- Formation of a diffraction pattern in the objective lens *back focal plane*,

5- Formation of an image of the specimen in the objective lens *image plane*.

6- Projection of the image (or the diffraction pattern) on the detector plane.

In the first step, electrons are generated either by thermoionic emission of a filament (tungsten or LaB_6) heated at high temperatures, by the Cold Field Emission (C-FEG) extraction from an extremely sharp tungsten tip (W(310)) at room temperature, or by the combination of both methods in a so-called Schottky Field Emission Gun (S-FEG). The C-FEG and S-FEG guns are highly coherent and bright electron sources, essential for EH and LM, while thermionic source provide more intense but poorly coherent beam. In the second step, the electron wave is accelerated (typically up to 60 kV to 300 kV) and the illumination system (a set of two or three condenser lenses) allows defining the beam (probe size, convergence angle, electron dose) that irradiates the top surface of the specimen. The electron wave then interacts with the sample through various processes of scattering, both elastic and inelastic. The exit electron wave coming out of the specimen is processed by the objective lens to form a diffraction pattern of the specimen in the back focal plane and subsequently an image of the object (Abbey's theory of image formation in the microscope [20–22]). A schematic representation of the image formation in TEM following this simple idea is displayed in Figure 2.1(right-side).

The electron-specimen interaction makes that the incident electron wave changes its initial state by elastic and inelastic scattering phenomena. A summary of the signals generated in the electron-specimen interaction is also illustrated in Figure 2.1. In inelastic scattering processes, the electrons lose a small amount of energy that is transferred to the specimen producing the emission of a wide range of secondary signals (x-rays, visible light, secondary electrons, phonons and plasmons excitations), also damaging the specimen [23]. These secondary signals are very useful to perform analytical TEM experiments such as x-ray energy-dispersive spectroscopy (XEDS),

electron energy-loss spectroscopy (EELS) or cathodoluminescence. On the other hand, in elastic processes the electrons are scattered without losing energy. In crystalline materials, the elastic scattering gives rise to Bragg diffraction related to the constructive interference of the scattered electron waves in a periodic crystal. Thus, Bragg scattering results in a series of diffracted beams scattered at angles dependent on the lattice periodicities of the crystal structure. The elastically scattered electron beams are the ones use to form images in TEM techniques such as diffraction-contrast TEM [24] and phase-contrast High Resolution TEM (HRTEM) [25].

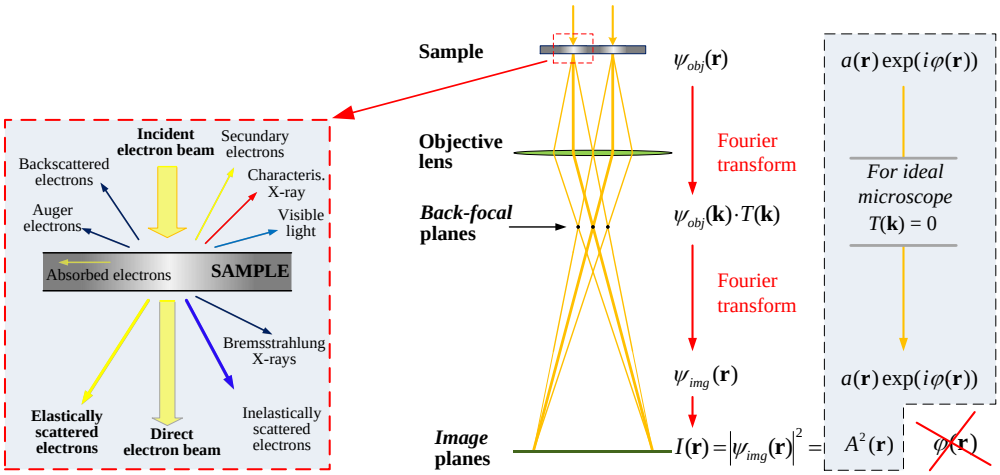

Figure 2.1 (*Left*) Signals generated by the electron beam-specimen interaction. (*Center*) Basic schematic representation of the image formation by the objective lens in a TEM. Yellow lines represent the optical path followed by the electrons during the image formation process. (*Right*) The corresponding mathematical description of the image formation for an aberration-free TEM, where the information of the phase shift is loss.

The mathematical description of the image formation process in a TEM is described as follows. According to the quantum mechanics, the scattering of a high-energy electron plane wave interacting with a crystalline specimen can be well explained by the relativistic time-independent Schrödinger equation, also known as Dirac equation [26,27]. Considering a *weak phase object approximation* (electrons are scattered elastically by a thin specimen and absorption effects are neglected), its solution

at the exit surface of the specimen is a transmitted wave function in the space **r** = (*x*, *y*, *z*) called *object electron wave*:

$$\varphi_{obj}(\mathbf{r}) = a(\mathbf{r})\exp(i\varphi(\mathbf{r})) \qquad \text{(Eq. 2.1)}$$

where $a(\mathbf{r})$ is the amplitude of the exit wave function and $\varphi(\mathbf{r})$ is a phase shift induced by the potential that the electrons interact with when passing through the sample. Next, the object electron wave is propagated by the objective lens to first create a diffraction pattern in its back focal plane and an image of the specimen in its image plane. According to diffraction theory, electrons scattered by the same lattice planes converge in a common point in the back focal plane of the objective lens, creating a representation of the specimen in the reciprocal space (i.e. a diffraction pattern). From a mathematical point of view, such diffraction pattern is the *Fourier transform* (*F*) of the object electron wave:

$$\psi_{obj}(\mathbf{k}) = F\{\psi_{obj}(\mathbf{r})\} \qquad \text{(Eq. 2.2)}$$

where **k** is the reciprocal vector. The Fourier transform $\psi_{obj}(\mathbf{k})$ is defined as

$$\psi_{obj}(\mathbf{k}) = \int \psi_{obj}(\mathbf{r})\exp(2\pi i\mathbf{k}\cdot\mathbf{r})d\mathbf{r}^3 . \qquad \text{(Eq. 2.3)}$$

In the image formation process the object electron wave is modified by the aberrations of the objective lens (mainly defocus, astigmatism and spherical aberration). These optical artifacts can be introduced by means of a *transfer function*, $T(\mathbf{k})$, multiplying the object electron wave in reciprocal space, $\psi_{obj}(\mathbf{k})$. Thus, the diffraction wave function, $\psi_{dif}(\mathbf{k})$, on the back focal plane becomes the following function

$$\psi_{dif}(\mathbf{k}) = \psi_{obj}(\mathbf{k})T(\mathbf{k}) . \qquad \text{(Eq. 2.4)}$$

In general, the transfer function can be expressed as

$$T(\mathbf{k}) = A(\mathbf{k})\exp(i\chi(\mathbf{k}))\exp(-g(\mathbf{k})) \qquad \text{(Eq. 2.5)}$$

where $A(\mathbf{k})$ is a pre-exponential function associated to the use of a cut-off aperture and magnification effects, $g(\mathbf{k})$ is a damping function which accounts for all microscope instabilities (lens current, acceleration voltage, etc.) and the incoherence of the electron probe, and $\chi(\mathbf{k})$ is the *phase contrast function*, which contains the phase shift introduced by the lens aberrations (defocus, astigmatism, coma, spherical aberration…). Neglecting high order aberration factors, $\chi(\mathbf{k})$ can be expressed as

$$\chi(\mathbf{k}) = \frac{2\pi}{\lambda}\left[\frac{C_S}{4}\lambda^4 k^4 + \frac{\Delta_z}{2}\lambda^2 k^2 - \frac{C_A}{2}\left(k_y^2 - k_x^2\right)\lambda^2\right] \qquad \text{(Eq. 2.6)}$$

where C_S is the spherical aberration coefficient, C_A is the axial astigmatism coefficient, λ is the electron wavelength and Δ_z is the defocus. Finally, the objective lens forms an image of the object in the image plane in real space, which corresponds to an *inverse Fourier transform* of $\psi_{dif}(\mathbf{k})$

$$\psi_{ima}(\mathbf{r}) = F\left\{\psi_{dif}(\mathbf{k})\right\} = F\left\{\psi_{obj}(\mathbf{k})T(\mathbf{k})\right\}. \qquad \text{(Eq. 2.7)}$$

Afterwards a series of projector lenses transfer the image of the object to a conjugated plane where the detector (e.g. fluorescent screen, charge-coupled-device (CCD) camera) records the image as an intensity map of the image electron wave, $\psi_{ima}(\mathbf{r})$. The image intensity is expressed as the squared modulus of $\psi_{ima}(\mathbf{r})$

$$I(\mathbf{r}) = \left|\psi_{ima}(\mathbf{r})\right|^2 = \psi_{ima}(\mathbf{r}) \cdot \left(\psi_{ima}(\mathbf{r})\right)^*. \qquad \text{(Eq. 2.8)}$$

In an ideal microscope free of optical defects where images are recorded at zero defocus (Gaussian focus), without aberrations, aperture cut-offs or incoherence, $T(\mathbf{k}) = 1$ and the image intensity is

$$I(\mathbf{r}) = \left|\psi_{ima}(\mathbf{r})\right|^2 = \left|a(\mathbf{r})\right|^2. \qquad \text{(Eq. 2.9)}$$

In such ideal case $I(\mathbf{r})$ only records the amplitude of the object electron wave, losing the information contain in the phase shift, $\varphi(\mathbf{r})$. Furthermore in weak phase objects the

amplitude is homogeneous, resulting an image without any contrast at all. As we will see in the next section, the study of magnetic materials by TEM experiments requires being able to record the phase shift of the object electron wave.

2.1.3 Electron beam phase shift measurements: recording the magnetism

The phase of an electron wave is modified when interacting with an object and with any electromagnetic field around it. From quantum mechanics, we know that the electron wave function that describes the behavior of relativistic electrons in an electromagnetic field can be deduced from the Dirac equation, where the electron spin would be neglected:

$$\frac{1}{2m_e}(-i\hbar\nabla + e\mathbf{A})^2\psi(x,y,z) = e[U^* + \gamma V]\psi(x,y,z) \qquad \text{(Eq. 2.10)}$$

where **A** and V are the magnetic and electric potential, respectively, e is the electron charge, m_e is the rest mass of the electron, γ is the relativistic Lorentz factor [$\gamma = 1 + eU/m_ec^2$] and U^* is the relativistic corrected accelerating potential [$U^* = (U/2)(1 + \gamma)$, where U is the non-relativistic accelerating potential]. The solution of this equation corresponds to the object electron wave of the equation 2.1, where its phase shift is modified due to the Aharonov-Bohm effect [28]:

$$\varphi(x,y) = \frac{\pi\gamma}{\lambda U^*}\int V(x,y,z)ds - \frac{e}{\hbar}\oint \mathbf{A}(x,y,z)\cdot d\mathbf{s} \qquad \text{(Eq. 2.11)}$$

where $\lambda = \hbar/(2em_eU^*)^{1/2}$ is the electron relativistic wavelength, and V and **A** are integrated over a closed path along two different electron trajectories. For a thin magnetic material laying in the x, y plane, from Equation 2.12 the projected potentials along z-axis can be calculated as [29]

$$\varphi(x,y) = \frac{\pi\gamma}{\lambda U^*}\int V_{MIP}(x,y,z)dz - \frac{e}{\hbar}\iint B_{\perp}(x,y,z)dxdydz \qquad \text{(Eq. 2.12)}$$

where V_{MIP} corresponds to the mean inner potential and $B_{\perp}$ is the magnetic induction vector orthogonal to the unitary vectors along *x* and *y*. Equation 2.11 underlines that when the electrons propagate through a ferromagnetic specimen, the phase shift would contain information about the electrostatic potential (mean inner potential, i.e., the composition and density) and the magnetic vector potential (magnetic induction). Therefore, the imaging of magnetic properties by TEM methods requires measuring the phase shift of the object electron wave having interacted with the magnetic induction.

A common strategy to extract information on the phase shift of the electron wave is to tune the transfer function of the microscope in order to modulate the electron wave and obtain an image whose intensity is related to the phase shift. This strategy is used in HRTEM to resolve atomic columns, and it is known as *phase-contrast imaging*. In advanced TEM with C_S-aberration corrector, the transfer function can be modulated through the phase contrast function by slight variation of the focal distance, Δ_z. This modulation could make that the intensity of the image electron wave only depends on the phase shift (by using a Zernike phase plate [30]) or partly depends on both amplitude and phase shift (by using an arbitrary phase plate). However, the efficiency of this reconstruction method to visualize atoms is not so useful to measure the magnetic contribution to the phase shift in magnetic materials. The main problem of such reconstruction is the fact HRTEM imaging requires the use of the conventional objective lens of the microscope, which cannot be used for magnetic imaging as we will discuss in the following paragraph.

2.1.4 The objective lens

The objective lens (OL) is the most important of the different lenses that constitute a TEM. It forms the first highly magnified image of the object and therefore determines the quality and the spatial resolution of the final image. The OL, as all lenses of the electron microscope, is an electromagnetic lens that creates a magnetic field with a focusing effect on the electron beam. It is composed by a copper coil winded inside a cylindrical magnetic yoke that is excited with a high electric current to generate an axial

magnetic field. The pole pieces of the yoke are designed to concentrate the flux lines in a small region where the electrons pass through the pole piece gap.

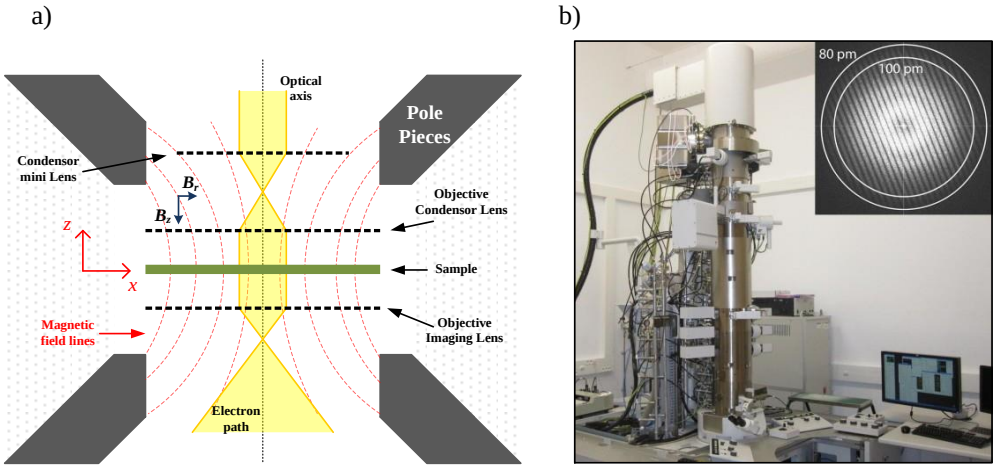

Figure 2.2. (a) Schematic representation of the magnetic field lines (dash red lines) inside a twin-type OL. (b) Column of I2TEM microscope (CEMES-CNRS). In inset, Young fringes experiment revealing the limit of the spatial resolution of the I2TEM in HRTEM mode (80 pm) (*Photo extracted to the CEMES webpage: www.cemes.fr*)

In Figure 2.2(a), we schematize a twin-type OL used in advanced microscopes. In this optical system, the specimen is placed just in the center of the gap between the pole pieces of two symmetric magnetic lenses, immersing the sample in the very intense and uniform magnetic field. The disposition of these two pole pieces, together with a mini-condenser lens placed in the upper part of the OL, gives the possibility to easily change the operation modes of the microscope between TEM (broad illumination with a nearly parallel beam) to Scanning Transmission Electron Microscopy - STEM (highly convergent beam) mode. The magnetic field between the pole pieces lens can be described considering that the pole pieces are magnetically coupled, working as a unique round magnetic lens. Considering cylindrical coordinates, the components of the magnetic field [$\mathbf{B} = (B_r, B_\theta, B_z)$] for a round lens can be expressed as [31]

$$B_r = \sum_{i=1}^{\infty} \frac{(-1)^i B^{(2i-1)}(z)}{i!(i-1)!}\left(\frac{r}{2}\right)^{2i-1} = -B'(z)\frac{r}{2} + B^{(3)}(z)\frac{r^3}{16} - \cdots \quad \text{(Eq. 2.13)}$$

$$B_z = \sum_{i=1}^{\infty} \frac{(-1)^i B^{(2i)}(z)}{(1!)^2}\left(\frac{r}{2}\right)^{2i} = B(z) - B''(z)\frac{r^2}{4} + B^{(4)}(z)\frac{r^4}{64} - \cdots \quad \text{(Eq. 2.14)}$$

where B_r and B_z are the radial- and axial components of the magnetic field, taken as reference the center of symmetry of the pole pieces gap. The cylindrical symmetric of the lens cancels the azimuthal component of the magnetic field, $B_\theta = 0$. Equations 2.13 and 2.14 show that B_r and B_z only depend on the magnitude of the magnetic field as function of z (optical axis), $B(z)$, and the radial distance to z-axis, r. The magnetic field lines represented in Figure 2.2(a) show how the magnetic field is aligned along the optical axis and therefore perpendicular to the sample plane. There are several alternatives to calculate $B(z)$ by numerical methods. Fortunately, the high symmetry of the lens allows obtaining an analytical solution [32]

$$B(z) = \frac{B_0}{1 + (z/a_g)^2} \quad \text{(Eq. 2.15)}$$

where B_0 is the magnetic field in the center of the pole pieces gap and a_g is a geometrical parameter ($a_g \sim 1$ mm) related to the extended shape of the field. For the OL of an electron microscope, B_0 can be experimentally measured using a special holder equipped with a dedicated Hall probe fitted in the sample position. We have measured in the FEI Titan^3 microscope used for this Thesis an approximate value of $B_0 = 2.4$ T in HRTEM mode [33]. Equations 2.13, 2.14 and 2.15 therefore demonstrate that the magnetic field of the OL is sufficiently high to saturate most ferromagnetic materials, aligning the magnetization almost parallel to the optical axis. This not only alters the magnetic state of the specimen, but also minimizes the magnetic contrast because, as we will demonstrate later, TEM magnetic imaging techniques are only sensitive to magnetic induction components perpendicular to the optical axis. Thus, operation in

HRTEM conditions is not adequate to study the magnetic configurations of ferromagnets.

The OL has then to be switched off for TEM magnetic studies and other optical alignments of the microscope have to be set in which the sample remains in a field free environment. In dedicated TEM a special lens, called *Lorentz lens*, located just below the OL is used in this case to magnify and form the image of the object. The Lorentz lens has a weak focusing power in order to produce a very weak magnetic field on the specimen. The combined effect of the Lorentz lens and the remanent field of the OL leads to a residual magnetic field of the order of few mT, which can be eventually compensated with the mini-condenser lens. This imaging mode is usually called a *Lorentz mode* and can be used in EH as well as in LM. Both allow studying magnetic materials in remanent state, without altering their magnetic states. Due to its long focal length (few tens of millimeters), the Lorentz lens has large spherical aberration (of about 8400 mm for an FEI Titan [34]), degrading the spatial resolution to few nanometers, and limiting magnification up to approximately ×70.000. Fortunately, recent developments on aberration correction hardware have made possible to correct the spherical aberration of the Lorentz lens, improving the spatial resolution below 1 nm [35]. Furthermore, recent prototypes of dedicated Lorentz microscopes like the Hitachi I2TEM (*Interferometry In-situ TEM*), designed between CEMES-CNRS (Toulouse-France) and Hitachi High Technology, can reach a spatial resolution of 0.5 nm in Lorentz mode due to an innovative setup which uses the conventional objective lens as Lorentz lens while the sample stage is placed above the OL to guarantee field-free conditions [36]. Once we provide a field free environment for the sample, a phase-contrast method is then able to recover the magnetic contribution to the phase shift of the electron wave using the Lorentz lens to form the image of the object. Under these conditions, the two magnetic imaging techniques currently available in TEM can come into play: Lorentz microscopy and Electron Holography.

2.2. Lorentz microscopy

From a classical point of view, LM is based on the Lorentz force ($\mathbf{F}_L$) that electrons moving with a velocity **v** experience in a magnetic induction field **B**

$$\mathbf{F}_L = -e\mathbf{v}\times\mathbf{B}\,. \qquad \text{(Eq. 2.16)}$$

Considering that the electrons travel along the optical axis (*z*-axis), the vector product **v** × **B** indicates that the Lorentz force induces a deflection of the electron trajectory only dependent on the component of the magnetic induction perpendicular to the optical axis ($\mathbf{B}_\perp = \mathbf{B}(x, z)$) (see Figure 2.3 left-side). If the electrons go through a thin sample of thickness *t*, its magnetic induction will deflect the electron trajectory an angle

$$\theta_L = \frac{e\lambda}{h} B_\perp t \equiv C B_\perp t \qquad \text{(Eq. 2.17)}$$

where $B_\perp$ is the magnitude of $\mathbf{B}_\perp$ and *h* is the Planck constant. *C* is a pre-factor that depends on the acceleration voltage of the electron microscope, with an approximate value of 0.5 μrad nm^{-1} T^{-1} for 300 kV. As an illustrative example, a 10 nm thick cobalt film with a magnetic induction of 1.772 T will produce a deflection angle of 0.086 mrad. Thus, the Lorentz deflection of such thin film is about two orders of magnitude lower than the typical Bragg diffraction angles produced by the low-index atomic planes (~5 mrad). In a quantum mechanical approach, if we treat the electron as a wave, the magnetic induction described by the vector potential inside the specimen, **A**(**r**), induces a phase shift on the scattered electrons, according to equation 2.11 (see Figure 2.3 right-side).

In focus, the image formation process in LM is similar to CTEM. The electron scattering process induced by the magnetic sample creates a diffraction pattern in the back focal plane of the Lorentz lens due to both the Bragg diffractions on the crystal lattice and the different "magnetic" beam deflections resulting of the different magnetic

induction directions lying in the sample. If we ignore the effects of the spherical aberration of the Lorentz lens (which is reasonable at low magnifications and weak scattering angle), the image intensity recorded in the image plane will only have information concerning the amplitude. Magnetic contrasts in LM can only be obtained by altering the transfer function of the microscope. There are two ways to do that: defocusing the image or using an aperture to select one deflected beam direction in the focal plane of the Lorentz lens. These two methods define the two main LM modes: Fresnel and Foucault modes [37].

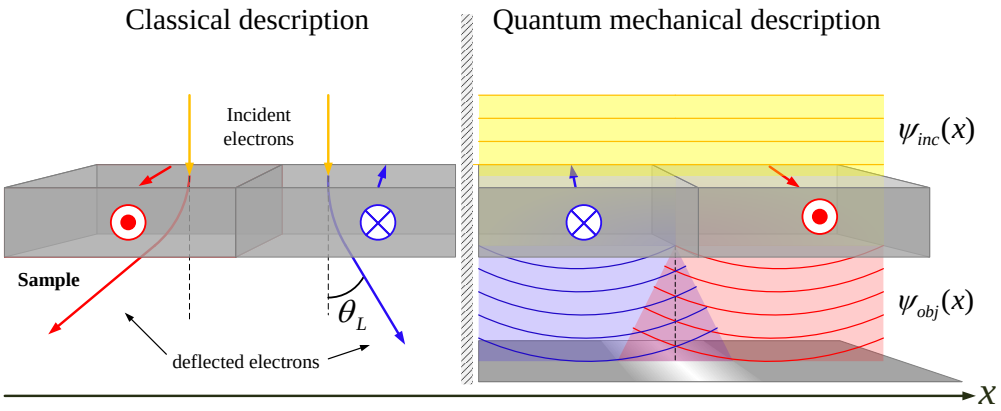

Figure 2.3. Schematic illustration of the electron beam deflection due to the Lorentz force (*left*) and quantum mechanical description (*right*) which lead to the overlap of beams coming from two different domains and the apparition of interference fringes. Small red and blue arrows represent the magnetization direction.

The most popular method is the **Fresnel mode** (or *out-of-focus mode*). In this imaging technique, magnetic contrasts due to magnetic *domain walls* (DWs) can be directly observed by defocusing the Lorentz lens in order to image a plane either located above or below the sample plane, see Fig. 2.4(a). From a classical view, the Lorentz force acting on the electrons when passing through each side of a magnetic domain wall

will be deflected in opposite directions. It results in either an electron convergence or divergence depending on the relative magnetization orientation in the two domains, see Figure 2.3(a), producing respectively bright or dark contrast lines. As the electron beam behaves as a wave, when the magnetic domain wall induces the overlap of the two beams, it results in the appearance of interference fringes parallel to the wall, see Figure 2.3(b). Then Fresnel contrast does not appear when images are taken in focus, where phase contrast is suppressed in weak phase approximation, but only in defocused images.

In the second approach, called **Foucault mode**, the magnetic domains are imaged using an objective aperture located in the Lorentz lens back focal plane to select a chosen magnetic deflection angle on the diffraction pattern. Such aperture will only let pass the electrons deflected by magnetic domains having the corresponding magnetic induction direction to create the image. It therefore will result in a bright contrast associated to these domains. Electrons deflected by domains of different magnetic induction direction are blocked and display darker contrasts in the Foucault image (Fig 2.4 b). There is an third LM mode called **differential phase contrast** (**DPC**) microscopy. Contrary to Fresnel and Foucault modes, which use a broad beam, in DPC a fine electron probe is scanned on the magnetic specimen and the Lorentz deflection is monitored by a segmented STEM detector [16,38,39].

Although Lorentz microscopy in Fresnel and Foucault modes offers the possibility to obtain a rapid and direct visualization of DWs, both techniques only provide a qualitative analysis of the magnetic states. Van Dyck *et. al*. [40–42] solved this problem by applying to electron optics a non-interferometric approach to the phase retrieval problem, originally developed in light optics, via the solution of the so-called Transport of Intensity Equation (TIE). In the TIE method, the processing of focal series of Lorentz images in Fresnel mode supplies semi-quantitative information of the magnetic configuration of the specimen.

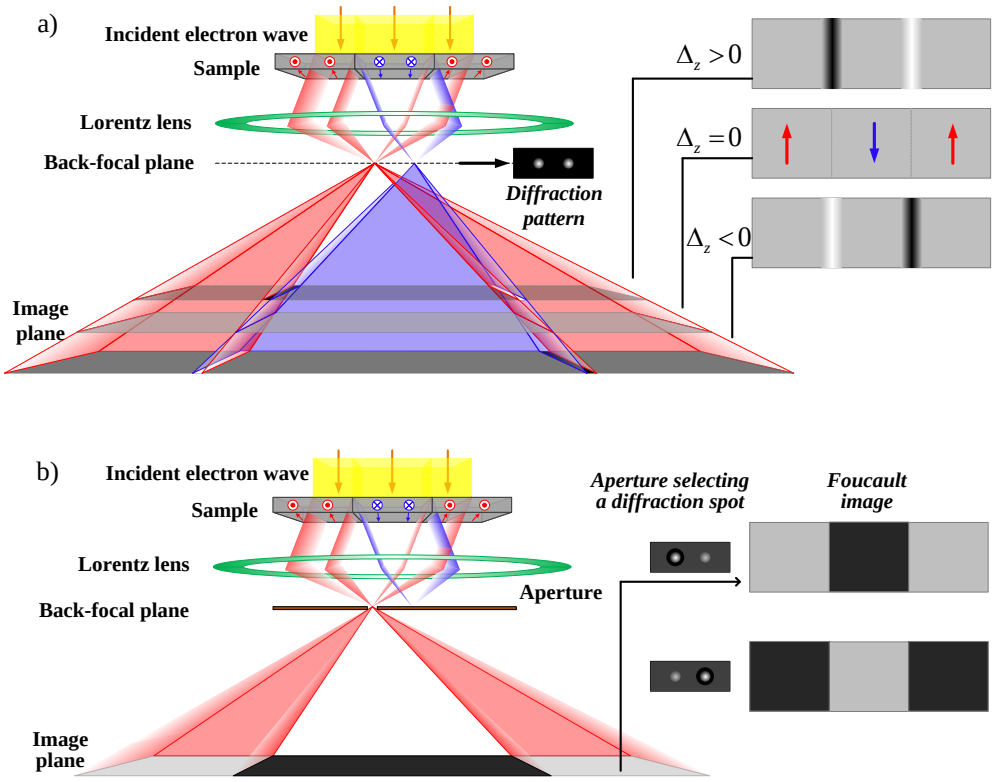

Figure 2.4. Schematic representation of the two imaging Lorentz microscopy modes: (a) Fresnel and (b) Foucault modes. Red and yellow arrows located on the sample indicate the magnetization direction of each magnetic domain.

2.2.1. Transport of Intensity Equation (TIE)

As we see in Equation 2.7, the transfer function of the microscope modulates the contrast of the image of the specimen. In the case of Lorentz microscopy, the image of the specimen is usually recorded at low magnifications, so that we can ignore the contribution of the spherical aberration. Thus, the image wave function can be expressed as:

$$\psi_{ima}(\mathbf{r}) = F^{-1}\left\{F\left[\psi_{obj}(\mathbf{r})\right]\right\} \cdot A(\mathbf{k}) \exp(i\pi\Delta_z \lambda k^2). \qquad \text{(Eq. 2.18)}$$

Making $A(\mathbf{k}) = 1$ (i.e. no aperture and neglecting the magnification effect) and considering a small defocus, we employ a Taylor expansion on the transfer function, and so the image wave function can be therefore expressed as

$$\psi_{ima}(\mathbf{r}) \approx F^{-1}\left\{F\left[\psi_{obj}(\mathbf{r})\right]\cdot[1-i\pi\Delta_z\lambda k^2]\right\}$$

$$\approx \psi_{obj}(\mathbf{r}) - i\pi\Delta_z\lambda F^{-1}\left\{k^2 F\left[\psi_{obj}(\mathbf{r})\right]\right\}. \qquad \text{(Eq. 2.19)}$$

Using the relation $F\left[\frac{d^n}{dr^n}\psi_{obj}(\mathbf{r})\right] = (2\pi ik)^n F\left[\psi_{obj}(\mathbf{r})\right]$, we can rewrite $\psi_{ima}(\mathbf{r})$ as:

$$\psi_{ima}(x,y,\Delta_z) = \psi_{obj}(x,y) + \frac{i\lambda\Delta_z}{4\pi}\left(\frac{\partial^2\psi_{obj}(x,y)}{\partial x^2} + \frac{\partial^2\psi_{obj}(x,y)}{\partial y^2}\right). \qquad \text{(Eq. 2.20)}$$

Mathematically, Equation 2.20 seems to indicate that for small defocus the image is formed by the *interference* of two plane wave functions (the object electron wave and a plane wave modulated by the transfer function). Computing the intensity of the image wave function:

$$I(x,y,\Delta_z) = \left|\psi_{ima}(x,y,\Delta_z)\right|^2 \approx a^2 - \frac{\lambda\Delta_z}{2\pi}\nabla\cdot(a^2\nabla\varphi(x,y)). \qquad \text{(Eq. 2.21)}$$

To obtain the Equation 2.21, several intermediate calculations were performed, but an exhaustive calculation can be found in the references [43,44]. Calculating the intensity differences between two images recorded in opposite, but symmetric, defocus distance (Δ_z and $-\Delta_z$), we get the following expression:

$$I(x,y,\Delta_z) - I(x,y,-\Delta_z) = -\frac{\lambda\Delta_z}{\pi}\nabla\cdot(a^2\nabla\varphi(x,y)). \qquad \text{(Eq. 2.22)}$$

From Equation 2.21, we find that the image intensity recorded at $\Delta_z = 0$ is the same as the *ideal microscope* of Equation 2.9 [$I(x, y, \Delta_z = 0) = a^2$]. Considering that, in the limit of small defocus the intensity difference can be expressed as [$\{I(x, y, \Delta_z) - I(x, y, -\Delta_z)\}/(2\Delta_z) \rightarrow \partial I(x, y, \Delta_z)/\partial\Delta_z$], Equation 2.22 can be rewritten as

$$-\frac{2\pi}{\lambda}\frac{\partial I(x,y,\Delta_z)}{\partial \Delta_z}\bigg|_{\Delta_z \to 0} = \nabla \cdot \left[I(x,y,0)\nabla\varphi(x,y)\right]. \qquad \text{(Eq. 2.23)}$$

Equation 2.23 is the so-called *Transport of Intensity Equation* (TIE). It shows that the derivative of the intensity with respect to the defocus is proportional to the gradient of the phase shift. Solving equation 2.23, we can extract quantitative information of the magnetism like the magnetization direction, type of magnetic domain walls, etc.

2.2.2. Phase reconstruction and magnetic induction mapping by Lorentz microscopy

The solution of Equation 2.23 can be expressed as [45,46]

$$\varphi(x,y) = -\frac{\pi}{\lambda\Delta_z}\nabla^{-2}\nabla\left[\frac{1}{I(x,y,0)}\nabla\left\{\nabla^{-2}\left[I(x,y,\Delta_z) - I(x,y,-\Delta_z)\right]\right\}\right]. \qquad \text{(Eq. 2.24)}$$

where ∇^{-2} is the two-dimensional inverse Laplacian operator that can be calculated via fast Fourier transform

$$\nabla^{-2}u(x,y) = F^{-1}\left\{\frac{F[u(x,y)]}{|\mathbf{k}|^2}\right\} \qquad \text{(Eq. 2.25)}$$

where $u(x, y)$ is an arbitrary function and $|\mathbf{k}|^2 \neq 0$. According to Equation 2.24, we find that the phase shift can be retrieved by recording a focal series of three images, recorded in-focus [$I(x, y, 0)$], over-focus [$I(x, y, \Delta_z)$] and under-focus [$I(x, y, -\Delta_z)$].

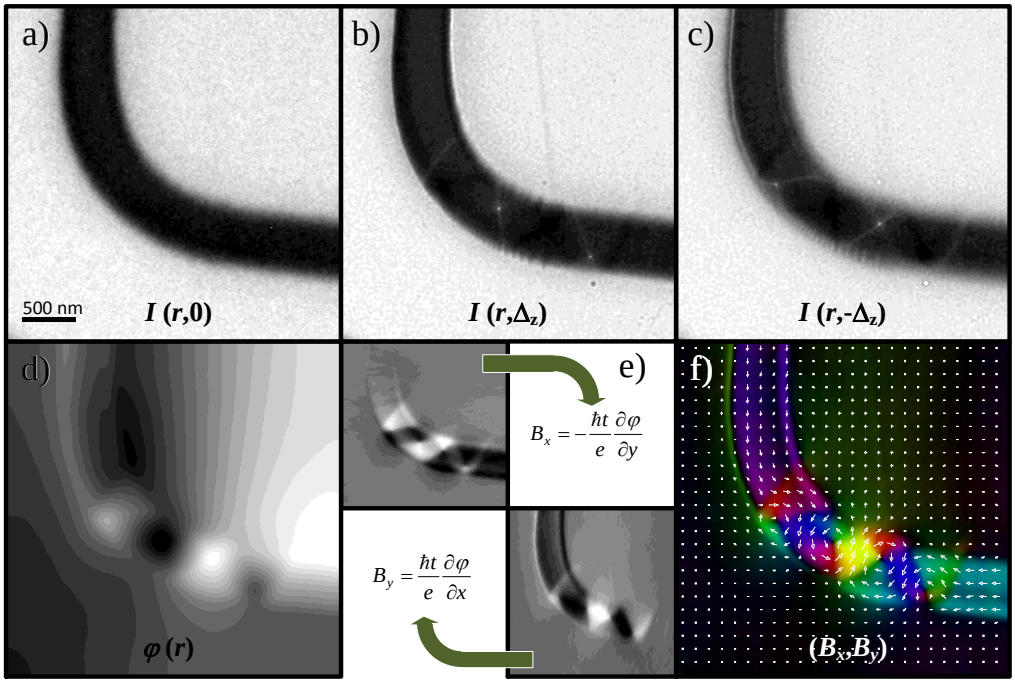

Figure 2.5. TIE reconstruction and magnetic induction mapping for a complex domain wall structure nucleated in an L-shape cobalt nanowire: focal series of Lorentz images taken at (a) in-, (b) over-, and (c) under-focus. d) TIE reconstruction of the phase shift. e) *x*- and *y*-components of the magnetic induction calculated from equation 2.27. f) Mapping of the magnetic induction (double vortex wall).

In Figure 2.5, we illustrate the phase shift reconstruction process for a complex magnetic domain wall structure nucleated in the curved region of a 30-nm-wide cobalt nanowire. The under- and over-focus images in Figures 2.5(b) and (c) illustrate how the bright and dark lines running inside to the magnetic DWs are reversed following the illustration in Figure 2.4(a). Equation 2.12 can be solved in order to calculate **B**(*x*, *y*). Assuming that the sample is chemically homogeneous and its thickness is constant, the mean inner potential is independent of *x* and *y*, and the gradient of phase shift only depends on the magnetic induction:

$$\nabla\varphi(x,y) = -\frac{e}{\hbar}[\mathbf{n}_z \times t\mathbf{B}(x,y)] \qquad \text{(Eq. 2.26)}$$

therefore

$$(B_x, B_y) = \frac{\hbar t}{e}\left(-\frac{\partial \varphi}{\partial y}, \frac{\partial \varphi}{\partial x}\right). \qquad \text{(Eq. 2.27)}$$

Thus we can reconstruct a vector map of the magnetic induction from Equation 2.27. This representation allows the visualization of the magnetization direction of each magnetic domain.

2.3. Off axis electron holography

In *off axis electron holography* (hereafter only called *electron holography*, EH), the phase shift can be extracted by performing an interferometry experiment where the object electron wave interferes with a reference electron wave. The resulting interference pattern, the *hologram*, is a set of fringes with local periodicity variations due to the relative difference of the phase shifts of the object wave and the reference wave. The hologram intensity and contrast are related to the amplitude of the object wave [47] and its stability over the exposure time. To implement this technique, the electron microscope requires the use of a high brightness and highly coherent electron source and an *electron biprism* to create the overlap of the two beams [48]. Particularly a high spatial coherence and a high brightness permits recording holograms with a very good fringe contrast and intensity within a short acquisition time, of few seconds, to avoid specimen and/or beam drift effects. In the last decades, this has been possible with the generalization of a new generation of instruments with high-brightness coherent and stable electron sources such as Schottky and Cold Field Emission Guns (S-FEG and C-FEG). The electron biprism is usually a very thin Au-coated glass fiber or a Pt wire used to deflect both object and reference electron wave to produce an overlap region that enables the interference phenomenon [49,50]. Such deflection is achieved by the application of a positive voltage to the biprism. Although there is an optimum geometric arrangement of the biprism in the column of the microscope to obtain the highest

hologram quality [51], most electron microscopes (for example, the FEI instruments) have to assemble it among the selected area apertures for technical reasons. To have the two electron waves interfering, the illumination has to be so that part of beam interacts with the specimen, while the rest passes through the vacuum. For this reason, a vacuum area close to the sample is required. Then, both electron waves are deflected by the electric potential induced by the biprism, they overlap and interfere to form a hologram in the image plane. A cartoon that describes the formation of an electron hologram is shown in Figure 2.6.

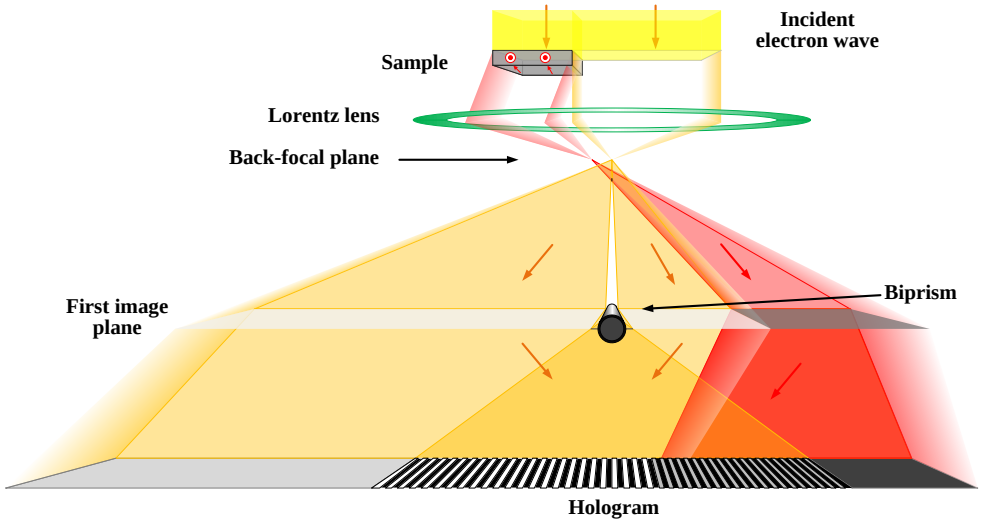

Figure 2.6. Schematic representation of electron holography.

Mathematically, the hologram formation is described as follow. We consider that the reference electron wave is a plane wave, $\psi_{ref}(\mathbf{r}) = \exp(i2\pi\mathbf{k}\cdot\mathbf{r})$, and the object electron wave is the wave function of Equation 2.1. The action of the biprism makes that both reference and object electron wave are tilted a certain angle ($\alpha_h/2$ and $-\alpha_h/2$, respectively). Thus, the wave function resulting from the interferences along the *x*-axis is given by

$$f_{int}(\mathbf{r}) = a(\mathbf{r})\exp\left(-\pi i\frac{\alpha_h}{\lambda}x + i\varphi(\mathbf{r})\right) + \exp\left(\pi i\frac{\alpha_h}{\lambda}x\right). \qquad \text{(Eq. 2.28)}$$

and the intensity is

$$I_{hol}(\mathbf{r}) = \left| f_{int}(\mathbf{r}) \right|^2 = 1 + a^2(\mathbf{r}) + 2a(\mathbf{r}) \cos\left(2\pi \frac{\alpha_h}{\lambda} x - \varphi(\mathbf{r}) \right). \quad \text{(Eq. 2.29)}$$

From Equation 2.29, we see that the hologram is formed by the conventional bright-field image, $I_{BF} = 1 + a^2(\mathbf{r})$, superposed over the sinusoidal term that represents mathematically the fringe pattern of the hologram, and depends on both amplitude and phase shift of the object wave. Thus, the hologram contains all the information of the object electron wave. The period of the interference fringes, λ/α_h, depends on the deflection angle induced by the biprism voltage, so that is possible to change the fringe spacing varying the intensity of the (positive) voltage. Performing a Fourier transform on the hologram, we obtain

$$\begin{aligned} F\left|I_{hol}(\mathbf{r})\right| = \delta(u) + F\left[a^2(\mathbf{r})\right] + F\left[a(\mathbf{r}) \exp(i\varphi(\mathbf{r}))\right] \otimes \delta\left(\mathbf{u} + \frac{\alpha_h}{\lambda} \hat{\mathbf{x}} \right) \\ + F\left[a(\mathbf{r}) \exp(-i\varphi(\mathbf{r}))\right] \otimes \delta\left(\mathbf{u} - \frac{\alpha_h}{\lambda} \hat{\mathbf{x}} \right). \end{aligned} \quad \text{(Eq. 2.30)}$$

where $\otimes$ indicates the convolution operation. In the Fourier space, the hologram is represented by a central spot (central band) and two collinear spots (sidebands) equally spaced with respect to the center. The central band contains the conventional bright-field image, while each sideband stores the information of the amplitude and phase. Choosing one of the sideband and performing the inverse Fourier transform the object electron wave can be recovered.

$$F^{-1}\left\{ F\left[a(\mathbf{r}) \exp(i\varphi(\mathbf{r}))\right] \otimes \delta(\mathbf{u}) \right\} = a(\mathbf{r}) \exp(i\varphi(\mathbf{r})) = \psi_{obj}(\mathbf{r}). \quad \text{(Eq. 2.31)}$$

From Equation 2.31, we can reconstruct the complete object electron wave

2.3.1. Phase reconstruction in electron holography

The reconstruction process starts calculating the fast Fourier transform of a digitally recorded hologram through, for instance, a CCD camera in order to obtain the spectrum image. Using a mask, one of the sidebands is isolated and centered before calculating its inverse Fourier transform. Finally, the calculation of the amplitude and phase shift of the resulting complex image can be done through the following expression:

$$\varphi(\mathbf{r}) = \arctan\left(\frac{\mathrm{Im}(\psi_{obj}(\mathbf{r}))}{\mathrm{Re}(\psi_{obj}(\mathbf{r}))}\right) \qquad \text{(Eq. 2.32)}$$

$$a(\mathbf{r}) = \sqrt{\left[\mathrm{Im}(\psi_{obj}(\mathbf{r}))\right]^2 + \left[\mathrm{Re}(\psi_{obj}(\mathbf{r}))\right]^2} \qquad \text{(Eq. 2.33)}$$

where $\mathrm{Im}(\psi_{obj}(\mathbf{r}))$ and $\mathrm{Re}(\psi_{obj}(\mathbf{r}))$ are the real and imaginary parts of the wave function, respectively. Although many EH users develop their own computational routines, there are commercial scripts that run under DigitalMicrograph® software to perform the complete phase reconstruction. In our case, we have used the *GPA* software developed by M. Hytch and extended for EH applications by C. Gatel to extract the amplitude and the phase [52]. A summary of the phase reconstruction process is represented in the Figure 2.7, using as example a Fe/MgO/FeV magnetic MTJ heterostructure. In addition, it is important to record a reference hologram in some place of the vacuum, free of electric and magnetic stray fields produced by the specimen. This reference hologram is used to remove unavoidable Fresnel fringes due to the biprism itself as well as to compensate for phase artifacts caused by distortions introduced by the imaging and recording system [53].

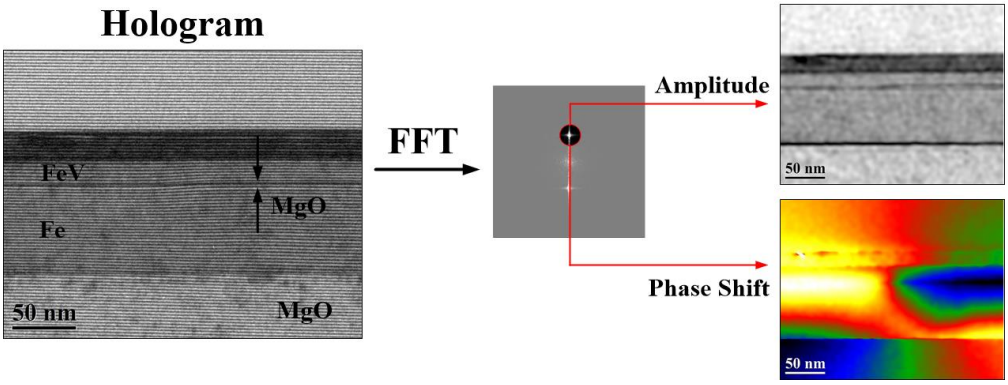

Figure 2.7. Amplitude and phase shift reconstruction process followed in EH on a Fe/MgO/FeV MTJ.

2.3.2. Phase shift separation and interpretation of the magnetic contribution

In LM, the magnetic information of the specimen is extracted from Equation 2.12 assuming the sample to be homogenous with no thickness variation. These approximations thus ignore the electrostatic contribution. However, in EH the contribution of the electrostatic potential is taken into account and can be separated from the magnetic contribution assuming that, according to Equation 2.12, the phase shift can be expressed as a lineal combination of each potential contribution given by

$$\varphi(x,y) = \varphi_{EL}(x,y) + \varphi_{MAG}(x,y) \qquad \text{(Eq. 2.34)}$$

where $\varphi_{EL}(x, y)$ and $\varphi_{MAG}(x, y)$ are the electrostatic and magnetic phase shift contributions (first and second term of Equation 2.12), respectively. Several procedures have been proposed to separate these two contributions, some of them are more or less suitable depending on the magnetic behavior of the sample:

1- Recording two holograms where one of them is taken after manually flipping the sample upside down. Probably, this is the most used method because the magnetic state of the specimen is not altered. It was proposed by Tonomura considering the "time-reversal operation of the electron beam" [54], where the sign of the

magnetic phase shift contribution is changed by flipping the sample while the electrostatic phase shift (a scalar) remains constant.

2- Recording two holograms after saturating the magnetization of the sample in two opposite direction. Proposed by Dunin-Borkowski [55], this method uses either the conventional OL excitation or a dedicated magnetizing holder to switch and saturate the magnetization in opposite directions. Similar to the previous method, perfectly antiparallel saturation states induce a change of the sign in the magnetic phase shift contribution keeping constant the electrostatic contribution. This method is very useful in nanostructures with high in-plane shape anisotropy (e.g. nanowires, nanostripes, TEM lamellas for polycrystalline magnets or in-plane magnetic anisotropy thin films) where the magnetostatic energy confines the magnetization in specific and stable orientations.

3- Recording two holograms at different electron acceleration voltages. In this way, the potential of the electron's relativistic acceleration, U*, is modified while the magnetic phase shift contribution remains constant (independent of the electron velocity) and therefore can be obtained by dividing both phase shifts. According to equations 2.12 and 2.34, such division can be expressed as:

$$\frac{U_2^*}{U_1^*} = \frac{\varphi_1(x,y) - \varphi_{MAG1}(x,y)}{\varphi_2(x,y) - \varphi_{MAG2}(x,y)} \qquad \text{(Eq. 2.35)}$$

where the subscripts 1 and 2 are associated to each acceleration voltage. As the magnetic phase shift does not depend on the electron acceleration, $\varphi_{MAG1} = \varphi_{MAG2} = \varphi_{MAG}$, and therefore

$$\varphi_{MAG}(x,y) = \frac{U_1^*\varphi_1(x,y) - U_2^*\varphi_2(x,y)}{U_1^* - U_2^*} \qquad \text{(Eq. 2.36)}$$

Unfortunately the change of the acceleration voltage modifies dramatically the optical alignment of the microscope such as the image magnifications, aberrations, resolution, the Lorentz deflection angles. This makes the image reconstruction difficult and also compromises the optical stability of the microscope.

4- Recording two holograms at two different temperatures above and below the Curie temperature (T_C) of the material [56,57]. In this way, at $T > T_C$, the phase shift only contains information of the electrostatic contribution. Subtracting this phase shift with those obtained at $T < T_C$, allows extracting the magnetic phase shift contribution. The implementation of this procedure requires the use of cooling/heating holders in order to induce the magnetic transition

Thus, using one of these strategies, the magnetic and electrostatic contributions to the phase shift can be separated. Electrostatic and magnetic phase shift images for the example of the Fe-based MTJ heterostructure are displayed in Figure 2.8. If we assume that $V(x, y)$ is constant (specimen chemically homogenous), qualitative and quantitative descriptions can be made if we calculate the gradient of the phase shift:

$$\nabla\varphi(x,y) = \nabla\varphi_{EL}(x,y) + \nabla\varphi_{MAG}(x,y)$$

$$= C_E V_{MIP} t(x,y) + \frac{e}{\hbar} B_{\perp}(x,y) t(x,y) \qquad \text{(Eq. 2.37)}$$

where V_{MIP} is the mean inner potential of the specimen and $C_E = (\pi\gamma/\lambda U^*)$ is an interaction constant that only depends on the energy of the incident electron beam ($C_E = 6.53 \times 10^6$ rad V^{-1} m^{-1} for 300 kV). From the second term of the right-side of equation 2.26, which is similar to those obtained in equation 2.37, we can compute and map the magnetic induction of the specimen.

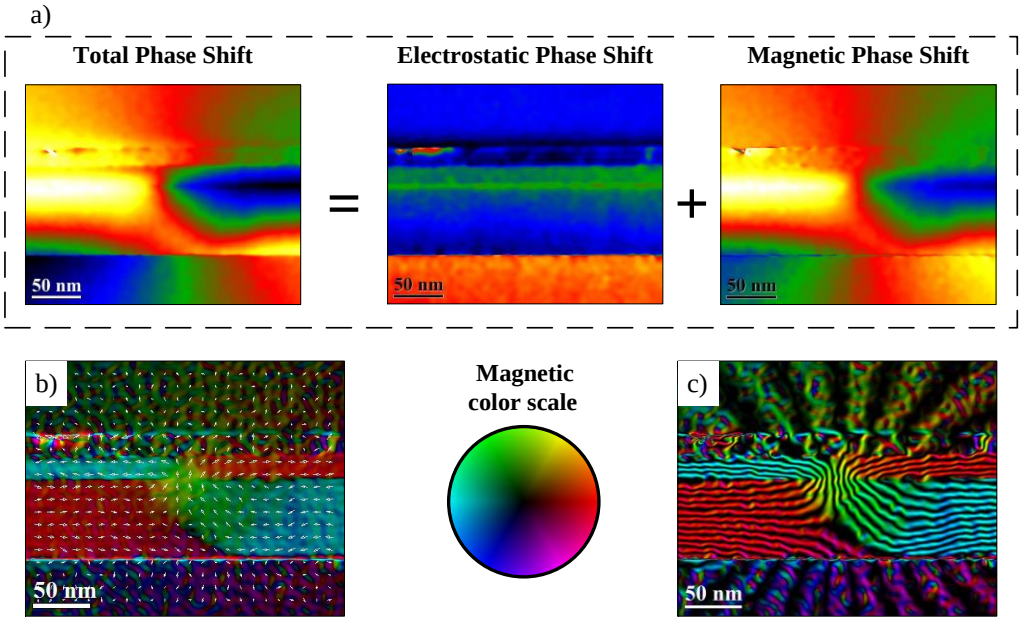

Figure 2.8. (a) Phase shift separation for the Fe/MgO/FeV MTJ heterostructure of Figure 2.7. Different representations of the magnetic induction are shown using (b) a vector color map or (c) a magnetic flux image. The magnetic color scale located between (b) and (c) represents the direction and magnitude of the magnetic induction.

As we illustrate in Figure 2.8(b) and (c), different representations can be used to visualize the magnetic configuration. A vector color map can be drawn (Fig. 2.8 b) or a cosine function of φ_{MAG}, $\cos(n\varphi_{MAG})$ where n is an amplifier factor, can be used to illustrate the magnetic flux created by the structure (Fig 2.8 c). For this MTJ heterostructure, a quantitative analysis of the magnetic induction allows deducing that the two magnetic layers are magnetically coupled by the formation of a transversal-type domain wall.

In nanostructures with simple geometries such as nanowires or even TEM lamellas, a qualitative description of the electrostatic and magnetic contributions can be done by means of the analysis of phase shift profiles. For example, in the case of cross sectional TEM specimens of thin films, where the shape and/or magnetocrystalline anisotropies

tend to align the magnetization along its length, the expected magnetic and electrostatic phase shift contribution along *y*-axis are shown schematically in Figure 2.9

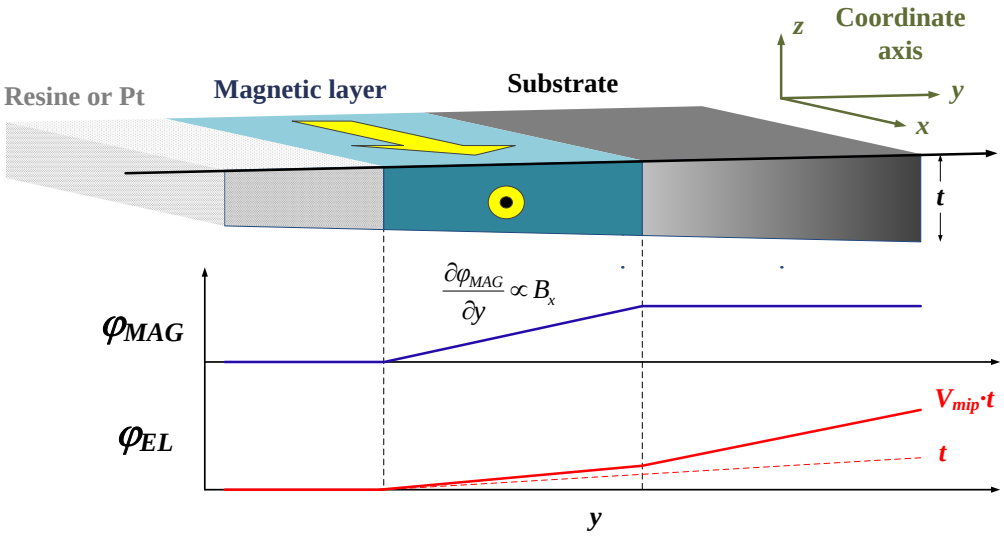

Figure 2.9. Schematic illustration for a magnetic phase shift profile perpendicular to a ferromagnetic TEM lamella.

We find that the magnetic phase shift follows a lineal variation with the distance (*y*) only inside the magnetic layer. Non-magnetic layers will show a flat phase profile. From Equation 2.37, we deduce that this lineal variation is proportional to the perpendicular magnetic induction component (B_x). On the other hand, the electrostatic phase shift will exhibit a lineal variation, with different slope values for each layer, when the thickness variation of the specimen is lineal, perpendicular to the layers. Variations of the electrostatic phase shift are proportional to the product $V_{MIP}t$.

2.4. Remarkable aspects of Lorentz microscopy and electron holography

As commented in the introduction of this section, due to their high spatial resolution, LM and EH have become essential tools for the study of Magnetism at the

nanoscale, and depending on the type of experiments to be carried out one or the other may be selected.

LM is an ideal technique to visualize magnetic domain structures as it allows studying the domain walls in large fields of view of several microns. For *in-situ* experiments, its temporal resolution permits to follow the evolution of quasi-dynamic processes from the nucleation and propagation of domain walls in nanostripes to the reversal magnetization switching in magnetic thin films. All these processes can be studied qualitatively while TIE reconstruction procedure is required for extracting quantitative information. The main issue of LM is however the correct alignment of the focal series images to solve TIE. Higher magnetic sensitivity requires larger values of defocus, which induces higher distortion in the defocused images and degrades the nominal spatial resolution. Image rotations and magnification changes can be easily adjusted, but complex distortion created by the projector lenses requires a complex mathematical algorithm to solve it. This problem can be partially solved focusing on the region of interest in the central part of the image, near the optical axis during the acquisition of the focal series, or solving TIE of small regions of the images.

On the other hand, EH is ideal to explore magnetic states that require high sensibility and spatial resolution. The possibility of separating the electrostatic and magnetic phase shifts makes EH technique suitable for fully quantitative analysis of the magnetic fields. However, the long acquisition times and the extreme stability of the optical setup required bring about the poor time resolution of the technique, and limit the capacity to analyze dynamical magnetic processes induced by *in-situ* external stimuli. In addition, as a reference area is needed, it is difficult to record magnetic phenomena occurring far from specimen edge (far from the vacuum) unless a dedicated instrument with multiple biprisms is used.

Depending on the topic we investigate, we have chosen in this Thesis the most suitable technique between LM and EH following these criteria.

2.5. DualBeam

2.5.1. Introduction

DualBeam is the commercial name given by FEI Company to an instrument that combines Scanning Electron Microscopy (SEM) and Focused Ion Beam (FIB) in the same system [58]. This combination presents a key advantage over single-beam SEM or FIB machines, as it allows the simultaneous ion etching/processing of a material or device while monitoring the process with the electron probe. This has got a strong impact in different fields such as nanolithography and nanofabrication devices, 3D characterization and reconstruction, TEM sample preparation, analytical characterization by x-ray and secondary ion mass spectroscopy (SIMS), among others.

A schematic diagram showing the configuration of a focused ion/electron DualBeam system is displayed in Figure 2.10(a). The SEM column is vertical while the FIB column is tilted 52° respect to the SEM column. The sample is located at the coincidence point of the SEM and FIB beams, and thanks to a wide range of tilt angles, between -10 to 60° in the case of a FEI Helios Nanolab^{TM} 650, it can orient the sample to face each of the columns depending on the process. This is the normal operation position of the instrument and gives the possibility to make simultaneous ion milling and electron imaging of the region of interest.

Most of the magnetic nanostructures studied in this work such as L-shape cobalt nanowires, a cobalt nanoring, cobalt antidot arrays and TEM lamellae of manganites were fabricated in a DualBeam. Cobalt nanoring and nanowires were lithographed by Focused Electron Beam Induce Deposition (FEBID) technique, while the cobalt antidot arrays and manganite-based on TEM lamellae where fabricated by FIB etching. Other techniques based on the focused ion/electron beam capability can be implemented in the DualBeam, like the ion counterpart of FEBID, Focused Ion Beam Induce Deposition (FIBID) [59]. However, next we will only describe in detail the techniques which have bee intensively used in this Thesis: FEBID and FIB.

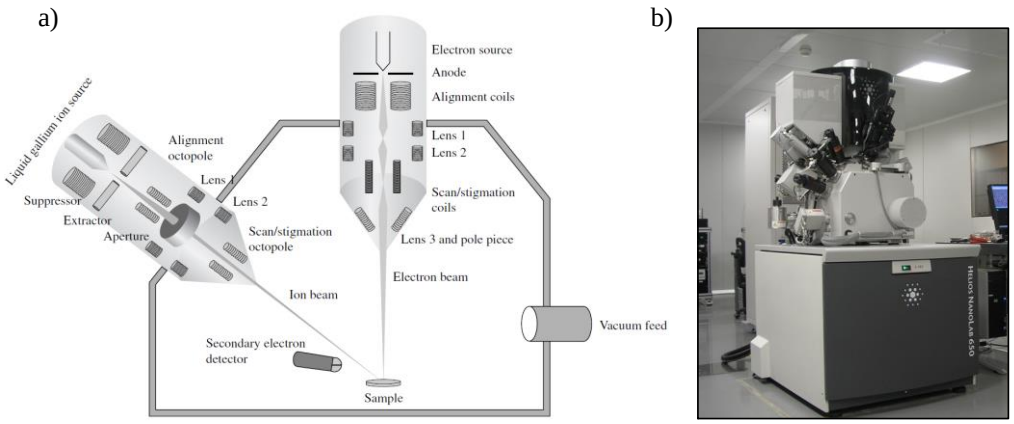

Figure 2.10. (a) Schematic diagram for the two-beams configuration in a DualBeam instrument [60]. (b) Picture of the FEI Helios Nanolab^{TM} 650 installed in the clean room of the LMA-INA.

2.5.2. Focused electron beam induced deposition, FEBID

FEBID is a direct-writing nanolithography technique used to deposit two-dimensional and three-dimensional materials with nanometer resolution [61,62]. A simple scheme of the FEBID operation is shown in the Figure 2.11. A needle-shape Gas-Injection-System (GIS) placed hundreds of microns above the substrate injects a precursor gas in the chamber, which is absorbed onto the substrate. Then a fine electron beam (5 – 30 kV) impinges on the substrate, causing the decomposition of the molecules of the precursor gas. The precursor is an organometallic molecule, so in the decomposition process the non-volatile metallic component is deposited on the substrate in the position where the beam is focused, while the volatile material is evacuated through the vacuum system. FIBID follows the same scheme employing a focused ion beam to decompose the gas precursor. Mixing the decomposition process with a controlled scanning of the electron beam, the FEBID nanolithography method can create complex nanopatterns, resembling a pencil writing on a paper. This is the main advantage of this method compared to other lithographic techniques, and makes it a very versatile tool to design nanostructures with good lateral resolution, of few tens of nanometers, in commercial DualBeam instruments. However, even though the number of gas precursors available enables the deposition of an increasing number of chemical

elements (Botman *et. al*. listed 23 elements in this reference [63]) and some intermetallic alloys like Pt-Si, Co-Pt and Pt-C [62], few can be deposited with a purity close to 100%.

For magnetic nanotechnology applications, special attention has been paid to the two magnetic chemical elements that can be deposited by FEBID: iron (Fe) and cobalt (Co). Different gas precursors have been tested for these elements: $Fe(CO)_5$, $Fe_2(CO)_9$ and $Fe_3(CO)_{12}$, for Fe-based deposits [64–69]; and $Co(CO)_3NO$ and $CO_2(CO)_8$, for Co-based deposits [70–76]. In the case of iron, most of the deposits reported have used $Fe(CO)_5$ as gas precursor. Working in high vacuum conditions, metallic deposits with a Fe content up to 80% have been reported. Even better results (up to 95%) have been achieved when working under ultra-high vacuum condition [67,77]. For Co-based deposits, several works confirm that the dicobalt octacarbonyl [$CO_2(CO)_8$] gas precursor permits obtaining deposits with higher Co content, which can overcome 90% purity when working in high vacuum conditions [72]. In both cases, only FEBID is able to produce deposits of this purity level. Very recently, Co-based FEBID nanostructures with lateral dimensions down to 30 nm have been reported with a purity of 93% and conserving the bulk ferromagnetic properties. As depicted in Figure 2.11, an quantitative EH analysis permitted the calculation of the magnetic induction for a 10-nm-thick ultra-small cobalt nanowires, B = 1.8 T, which is quite similar to those of bulk cobalt [75]. In addition, Co deposition has also been optimized for the fabrication of functional 3D nanostructures with complex geometries [76]. The next step is to understand and control their magnetic states in order to use them in Spintronic applications such as magnetic information storage, logic or sensor devices based on magnetic DWs as functional entities to store, transfer and process information in ferromagnetic media. Previous works have been performed to study, for example, the domain wall conduit properties of cobalt nanowires using MFM, MOKE, XMCD and scanning transmission x-ray microscopy (STXM) techniques [76,78–81]. In this Thesis, we will report the first results of the study of DWs by TEM-based magnetic characterization techniques, in particular by LM.

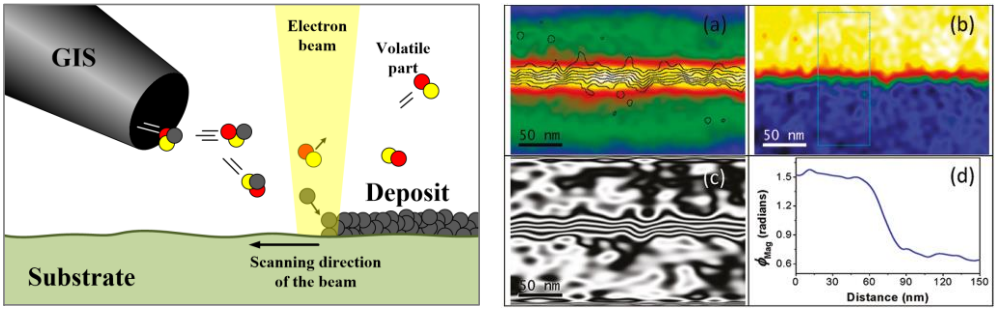

Figure 2.11. (*Left*) A basic schematic representation of the FEBID process. (*Right*). EH characterization for a ultra-small cobalt nanowires of 30 nm width: (a) Electrostatic phase shift image with a contour representation of the magnetic flux, (b) magnetic phase shift image, (c) magnetic flux image, and (d) magnetic phase shift profile traced perpendicular to the nanowire (image extracted of Ref. [75])

2.5.3. Focused ion beam (FIB)

The FIB column of a DualBeam is a scanning ion microscope, and also a precision machining tool. As ion source, modern FIBs utilize a liquid-metal ion source (LMIS) to produce ions, usually Ga^+. The gallium metal is heated and extracted through a tungsten needle by the application of the electric field. This process creates a Ga^+ probe of high brightness (~ 106 A/cm^2) and very small lateral size (~ 2 nm) that is accelerated by using an electric potential ranging from 5 to 30 kV. Similar to the SEM column, the optical system is composed by lenses and apertures that focus and deflect the ion beam to scan the specimen surface with a very small ion probe of approximately 5 nm of diameter. The interaction between the high-energy ion beam of a relatively massive element as Ga^+ with the specimen surface can be used to etch its surface or to deposit materials (by FIBID), and also produce several secondary signals, which can be used for different imaging techniques. From an application point of view, the FIB can be used to design micro-mechanical system (MEMS) or hard disk write head devices by micro-machining process, prepare very thin SEM/TEM specimens, perform ion imaging and (SIMS), repair lithographic masks by modification and defect removal, modify integrated circuits by cut-and-paste operations, and implant ions in the specimen [59]. In this work,

the milling capability of the FIB was used to fabricate periodic arrays of holes (antidots) in a cobalt thin film and prepare TEM lamellae.

2.5.3.1. *FIB milling: lithographic patterning*

Considered the most powerful and versatile application, the FIB milling allows etching and sculpting the surface of the material with any desired shape [82]. Such etching effect is caused by the collisions between the high-energy heavy ions of the beam with the atoms on the specimen surface, transferring sufficient energy to cause a displacement of the target atoms and trigger a recoil cascade whereby the energy is transferred from one atom to another. The atoms are then either removed of the specimen through the vacuum system or re-deposited in a region close to the ion irradiation occurs. This milling process can be applied to almost any material. Tuning some FIB milling parameters such as the ion beam current (*I*), the acceleration voltage (*V*) and the dwell time (residence time that the ion beam remain in a position) the patterning of nanostructures in the sub-100 nm regime is possible following a top-bottom lithography approach. In Figure 2.12(a), a SEM image shows an array of holes, also called antidot array, fabricated on a ferromagnetic thin film of cobalt. To create holes of diameter as small as possible, each hole was etched with a single spot of the ion beam, and the regular matrix was fabricated by deflecting the beam from point to point [83]. As we will show later, using a beam current of 24 pA, an acceleration voltage of 30 kV and a dwell time of 10 ms, we can fabricate holes of ~55 nm of diameter. In general, the higher the beam current, the faster the material is sputtered from the surface, but the ion beam irradiation also produce secondary effects such as local heating, lattice defects, amorphization of the specimen surface and ion implantation [59,84]. As we will show later, the FIB milling lithography induces Ga^+ implantation and the amorphization of the edge of the holes in our metallic antidot arrays. To avoid such unwanted effects, FIB milling processes can be performed in two stages: a high-current beam operation is first used to rapidly remove material of the surface, then a low current beam operation is carried out for a fine polishing. This procedure, for instance, is used in the preparation of TEM lamellae.

2.5.3.2. *FIB milling: TEM sample preparation*

FIB milling supposed a revolutionary method in the field of TEM sample preparation to prepare high-quality electron-transparent cross-section TEM specimens or lamellae with a uniform thickness of typically 50 nm [59,82,84]. The main advantage of FIB is the possibility to extract or "lift-out" a TEM specimen directly from the bulk sample without previous cutting or mechanical polishing process. Furthermore, a TEM lamella can be extracted from a specific sub-micrometer region of a sample without damaging the entire sample. In hard materials, the lift-out process is directly performed on the bulk material and permits a rapid TEM specimen preparation with minimal mechanical damage or ion implantation. For particular materials, additional steps have to be taken before lifting out the specimen: for insulating materials, a conductive coating may be applied on the material surface in order to prevent surface charging effects that difficult a controlled FIB milling process; for small, light-weight or fragile materials, the specimen can be embedded in a low-viscosity epoxy resin, thus the milling process is realized on a hardened resin as a bulk specimen [85].

The TEM lamella preparation process starts locating the region of interest by imaging the surface of the material using the SEM column of the DualBeam. On this region, a metallic layer of 0.5-1 μm thickness by few microns width and by few tens of microns length is deposited on the region of interest in order to protect the surface of the TEM specimen from the milling process. This protective metallic layer, usually of tungsten or platinum, is deposited by FEBID and/or FIBID. A high beam current operation is then used to rapidly mill large amounts of material to form two trenches at each side of the deposited metallic layer, creating a vertical lamella of material of about 1 μm thick at its center. Next, this lamella is lifted-out of the bulk sample using a micromanipulator whose tip is welded to the sample by FE(I)BID of platinum or tungsten, then detached from the bulk, and transferred to a metallic TEM grid. Eventually, a final milling is carried out using a low beam current to reduce the thickness of the lamella to the desired value, usually below 50 nm. A SEM micrograph of a TEM lamella is shown in Figure 2.12(b). For EH experiments, an additional step is carried

out on the TEM lamella, which is the partial removal of the protecting metallic layer to reduce the distance between the region of interest and the vacuum.

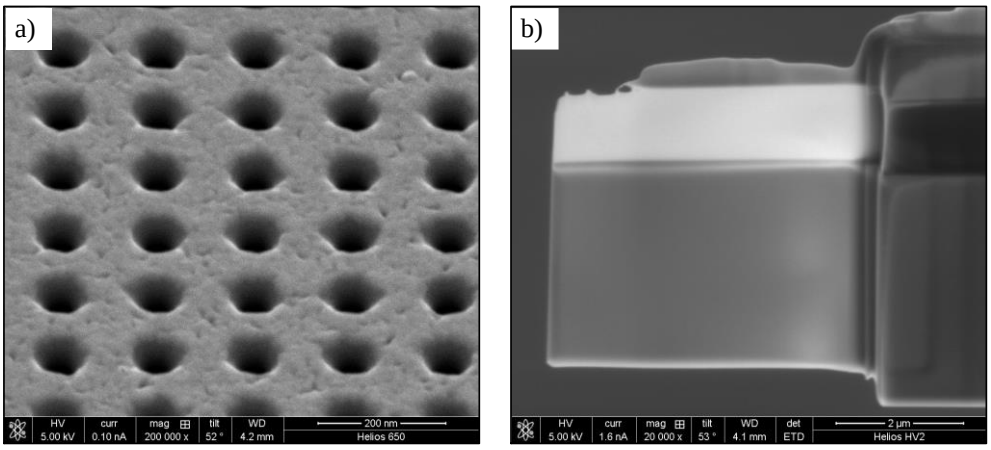

Figure 2.12. SEM images for (a) an antidot array and (b) a manganite-based TEM lamella.

2.6. Image-corrected FEI Titan^3 60-300

For this work, LM and EH were performed in a FEI Titan Cube (Titan^3) 60-300 microscope belonging to the *Laboratorio de Microscopias Avanzadas* (LMA) at the *Instituto de Nanociencia de Aragón* (INA) of the University of Zaragoza (UNIZAR) (see Figure 2.13). To minimize acoustic and mechanical perturbations, and thermal fluctuations, this microscope is located inside a box ("cube") and can be operated remotely. The acceleration voltage ranges from 60 to 300 kV. The electron source of the microscope is an S-FEG that emits a high brightness electron beam of high spatial coherence suitable to LM and EH experiments. It is equipped with a SuperTwin® OL and a CETCOR Cs image corrector from CEOS Company. In HRTEM mode, both SuperTwin objective lens and *Cs* corrector allow reaching a point resolution of 0.08 nm at 300 kV. To perform LM and EH, the microscope uses the first transfer lens (TL1) of the corrector as Lorentz lens and the *Cs* image corrector can also be aligned to correct the spherical aberration of the Lorentz lens allowing a spatial resolution of around 1 nm.

For EH mode, a motorized electrostatic biprism is assembled in one of the selected area apertures. It can be excited up to 1000 V, rotated and moved in any direction within the aperture plane. For the image acquisition, the microscope is fitted with a Gatan Ultrascan 2k × 2k CCD camera. In addition to TEM and Lorentz modes, it is also possible to perform STEM imaging at medium resolution using bright- and dark-field detectors, and a Gatan Energy Filter Tridiem 863 allows performing EELS and energy filtered TEM experiments with an energy resolution of ~0.7 eV.

Figure 2.13. Photo of the FEI Titan Cube 60-300 installed at the LMA-INA laboratory.

References

[1] Nasirpouri F and Nogaret A 2011 *Nanomagnetism and Spintronics: Fabrication, Materials, Characterization and Applications* (World Scientific)

[2] Giri P K, Goswami D K and Perumal A 2013 *Advanced Nanomaterials and Nanotechnology: Proceedings of the 2nd International Conference on Advanced Nanomaterials and Nanotechnology, Dec 8-10, 2011, Guwahati, India* (Springer)

[3] Shinjo T 2013 *Nanomagnetism and Spintronics* (Elsevier Science)

[4] Zhu Y 2005 *Modern Techniques for Characterizing Magnetic Materials* (Springer)

[5] Hopster H and Oepen H P 2005 *Magnetic Microscopy of Nanostructures* (Springer)

[6] Kuch W 2006 Magnetic Imaging *Magn. A Synchrotron Radiat. Approach. Lect. Notes Phys.* **320** 275–320

[7] Celotta R J, Unguris J, Kelley M H and Pierce D T 2002 *Characterization of Materials* ed E N Kaufmann (Hoboken, NJ, USA: John Wiley & Sons, Inc.)

[8] Livingston J D and Becker J J 1958 J *AIME Trans.* **212** 316

[9] Livingston J D 1959 J *AIME Trans.* **215** 566

[10] Mayer L 1957 Electron Mirror Microscopy of Magnetic Domains *J. Appl. Phys.* **28** 975

[11] Hale M E, Fuller H W and Rubinstein H 1959 Magnetic Domain Observations by Electron Microscopy *J. Appl. Phys.* **30** 789

[12] Fuller H W and Hale M E 1960 Domains in Thin Magnetic Films Observed by Electron Microscopy *J. Appl. Phys.* **31** 1699

[13] Chapman J N, Batson P E, Waddell E M and Ferrier R P 1978 The direct determination of magnetic domain wall profiles by differential phase contrast electron microscopy *Ultramicroscopy* **3** 203–14

[14] Waddell E M and Chapman J N 1979 Linear imaging of strong phase objects using asymmetrical detectors in STEM *Optik (Stuttg).* **54** 83–96

[15] Chapman J N 1984 The investigation of magnetic domain structures in thin foils by electron microscopy *J. Phys. D. Appl. Phys.* **17** 623–47

[16] Chapman J N, McFadyen I R and McVitie S 1990 Modified differential phase contrast Lorentz microscopy for improved imaging of magnetic structures *IEEE Trans. Magn.* **26** 1506–11

[17] Tonomura A, Matsuda T, Endo J, Arii T and Mihama K 1980 Direct Observation of Fine Structure of Magnetic Domain Walls by Electron Holography *Phys. Rev. Lett.* **44** 1430–3

[18] Tonomura A 1987 Applications of electron holography *Rev. Mod. Phys.* **59** 639–69

[19] Gabor D 1949 Microscopy by Reconstructed Wave-Fronts *Proc. R. Soc. A Math. Phys. Eng. Sci.* **197** 454–87

[20] Abbe E 1873 Beiträge zur Theorie des Mikroskops und der mikroskopischen Wahrnehmung *Arch. für Mikroskopische Anat.* **9** 413–8

[21] Abbe E 1911 Die Lehre von der Bildentstehung im Mikroskop von Ernst Abbe *Nature* **87** 141–141

[22] Köhler H 1981 On Abbe's Theory of Image Formation in the Microscope *Opt. Acta Int. J. Opt.* **28** 1691–701

[23] Williams D B and Carter C B 2009 The Transmission Electron Microscopy *Transmission Electron Microscopy* (Boston, MA: Springer US) pp 3–22

[24] Fultz B 2008 Diffraction Contrast in TEM images *Transmission Electron Microscopy and Diffractometry of Materials* (Berlin, Heidelberg: Springer Berlin Heidelberg) pp 339–422

[25] Williams D B and Carter C B 2009 Phase-Contrast Images *Transmission Electron Microscopy* (Boston, MA: Springer US) pp 389–405

[26] Jagannathan R, Simon R, Sudarshan E C G and Mukunda N 1989 Quantum theory of magnetic electron lenses based on the Dirac equation *Phys. Lett. A* **134** 457–64

[27] Jagannathan R 1990 Quantum theory of electron lenses based on the Dirac equation *Phys. Rev. A* **42** 6674–89

[28] Aharonov Y and Bohm D 1959 Significance of Electromagnetic Potentials in the Quantum Theory *Phys. Rev.* **115** 485–91

[29] Lichte H and Lehmann M 2008 Electron holography—basics and applications *Reports Prog. Phys.* **71** 016102

[30] Zernike F 1935 Das Phasenkontrastverfahren bei der mikroskopischen Beobachtung *Z. Techn. Phys.* **16** 454–7

[31] De Graef M 2003 The Transmission Electron Microscope *Introduction to Conventional Transmission Electron Microscopy* (Cambridge University Press) pp 140–233

[32] Dosse J 1941 Strenge Berechnung magnetischer Linsen mit unsymmetrischer Feldform nachH=H 0/1+(z/a)2 *Zeitschrift für Phys.* **117** 316–21

[33] Rodríguez L A, Magén C, Snoeck E, Gatel C, Marín L, Serrano-Ramón L, Prieto J L, Muñoz M, Algarabel P A, Morellon L, De Teresa J M and Ibarra M R 2013 Quantitative in situ magnetization reversal studies in Lorentz microscopy and electron holography. *Ultramicroscopy* **134** 144–54

[34] Dunin-Borkowski R E, Feuerbacher M, Heggen M, Houben L, Kovács A, Luysberg M, Thust A and Tillmann K 2012 Advanced Transmission Electron Microscopy Techniques and Applications *Lecture Notes of the 43rd IFF Spring School "Scattering Methods for Condensed Matter Research: Towards Novel Applications at Future Souces"* (Forschungszentrum, Jülich) pp 1–28

[35] Nuhfer N, Budruk A and De Graef M 2010 Aberration-Corrected Lorentz Microscopy *Microsc. Microanal.* **16** 142–3

[36] Donahue M J and Porter D G http://math.nist.gov/oommf/ **87**

[37] De Graef M 2001 Lorentz microscopy: Theoretical basis and image simulations *Magnetic Imaging and Its Applications to Materials. Experimental Methods in the Physical Sciences* vol 36 pp 27–67

[38] Dekkers N H and De Lang H 1974 Differential Phase contrast in STEM *Optik (Stuttg).* **41** 452–6

[39] Shibata N, Findlay S D, Kohno Y, Sawada H, Kondo Y and Ikuhara Y 2012 Differential phase-contrast microscopy at atomic resolution *Nat. Phys.* **8** 611–5

[40] Dyck D Van 1983 High-speed computation techniques for the simulation of high resolution electron micrographs *J. Microsc.* **132** 31–42

[41] Van Dyck D and Coene W 1987 A new procedure for wave function restoration in high resolution electron microscopy *Optik (Stuttg).* **3** 125–8

[42] Van Dyck D and Op de Beek M 1993 A new approach to object wavefunction reconstruction in electron microscopy *Optik (Stuttg).* **3** 103–7

[43] Beleggia M, Schofield M A, Volkov V V and Zhu Y 2004 On the transport of intensity technique for phase retrieval. *Ultramicroscopy* **102** 37–49

[44] Tanji T 2005 Imaging Magnetic Structures Using TEM *Handbook of Microscopy for Nanotechnology* ed N Yao and Z L Wang (Boston: Kluwer Academic Publishers) pp 683–715

[45] Paganin D and Nugent K 1998 Noninterferometric Phase Imaging with Partially Coherent Light *Phys. Rev. Lett.* **80** 2586–9

[46] Volkov V V, Zhu Y and De Graef M 2002 A new symmetrized solution for phase retrieval using the transport of intensity equation *Micron* **33** 411–6

[47] Tonomura A 1992 Electron-holographic interference microscopy *Adv. Phys.* **41** 59–103

[48] Lichte H 1993 Parameters for high-resolution electron holography *Ultramicroscopy* **51** 15–20

[49] Möllenstedt G and Düker H 1956 Beobachtungen und Messungen an Biprisma-Interferenzen mit Elektronenwellen *Zeitschrift für Phys.* **145** 377–97

[50] Dunin-Borkowski R E, Kasama T, Beleggia M and Pozzi G 2012 *Handbook of Nanoscopy* ed G Van Tendeloo, D Van Dyck and S J Pennycook (Weinheim, Germany: Wiley-VCH Verlag GmbH & Co. KGaA)

[51] Lichte H 1996 Electron holography: optimum position of the biprism in the electron microscope *Ultramicroscopy* **64** 79–86

[52] Hÿtch M J, Snoeck E and Kilaas R 1998 Quantitative measurement of displacement and strain fields from HREM micrographs *Ultramicroscopy* **74** 131–46

[53] De Ruijter W J and Weiss J K 1993 Detection limits in quantitative off-axis electron holography *Ultramicroscopy* **50** 269–83

[54] Tonomura A, Matsuda T, Endo J, Arii T and Mihama K 1986 Holographic interference electron microscopy for determining specimen magnetic structure and thickness distribution *Phys. Rev. B* **34** 3397–402

[55] Dunin-Borkowski R E, McCartney M R, Kardynal B and Smith D J 1998 Magnetic interactions within patterned cobalt nanostructures using off-axis electron holography *J. Appl. Phys.* **84** 374

[56] Loudon J C, Mathur N D and Midgley P A 2002 Charge-ordered ferromagnetic phase in La(0.5)Ca(0.5)MnO3. *Nature* **420** 797–800

[57] Yoo J, Murakami Y, Shindo D, Atou T and Kikuchi M 2002 Behavior of magnetic domains in $La_{0.46}Sr_{0.54}MnO_3$ during the ferromagnetic phase transformation studied by electron holography *Phys. Rev. B* **66** 212406

[58] Young R J and Moore M V 2005 Dual-Beam (FIB-SEM) Systems *Introduction to Focused Ion Beams* (Springer US) pp 247–68

[59] Reyntjens S and Puers R 2001 A review of focused ion beam applications in microsystem technology *J. Micromechanics Microengineering* **11** 287–300

[60] Yao N 2007 *Focused Ion Beam Systems: Basics and Applications* (Cambridge University Press)

[61] Van Dorp W F and Hagen C W 2008 A critical literature review of focused electron beam induced deposition *J. Appl. Phys.* **104** 081301

[62] Huth M, Porrati F, Schwalb C, Winhold M, Sachser R, Dukic M, Adams J and Fantner G 2012 Focused electron beam induced deposition: A perspective. *Beilstein J. Nanotechnol.* **3** 597–619

[63] Botman A, Mulders J J L and Hagen C W 2009 Creating pure nanostructures from electron-beam-induced deposition using purification techniques: a technology perspective. *Nanotechnology* **20** 372001

[64] Bruk M A, Zhikharev E N, Grigor'ev E I, Spirin A V., Kal'nov V A and Kardash I E 2005 Focused electron beam-induced deposition of iron- and carbon-containing nanostructures from triiron dodecacarbonyl vapor *High Energy Chem.* **39** 65–8

[65] Shimojo M, Takeguchi M and Furuya K 2006 Formation of crystalline iron oxide nanostructures by electron beam-induced deposition at room temperature *Nanotechnology* **17** 3637–40

[66] Takeguchi M, Shimojo M and Furuya K 2007 Nanostructure Fabrication by Electron-Beam-Induced Deposition with Metal Carbonyl Precursor and Water Vapor *Jpn. J. Appl. Phys.* **46** 6183–6

[67] Lukasczyk T, Schirmer M, Steinrück H-P and Marbach H 2008 Electron-beam-induced deposition in ultrahigh vacuum: lithographic fabrication of clean iron nanostructures. *Small* **4** 841–6

[68] Lavrijsen R, Córdoba R, Schoenaker F J, Ellis T H, Barcones B, Kohlhepp J T, Swagten H J M, Koopmans B, De Teresa J M, Magén C, Ibarra M R, Trompenaars P and Mulders J J L 2011 Fe:O:C grown by focused-electron-beam-induced deposition: magnetic and electric properties. *Nanotechnology* **22** 025302

[69] Lichte H and Lehmann M 2008 Electron holography—basics and applications *Reports Prog. Phys.* **71** 016102

[70] Thong J T L, Oon C H, Yeadon M and Zhang W D 2002 Field-emission induced growth of nanowires *Appl. Phys. Lett.* **81** 4823

[71] Utke I 2004 Thermal effects during focused electron beam induced deposition of nanocomposite magnetic-cobalt-containing tips *Microelectron. Eng.* **73-74** 553–8

[72] Fernández-Pacheco A, De Teresa J M, Córdoba R and Ibarra M R 2009 Magnetotransport properties of high-quality cobalt nanowires grown by focused-electron-beam-induced deposition *J. Phys. D. Appl. Phys.* **42** 055005

[73] Córdoba R, Sesé J, De Teresa J M and Ibarra M R 2010 High-purity cobalt nanostructures grown by focused-electron-beam-induced deposition at low current *Microelectron. Eng.* **87** 1550–3

[74] Mulders J J L, Belova L M and Riazanova A 2011 Electron beam induced deposition at elevated temperatures: compositional changes and purity improvement. *Nanotechnology* **22** 055302

[75] Serrano-Ramón L, Córdoba R, Rodríguez L A, Magén C, Snoeck E, Gatel C, Serrano I, Ibarra M R and De Teresa J M 2011 Ultrasmall functional ferromagnetic nanostructures grown by focused electron-beam-induced deposition. *ACS Nano* **5** 7781–7

[76] Fernández-Pacheco A, Serrano-Ramón L, Michalik J M, Ibarra M R, De Teresa J M, O'Brien L, Petit D, Lee J and Cowburn R P 2013 Three dimensional magnetic nanowires grown by focused electron-beam induced deposition. *Sci. Rep.* **3** 1492

[77] Porrati F, Sachser R, Walz M-M, Vollnhals F, Steinrück H-P, Marbach H and Huth M 2011 Magnetotransport properties of iron microwires fabricated by focused electron beam induced autocatalytic growth *J. Phys. D. Appl. Phys.* **44** 425001

[78] Fernández-Pacheco A, De Teresa J M, Szkudlarek A, Córdoba R, Ibarra M R, Petit D, O'Brien L, Zeng H T, Lewis E R, Read D E and Cowburn R P 2009 Magnetization reversal in individual cobalt micro- and nanowires grown by focused-electron-beam-induced-deposition. *Nanotechnology* **20** 475704

[79] Jaafar M, Serrano-Ramón L, Iglesias-Freire O, Fernández-Pacheco A, Ibarra M R, De Teresa J M and Asenjo A 2011 Hysteresis loops of individual Co nanostripes measured by magnetic force microscopy. *Nanoscale Res. Lett.* **6** 407

[80] Jaafar M, Iglesias-Freire O, Serrano-Ramón L, Ibarra M R, de Teresa J M and Asenjo A 2011 Distinguishing magnetic and electrostatic interactions by a Kelvin probe force microscopy-magnetic force microscopy combination. *Beilstein J. Nanotechnol.* **2** 552–60

[81] Fernández-Pacheco A, Serrano-Ramón L E, Tyliszczak T, Chou K W, Córdoba R, Szkudlarek A, Brien L O, Kapusta C, Ibarra M R and De Teresa J M 2012 Correlation between the magnetic imaging of cobalt nanoconstrictions and their magnetoresistance response. *Nanotechnology* **23** 105703

[82] Minami T, Tatsumisago M, Wakihara M, Iwakura C, Kohjiya S and Tanaka I 2005 *Solid State Ionics for Batteries* vol 480, ed T Minami, M Tatsumisago, M Wakihara, C Iwakura, S Kohjiya and I Tanaka (Tokyo: Springer-Verlag)

[83] Castán-Guerrero C, Herrero-Albillos J, Bartolomé J, Bartolomé F, Rodríguez L A, Magén C, Kronast F, Gawronski P, Chubykalo-Fesenko O, Merazzo K J, Vavassori P, Strichovanec P, Sesé J and García L M 2014 Magnetic antidot to dot crossover in Co and Py nanopatterned thin films *Phys. Rev. B* **89** 144405

[84] Li J, Malis T and Dionne S 2006 Recent advances in FIB–TEM specimen preparation techniques *Mater. Charact.* **57** 64–70

[85] Cairney J . and Munroe P . 2001 Preparation of transmission electron microscope specimens from FeAl and WC powders using focused-ion beam milling *Mater. Charact.* **46** 297–304

Chapter 3

In situ TEM characterization of magnetic nanostructures under external magnetic field

3.1. Motivation

LM and EH offer the possibility to study the magnetic configurations of materials in the environmental conditions of TEM in Lorentz mode: ultra-high vacuum (typically 10^{-6} Pa), room temperature and zero (or residual) magnetic field. Such conditions are ideal to explore the remanent states of ferromagnetic materials. However, more interesting scientific problems can be tackled under the application of *in situ* external stimuli (magnetic [1–18] and electric fields [19,20], temperature changes [17,21–25], electric currents [26,27] or strain [28]) in order to analyze the quasi-dynamic evolution of the magnetic states. The magnetic field is the most relevant external parameter to be modified for the study of ferromagnets. In the case of *in situ* LM and EH, there are two ways to perform experiments under the application of magnetic fields using either a dedicated magnetizing holder or the magnetic field generated by the OL.

In situ TEM magnetizing holders are designed to apply magnetic fields within the sample plane. Most of them are custom-made and use micro-coils [7–9,12] or sharp magnetic needles [11] as sources of magnetic field. There are also commercial magnetizing stages, such as the one produced by Hummingbird Scientific, able to

apply in-plane magnetic fields up to ±900 Oe with an integrated magnetic compensation setup for the electron beam deflection up to ±300 Oe [18]. A picture of this commercial magnetizing holder is shown in Figure 3.1(a). The small range of magnetic fields applicable is the main limitation of magnetizing holders when it comes to analyze magnetization reversal processes in high-coercivity systems such as hard magnetic materials, low dimensionality magnetic nanostructures (e.g., nanowires, nanoparticles) and nanopatterned structures (e.g., dot/antidot arrays), whose coercive field values can easily be higher than 300 Oe [29,30]. Furthermore, the magnetic field orientation in most of the magnetizing stages is limited to the holder axis, so the possibilities for in-situ experiments are very restricted.

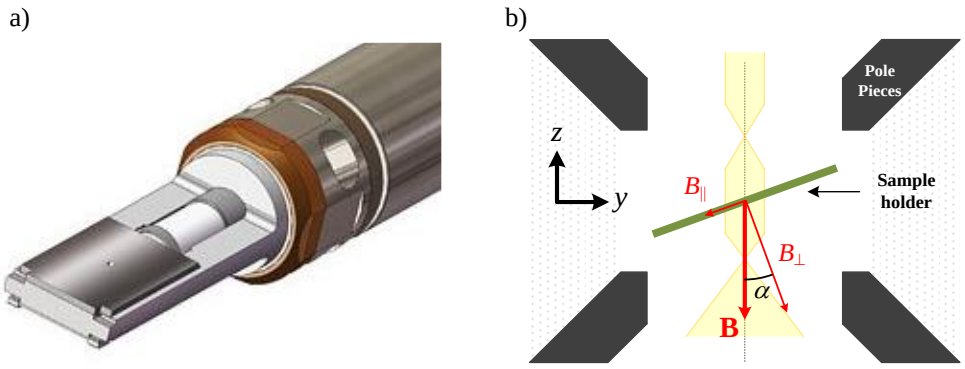

Figure 3.1. Two different ways to apply magnetic fields in TEM: a) Using a magnetizing holder (image from Hummingbird Scientific), b) using the magnetic field created by the microscope objective lens.

The use of the OL as a source of "external" magnetic field is the most simple and straightforward option [1–6,10,14–17]. As discussed in *Chapter 2*, the OL produces a strong magnetic field perpendicular to the sample plane whose magnitude can be tuned changing the electric current passing through the lens coils. Furthermore, it is possible to project a magnetic field component in the sample plane by tilting the specimen. If the sample is simply tilted around a single axis (e.g., *x*-axis), the in-plane

component of the magnetic field is just $B_0 \cdot \sin(\alpha)$, where B_0 is the magnetic field intensity of the OL at the sample plane in the optical axis, and α is the tilt angle, see Figure 3.1(b). Due to its simplicity, this procedure to perform *in situ* magnetic field TEM experiments has been widely used to study locally the evolution of magnetic configurations as a function of the in-plane magnetic field in various types of magnetic nanostructures such as nanoparticles, nanowires, heterostructures or magnetic tunnel junctions (MTJ) [1–6,14,15]. The versatility of this procedure can be improved using a double-tilt TEM stage where, combining two orthogonal tilt angles, the orientation of the in-plane component of the field in any desired direction can be achieved. This however requires performing a series of calculations to determine the modulus and direction of the in-plane magnetic field. Mathematical procedures to make a precise control of double-tilt rotations in a double-tilt stage have been reported in different TEM techniques such as electron diffraction, diffraction-contrast and phase-contrast imaging, electron tomography, among others [31–40] but, to our knowledge, never yet to control the direction of the magnetic fields generated by the OL. The main drawback of this method is that we cannot apply solely an in-plane field, as the out-of-plane component of the magnetic field on the sample is always present. Few works have analyzed the effect of this unavoidable out-of-plane component of the applied field [3,4] which, as we will show later, under certain circumstances can drastically influence the quantitative magnetic measurements and the magnetization switching process.

In this work, we have established the mathematical expressions to control and determine the in-plane magnetic field component. These formulae have been tested experimentally by manipulating domain walls (DWs) in a Co nanoring. We have analyzed the role of the intrinsic out-of-plane magnetic field component in two paradigmatic systems, a polycrystalline L-shaped cobalt nanowire and single crystalline $La_{2/3}Sr_{1/3}MnO_3$ (LSMO) and $La_{2/3}Ca_{1/3}MnO_3$ (LCMO) thin films, by determining the dependence of the coercive fields as a function of the out-of-plane magnetic field component. Finally, we have developed a suitable method to reconstruct accurately hysteresis loops by EH. It has been applied to a Fe/MgO/FeV

MTJ to evaluate the method and illustrate its potential application to make quantitative local magnetization studies of nanostructures.

3.2. Magnetic field calibration

The calibration of the magnetic field intensity produced by the OL at the sample plane position was made with a special TEM holder equipped with a dedicated Hall probe fitted in the sample position. This special Hall-probe TEM holder was designed and provided by Dr. Juergen Gruendmayer and Prof. Josef Zweck from University of Regensburg. The Hall probe is a high-sensitivity Hall sensor of MOVPE GaAs (KSY 44 from Infineon) with a linearity of the Hall voltage better than 0.2% up to 0.5 T, and a thermal stability better than 0.02%/K at room temperature. This calibration was performed in a FEI Titan microscope with the support of Dr. Sergei Lopatin from FEI. Calibration plots for a full range (from -9.5% to +100%) and low excitation range (from -9.5% to +12%) of the OL are represented in Figure 3.2. A linear dependence is measured for weak OL excitations (up to approximately 40%), which tends to saturate for higher OL excitations, achieving a maximum magnetic field value close to 2.2 T. This lens presents a narrow hysteresis effect with a remanent coercive field of approximately 30 Oe, which we have considered as an experimental error parameter.

The low current regime, which was used for quantitative *in situ* experiments, was fitted to linear dependences within the excitation range between -9.5% and 12%, obtaining the following lineal regressions:

$$H_{inc}(X) = 331.6X + 61 \qquad \text{(Eq. 3.1)}$$

$$H_{dec}(X) = 328.3X \qquad \text{(Eq. 3.2)}$$

for increasing (Equation 3.1) and decreasing (Equation 3.2) magnetic fields. H and X are the applied magnetic field (expressed in Oe) and the OL excitation (expressed in percentage), respectively. From the calibration plot of Figure 3.2(b), we see that this

weak linear excitation regime is able to apply magnetic fields between -3000 Oe and +4000 Oe, which was sufficiently large to perform the *in situ* LM and EH experiments presented in this Thesis.

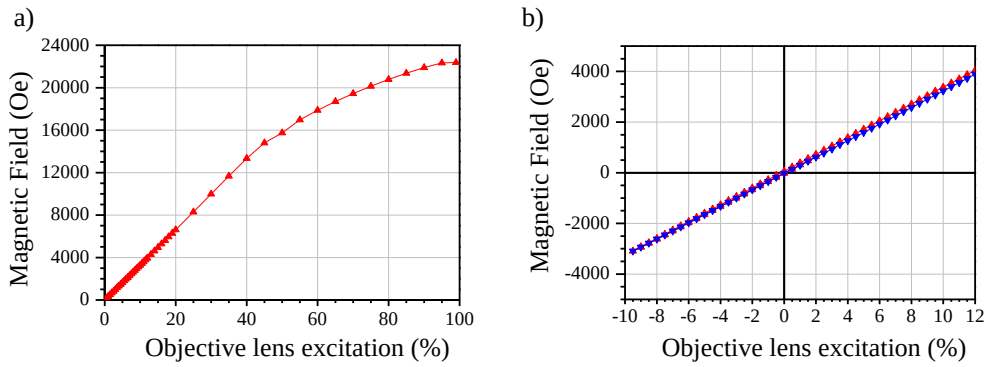

Figure 3.2. Calibration plots of the magnetic field produced by the OL for (a) high and (b) small OL excitations. Red and blue triangles represent increasing and decreasing variations of the OL excitation, respectively.

3.3. Calculation of the in-plane component of the OL magnetic field

A double-tilt TEM holder rotates as a goniometric system, see Figure 3.3(a), and its rotations can be well defined by means of a rotation linear transformation

$$\mathbf{V'} = \mathbf{V} \cdot \mathbf{G}_x \cdot \mathbf{G}_y \qquad \text{(Eq. 3.3)}$$

where $\mathbf{V} = (V_x, V_y, V_z)$ is a vector in the Cartesian coordinates of the initial reference system, i.e. the *z*-axis is parallel to the optical axis (opposite to the electron beam trajectory) and the (*x*, *y*) plane perpendicular to *z* as shown in Figure 3.3(b). $\mathbf{V'} = (V'_x, V'_y, V'_z)$ is the same vector **V** viewed from a rotated reference system, i.e. *x'* and *y'* axes are in the tilted sample plane and *z'* perpendicular to it. In our case, **V** and **V'** are the magnetic field vectors viewed from the sample holder plane before tilting (**H**) and

after tilting (**H'**), respectively. $\mathbf{G}_x$ and $\mathbf{G}_y$ are rotation matrices around the *x* and *y* axes in Figure 3.3(a), respectively:

$$\mathbf{G}_x = \begin{pmatrix} 1 & 0 & 0 \\ 0 & \cos(\alpha) & \sin(\alpha) \\ 0 & -\sin(\alpha) & \cos(\alpha) \end{pmatrix} \quad \mathbf{G}_y = \begin{pmatrix} \cos(\beta) & 0 & -\sin(\beta) \\ 0 & 1 & 0 \\ \sin(\beta) & 0 & \cos(\beta) \end{pmatrix} \qquad \text{(Eq. 3.4)}$$

where α and β are the rotation angle around *x* and *y*, respectively. The matrix expression in Equation 3.3 is

$$\left(V_{x'}, V_{y'}, V_{z'}\right) = \left(V_x, V_y, V_z\right) \begin{pmatrix} \cos(\beta) & 0 & -\sin(\beta) \\ \sin(\alpha)\sin(\beta) & \cos(\alpha) & \sin(\alpha)\cos(\beta) \\ \cos(\alpha)\sin(\beta) & -\sin(\alpha) & \cos(\alpha)\cos(\beta) \end{pmatrix}. \qquad \text{(Eq. 3.5)}$$

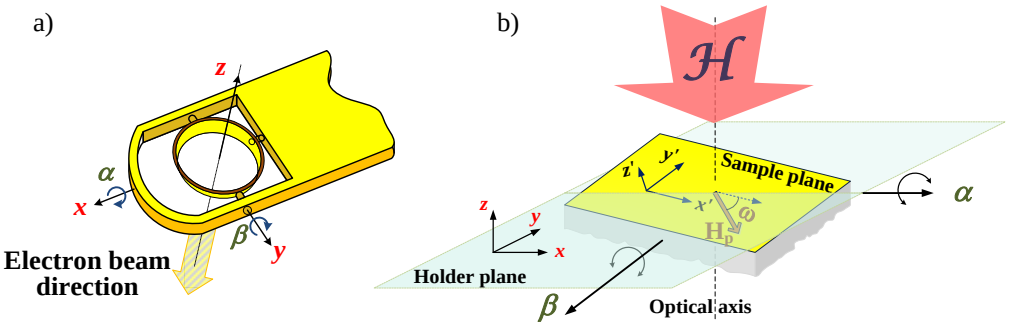

Figure 3.3. (a) Rotation modes of the double-tilt holder. (b) Schematic representation of the initial (*x*, *y*, *z*) and rotated (*x'*, *y'*, *z'*) reference systems.

This can be used to determine the in-plane magnetic field components. In the reference system before tilting, **H** = (0, 0, -*H*). Hence, according to Equation 3.5, **H'** will be

$$H_{x'} = -H\cos(\alpha)\sin(\beta) \qquad \text{(Eq. 3.6)}$$

$$H_{y'} = H\sin(\alpha) \qquad \text{(Eq. 3.7)}$$

$$H_{z'} = -H\cos(\alpha)\cos(\beta). \qquad \text{(Eq. 3.8)}$$

We can define the in-plane component of the magnetic field in the tilted reference system by its modulus (H_p) and the angle (ω) formed with respect to the positive *x'*-axis measured counterclockwise. Thus, H_p and ω can be expressed as

$$H_p = \sqrt{H_{x'}^2 + H_{y'}^2} = H\sqrt{\sin^2(\alpha) - \sin^2(\alpha)\sin^2(\beta) + \sin^2(\beta)} \qquad \text{(Eq. 3.9)}$$

$$\omega = \tan^{-1}\left(\frac{H_{y'}}{H_{x'}}\right) = \tan^{-1}\left(\frac{-\tan(\alpha)}{\sin(\alpha)}\right). \qquad \text{(Eq. 3.10)}$$

Using Equations 3.9 and 3.10 and the calibration of the OL magnetic field, we can calculate the modulus and direction of the in-plane magnetic field. The out-of-plane magnetic field component of the magnetic field with respect to the tilted sample plane will correspond to $H_{z'}$ and is calculated through Equation 3.8. Experimentally, it could be also useful to express α, β and H in terms of H_p and ω. From Equation 3.9 and 3.10, we can obtain

$$\alpha = \sin^{-1}\left(\frac{-k\sin(\omega)}{\sqrt{1+k^2}}\right) \qquad \text{(Eq. 3.11)}$$

$$\beta = \sin^{-1}\left(\frac{k\cos(\omega)}{\sqrt{1+k^2\cos^2(\omega)}}\right) \qquad \text{(Eq. 3.12)}$$

$$H = \frac{H_p}{k}\sqrt{1+k^2} \qquad \text{(Eq. 3.13)}$$

where k is the ratio between the in-plane and out-of-plane magnetic field components ($k = H_p/H_{z'}$). k is a free parameter within the experimental limits of the tilt angles, so the same in-plane field component can be obtained from numerous combinations of α, β and H, i.e. for multiple values of the out-of-plane magnetic field components. This is an important feature of this procedure, as it allows quantifying the out-of-plane component, which is experimentally unavoidable, and analyzing its influence often neglected in the literature. A freeware script for DigitalMicrograph™ has been developed to facilitate the calculation of the tilt angles and OL excitation required to apply a certain in-plane magnetic field along the desired in-plane orientation and for a given value of k (*this code can be downloaded from the website www.esteem2.eu*).

Experimentally, the calculation of the in-plane magnetic field orientation (Equation 3.10) has been tested in a ferromagnetic Co-FEBID nanoring grown by Dr. Luis Serrano in the LMA. This nanoring has an outer diameter of 10 μm, a corona width of 1 μm and a thickness of 30 nm. Its circular geometry and dimensions guarantee that two head-to-head and tail-to-tail transversal walls (TWs), located at opposite sides of the nanoring, are nucleated parallel to the in-plane component of the magnetic field. The experimental values of ω have been estimated by observing the position of the nucleated head-to-head TW after applying a strong magnetic field, and then reduce to zero, for different $\omega = \omega(\alpha, \beta)$ directions. Figure 3.4(a) represents three LM images of the Co nanoring after generating the nucleation of TWs for various values of ω and for H_p = 320 Oe. A polar representation of the experimental and theoretical values of ω for selected values of α and β such that $0 < \omega < 180°$ is reported in Figure 3.4(b). Both representations demonstrate the good agreement between the predictions of Equation 3.10 and the experimental results. The error bars used in the polar plot are overestimated since they have been calculated as the total angular range of the magnetic contrasts of the TWs. They would be much reduced if we use a ring with a narrower corona producing smaller TWs.

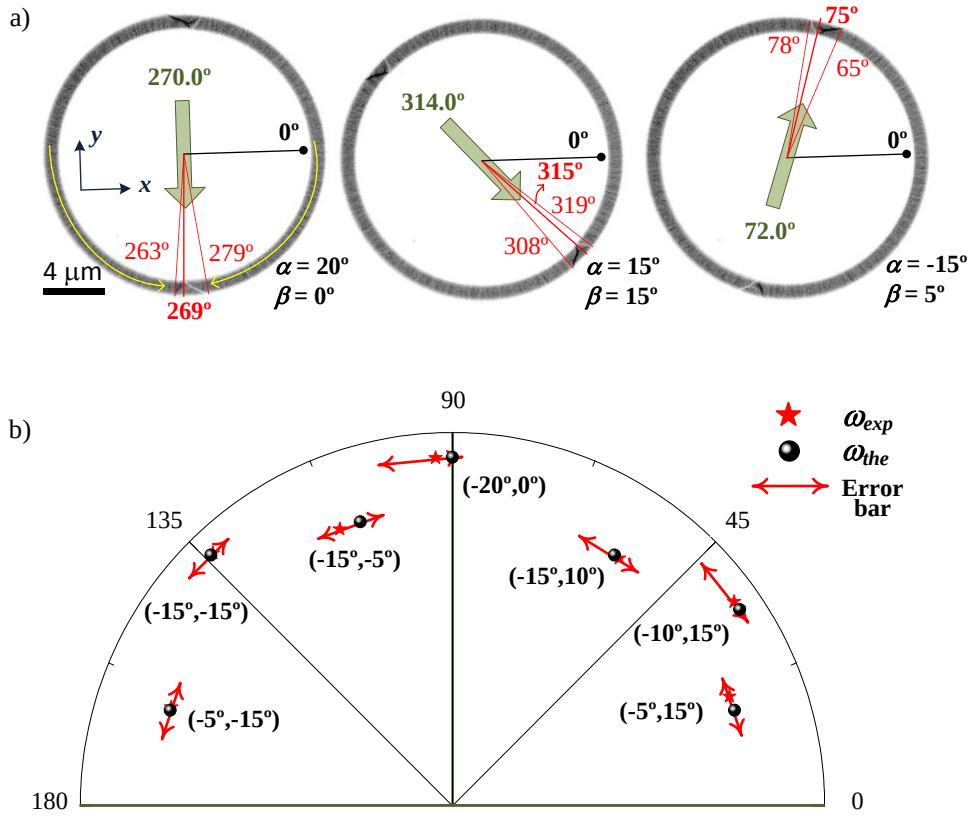

Figure 3.4. (a) Series of LM images for a Co-FEBID nanoring after applying a strong in-plane magnetic field in three different directions. Localized bright and dark contrast lines inside the ring correspond to the two nucleated TWs. Yellow and green arrows indicate the magnetization orientation and the theoretical direction of the in-plane component of the magnetic field, respectively. Values in red indicate the experimental angle measured in different parts of the TW (the edge and the interception point of the two bright and dark contrast lines). (b) Polar representation of the experimental (black balls) and predicted (red stars) values of ω. The error bars of the experimental values are estimated considering the whole size of the TWs. The red stars are the positions of the interception points of the TWs.

The previous calculation is performed considering $\alpha = \beta = 0$ as initial reference. This assumption is valid for plane samples perfectly oriented perpendicular to the optic axis. This is the case, for instance, in polycrystalline nanostructures grown on a flat surface, where the sample lies perfectly in the (x, y) plane of the stage. Other systems

however require to be reoriented because either the sample does not lie flat on the stage plane, or the sample is single crystalline and the orientation of the magnetic field has to be defined with respect to a specific crystal orientation, which usually does not correspond to $\alpha = \beta = 0$. Therefore, a more general expression is needed to estimate the magnetic field components with respect to an arbitrary initial reference. This generalization implies the introduction of two additional matrix transformations to bring the new initial tilted reference to (α, β) = (0, 0). These two transformation matrices, $\mathbf{G}_{x0}$ and $\mathbf{G}_{y0}$, are inverse rotation matrices similar to $\mathbf{G}_x$ and $\mathbf{G}_y$, and produce rotations in -α and -β directions, respectively. They are expressed as

$$\mathbf{G}_{x_0} = \begin{pmatrix} 1 & 0 & 0 \\ 0 & \cos(\alpha_0) & -\sin(\alpha_0) \\ 0 & \sin(\alpha_0) & \cos(\alpha_0) \end{pmatrix} \quad \mathbf{G}_{y_0} = \begin{pmatrix} \cos(\beta_0) & 0 & \sin(\beta_0) \\ 0 & 1 & 0 \\ -\sin(\beta_0) & 0 & \cos(\beta_0) \end{pmatrix} \qquad \text{(Eq. 3.14)}$$

where α_0 and β_0 are the tilt angles of the new reference. The general rotation transformation is expressed as

$$\mathbf{V'} = \mathbf{V} \cdot \mathbf{G}_{x_0} \cdot \mathbf{G}_{y_0} \qquad \text{(Eq. 3.15)}$$

thus the magnetic field components are

$$\begin{aligned} H_{x'} = -H[&\cos(\beta)\sin(\beta_0) - \sin(\alpha)\sin(\beta)\sin(\alpha_0)\cos(\beta_0) \\ &- \cos(\alpha)\sin(\beta)\sin(\alpha_0)\cos(\beta_0)] \end{aligned} \qquad \text{(Eq. 3.16)}$$

$$H_{y'} = -H[-\cos(\alpha)\sin(\alpha_0)\cos(\beta_0) + \sin(\alpha)\cos(\alpha_0)\cos(\beta_0)] \qquad \text{(Eq. 3.17)}$$

$$\begin{aligned} H_{z'} = H[&-\sin(\beta)\sin(\beta_0) - \sin(\alpha)\cos(\beta)\sin(\alpha_0)\cos(\beta_0) \\ &- \cos(\alpha)\cos(\beta)\cos(\alpha_0)\cos(\beta_0)] \end{aligned} \qquad \text{(Eq. 3.18)}$$

and the modulus and direction of the in-plane magnetic field are calculated using the same $H_{x'}$ and $H_{y'}$ dependence of the H_p and ω shown in Equation 3.9 and 3.10. These new expressions generalize the method to estimate the in-plane magnetic field

component, but complicate the determination of α, β and the OL excitation as a function of H_p and ω, and numerical method are required to solve this equation. As we will see along this Thesis, this procedure will be essential to perform quantitative *in situ* TEM experiments under magnetic fields.

3.4. Influence of the out-of-plane magnetic field component in the *in situ* experiment

The theoretical results obtained in the previous section allow developing numerous experiments that require a perfect control on the magnitude and orientation of the magnetic field in the sample plane. However, the main drawback of this procedure is the unavoidable presence of an important out-of-plane magnetic field component, $H_{z'}$. Considering $H_p/H = \sin(\theta_z)$, where θ_z is the tilt angle of the sample plane with respect to a plane perpendicular to the optical axis, $k = H_p/H_{z'}$ can be rewritten as

$$k = \tan(\theta_z). \qquad \text{(Eq. 3.19)}$$

Equation 3.19 shows that, to reduce the modulus of the out-of-plane component (i.e. increase the value of k), θ_z has to increase as much as possible. For example, for θ_z = 10° (k = 0.176) the out-of-plane component is almost 6 times larger than the in-plane component; both will be equal for θ_z = 45°, which is however an angle experimentally inaccessible in conventional microscopes (e.g., in a FEI Titan^3, the maximum tilt angle to α and β is limited to ± 35° - 40°). In addition, large tilt angles induce shadowing effects, increase the projected sample thickness and change the aspect ratio of the specimen in the image. Thus, the intensity of the out-of-plane component of the magnetic field is often sufficiently high to influence the quantitative analysis of the *in situ* magnetization reversal studies by LH and EH on nanostructures.

For this reason, we have evaluated the influence of $H_{z'}$ in magnetization switching processes on stripe-shaped high aspect ratio magnetic nanostructures with particular magnetic anisotropies controlled by their geometry, microstructure and composition. Such evaluation was carried out by measuring the coercive field, H_c, from LM experiments in three different systems: a polycrystalline Co nanowire and two TEM lamellae of single-crystalline LSMO and LCMO thin films and for different values of k (i.e. different in-plane to out-of-plane field ratio):

- The Co-FEBID nanowire was fabricated in the LMA laboratory by Dr. Luis Serrano on a 50-nm-thick Si_3N_4 membrane, with a geometric dimension of 8 μm length, 250 nm width and 30 nm thickness.

- The high quality epitaxial 40-nm-thick LSMO and 30-nm-thick LCMO thin films were grown on (100)-oriented $SrTiO_3$ substrates by Pulsed Laser Deposition (PLD) in the Growth Thin Film Group of the INA by Lorena Marín (see Chapter 6). Cross-section TEM lamellae were fabricated by FIB technique defining a defect-free electron transparent length of 3-4 μm and an estimated thickness of approximately 60 nm. These TEM specimen were fabricated by Dra Rosa Córdoba and Laura Casado in the LMA.

The calculation of H_c was carried out by performing hysteresis cycles in which the in-plane magnetic field component was applied along the nanowire and TEM lamellae. H_c was estimated by the observation of the contrast change of the Fresnel fringes along the edge of the samples in LM. At $H = H_c$, a bright magnetic contrast line moves from one edge to another, almost spontaneously, revealing that the magnetization reversal process has occurred, see Figure 3.5(a). Finally, H_c for Co nanowires was measured at room temperature, while for LSMO and LCMO thin films was measured at 100 K, temperature at which both systems are ferromagnetic.

A plot representing H_c as a function of θ_z for the three systems is shown in Figure 3.5(b). The reported value of H_c corresponds to the mean value of 5 different measurements for each θ_z, leading to a small dispersion of approximately 5% in most

of the data, and up to 11 % at θ_z = 35 for the LSMO film. For the Co nanowires, we find that H_c is independent of θ_z within the experimental range measured (5° < θ_z < 25.3°), with an average value of 284 Oe, while the coercive fields measured in the manganite systems significantly depend on θ_z. Whereas in LCMO the coercive field measured decreases with θ_z from 586 ± 5 Oe to 474 ± 5 Oe, in LSMO the coercive field follow an irregular behavior between 159 ± 16 Oe and 231 ± 6 Oe. These results reflect the importance of the microstructure and magnetic anisotropy of the materials when analyzing micromagnetic parameters such as the coercive field through this *in situ* LM procedure.

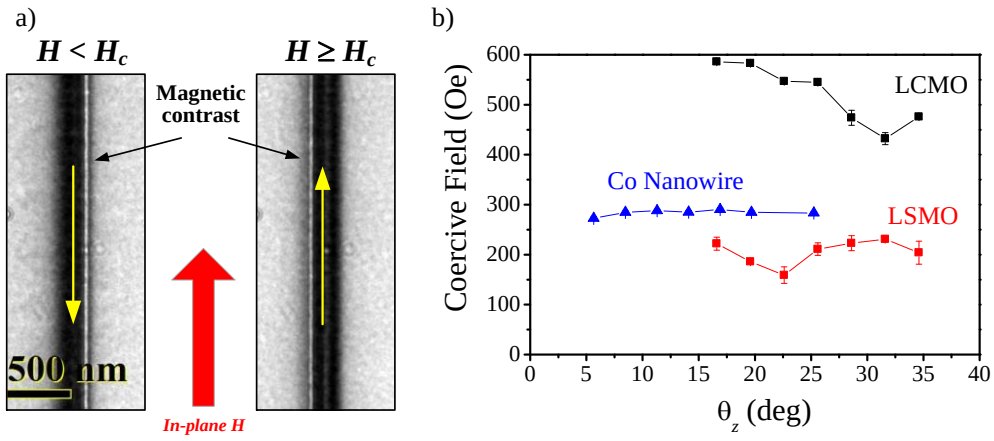

Figure 3.5. (a) Two defocused LM images of the FEBID Co nanowire recorded at $H < H_c$ and $H > H_c$ showing the switching of the bright magnetic Fresnel contrast from one edge of the wire to the other. (b) Dependence of the coercive field as a function of the out-of-plane magnetic field component (represented by θ_z) for the three different ferromagnetic systems analyzed.

FEBID cobalt nanowires are polycrystalline, composed of nanocrystals so small (2-3 nm) [41] that the magnetocrystalline anisotropy is averaged to zero and the magnetization processes are determined by the exchange energy, intrinsic to the material, and the magnetostatic energy, which is extremely dependent on the geometry of the ferromagnetic object. In the case of a flat elongated object like a nanowire, the

large shape anisotropy dominates the micromagnetic behavior and tends to confine the magnetization along the nanowire's axis due to the large demagnetizing fields on any other direction. For these reasons, the out-of-plane magnetic field does not play a major role in the magnetization processes. On the contrary, epitaxial manganite thin films, which also present a large shape anisotropy, are single crystalline materials with a specific magnetocrystalline anisotropy and easy magnetization axis different in the two manganite: [110] for LSMO and [100] for LCMO [42] so they present a thoroughly different dependence. The analysis of the microscopic origin of the magnetization processes in these two manganite films as a function of the specific magnetocrystalline anisotropy is beyond the scope of this work. It is however clear that when magnetocrystalline anisotropy is relevant, the out-of-plane component of the magnetic field cannot be neglected, even in the case of highly anisotropic nanopatterned materials.

3.5. Quantitative hysteresis loops in nanostructures with high shape anisotropy

The tools we have developed to make *in situ* quantitative LM experiments applying magnetic fields via OL can also be applied for a local quantitative measurement of magnetization hysteresis loops in heterostructures by EH or TIE reconstruction in LM. As discussed in the *Chapter 2*, EH and LM enable to extract quantitative information of the magnetic induction of the sample by calculating the phase shift of the object electron wave. Depending on the shape of the nanostructure, the calculation of the magnetic induction can be rather complicated, but in the case of a system of uniform thickness where the electrostatic potential (V_{MIP}) is constant along the whole thickness, the in-plane magnetic induction components can be easily calculated via Equation 2.27 (*Chapter 2*).

$$\mathbf{B}(x,y) = (B_x, B_y) = \frac{\hbar t}{e}\left(-\frac{\partial\varphi}{\partial y}, \frac{\partial\varphi}{\partial x}\right)$$

and the in-plane components of the magnetization can be calculated as

$$\mathbf{M}(x,y) = \frac{\mathbf{B}(x,y)}{\mu_0} - \mathbf{H}(x,y)\,. \qquad \text{(Eq. 3.20)}$$

Thus, either by means of Equation 2.27 or 3.20, the hysteresis loops of one of the in-plane magnetization components can be reconstructed when it is confined in the plane of the specimen.

The simpler the geometry and magnetic anisotropy of the nanostructure, the easier will be the local hysteresis loop measurement by EH and LM. For instance, very elongated nanostructures with a polycrystalline microstructure (e.g. a FEBID Co nanowires) or with a single crystalline structure where the easy magnetization axis is parallel to the longest length (e.g. a TEM lamella of a LCMO manganite grown on (100)-oriented STO substrate) are simple systems to reconstruct local hysteresis loops. Indeed in these systems the magnetization tends to be aligned along the preferential easy direction along which the in plane applied magnetic field can be easily oriented (for instance the *x*-axis). The total magnetic induction of the sample that then is equal to the component of the magnetic induction along the easy axis (the *x*-axis) can therefore be estimated by calculating the gradient of the phase shift along the perpendicular axis (*y*-axis in our example):

$$B_x = -\frac{\hbar t}{e}\frac{\partial \varphi}{\partial y}. \qquad \text{(Eq. 3.21)}$$

As already discussed, *in situ* LM and EH experiments using the OL to apply an "external" magnetic field require tilting the sample for the application of the in-plane fields and therefore the unavoidable appearance of an out-of-plane magnetic field component. This implies that the quantitative information extracted has to be corrected to compare with results obtained by dedicated magnetometry equipments or micromagnetic simulations. LM and EH are only sensitive to the magnetic induction components perpendicular to the electron beam trajectory. Therefore, if we consider a simple case where the magnetization of the sample is oriented along the *x*-axis, the

"apparent" magnetization recorded, M_x, is the projection of the *x*-component of the magnetization in the plane perpendicular to the optical axis. In case the sample is not perfectly perpendicular to the optical axis, it will not correspond to the projection of the *x*-component in the sample plane ($M_{x'}$), see Figure 3.6(a).

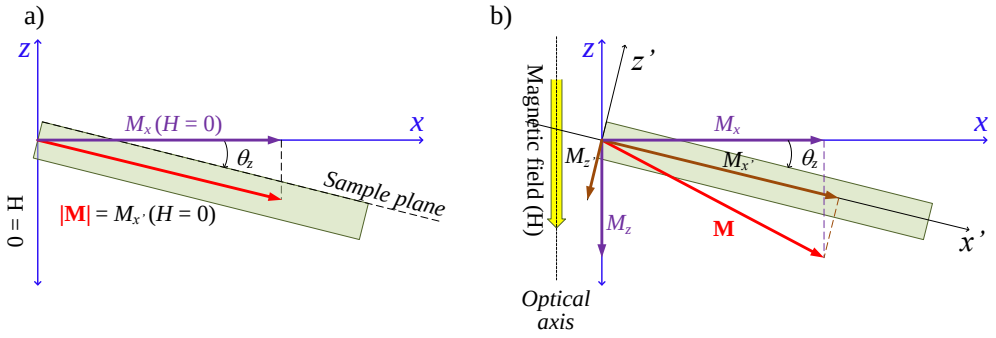

Figure 3.6. Schematic representation of the magnetization vector in a high-shape anisotropic object measured from the microscope (*x*, *z* axis) and the sample plane (*x'*, *z'* axis) reference systems: (a) at $H = 0$ and (b) after saturation.

For this situation, $M_{x'}$ can easily be determined as

$$M_{x'} = \frac{M_x}{\cos(\theta_z)} = |\mathbf{M}| \qquad \text{(Eq. 3.22)}$$

where |**M**| is the magnitude of the total magnetization. This is applicable in a remanent state ($H = 0$) for polycrystalline nanowires or thin cross sectional TEM lamellae with a magnetocrystalline anisotropy parallel to the longest dimension in the substrate plane. The relationship between M_x and $M_{x'}$ will be more complex when we use the OL to apply an external magnetic field and perform magnetic hysteresis loops measurements. In saturation conditions, the out-of-plane magnetic field components could be sufficiently strong to rotate the magnetization out of the sample plane, see Figure 3.6(b), and a rotation linear transformation must be used to calculate $M_{x'}$. If we assume that the magnetization vector only rotates in the plane containing the high

shape anisotropy axis of the nanostructure and the optical axis, the rotation linear transformation can be expressed as

$$\mathbf{M}' = \mathbf{M} \cdot \mathbf{R}(\theta_z) \qquad \text{(Eq. 3.23)}$$

where $\mathbf{M} = (M_x, M_y, M_z)$ and $M' = (M_{x'}, M_{y'}, M_{z'})$ are the same magnetization vector expressed in two different reference systems where z-axis is parallel to the optical axis and z'-axis is normal to the sample plane, respectively. $\mathbf{R}(\theta_z)$ is a rotation matrix related to the tilt angle of the sample (θ_z) defined as

$$\mathbf{R}(\theta_z) = \begin{pmatrix} \cos(\theta_z) & \sin(\theta_z) \\ -\sin(\theta_z) & \cos(\theta_z) \end{pmatrix}. \qquad \text{(Eq. 3.24)}$$

Solving the matrix expression in Equation 3.24 for $M_{x'}$, we get

$$M_{x'} = M_x \cos(\theta_z) - M_z \sin(\theta_z). \qquad \text{(Eq. 3.25)}$$

Equation 3.25 indicates that the calculation of $M_{x'}$ requires the knowledge of the z-component of the magnetization, M_z, which cannot be measured by LM and/or EH. Considering that $|\mathbf{M}|$ remains constant and assuming that the magnetization is confined in the (x, z) plane, $|\mathbf{M}|^2 = (M_x^2 + M_z^2)^{1/2}$, Equation 3.25 can be rewritten as

$$M_{x'} = M_x \cos(\theta_z) \mp \sqrt{|\mathbf{M}|^2 - M_x^2} \sin(\theta_z). \qquad \text{(Eq. 3.26)}$$

Thus, we find that $M_{x'}$ only depends of M_x and $|\mathbf{M}|$. The magnitude of the total magnetization can be estimated using Equation 3.22 in the remanent state, where the total magnetization of the specimen is completely aligned along the sample plane. The sign choice for the second term will depend on whether the magnetization is tilted downward or upward with respect to the sample plane.

This procedure has been applied for the quantitative determination of hysteresis loops by EH measurements. The object of study is a cross-section TEM lamella of a

MTJ heterostructure fabricated by molecular beam epitaxy (MBE): Fe (68 nm)/MgO (2 nm)/FeV (18 nm)/Au (20 nm), grown on a (001)-oriented MgO substrate. An intermediate magnification bright-field TEM image of this heterostructure is shown in Figure 3.7(a). The EH experiments have been performed at the highest magnification possible in LM mode on the Titan^3 microscope (×70000) using a biprism voltage of 250 V, which provides a fringe spacing of 2 nm. Holograms of 1024 × 1024 pixels were obtained with an exposure time of 5 s, giving rise to a fringe contrast higher than 20%. A magnetic field cycle was carried out by exciting the OL magnetic field between -3000 Oe and 4000 Oe, and tilting the sample an angle θ_z = 23°.

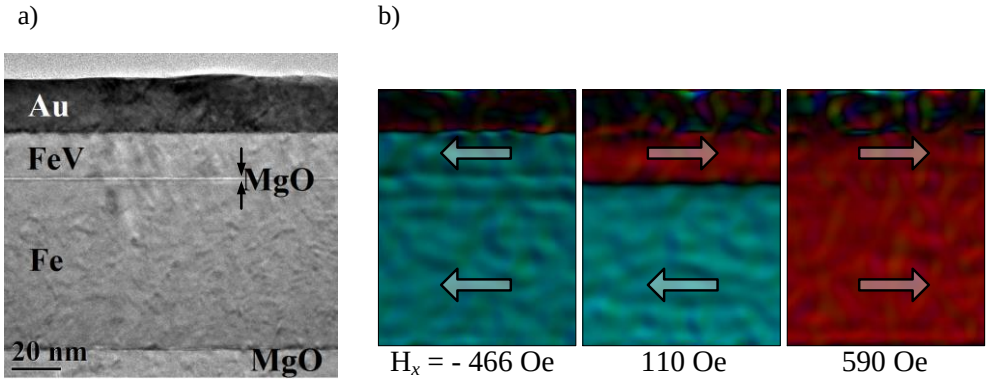

Figure 3.7. (a) TEM image of the Fe/MgO/FeV/Au MTJ. (b) Magnetic induction reconstruction of the MTJ for three different applied magnetic fields showing a local magnetic decoupling of the ferromagnetic electrodes. The arrows represent the direction of the magnetization.

Figure 3.7(b) illustrates how the spatial and phase resolution of EH allows reconstructing the hysteresis loops for each layer by measuring the magnetic induction of each layer with an accuracy better than 2%. Subsequently, the hysteresis loop for the whole MTJ can be obtained by adding both contributions, as shown in Figure 3.8. Similar to previous reports on other Fe and FeV based MTJ heterostructures [15,43], the two ferromagnetic electrodes are magnetically decoupled, and the particular configuration of this MTJ heterostructure makes that the magnetization switching first occurs in the upper thin electrode (FeV). The stripe-like geometry of the

heterostructures, with a length of several microns and film thicknesses of 68 nm (Fe) and 18 nm (FeV) and TEM specimen thickness between 40-70 nm for both layers, induces a magnetization reversal by the nucleation and propagation of one or two single DWs along each ferromagnetic layer. The magnetic configuration of the propagated DW is depicted in Figure 2.8(b) and (c) of the *Chapter 2*, where two transversal domain walls (TWs) are coupled in a particular region of the heterostructure. This reversal magnetization mechanism is similar to that reported in ferromagnetic nanowires [44–46]. In addition, both hysteresis loops present a substantial shift toward positive values of magnetic field, as we can see through the coercive field values (for Fe layer, H_c = -81 and 151 ± 11 Oe, and for FeV layer, H_c = -11 and 75 ± 11 Oe). This displacement of about 35 ± 11 Oe could be attributed to different factors, such as the stochastic behavior of the depinning process of DWs in some defects or the exchange bias caused the formation of small antiferromagnetic Fe oxide layers in the unprotected surface of the Fe and FeV layers by the exposition of the lamella to the atmosphere [47]. Another possible cause like the effect of the hysteresis of the OL calibration has been discarded due to its effect in the measurements of H_c is included in their absolute error and estimated as ΔH_c = $\sin(23°)\cdot\Delta H$, being ΔH = 30 Oe, which is the remanent coercive field of the small hysteretic effect of the OL.

The comparison between the uncorrected hysteresis loops and the ones corrected via Equation 3.26 is depicted in Figure 3.8(a), revealing a substantial difference. The correction induces a counter-clockwise rotation of the cycles, decreasing the "apparent" tilt of the magnetization outward the sample plane. To test the validity of our correction method, we have performed micromagnetic simulations of individual Fe and FeV layers following the same experimental procedure and using as magnetic parameters those reported in Refs [43,48,49]. Comparing *M*-*H* curves after saturation, we have found a good agreement between the corrected and simulated data. This comparison is only highlighted for the FeV layer in the inset of Figure 3.8(a), but similar results are obtained in the Fe layer. Once this correction has been taken into account, a precise evaluation of the effect induced by the out-of-plane magnetic field

component can be carried out, observing a slight inclination of the hysteresis loops, where M_x in both layers is reduced by ~5% for the highest applied magnetic field (H_x = 1167 Oe). In our experimental setup (sample tilt of θ_z = 23°), that means that an out-of-plane magnetic field value of 2660 Oe tilts the magnetization approximately 18° out of the sample plane. This result demonstrates again the importance of the out-of-plane magnetic field component, which in this case can induce a non-negligible tilt of the magnetization out the sample plane, even in systems with very high shape anisotropy.

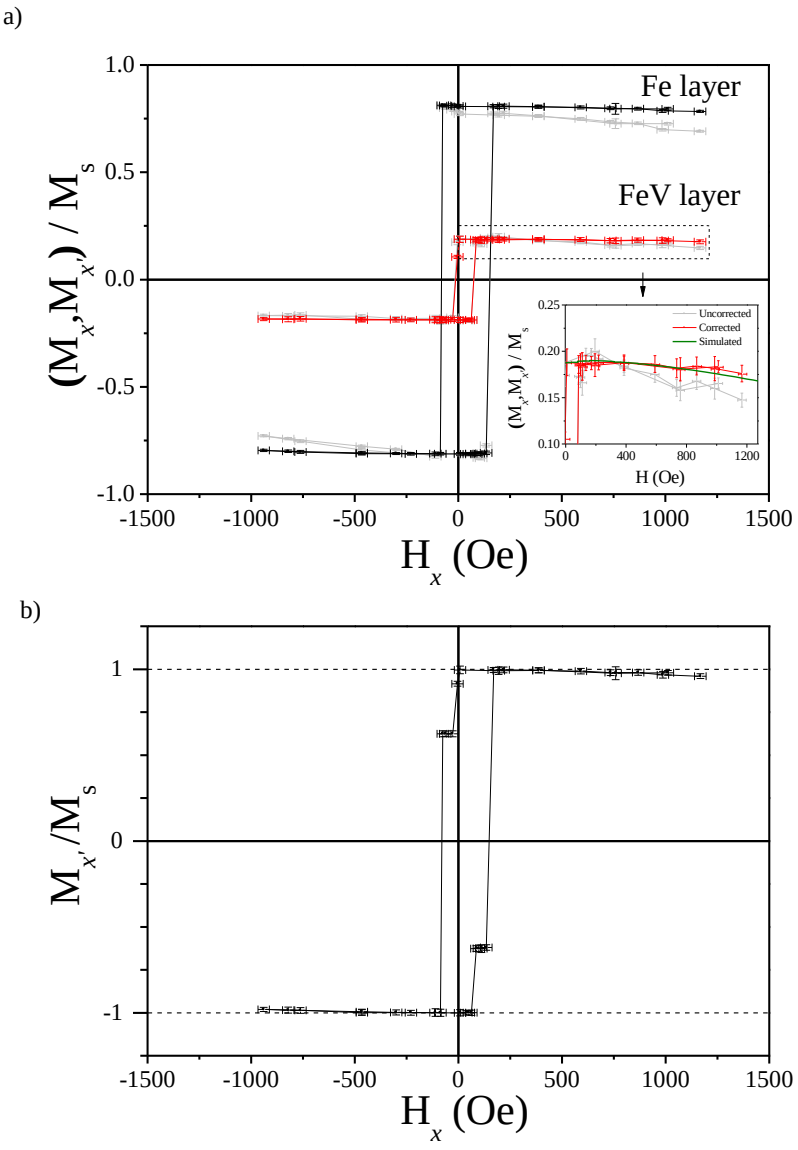

Figure 3.8. (a) Corrected (black and red dots) and uncorrected (gray dots) hysteresis cycles of the individual Fe and FeV layers in the Fe/MgO/FeV/Au MTJ. The values of M_x and $M_{x'}$ have been normalized to the total saturation magnetization (M_s) of the MTJ. A zoom of the saturation curve for FeV is showed in the inset, where the green line represents the simulated curve. (b) Hysteresis cycle of the MTJ by adding of the corrected magnetization ($M_{x'}$) of each layer.

3.6. Conclusions

In this Chapter, we have presented an optimized procedure to perform *in situ* LM and EH magnetometry using the OL as a source of magnetic fields. The improvement of this method was achieved through the use of a conventional FEI double-tilt TEM stage, where matrix expressions based on lineal rotation transformations allowed a precise orientation of a variable in-plane component of the magnetic field produced by the OL. The validity of this method was experimentally tested by manipulating the position of TWs in a FEBID Co nanoring, finding a very good agreement between the predicted and experimental direction of the in-plane magnetic field component. The potential of this *in situ* procedure can be widely exploited to perform magnetization reversal studies that require magnetic fields perfectly oriented. We ourselves will further demonstrate in this Thesis the potential of this method to perform quantitative and qualitative magnetization reversal studies such as the manipulation and characterization of DWs in nanostructures (*Chapter 4*) or the nucleation and propagation of superdomain walls inside antidot arrays by application of parallel and transversal magnetic fields (*Chapter 5*).

The OL also generates an unavoidable out-of-plane magnetic field component, which is always more intense than the in-plane component. Its influence was evaluated in two particular cases: (*i*) in the calculation of coercive fields and (*ii*) in the reconstruction of magnetization hysteresis loops of magnetic nanostructures with high shape anisotropy. In the first case, we found that the value of H_c in single-crystal structures such as LCMO and LSMO films can be strongly dependent on the out-of-plane component, while its effect can be neglected in a polycrystalline Co nanowire. In the second case, we showed that the out-of-plane magnetic field is able to tilt the saturated magnetization of a Fe/FeV based on MTJ heterostructure out of the sample's plane. These results demonstrate that an accurate analysis of local magnetic properties based on this *in situ* procedure has to take into account the effect of the out-of-plane magnetic field component.

Finally, we have determined the procedure to accurately reconstruct quantitative hysteresis loops in highly shape anisotropic heterostructures such a TEM lamella of a MTJ, even accounting for the influence of the out-of-plane magnetic field and the sample tilt in the magnetization direction after saturation. The high accuracy of the method allowed the observation of the local magnetic decoupling of the two ferromagnetic electrodes, which could be switched independently by the nucleation and propagation of single DWs, and the shift of the hysteresis loop towards positive fields that could be originated by stochastic or exchange bias effects.

References

[1] Dunin-Borkowski R E, McCartney M R, Smith D J and Parkin S S P 1998 Towards quantitative electron holography of magnetic thin films using in situ magnetization reversal *Ultramicroscopy* **74** 61–73

[2] Marshall A F, Klein L, Dodge J S, Ahn C H, Reiner J W, Mieville L, Antagonazza L, Kapitulnik A, Geballe T H and Beasley M R 1999 Lorentz transmission electron microscope study of ferromagnetic domain walls in $SrRuO_3$: Statics, dynamics, and crystal structure correlation *J. Appl. Phys.* **85** 4131

[3] Dunin-Borkowski R E, McCartney M R, Kardynal B, Smith D J and Scheinfein M R 1999 Switching asymmetries in closely coupled magnetic nanostructure arrays *Appl. Phys. Lett.* **75** 2641

[4] Dunin-Borkowski R E, McCartney M R, Kardynal B, Parkin S S, Scheinfein M R and Smith D J 2000 Off-axis electron holography of patterned magnetic nanostructures. *J. Microsc.* **200** 187–205

[5] Schneider M, Hoffmann H and Zweck J 2001 Magnetic switching of single vortex permalloy elements *Appl. Phys. Lett.* **79** 3113

[6] Harrison R J, Dunin-Borkowski R E and Putnis A 2002 Direct imaging of nanoscale magnetic interactions in minerals. *Proc. Natl. Acad. Sci. U. S. A.* **99** 16556–61

[7] Uhlig T, Heumann M and Zweck J 2003 Development of a specimen holder for in situ generation of pure in-plane magnetic fields in a transmission electron microscope *Ultramicroscopy* **94** 193–6

[8] Zaluzec N J, Hiller J, Cook R E, Kabius B, Miller D, Metlushko V V, Swihart T C, Smith D W, Matesa J M, Gronsky J J and Fischione P E 2004 In-Plane Magnetic Field Lorentz Stage for Use in a TEM/STEM *Microsc. Microanal.* **10** 522–3

[9] Inoue M, Tomita T, Naruse M, Akase Z, Murakami Y and Shindo D 2005 Development of a magnetizing stage for in situ observations with electron holography and Lorentz microscopy. *J. Electron Microsc. (Tokyo).* **54** 509–13

[10] Lau J W, Bording J K, Beleggia M and Zhu Y 2006 Energy barrier to magnetic vortex nucleation *Appl. Phys. Lett.* **88** 012508

[11] Aiso T, Shindo D and Sato T 2007 In Situ Lorentz Microscopy and Electron Holography of Magnetization Process in Ferrite Magnets *Mater. Trans.* **48** 2621–5

[12] Kasahara T, Shindo D, Yoshikawa H, Sato T and Kondo K 2007 In situ observations of domain structures and magnetic flux distributions in Mn-Zn and Ni-Zn ferrites by Lorentz microscopy and electron holography. *J. Electron Microsc. (Tokyo).* **56** 7–16

[13] Liu H H, Duan X K, Che R C, Wang Z F and Duan X F 2009 In Situ Lorentz Microscopy Observation of Displaced Chain Walls in Permalloy *Mater. Trans.* **50** 1660–3

[14] Masseboeuf A, Gatel C, Bayle-Guillemaud P, Lamy Y and Viala B 2009 The use of Lorentz microscopy for the determination of magnetic reversal mechanism of exchange-biased $Co_{30}Fe_{70}$/NiMn bilayer *J. Magn. Magn. Mater.* **321** 3080–3

[15] Javon E, Gatel C, Masseboeuf A and Snoeck E 2010 Electron holography study of the local magnetic switching process in magnetic tunnel junctions *J. Appl. Phys.* **107** 09D310

[16] Akase Z and Shindo D 2010 In situ Lorentz microscopy in an alternating magnetic field. *J. Electron Microsc. (Tokyo).* **59** 207–13

[17] Yu X Z, Onose Y, Kanazawa N, Park J H, Han J H, Matsui Y, Nagaosa N and Tokura Y 2010 Real-space observation of a two-dimensional skyrmion crystal. *Nature* **465** 901–4

[18] Budruk A, Phatak C, Petford-Long A K and De Graef M 2011 In situ Lorentz TEM magnetization studies on a Fe–Pd–Co martensitic alloy *Acta Mater.* **59** 6646–57

[19] Cumings J, Zettl A, McCartney M and Spence J 2002 Electron Holography of Field-Emitting Carbon Nanotubes *Phys. Rev. Lett.* **88** 056804

[20] Brintlinger T, Lim S-H, Baloch K H, Alexander P, Qi Y, Barry J, Melngailis J, Salamanca-Riba L, Takeuchi I and Cumings J 2010 In situ observation of reversible nanomagnetic switching induced by electric fields. *Nano Lett.* **10** 1219–23

[21] De Graef M, Willard M A and McHenry M E 2001 In-situ Lorentz TEM cooling study of magnetic domain configurations in Ni/sub 2/MnGa *IEEE Trans. Magn.* **37** 2663–5

[22] Loudon J C, Mathur N D and Midgley P A 2002 Charge-ordered ferromagnetic phase in La(0.5)Ca(0.5)MnO3. *Nature* **420** 797–800

[23] Sugawara A, Fukunaga K, Scheinfein M R, Kobayashi H, Kitagawa H and Tonomura A 2007 Electron holography study of the temperature variation of the magnetic order parameter within circularly chained nickel nanoparticle rings *Appl. Phys. Lett.* **91** 262513

[24] Murakami Y, Kasai H, Kim J J, Mamishin S, Shindo D, Mori S and Tonomura A 2010 Ferromagnetic domain nucleation and growth in colossal magnetoresistive manganite. *Nat. Nanotechnol.* **5** 37–41

[25] Yu X Z, Kanazawa N, Zhang W Z, Nagai T, Hara T, Kimoto K, Matsui Y, Onose Y and Tokura Y 2012 Skyrmion flow near room temperature in an ultralow current density. *Nat. Commun.* **3** 988

[26] Junginger F, Kläui M, Backes D, Rüdiger U, Kasama T, Dunin-Borkowski R E, Heyderman L J, Vaz C A F and Bland J A C 2007 Spin torque and heating effects in current-induced domain wall motion probed by transmission electron microscopy *Appl. Phys. Lett.* **90** 132506

[27] Hempe E-M, Kläui M, Kasama T, Backes D, Junginger F, Krzyk S, Heyderman L J, Dunin-Borkowski R and Rüdiger U 2007 Domain walls, domain wall transformations and structural changes in permalloy nanowires when subjected to current pulses *Phys. status solidi* **204** 3922–8

[28] Tirry W and Schryvers D 2008 In situ transmission electron microscopy of stress-induced martensite with focus on martensite twinning *Mater. Sci. Eng. A* **481-482** 420–5

[29] Sellmyer D and Skomski R 2006 *Advanced Magnetic Nanostructures* (Boston: Kluwer Academic Publishers)

[30] Ashby M, Shercliff H and Cebon D 2007 *Engineering , Science , Processing and Design*

[31] Kelly P M, Wauchope C J and Zhang X 1994 Calculation of overall tilt angles for a double tilt holder in a TEM. *Microsc. Res. Tech.* **28** 448–51

[32] Liu Q 1995 A simple and rapid method for determining orientations and misorientations of crystalline specimens in TEM *Ultramicroscopy* **60** 81–9

[33] Penczek P, Marko M, Buttle K and Frank J 1995 Double-tilt electron tomography *Ultramicroscopy* **60** 393–410

[34] Qin W and Fraundorf P 2003 Lattice parameters from direct-space images at two tilts *Ultramicroscopy* **94** 245–62

[35] Moeck P, Qin W and Fraundorf P 2005 Image-based nanocrystallography by means of transmission electron goniometry *Nonlinear Anal. Theory, Methods Appl.* **63** e1323–e1331

[36] Mitchell D R G and Schaffer B 2005 Scripting-customized microscopy tools for Digital Micrograph. *Ultramicroscopy* **103** 319–32

[37] Díez D C, Seybert A and Frangakis A S 2006 Tilt-series and electron microscope alignment for the correction of the non-perpendicularity of beam and tilt-axis. *J. Struct. Biol.* **154** 195–205

[38] Zhao H, Wu D, Yao J and Chang A 2008 QtUCP-a program for determining unit-cell parameters in electron diffraction experiments using double-tilt and rotation-tilt holders. *Ultramicroscopy* **108** 1540–5

[39] Zhang D, Oleynikov P, Hovmöller S and Zou X 2010 Collecting 3D electron diffraction data by the rotation method *Zeitschrift für Krist.* **225** 94–102

[40] Cantele F, Paccagnini E, Pigino G, Lupetti P and Lanzavecchia S 2010 Simultaneous alignment of dual-axis tilt series. *J. Struct. Biol.* **169** 192–9

[41] Córdoba R, Fernández-Pacheco R, Fernández-Pacheco A, Gloter A, Magén C, Stéphan O, Ibarra M R and De Teresa J M 2011 Nanoscale chemical and structural study of Co-based FEBID structures by STEM-EELS and HRTEM. *Nanoscale Res. Lett.* **6** 592

[42] Ziese M, Semmelhack H C and Busch P 2002 Sign reversal of the magnetic anisotropy in $La_{0.7}A_{0.3}MnO_3$ (A=Ca, Sr, Ba, □) films *J. Magn. Magn. Mater.* **246** 327–34

[43] Bonell F, Andrieu S, Bertran F, Lefevre P, Ibrahimi A T, Snoeck E, Tiusan C-V and Montaigne F 2009 MgO-Based Epitaxial Magnetic Tunnel Junctions Using Fe-V Electrodes *IEEE Trans. Magn.* **45** 3467–71

[44] Leven B and Dumpich G 2005 Resistance behavior and magnetization reversal analysis of individual Co nanowires *Phys. Rev. B* **71** 064411

[45] Brands M, Wieser R, Hassel C, Hinzke D and Dumpich G 2006 Reversal processes and domain wall pinning in polycrystalline Co-nanowires *Phys. Rev. B* **74** 174411

[46] Jaafar M, Serrano-Ramón L, Iglesias-Freire O, Fernández-Pacheco A, Ibarra M R, De Teresa J M and Asenjo A 2011 Hysteresis loops of individual Co nanostripes measured by magnetic force microscopy. *Nanoscale Res. Lett.* **6** 407

[47] Nogués J and Schuller I K 1999 Exchange bias *J. Magn. Magn. Mater.* **192** 203–32

[48] Scheck C, Cheng L, Barsukov I, Frait Z and Bailey W 2007 Low Relaxation Rate in Epitaxial Vanadium-Doped Ultrathin Iron Films *Phys. Rev. Lett.* **98** 117601

[49] Mitsuzuka K, Lacour D, Hehn M, Andrieu S and Montaigne F 2012 Magnetic vortices in single crystalline Fe-V disks with four folds magnetic anisotropy *Appl. Phys. Lett.* **100** 192406

Chapter 4

Domain wall manipulation in Co and notched $Co_{50}Fe_{50}$ nanowires

4.1. Motivation

In the last decade, several pioneering works have envisaged different strategies to design new information storage, logic or sensor devices based on magnetic DWs as functional entities to store, transfer, and process information in ferromagnetic media [1–6]. The *magnetic DW logic* [3] developed by D. A. Allwood *et al*., see Figure 4.1(a), and the *racetrack memory* [5] proposed by S. Parkin *et al*., see Figure 4.1(b), are the most relevant proofs of concept where the DWs manipulation is achieved by external magnetic fields and/or spin-polarized currents. In the magnetic DW logic, the high shape anisotropy of NWs is used to ensure that the magnetization lies only in two possible orientations, which are used as "1" and "0" to form the basic binary system needed for logical operations, while a single DW acts as the transition edge in a changing signal [3]. In the racetrack memory, a pattern of DWs is created to store information in the only two possible orientations of the magnetic domains between them. It is however challenging to store and move a train of DWs in a defect-free NW without annihilation. Optimal DW pinning sites are therefore created along the racetrack (e.g., notches in the edge of the wire) to locate DWs on these particular sites of the NW. A competitive racetrack memory should therefore support between 10-100 bits per racetrack (in a vertical array, the store capacity will be 100 times higher than is possible today), be very stable under external perturbations (thermal fluctuations and stray magnetic fields from nearby racetracks) and implement a method to

manipulate and move the DWs pattern from one bit to the other within 10 to 50 ns (DW velocity), which is much faster that in a modern hard disk devices (5 ms) and very similar to what is obtained in advanced MRAM (10 ns) [5]. These two innovative and promising DW-based technologies have motivated countless studies, in which careful analyses of the DW properties have been carried out as a function of different physical parameters of the nanostructures such as dimensions, geometry, shape of constrictions, type of material, etc. in order to find the optimal conditions for an efficient manipulation of DWs upon the application of external magnetic fields or electric currents [7–27].

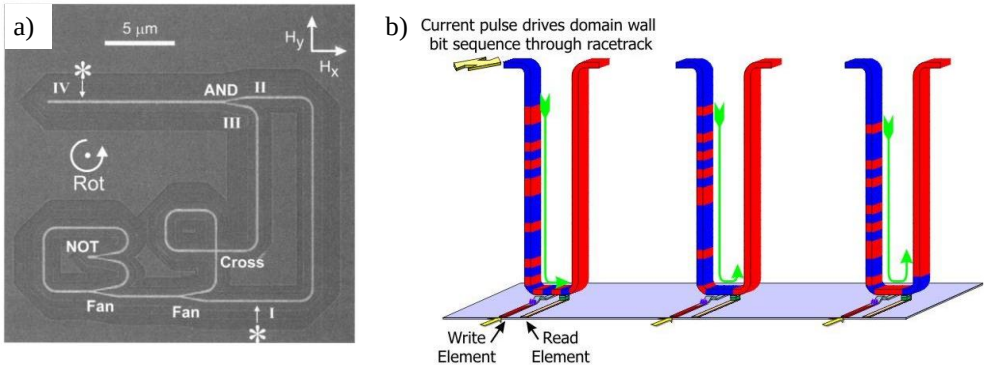

Figure 4.1. (a) SEM image of a magnetic DW logic device [3]. (b) Schematic illustration of magnetic DW racetrack memories (Image extracted of the physicsworld.com webpage of the article "*Racetrack memory near the finish line*")

In this work, we have combined the high spatial resolution of LM to study quantitatively the local magnetic configurations at remanence in two ferromagnetic nanostructures: FEBID Co NWs and electron beam lithography (EBL) notched $Co_{50}Fe_{50}$ NWs. We have also performed *in situ* LM experiments upon the application of a controlled in-plane magnetic field to analyze in detail some relevant magnetic properties of DWs by field-driven manipulation. The Co NWs are grown by FEBID using the FEI Helios 650 DualBeam instrument which allows fabricating Co nanostructures of reduced lateral size down to 30 nm width and with high Co content (> 90%) [28–30]. The notched $Co_{50}Fe_{50}$ NW is an alternative soft magnetic material

with a high saturation magnetization, low coercive field and elevated Curie temperature [31–33]. We have studied *in situ* the nucleation processes of DWs in L-shape Co NWs as a function of the geometry (thickness and width) of the NW and the applied magnetic field. In the L-shape notched $Co_{50}Fe_{50}$ NWs, we have analyzed the magnetic field driven propagation of DWs through a pattern of notches of different geometries and sizes.

4.2. Experimental details

Two series of L-shaped Co and $Co_{50}Fe_{50}$ NWs were fabricated by FEBID and EBL techniques, respectively. The fabrication of the Co-FEBID NWs was carried out by Dr. Luis Serrano and Dr. Rosa Córdoba during their Ph. D. studies in the LMA, while the $Co_{50}Fe_{50}$ NWs were fabricated by Dr. Jose Luis Prieto and Dr. Manuel Muñoz at the *Instituto de Sistemas Optoelectrónicos y Microtecnología (ISOM) of the Universidad Politécnica de Madrid.* Both systems were grown on electron-transparent 50-nm thick Si_3N_4 membranes, which are suitable for TEM magnetic imaging experiments. In the case of Co NWs, the growth parameters of the FEBID were optimized to obtain structures with a high Co content (> 90%) [29,30]. Low magnification bright-field TEM images of Figures 4.2 and 4.3(a) show the morphology of the two ferromagnetic L-shape NWs. For each batch, the length of the two branches of the NWs was fixed. In the case of $Co_{50}Fe_{50}$ NWs, both branches were 8.0 μm long, whereas the FEBID Co NWs had a long branch of 8.5 μm and a short branch of 3.5 μm. In the case of Co NWs, the lateral dimensions, i.e. width (w) and thickness (t), were varied through an array composed by 36 wires: w = 125, 250, 500 and 1000 nm and t = 5, 8, 10, 13, 16, 19, 22, 25 and 30 nm. On the other hand, 3 $Co_{50}Fe_{50}$ NWs of 350 nm width and 30 nm thickness were fabricated with a set of three notches equally spaced and with a particular profile: triangular (TNW), curved (CNW) and rectangular (RNW). In addition, the size of notches was progressively varied as shown in Figures 4.3(c)-(e). A complete characterization of the structure of the DW nucleated in the corner of both systems was carried out by LM and TIE

reconstructions, and the *in situ* analysis of the DW nucleation and propagation was performed following the procedure for application of magnetic fields described in *Chapter 2*. As shown in Figure 4.3(a), the total control of the in-plane field component gives the possibility to apply a magnetic field along any selected orientation to conduit the DW along the NW. For all experiments, the in-plane component of the magnetic field was obtained by tilting the NW plane at 14.1° with respect to the zero-tilt plane, so the ratio between the in-plane and out-of-plane components was set to $k = 0.25$. To support the experimental results, micromagnetic simulations were performed using the GPMagnet software package, considering the following magnetic parameters: Co saturation magnetization (M_s) = 1400×10^3 A m^{-1}, Co exchange constant (A) = 30×10^{-12} J m^{-1}; $Co_{50}Fe_{50}$ M_s = 1900×10^3 A m^{-1}, $Co_{50}Fe_{50}$ A = 30×10^{-12} J m^{-1}. The magnetocrystalline anisotropy constants were neglected in both systems considering their polycrystalline nature and small grain size. Most of the micromagnetic simulations were performed using a cell size of $5 \times 5 \times t$ nm^3. Cell sizes of $5 \times 5 \times 5$ nm^3 and $5 \times 5 \times 10$ nm^3 were used to simulate the values of H_c for Co NWs with bell-shape profiles and the nucleation of a DW in the curved kink of a 500-nm-wide and 30-nm-thick Co NW, respectively.

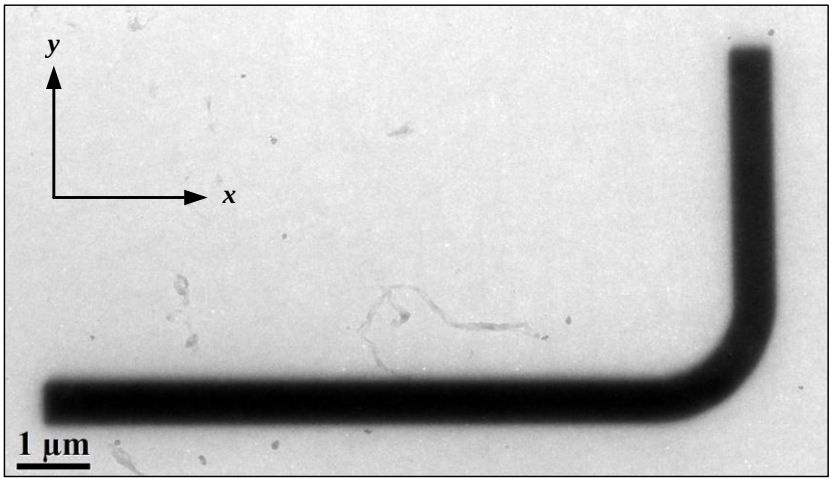

Figure 4.2. Low magnification TEM image of a 500-nm-wide and 30-nm-thick L-shaped FEBID Co NW.

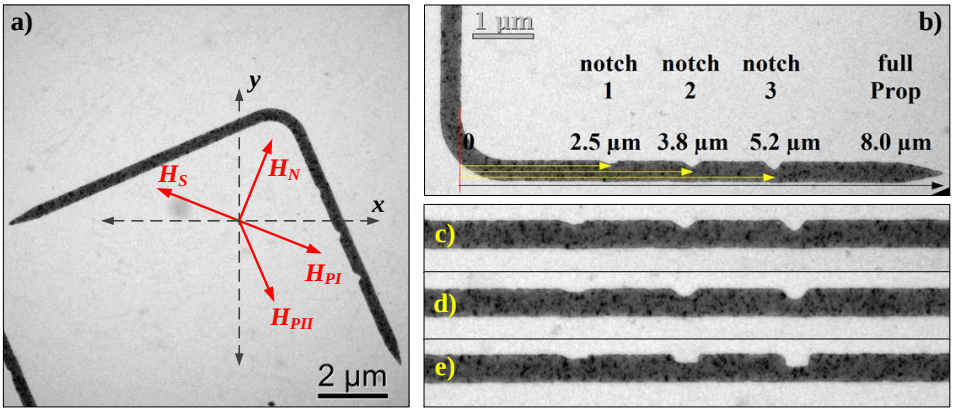

Figure 4.3. Low magnification TEM image of a notched L-shape $Co_{50}Fe_{50}$ NW. *x* and *y* axes represent the Cartesian coordinates of the initial in-plane system. H_S, H_N, H_{PI} and H_{PII} are vectors that indicate the direction of the saturation, nucleation, propagation *type I* and propagation *type II* magnetic fields, respectively. (b) TEM image of a set of notches that show their distribution along the wires. This setup is the same for all notched nanowires: (c) triangular, (d) curved and (e) rectangular notches.

4.3. Optimized cobalt nanowires grown by FEBID for domain wall manipulation

4.3.1 Lateral size and thickness dependence of the DW nucleation

The DW nucleation process in the round corner of the L-shaped Co NWs was studied following the procedure schematized in Figure 4.4 and inspired in Refs [15,19]. Before nucleating the DW in the corner, the magnetization is first saturated applying a large in-plane magnetic field of approximately 400 Oe, in a tangential direction to the corner edge [225° with respect to positive *x*-direction (see stage 1 in Figure 4.4)] and then decreased down to zero. Thus, the high shape anisotropy of the NWs makes that the magnetization is oriented in the (*x*, *y*) plane and parallel to the wire edges forming a single magnetic domain without any DW (see stage 2 in Figure 4.4). To nucleate a DW, the in-plane component of the magnetic field is applied

normal to the corner edge [-45° with respect to the positive *x*-direction (see stage 3 of Figure 4.4) and its magnitude is progressively increased until a DW is formed in the corner. Because the temporal resolution of LM is quite low (about 0.1 s), the DW appears instantaneously in the curved kink. The minimum magnetic field needed to make a DW appear is therefore defined as the *nucleation field* (H_N). The *propagation field* (H_P) can be determined immediately after measuring H_N by decreasing the magnetic field down to zero (stage 4 of Figure 4.4) and increasing it up in the same initial saturation direction before the nucleation process (stage 5 of Figure 4.4). We define H_P as the minimum magnetic field needed to move the DW out of the kink. H_P was only measured for the 500-nm-wide NWs, while H_N was been measured in different series of NWs of various widths in order to evaluate the most favorable dimensions for the best DW conduit.

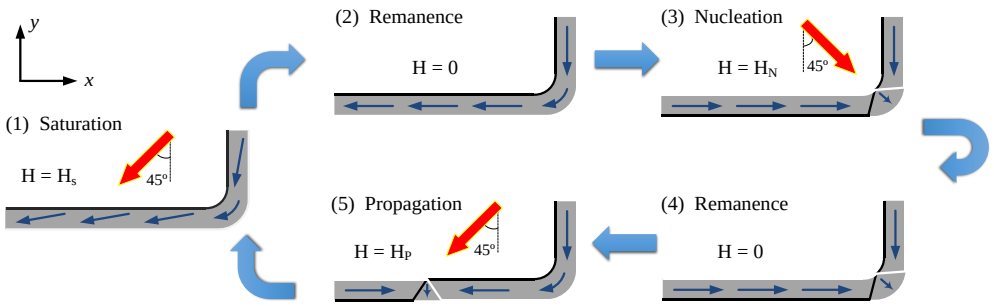

Figure 4.4. Schematic illustration of the procedure to determine the DW nucleation (H_N) and propagation (H_P) fields in the round corner of L-shape Co NWs. Blue arrows inside the NW indicate the local magnetization orientation, while red arrows represent the direction of the in-plane external magnetic field at each stage.

For NWs of intermediate widths (i.e., w = 250 and 500 nm), the formation of a DW in the corner is easily deduced from the observation of defocused Fresnel LM images recorded at $H = H_N$, see Figures 4.5(b) and (c), where bright and dark lines are formed in the corner, caused by the electron beam deflection of the magnetic

configuration of the DW. The DWs in the narrowest and the widest NWs, (i.e., w = 125 and 1000 nm, respectively) are difficult to visualize from the defocused LM images, see Figure 4.5(a) and (e). In the case of the narrowest NWs, the combination of their reduced widths and the large defocus value ($\Delta_z = \pm 1$ mm) used to obtain the LM images make the Fresnel fringes coming from the edges overlap, hiding the magnetic contrast produced by the DW itself. On the other hand, in the 1000-nm-wide NWs, the weak bright and dark contrast suggests a progressive rotation of the magnetization in the corner without producing a sharp DW separating the head-to-head magnetic configuration of the branches. In such NWs, H_N is however determined univocally by the observation of the contrast change of the Fresnel fringes along the edges of the branches, following a procedure similar to the measurement of the coercive field (H_c) in a straight cobalt NW in *Chapter 3*, see Figure 3.5(a). A contrast change from bright (dark) to dark (bright) along the edges of one of the branches of the NW indicates a reversal of the magnetization direction in that branch and, therefore, the appearance of a DW in the kink. This effect is illustrated in Figures 4.5(d) and (e), which depict the defocused LM images of a 1000-nm-wide Co NW recorded at saturation and remanence after the nucleation of the DW, respectively. A continuous bright (dark) contrast in the outer (inner) edge of the NW is observed in Figure 4.5(d) because in saturation the magnetization deflects the electrons towards the same side of the NW in both branches. When only the magnetization of the long branch is reversed, a head-to-head DW is formed at the kink, leading to a contrast reversal of the fringes along the long (horizontal) edges. In this case, the magnetization of the two branches deflects the electrons in opposite directions, as observed in Figure 4.5(e). Both the abrupt formation of a DW in the corner and the sudden change of the magnetic contrast formed at the edges indicate a magnetization switching in the long branch and the nucleation of a DW. In our method, the DW is previously created in the tip of the longer branch and then propagated at an applied field $H = H_N$ instantaneously to reach the curved kink of the NW. This magnetization reversal mechanism is typical of Co nanowires with reduced lateral dimensions [26,34,35].

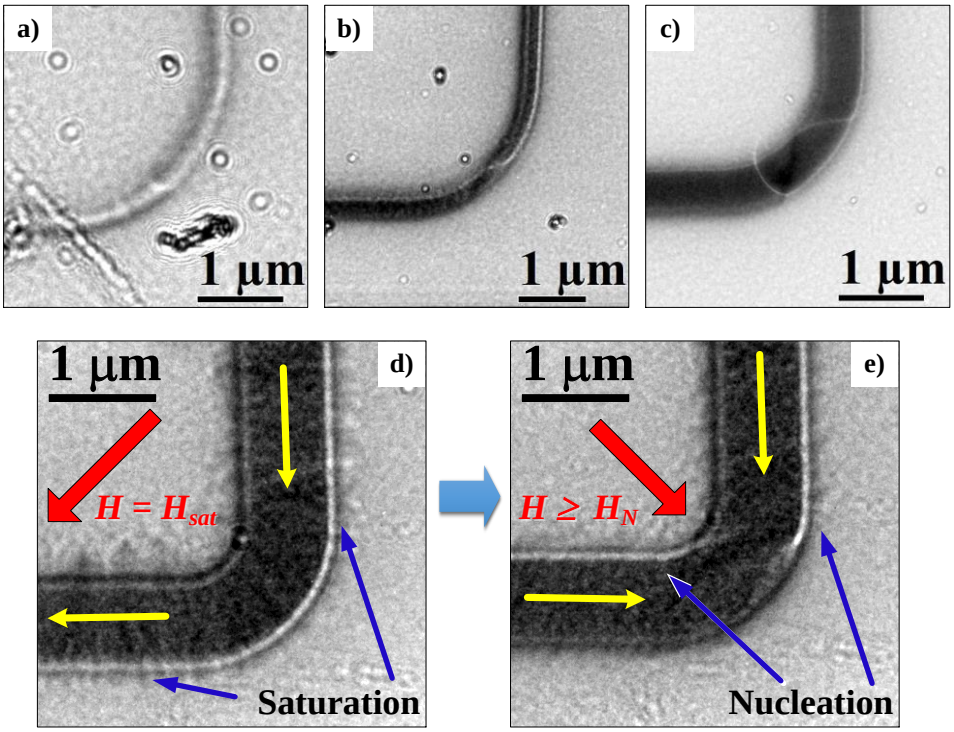

Figure 4.5. Defocused LM images recorded after nucleating the DW in the round kink of NWs with 16 nm thickness and (a) 125, (b) 250, (c) 500 and (e) 1000 nm width. (d) and (e) illustrate how the formation of DW in the corner is detected from the contrast variation in the edges of the long branch of the NWs.

Experimental values of H_N as a function of the width and thickness are plotted in Figures 4.6(a) and 4.7(a), respectively. NWs with the largest (30-nm-thick and 1000-nm-wide) and smallest (5-nm-thick and 125-nm-wide) lateral dimensions were discarded in this study due to the fact that their structures are not well defined after the FEBID fabrication. The different experimental points were obtained by averaging the nucleation fields measured for several cycles (up to 5), and the error bars were calculated as the standard deviation of the measured values taking into account the small hysteretic effects of the objective lens and the small variations in the assessment of the magnetic field values at which the DW is created and propagates. Despite the low number of different widths of our experiments (only 4), we detected an unusual

behavior of the nucleation fields as a function of the width. In the range of dimensions studied, we observe that H_N increases when w is reduced from w = 1000 to 250 nm, whatever the NW thickness. For the smallest width (w = 125 nm), H_N decreases to a value between 75 Oe (for t = 8 nm) and 94 Oe (for t = 30 nm). For the thickest wires of t = 30 nm, the H_N decay is quite abrupt from 285 to 94 Oe. The nucleation field H_N (that can be considered as the coercive field H_c of the long branch) dependence versus the NW width does not follow the classical behavior: H_c proportional to 1/w observed in single Co NWs by various experimental measurements and simulations [10,11,24,34,36,37]. However, most of these Co NWs have been fabricated by high resolution EBL which achieves patterning nanostructures with sharp edges and a thickness profiles almost rectangular [38–40]. The FEBID allows growing thin and narrow NWs but with a non-uniform thickness distribution, presenting a bell-like shape in which the thickness at the center is larger than at the edges [24]. Taking into account these morphological features, micromagnetic simulations were performed to determine the variations of H_c as a function of w in straight cobalt nanowires of 3 μm length considering a rectangular and a bell-shape profile for two different thicknesses, 10 and 20 nm. The results of these simulations are plotted in Figure 4.6(b). For NWs with a rectangular profile, we found the typical behavior of the coercive field with respect to the width: H_c proportional to 1/w. In NWs with a bell-shape profile, the H_c variation with the width is drastically different. For t = 20 nm, as the width decreases, there is a slight increase of H_c which tends to saturate for the smallest widths. For a smaller thickness (t = 10 nm) H_c even decays for small width. Even though we could not reproduce exactly the experimental dependence of H_c as a function of the NW width, the micromagnetic simulations support the fact that the anomalous behavior of H_N as a function of w in the FEBID Co NWs could be related to the bell-shape profile.

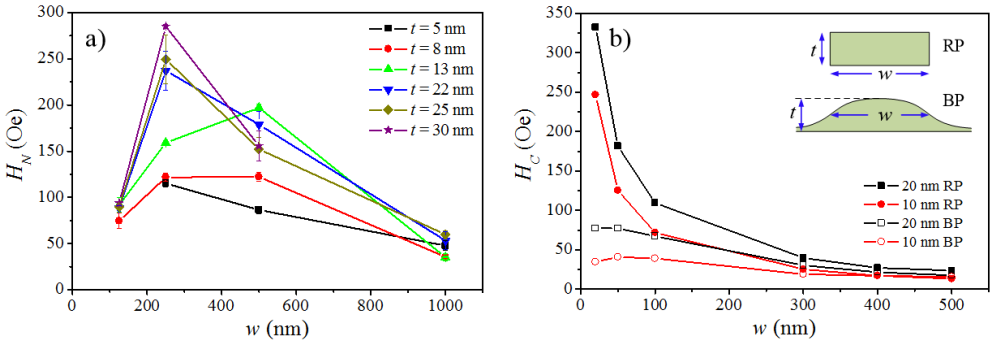

Figure 4.6. (a) Dependence of the nucleation fields as a function of the width for the Co NWs. For the sake of clarify, some thickness values are not plotted. (b) Micromagnetic simulation of the coercive field as a function of the width in nanowires of 10 and 20 nm thickness and with two different profiles: rectangular (RP) and bell-shape (BP).

An unusual behavior was also found when studying the nucleation field as a function of the thickness. We observe in Figure 4.7(a) that, in the widest (w = 1000 nm) and narrowest (w = 125 nm) NWs, H_N does not depend much on the NW thickness and is almost constant around 50 Oe and 110 Oe, respectively. A different tendency was found in the 250-nm-wide NWs, where a progressive increase of H_N with t is observed from 115 Oe (at t = 5 nm) to 285 Oe (at t = 30 nm). An even more interesting dependence is observed in the 500-nm-wide NWs, where H_N first increases with t at low thicknesses, from 86 Oe (at t = 5 nm) until reaching a maximum value of 196 Oe at t = 13 nm; then, H_N slightly decreases down to 155 Oe in the thickest NWs. Later we will show that this is related to the type of DW nucleated in the corner of the NW. A fascinating result was found after measuring the propagation field for the 500-nm-wide NWs. As seen in Figure 4.7(b), the *in situ* LM experiments show that in the 500-nm-wide cobalt nanowires H_N is larger than H_P for all thicknesses, demonstrating the excellent DW conduit properties of the FEBID Co based NWs. Indeed, with such a H_N and H_P difference the DWs can be driven thanks to an external field (H_P) without creating additional DWs. This result is consistent with the observations reported by A. Pacheco-Fernandez *et al.* in L-shape Co-FEBID NWs by MOKE measurements [19]. As a result, there is an optimal thickness (t = 13 nm) that leads to a maximum nucleation field for the 500-nm-wide NWs (H_N = 196 Oe) and gives rise to the largest

difference between H_N and H_P (ΔH) of 142 Oe. Such a large ΔH is important for a good DW conduit and an optimum manipulation of DWs for information storage or processing, as it facilitates their independent nucleation and propagation with largely different applied fields. This is a crucial point to minimize the writing/reading errors due to external perturbations like random thermal DW depinning or small fabrication inhomogeneities.

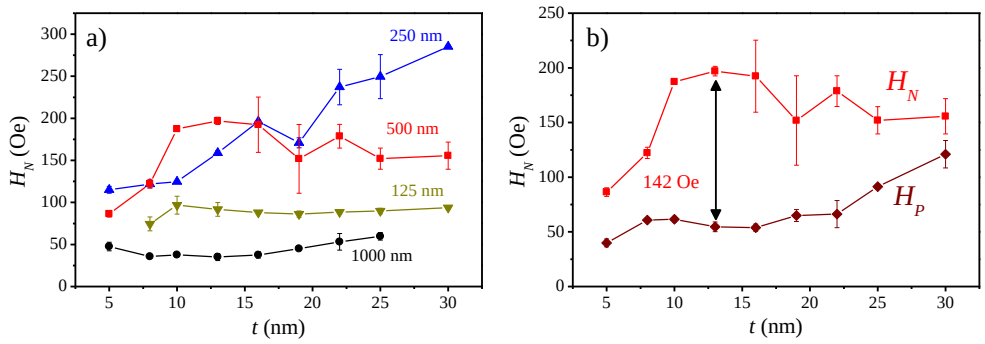

Figure 4.7. Dependence of the nucleation fields as a function of the thickness for the Co NWs. (d) Comparison between the nucleation and propagation fields for the 500-nm-wide Co NWs as a function of the thickness.

4.3.2 Magnetic configuration of domain walls in 500-nm-wide FEBID cobalt nanowires

The potential of the *in situ* LM experiments to measure the H_N and H_P values of DWs in Co NWs not only permits studying their variations with their dimensions and morphologies, but also gives the possibility to image the magnetic configuration of the DWs nucleated in the kink using the TIE analysis of image focal series. As the 500-nm-wide NWs exhibit the most interesting H_N evolution as function of thickness with an anomalous behavior and the appearance of an optimal ΔH value, we have focused our studies on the analysis of the DW configuration of this set of NWs. The series of defocused LM images displayed in the left column of Figure 4.8 shows the magnetic contrasts produced by the DWs for various thicknesses.

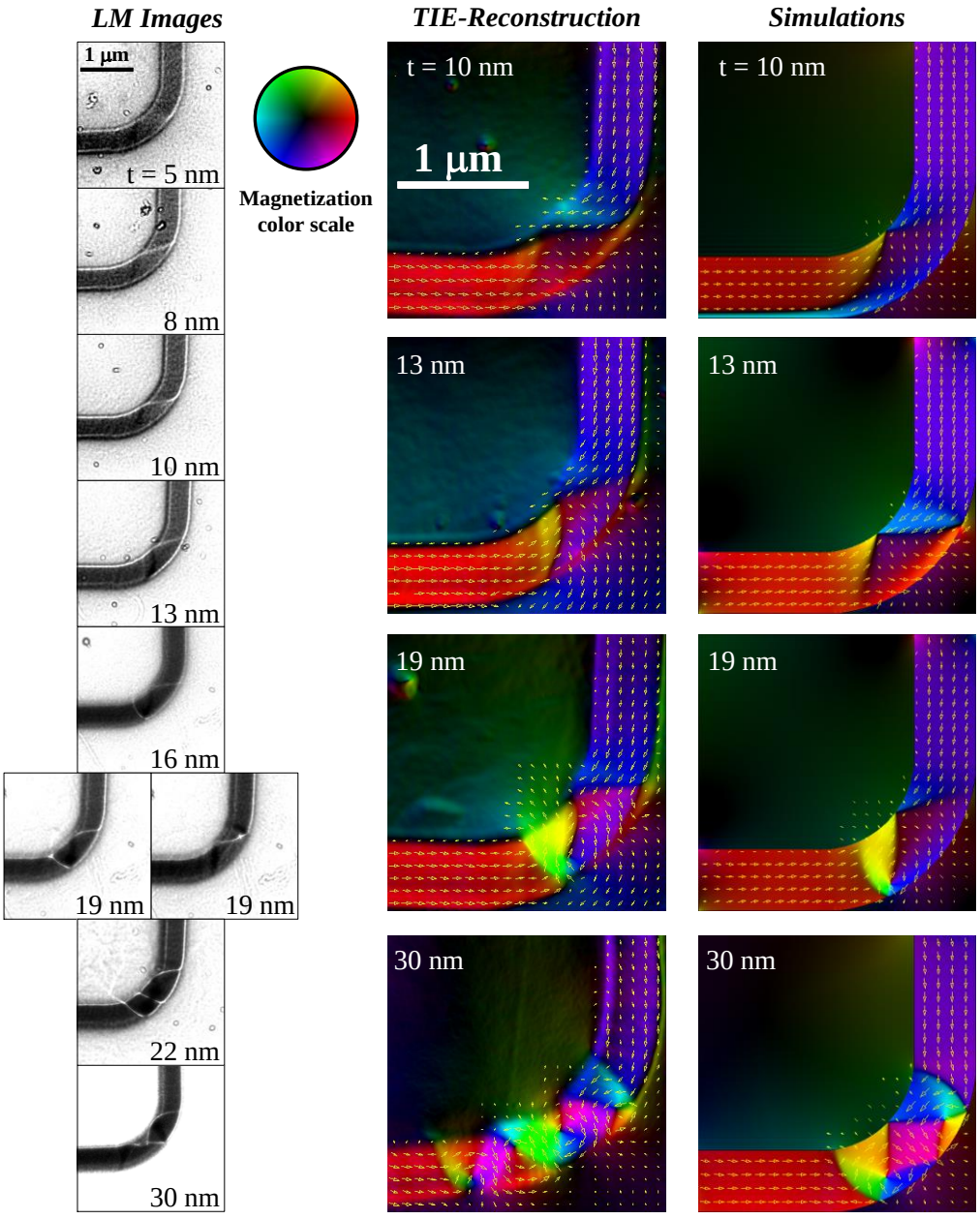

Figure 4.8. (*Left*) Sequence of out-of-focus LM images for different thicknesses in 500-nm-wide Co NWs. (*Center*) TIE-reconstructed in-plane magnetic induction of a Co NW in the TW (t = 10 nm), ATW (t = 13 nm), AVW (t = 19 nm) and 2VW (t = 30 nm) regimes. (*Right*) Micromagnetic simulations of the NWs reconstructed by TIE. The arrows and color code displayed in the top are used to indicate the local orientation of the magnetization.

From Figure 4.8, we found that:

- For NWs with $t \leq 13$ nm, the magnetic structure of the DW produces two bright and dark lines, forming a "V" shape.

- At t = 16 and 19 nm, a new type of magnetic contrast appears forming either an "N" (t = 19 nm right-side) or inverted "N" (t = 16 nm and 19 nm left-side) shape. As we report in the Figure 4.8 for the NW with t = 19 nm, two different magnetic structures were observed with equal probability i.e. we performed the H_N measurements 6 times and observed 3 times a N-shape DW contrast and 3 times an inverted N-shape DW contrast. In addition, a considerable difference in the mean value of H_N was found for the two configurations. Calculating the mean value and error of H_N from 3 repetitions, we obtained values of 195 ± 5 Oe and 124 ± 13 Oe for the normal and inverted N-shapes, respectively. This fact explains the large error bar observed in Figures 4.6(a) and 4.7 of H_N for t = 19 nm.

- For the thickest NWs ($t \geq 22$ nm), the number of magnetic contrast lines increases indicating that the nucleated DW has a complex magnetic structure.

A detailed analysis of the TIE reconstructions (see the central column of Figure 4.8) reveals that in NWs of $t \leq 10$ nm the DWs that nucleate are *Transverse Walls* (TWs). This DW configuration is very common in flat and narrow nanowires with small thickness, and it is characterized by a purely in-plane magnetization rotation of 180° between two head-to-head magnetic domains, with a wide side in one of the NW edges and a pointy end in the other [16,41,42]. At t = 13 nm, we observed that the TW is slightly deformed, resulting in a non-symmetric triangular shape DW. This type of DW is usually called *Asymmetric TW* (ATW). At t = 19 nm, we note that the ATW is modified and the in-plane 180° rotation of the magnetization is now combined with an additional flux closure in the lower side of the ATW, forming a magnetic vortex. We will refer to this DW configuration as an *Asymmetric Vortex Wall* (AVW) where the

vortex is not located at the center of the DW. Thus, in the 19-nm-thick NW the two different kinds of LM contrast observed are associated to the nucleation of an AVW with the vortex placed either in the upper or in the lower part of the DW. In addition, the contrast inversion observed in the defocused LM image indicates that the chirality is different in each case. Finally, the complex structure observed in the defocused LM images of the thickest NWs ($t \geq 22$ nm), is produced by two magnetic vortices (2VW) with antiparallel chirality. It has been found in Ref [12] that this exotic DW structure is more favorable in thicker and wider wires. A similar change of the DW configuration as a function of their dimension has been predicted in Permalloy NWs [42]. Micromagnetic simulations of the DW nucleation processes using the real size of the L-shape nanowires have been performed to support our experimental observations. Perfect defect-free NWs with a rectangular profile have been assumed to make these simulations, which were carried out following the experimental procedure to nucleate the DW in the corner of the NWs schematized in Figure 4.4. Simulated images of the DW just after its nucleation in the corner are depicted in the right column of Figure 4.8. Despite the small differences in the positions of the DW, most likely due to morphological differences between the real and the simulated defect-free nanostructure (roughness, bell-shape transversal profile, irregularities in the edges), the micromagnetic simulations are in very good agreement with the TIE reconstructions. They indicate the same evolution of the DW configuration (TW → ATW → AVW → 2VW) in the 500-nm wide NWs as a function of the thickness. Comparing these DW configurations with the nucleation field measurements, we find that the maximum value of H_N corresponds to the nucleation of an AVW. We also observe that H_N increases with t when a TW is nucleated, while it tends to saturate when an ATW is formed. In the case of the formation of AVW and 2VW this tendency is opposite and H_N is reduced when t increases.

The complete analysis of the magnetic configuration of the DW nucleated in the 500-nm- wide can be extrapolated for the 250 nm width NWs. In this particular series of NWs, for all thicknesses all the DWs are TWs. This can be deduced from the defocused LM images of Figure 4.9, where a V-shape contrast configuration is always

observed whatever the NW thickness between t = 5 nm and t = 30 nm, see Figure 4.5 (b). Similar to 500-nm wide NWs, to this TW configuration is associated an increasing behavior of H_N with t, reaching the maximum value of 285 Oe for t = 30 nm.

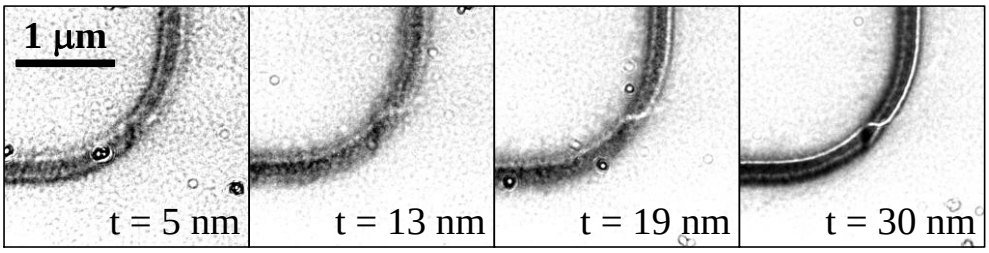

Figure 4.9. Sequence of out-of-focus LM images for different thicknesses in 250-nm-wide Co NWs.

4.4. Field-driven domain-wall manipulation in $Co_{50}Fe_{50}$ nanowires with nanoconstrictions

4.4.1 Domain wall nucleation and depinning process in the corner of L-shaped $Co_{50}Fe_{50}$ nanowires

The study of the DW depinning and transmission processes through an increasing magnetic field in notched $Co_{50}Fe_{50}$ NWs was performed on DWs previously nucleated in the round corner. The procedure we followed to nucleate and then transmit DWs is similar to that used in the previous study, and is schematized in Figure 4.10. First, the magnetization of the NW is saturated by applying a transversal magnetic field at 45° with respect to the nanowire branches (stage 1 of Figure 4.10); the field is then decreased down to zero and increased again perpendicular to the previous direction of the saturation field. The magnetic field is increased until a DW is formed in the rounded corner of the NW by the magnetization switching of the branch without notches (stage 2 of Figure 4.10). Before propagating the DW along the NW, the

magnetic field is again reduced to zero. Then two different strategies to depin and force the transmission of the DW were explored:

- *Type 1*, depinning/transmission of the DW by applying the magnetic field transversal to the notched branch, as shown in the stage 3 of Figure 4.10;

- *Type 2*, depinning/transmission of the DW by applying the field parallel to the notched branch (stage 4, Figure 4.10).

Due to the presence of notches in the NW, the DW transmission occurs discontinuously by the sequential pinning-depinning process of the DW from notch to notch. We will refer to the minimum field needed to propagate the DW through all notches after its complete depinning as the *transmission field* (H_T). Thus, we calculated the nucleation (H_N) and depinning (H_D) fields in the corner, and the transmission field (H_T) through the notches. Following the previous work in FEBID Co nanowires, we will define the *propagation field* (H_P) as the minimum field needed to depin the DW from the corner. This definition is coherent with the fact that if the notches do not exist, H_P is the field that conduits the DW all along the NW.

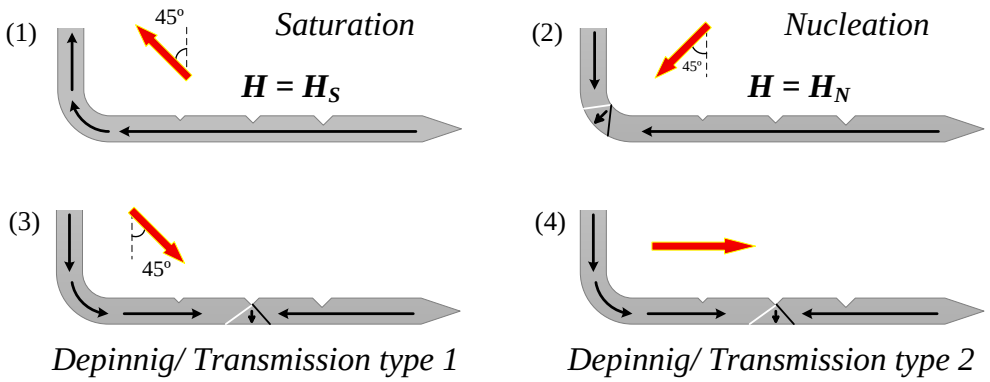

Figure 4.10. Schematic representation of the procedure followed for nucleation, depinning and transmission of DWs along the notched branch.

Experimental H_N values for the three different $Co_{50}Fe_{50}$ NWs are depicted in Figure 4.11(a). H_N was measured 3 times for each NW, so the mean value is represented and the error bars are the standard deviation of the measurements. As expected, H_N is very similar in all the wires, as the nucleation process is only related to the magnetization switching of the vertical branch without notches, which has the same morphology in all wires. With a difference less than 18 Oe between the highest (1041 Oe, for RNW) and lowest (1023 Oe, for TNW) H_N mean values, this result confirms the potential of EBL to produce nanostructures with a good reproducibility in their final geometry, and subsequently in their magnetic response to the applied field. It also shows the good accuracy of the *in situ* LM experiment to determine H_N, (1032 Oe) with a relative statistical error of less than 1.4%. Furthermore, defocused LM images of the DW in the kink after nucleation as well as TIE reconstructions, both depicted in Figure 4.11(b), show that the type of DW nucleated in all nanowires is always a head-to-head TW, similar to that observed in the 250- and 500-nm-wide FEBID Co NWs with small thickness.

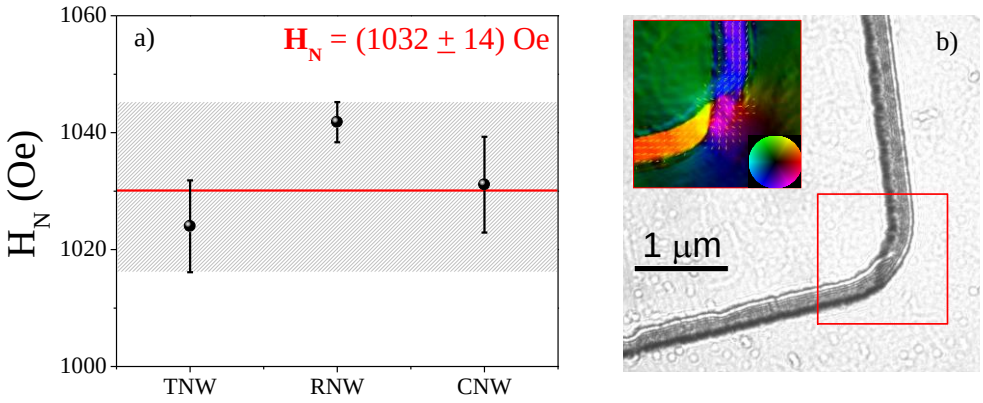

Figure 4.11. (a) Plot of the nucleation fields of the DW for all L-shape $Co_{50}Fe_{50}$ nanowires. Red line and the shadow region indicate the average value and the statistical deviation of H_N, respectively. (a) Defocused LM image of the corner of a NW after DW nucleation. *Inset:* TIE-reconstructed in-plane magnetic induction of the area enclosed in a red square showing a TW nucleated in the kink.

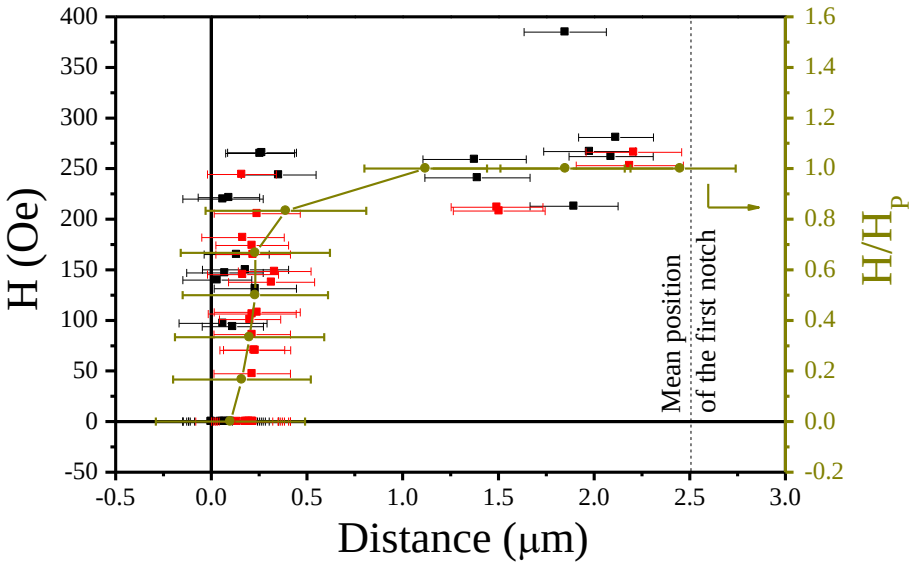

Figure 4.12. Dependence of the magnetic field applied in parallel (red squares) and transverse (black squares) directions as a function of the DW position. Micromagnetic simulation is plotted as H/H_P vs DW position (or distance) (green line and dots).

After nucleation, the DW was depinned from the corner by applying a magnetic field, which was progressively increased. As described previously, the DW propagation process was analyzed by orienting the magnetic field in two different directions, transversal (*Type 1*) and parallel (*Type 2*) to the notched branch. In both cases, the process was carefully studied in detail by recording sequences of defocused LM images while the magnitude of the magnetic field is increased. Similarly to the DW nucleation, the DW depinning experiments were repeated 3 times for each magnetic field direction. The plot of the DW position as a function of the magnetic field is displayed in Figure 4.12. It does not evidence a strong difference in the DW depinning processes for the two (*Type 1*) and (*Type 2*) magnetic field orientations. In this plot, the error bars along the *x*-axis indicate the size of the DW measured from the defocused LM images, while the dot itself corresponds to the position measured at the center of the DW. When a small magnetic field of 50 Oe is applied, the DW is only slightly stretched in the kink, but remains pinned until a magnetic field of approximately 250 Oe is applied. In most cases, the DW is then suddenly depinned

from the corner and moves to the first notch. The dependence of H/H_P as a function of the DW position with respect to the kink has been simulated, and shows a very good agreement with the experimental results as illustrated in Figure 4.12.

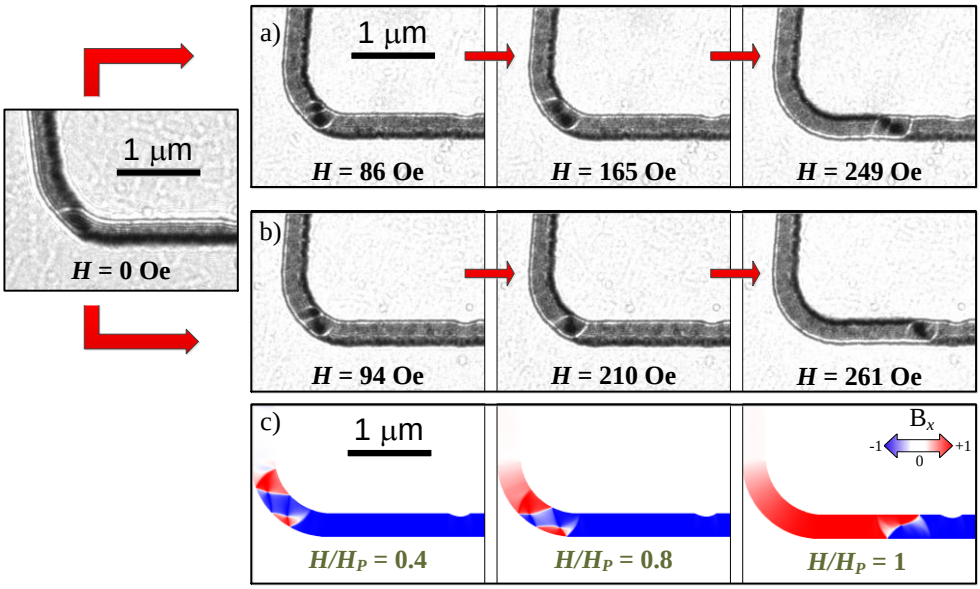

Figure 4.13. Sequence of defocused LM images of the kink showing the evolution of the magnetic configuration of DWs after depinning of the curved kink. The nucleated TW is transformed into a 2VW and propagated either (a) conserving its 2VW configuration or (b) turning into a single VW. (c) Micromagnetic simulation of the depinning process.

Sequences of defocused LM images collected during the depinning processes at the corner are shown in Figure 4.13(a) and (b), where we can see that the nucleated TW is transformed either into a *Vortex Wall* (VW) or a 2VW. In the defocused LM images, the VW produces two curved and parallel bright contrast lines that delimit the DW size, and a dark spot in the center of the DW structure (see Figure 4.13(b) at H = 261 Oe), while the 2VW produces three bright contrast lines and two dark spots between them (see Figure 4.13 (a) at H = 249 Oe). Independently of the magnetic field direction (transverse or parallel), the DW depinning occurs following one of these two modes:

(1) The initial TW is slightly displaced and transformed into a 2VW. Then it propagates conserving the 2VW structure (Figure 4.13(a)),

(2) The initial TW is slightly displaced and transformed into a 2VW. Just before propagation, it is again transformed into a VW. Then, it propagates conserving the VW structure (Figure 4.13(b)).

Micromagnetic simulation of the depinning process considering the real size of a defect-free $Co_{50}Fe_{50}$ NW are shown in Figure 4.13(c). These calculations reveal the same type of DW transformation observed experimentally, and show that the second mode (2VW → VW transformation) is the most favorable energetically.

4.4.2 Domain wall transmission through the nanoconstrictions

Finally, we measured the DW depinning and transmission fields, for the different shapes and sizes of the notches in the wire. Figure 4.14 plots the position of the DWs with respect to the notches as a function of the in-plane magnetic field. We refer to the depinning fields for the notches #1, #2 and #3 as H_{D1}, H_{D2} and H_{D3}, respectively. As the transmission of the DW is complete when it is depinned off the notch #3, the transmission field will be H_{D3} ($H_T = H_{D3}$). In all cases, both H_D and H_T for *Type 1* were slightly higher than for *Type 2*. This result demonstrates that a transversal magnetic field can be efficient for driving DWs in nanowires, but requests a higher field. Contrary to the H_N measurements, there is a substantial dispersion in the measurements of H_D and H_T, with relative errors up to 35%. We assume this is mainly caused by the stochastic nature of the DW depinning processes observed in notched nanowires. This effect has been also observed previously in ferromagnetic nanowires by M-TXM, anisotropic magnetoresistance and Hall effect measurements [20,43,44]. In addition, these results reported in Figure 4.13 show how the structure of the DW depinned from the kink could vary. These changes in the magnetic configuration of the DW indicate once more the stochasticity of the phenomenon, so the final state may be different for each experiment generating a significant data dispersion. Such dispersion could however be reduced by tuning the lateral dimensions of the wire to

propagate single DW with a stable and constant magnetic structure. In this aspect, *in situ* LM experiments would play an important role enabling the direct observation of the DW evolution in the depinning process in similar systems.

We can conclude from the *in situ* LM experiments reported in Figure 4.14 that the curved notches are the most suitable nanoconstrictions because they exhibit an efficient DW pinning and depinning process through all notches, see Figure 4.14(c). This is not the case for the other notched nanowires, which demonstrate to be less reliable. For instance, after 6 repetitions the DW was pinned only once in the notch #1 of the TNW and in notch #2 of RNW. We deduce from this fact that the performance of round notches is less dependent on the small irregularities in the geometry.

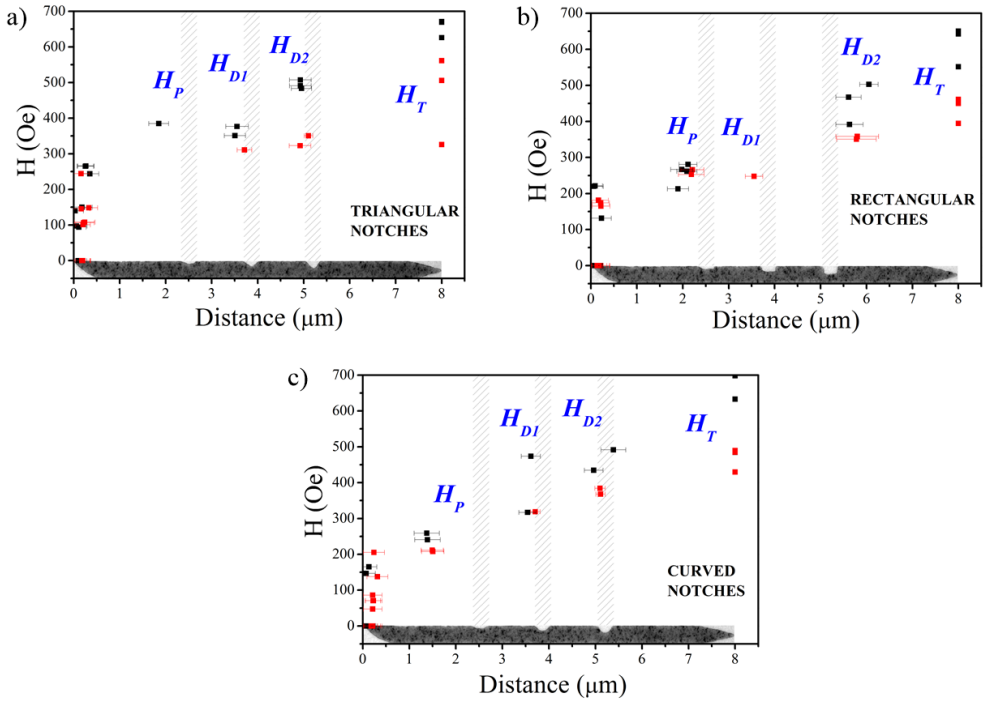

Figure 4.14. Plots of the depinning from the corner (H_P) and depinning fields (H_{D1}, H_{D2}, H_{D3} = H_T) of the DW as a function of the distance for (a) triangular, (b) curved, and (c) rectangular notched wires by application of parallel (red dots), or transverse (black dots) magnetic fields.

4.5. Conclusions

The *in situ* capability to apply controlled in-plane magnetic field in LM experiments has been successfully exploited to investigate the nucleation, propagation and morphology of single DWs in L-shape Co and notched $Co_{50}Fe_{50}$ NWs. From a technological application point of view, these *in situ* experiments have allowed determining the most favorable dimensions for the best DW conduit in Co-FEBID nanowires (500 nm of width and 13 nm of thickness) and the most suitable configuration of notches to control the pinning and transmission of DWs.

In the case of Co-FEBID NWs, the nucleation process of DWs in the curved kink as a function of the lateral dimensions was studied. We found that the width dependence of the nucleation field does not follow the typical behavior observed in ferromagnetic nanowires ($H_c \propto 1/w$). Preliminary micromagnetic simulations demonstrated that this unusual behavior is strongly affected by the bell-shape profile of the nanowires induced by the FEBID fabrication. On the other hand, the dependence of H_N as a function of thickness revealed a varied behavior in the four series of NW widths in study. The most exotic response was found in the 500-nm-wide NWs, where H_N first increases with the thickness to reach a maximum value of 196 Oe at t = 13 nm, and then slightly decreases down to 155 Oe in the thickest NWs. A quantitative analysis by TIE reconstruction demonstrated that such unexpected behavior of H_N vs t is associated to the type of DW nucleated. In the thickness range of study, the DW presented four different magnetic configuration: (1) in the lower thickness, we found a TW that favors an increasing H_N with the thickness; (2) in the thickness of maximum H_N, an ATW was observed; (3) the decreasing behavior of H_N was favoured by an AVW and; (4) the thicker NWs evidenced a complex DW structure composed by 2VW. Measurements of H_P have revealed that the most favorable dimensions for the best DW conduit correspond to the thickness where maximum value of H_N is obtained.

In the case of notched $Co_{50}Fe_{50}$ NWs, characteristic fields of nucleation, propagation, depinning and transmission for a single DW have been studied in three

NWs with different notch geometries and shapes. In all NWs, the DW nucleation had the same value. This is due to the fact that nucleation process takes place by the magnetization switching of the non-notched brand, which has the same geometry in the three L-shape NWs. TIE reconstruction and micromagnetic simulations showed that the DW nucleated in the corner of the L-shape NWs is a TW, but its magnetic configuration changed when it is depinned to the corner, transforming into either a VW or a 2VW. The DW depinning and transmission process through the notches was evaluated by applying magnetic field in parallel and transversal direction to the notched branch. In all cases, the DW depinning/transmission process required a magnetic field slightly lower when it was applied parallel to the notched branch. Contrary to that observed in the H_N measurements, there was a substantial dispersion in the measurements of H_D and H_T due to stochastic nature of the DW depinning mechanism, finding that the series of curved notches present the most suitable configuration to produce a sequential propagation of the DW.

References

[1] Ono T 1999 Propagation of a Magnetic Domain Wall in a Submicrometer Magnetic Wire *Science (80-.).* **284** 468–70

[2] Atkinson D, Allwood D A, Xiong G, Cooke M D, Faulkner C C and Cowburn R P 2003 Magnetic domain-wall dynamics in a submicrometre ferromagnetic structure. *Nat. Mater.* **2** 85–7

[3] Allwood D A, Xiong G, Faulkner C C, Atkinson D, Petit D and Cowburn R P 2005 Magnetic domain-wall logic. *Science* **309** 1688–92

[4] Allwood D A, Xiong G and Cowburn R P 2006 Writing and erasing data in magnetic domain wall logic systems *J. Appl. Phys.* **100** 123908

[5] Parkin S S P, Hayashi M and Thomas L 2008 Magnetic domain-wall racetrack memory. *Science* **320** 190–4

[6] Hayashi M, Thomas L, Moriya R, Rettner C and Parkin S S P 2008 Current-controlled magnetic domain-wall nanowire shift register. *Science* **320** 209–11

[7] Ono T, Ooka Y, Kasai S, Miyajima H, Nakatani N, Hayashi N, Shigeto K, Mibu K and Shinjo T 2001 Magnetization reversal and electric transport in ferromagnetic nanowires *Mater. Sci. Eng. B* **84** 126–32

[8] Yamaguchi A, Ono T, Nasu S, Miyake K, Mibu K and Shinjo T 2004 Real-Space Observation of Current-Driven Domain Wall Motion in Submicron Magnetic Wires *Phys. Rev. Lett.* **92** 077205

[9] Kläui M, Ehrke H, Rüdiger U, Kasama T, Dunin-Borkowski R E, Backes D, Heyderman L J, Vaz C A F, Bland J A C, Faini G, Cambril E and Wernsdorfer W 2005 Direct observation of domain-wall pinning at nanoscale constrictions *Appl. Phys. Lett.* **87** 102509

[10] Brands M, Leven B and Dumpich G 2005 Influence of thickness and cap layer on the switching behavior of single Co nanowires *J. Appl. Phys.* **97** 114311

[11] Brands M and Dumpich G 2005 Multiple switching fields and domain wall pinning in single Co nanowires *J. Phys. D. Appl. Phys.* **38** 822–6

[12] Hempe E-M, Kläui M, Kasama T, Backes D, Junginger F, Krzyk S, Heyderman L J, Dunin-Borkowski R and Rüdiger U 2007 Domain walls, domain wall transformations and structural changes in permalloy nanowires when subjected to current pulses *Phys. status solidi* **204** 3922–8

[13] McGrouther D, McVitie S, Chapman J N and Gentils A 2007 Controlled domain wall injection into ferromagnetic nanowires from an optimized pad geometry *Appl. Phys. Lett.* **91** 022506

[14] Backes D, Schieback C, Kläui M, Junginger F, Ehrke H, Nielaba P, Rüdiger U, Heyderman L J, Chen C S, Kasama T, Dunin-Borkowski R E, Vaz C A F and Bland J A C 2007 Transverse domain walls in nanoconstrictions *Appl. Phys. Lett.* **91** 112502

[15] Petit D, Jausovec A-V, Read D and Cowburn R P 2008 Domain wall pinning and potential landscapes created by constrictions and protrusions in ferromagnetic nanowires *J. Appl. Phys.* **103** 114307

[16] Kläui M 2008 Head-to-head domain walls in magnetic nanostructures *J. Phys. Condens. Matter* **20** 313001

[17] O'Shea K J, McVitie S, Chapman J N and Weaver J M R 2008 Direct observation of changes to domain wall structures in magnetic nanowires of varying width *Appl. Phys. Lett.* **93** 202505

[18] Sandweg C W, Wiese N, McGrouther D, Hermsdoerfer S J, Schultheiss H, Leven B, McVitie S, Hillebrands B and Chapman J N 2008 Direct observation of domain wall structures in curved permalloy wires containing an antinotch *J. Appl. Phys.* **103** 093906

[19] Fernández-Pacheco A, De Teresa J M, Córdoba R, Ibarra M R, Petit D, Read D E, O'Brien L, Lewis E R, Zeng H T and Cowburn R P 2009 Domain wall conduit behavior in cobalt nanowires grown by focused electron beam induced deposition *Appl. Phys. Lett.* **94** 192509

[20] Im M-Y, Bocklage L, Fischer P and Meier G 2009 Direct Observation of Stochastic Domain-Wall Depinning in Magnetic Nanowires *Phys. Rev. Lett.* **102** 147204

[21] He K, Smith D J and McCartney M R 2009 Observation of asymmetrical pinning of domain walls in notched Permalloy nanowires using electron holography *Appl. Phys. Lett.* **95** 182507

[22] Lepadatu S, Vanhaverbeke A, Atkinson D, Allenspach R and Marrows C 2009 Dependence of Domain-Wall Depinning Threshold Current on Pinning Profile *Phys. Rev. Lett.* **102** 1–4

[23] Huang S-H and Lai C-H 2009 Domain-wall depinning by controlling its configuration at notch *Appl. Phys. Lett.* **95** 032505

[24] Fernández-Pacheco A, De Teresa J M, Szkudlarek A, Córdoba R, Ibarra M R, Petit D, O'Brien L, Zeng H T, Lewis E R, Read D E and Cowburn R P 2009 Magnetization reversal in individual cobalt micro- and nanowires grown by focused-electron-beam-induced-deposition. *Nanotechnology* **20** 475704

[25] Eltschka M, Wötzel M, Rhensius J, Krzyk S, Nowak U, Kläui M, Kasama T, Dunin-Borkowski R E, Heyderman L J, van Driel H J and Duine R A 2010 Nonadiabatic Spin Torque Investigated Using Thermally Activated Magnetic Domain Wall Dynamics *Phys. Rev. Lett.* **105** 056601

[26] Jaafar M, Serrano-Ramón L, Iglesias-Freire O, Fernández-Pacheco A, Ibarra M R, De Teresa J M and Asenjo A 2011 Hysteresis loops of individual Co nanostripes measured by magnetic force microscopy. *Nanoscale Res. Lett.* **6** 407

[27] Serrano-Ramón L, Fernández-Pacheco A, Ibarra M R, Petit D, Cowburn R P, Tyliszczak T and Teresa J M 2013 Modification of domain-wall propagation in Co nanowires via Ga+ irradiation *Eur. Phys. J. B* **86** 97

[28] Fernández-Pacheco A, De Teresa J M, Córdoba R and Ibarra M R 2009 Magnetotransport properties of high-quality cobalt nanowires grown by focused-electron-beam-induced deposition *J. Phys. D. Appl. Phys.* **42** 055005

[29] Córdoba R, Sesé J, De Teresa J M and Ibarra M R 2010 High-purity cobalt nanostructures grown by focused-electron-beam-induced deposition at low current *Microelectron. Eng.* **87** 1550–3

[30] Serrano-Ramón L, Córdoba R, Rodríguez L A, Magén C, Snoeck E, Gatel C, Serrano I, Ibarra M R and De Teresa J M 2011 Ultrasmall functional ferromagnetic nanostructures grown by focused electron-beam-induced deposition. *ACS Nano* **5** 7781–7

[31] Turgut Z, Scott J H, Huang M Q, Majetich S A and McHenry M E 1998 Magnetic properties and ordering in C-coated Fe_xCo_{1-x} alloy nanocrystals *J. Appl. Phys.* **83** 6468

[32] Yu R H, Ren L, Basu S, Unruh K M, Parvizi-Majidi a. and Xiao J Q 2000 Novel soft magnetic composites fabricated by electrodeposition *J. Appl. Phys.* **87** 5840

[33] Fodor P S, Tsoi G M and Wenger L E 2002 Fabrication and characterization of $Co_{1-x}Fe_x$ alloy nanowires *J. Appl. Phys.* **91** 8186

[34] Leven B and Dumpich G 2005 Resistance behavior and magnetization reversal analysis of individual Co nanowires *Phys. Rev. B* **71** 1–7

[35] Brands M, Wieser R, Hassel C, Hinzke D and Dumpich G 2009 Reversal processes and domain wall pinning in polycrystalline Co-nanowires *Phys. Rev. B* **74** 1–6

[36] Dumpich G, Krome T P and Hausmanns B 2002 Magnetoresistance of single Co nanowires *J. Magn. Magn. Mater.* **248** 241–7

[37] Hausmanns B, Krome T P and Dumpich G 2003 Magnetoresistance and magnetization reversal process of Co nanowires covered with Pt *J. Appl. Phys.* **93** 8095

[38] Raptis I, Glezos N, Valamontes E, Zervas E and Argitis P 2001 Electron beam lithography simulation for high resolution and high-density patterns *Vacuum* **62** 263–71

[39] Elsner H and Meyer H-G 2001 Nanometer and high aspect ratio patterning by electron beam lithography using a simple DUV negative tone resist *Microelectron. Eng.* **57-58** 291–6

[40] Bartolf H, Inderbitzin K, Gómez L B, Engel A and Schilling a 2010 Nanoscale fabrication by intrinsic suppression of proximity-electron exposures and general considerations for easy and effective top–down fabrication *J. Micromechanics Microengineering* **20** 125015

[41] McMichael R D and Donahue M J 1997 Head to head domain wall structures in thin magnetic strips *IEEE Trans. Magn.* **33** 4167–9

[42] Nakatani Y, Thiaville A and Miltat J 2005 Head-to-head domain walls in soft nano-strips: a refined phase diagram *J. Magn. Magn. Mater.* **290-291** 750–3

[43] Akerman J, Muñoz M, Maicas M and Prieto J L 2010 Stochastic nature of the domain wall depinning in permalloy magnetic nanowires *Phys. Rev. B* **82** 064426

[44] Wuth C, Lendecke P and Meier G 2012 Temperature-dependent dynamics of stochastic domain-wall depinning in nanowires. *J. Phys. Condens. Matter* **24** 024207

Chapter 5

High-resolution imaging of remanent states and magnetization reversal processes in high-density cobalt antidot arrays

5.1. Motivation

The advances in nanofabrication techniques offer an unprecedented capability to pattern nanostructures in ferromagnetic thin films and tailor their magnetic properties, opening new routes to design innovative magnetic devices in the field of Spintronics and magnetic recording [1,2]. One promising alternative is the fabrication of a regular array of holes on a continuous magnetic thin film. Commonly called "*antidots*" (they are the counterpart of dots), these holes act as pinning centers that control the nucleation and propagation of DWs through the film [3,4], inducing a local shape anisotropy that tends to align the magnetization tangentially to the holes edges. As a consequence, the presence of antidots in ferromagnetic thin films induces important changes in the magnetic properties of the film such as a dramatic increase of the coercive field [3,5–15], a geometry-dependent magnetoresistance behavior [3,7,16–19], and the formation of complex magnetic domain structures at remanence due to the local confinement of the magnetization [6,9,11,13,18,20–23]. This confinement effect is the mechanism to form individual magnetic entities that could be used as magnetic bits of information in storage media with densities up to 10 Gbits cm^{-2} [5,24–26], see

Figure 5.1(a). Other potential applications are expected in the field of magnonics. Antidot arrays could be used as a magnonic crystals for spin wave filters and guides in which the spin wave excitations would depend on the period and the size of the holes, see Figure 5.1(b) [27–32]. To achieve these aims, great efforts are dedicated to understand and control the local magnetic states, and optimize the nanofabrication processes for producing high-performance devices with high storage capacity or suitable spin wave filters and guides.

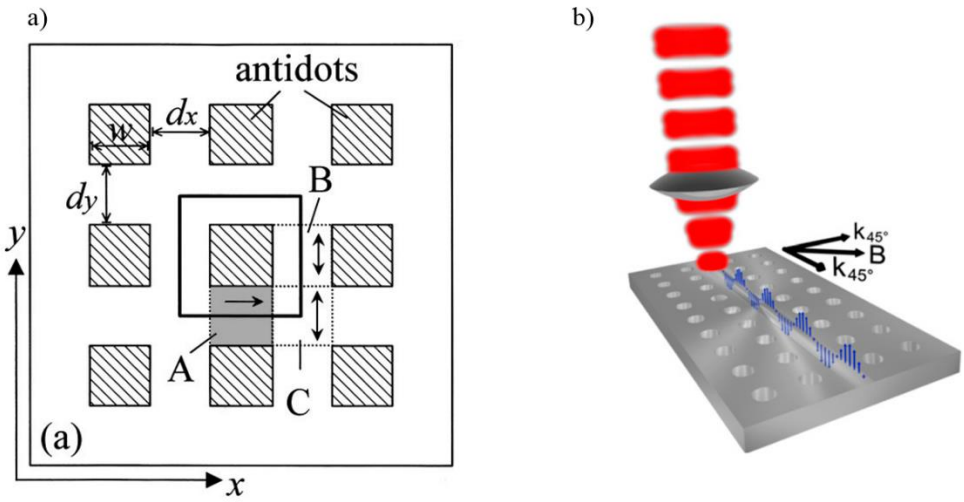

Figure 5.1. Promising applications of magnetic antidot arrays: (a) high-density magnetic storage devices [8] (gray region corresponds to a *memory bit*), (b) magnonic crystal for spin wave guide [28].

Different antidot geometries have been explored: holes with circular, rectangular or irregular shapes; ordered in rectangular, hexagonal or irregular arrays; fabricated by EBL, porous templates, or self-assembly [3–13,16–27,29,32–47]. More recently, a modern nanolithography technique such as FIB etching has been used to fabricate high-density antidot arrays with nanoscale hole diameters and sub-micron periodicities [14,15,28,30,31,48]. Such patterning methods have been optimized to reduce the dimensions of the magnetic region and therefore increase the storage density, or fine-tune the magnonic band structure. The scale reduction down to micron or sub-micron ranges then requires the use of advanced magnetic characterization techniques to

perform quantitative studies of the magnetic states, either at remanence or during the magnetization reversal process, with high spatial resolution and sensitivity.

In this Chapter we exploit the full potential of *in situ* LM and EH to explore the magnetic configurations of high-density square cobalt antidot arrays. In previous works, LM was used to study remanent states and magnetization reversal processes in magnetic antidot arrays with periodicities larger than 1 μm [20,36,48]. We have optimized LM to image magnetic domains in cobalt antidot arrays with periodicities down to 116 nm, achieving to resolve the local magnetization orientation of magnetic superdomains (SD). Due to its large field of view, we have employed LM and TIE reconstructions to analyze qualitative and quantitatively the remanent state of square cobalt antidot arrays of 5.3×5.3 μm^2 of area, with a hole diameter $d \sim 55$ nm and over a wide range of periodicities p = 95-524 nm. EH was used to analyze the morphology of the arrays, and the effect of hole proximity and FIB beam damage in the local magnetic properties. For p = 160 nm, *in situ* LM experiments were carried out to study its magnetization reversal processes by application of magnetic fields parallel and transversal to the antidot rows.

5.2. Experimental details

A series of square cobalt antidot arrays were fabricated on a 50 nm-thick Si_3N_4 electron-transparent membrane at the LMA by Celia Castán-Guerrero from the *Instituto de Ciencia de Materiales de Aragón* (ICMA). Following the protocol published in Ref. [15], a continuous 10-nm-thick polycrystalline film of cobalt was firstly deposited by magnetron sputtering, covering the whole area of the membrane (250×250 μm^2). The hole arrays were then patterned by FIB etching using the focused Ga^+ ion beam of the FEI Helios 650 DualBeam system. Each hole was etched by a single spot of the ion beam tuning the beam parameters such as the ion beam current, I, the acceleration voltage, V, and dwell time, in order to create holes with the smallest diameter possible. Using I = 24 pA, V = 30 kV and dwell time = 10 ms, we

achieved fabricating holes with approximately 55 nm of diameter, as shown later. The large area of the Si_3N_4 membrane allowed the design of 7 square antidot arrays of 5.3 × 5.3 μm^2, where the array periodicity (p), defined as the center-to-center hole distance, was varied from 524 to 85 nm. As commented before, imaging of the remanence states for all arrays and reversal magnetization processes for one particular antidot array (p = 160 nm) was carried out by *in situ* LM following the procedure described in the *Chapter 3*. The changes in morphology and composition of the different regions around the holes were qualitatively studied by EH analyzing locally the mean inner potential (V_{MIP}) while the microstructure was checked by conventional TEM. To support the experimental evidences, micromagnetic simulations were performed using the GPMagnet software package.

5.3. Microstructural characterization of the antidot arrays

The low-magnification bright-field TEM image of the cobalt antidot array with p = 160 nm shown in Figure 5.2(a) gives us a first view of the configuration of the systems, where bright spots corresponding to the holes form a square lattice on the continuous cobalt film (gray region). At such magnification, dark regions are produced by residual material located above the film, or below the membrane, coming from the air exposition after the fabrication. We did not evidence any influence of this residue on the magnetic properties of the arrays. The bright-field TEM image of the Figure 5.2(b) taken at high-magnification evidences that the optimized FIB etching process creates holes slightly elliptical. The hole size was measured considering the brightest regions in the TEM images of Figures 5.2(b) and (c), and we found that the average hole diameters are 54 ± 1 nm and 58 ± 1 nm along the x- and y-direction, respectively. Furthermore, small differences between center-to-center hole distance along x- and y-direction, p_x and p_y, indicate that the "unit cell" of the arrays is not perfectly squared either. The lattice parameters of the antidot arrays studied are presented in the Table 5.1. For the sake of clarify, we will refer to the antidot arrays as "square array" and use the value of p_x to define the array periodicity, p.

Figure 5.1. Center-to-center distance for the antidot arrays measured along the x (p_x) and y (p_y) directions.

Array	***p_x [nm]*** ***(± 1nm)***	***p_y [nm]*** ***(± 1nm)***	***Array***	***p_x [nm]*** ***(± 1nm)***	***p_y [nm]*** ***(± 1nm)***
I	524	534	**V**	116	118
II	327	334	**VI**	95	97
III	160	162	**VII**	85	86
IV	138	141			

From the bright-field TEM images displayed in Figures 5.2(b) and (c), we identify four distinctive regions within the lattice which are differently affected by the Ga irradiation of the nanofabrication process:

Region (*i*) brightest regions correspond to the physical holes, where the FIB has pierced completely the film and the membrane.

Region (*ii*) a small corona ~6 nm wide surrounding the holes edges associated to a thickness variation due to the Gaussian-shaped FIB probe.

Region (*iii*) amorphous areas caused by the Ga+ ion irradiation from the FIB etching that degrade the cobalt thin film quality, inducing Ga implantation and Co/substrate intermixing [15].

Region (*iv*) unaltered areas between the holes where the microstructure of the original cobalt thin film is preserved.

Thus, we find that the cobalt antidots studied in this work have the typical morphology reported previously for those fabricated by FIB [12,15,48]. Comparing Figure 5.2(b) and (c), we observe a progressive increase of the FIB-damaged area when p is reduced, leading to a complete isolation of the original cobalt regions between the holes [*Region* (*iv*)] at p = 85 nm.

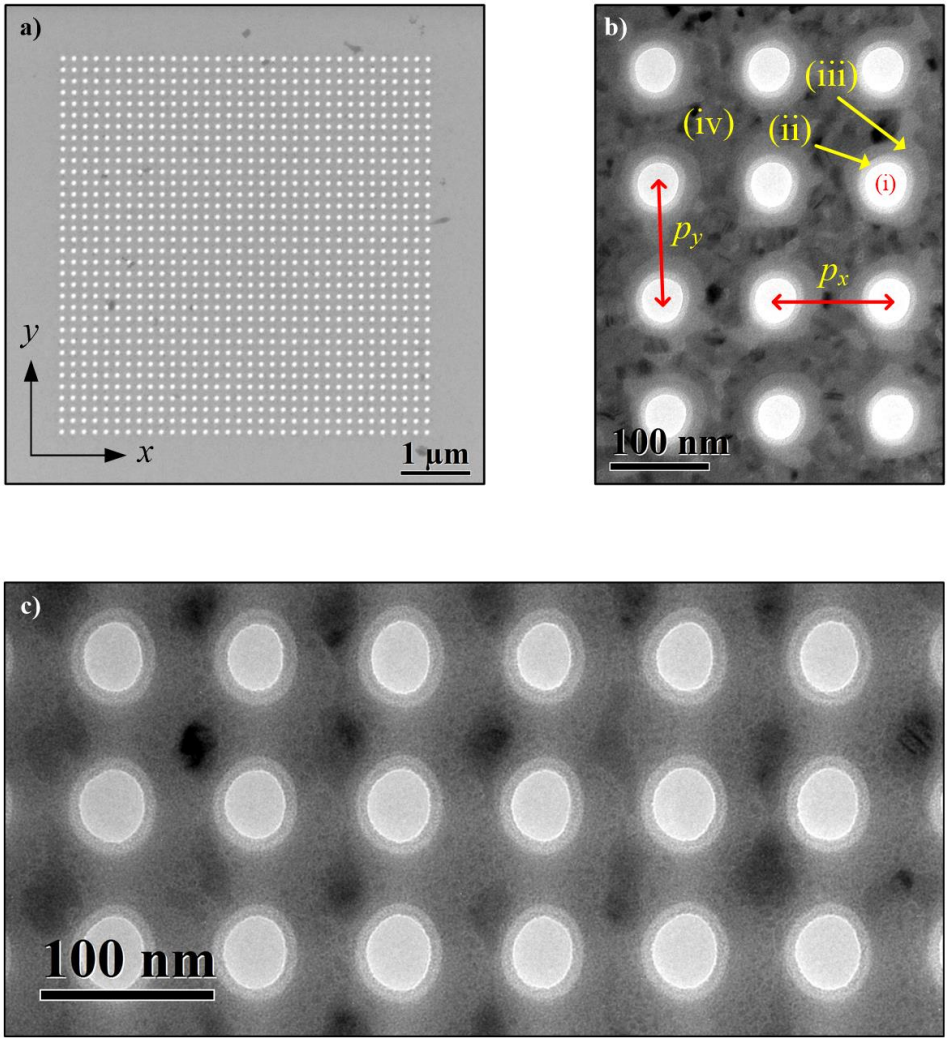

Figure 5.2. (a) Low-magnification TEM image of a cobalt antidot array with p = 160 nm. (b) and (c) High-magnification TEM images of the antidot arrays with p = 116 nm and p = 85 nm, respectively. Four different regions are identified inside the array in (b).

An additional study of the Ga-irradiated areas have been carried out by EH experiments. Electrostatic and magnetic phase images have been extracted from EH experiments performed around the last antidot rows next to the continuous film for arrays with p = 160 and 95 nm. These phase images are displayed in Figure 5.3.

According to Equation 2.37, the electrostatic phase shift is proportional to the product of the mean inner potential and the thickness of the film, $V_{MIP} \cdot t$, so color variations in Figures 5.3(a) and (c) indicate changes of this product. A continuous homogeneously thick cobalt area, represented by a yellow tone, is observed in the continuous film and in the areas between neighboring holes for the antidot array with p = 160 nm. The strong color variation from red to black in the holes edges is associated to the thickness variations in *Regions* (*ii*). The amorphous areas formed by the Ga irradiation present a reddish tone that surrounds each hole in the array of p = 160 nm, but it is extended to the whole area between every two consecutive holes in the array of p = 95 nm. Line profiles traced in the middle of two horizontal hole rows, see Figure 5.3(e), demonstrate that, whereas in the array with p = 160 nm the areas between the antidots remains virtually unchanged, in p = 95 nm there is a clear decrease in the electrostatic phase shift down to 60% with respect to the value measured in the continuous film. This considerable variation is interpreted as a local reduction of the thickness and/or density ($V_{MIP} \cdot t$) caused by beam damage. This should produce important changes in the magnetic properties of the cobalt film areas between the nearest neighboring holes, as deduced from magnetic induction images of Figures 5.3(b) and (d). A clearly magnetized state is seen between the holes for p = 160 nm, as evidenced by continuous flux lines contouring the antidots. However, a similar study carried out in the array with p = 95 nm presents no, or very sparse magnetic flux lines, with no clear geometric distribution, as a consequence of the depressed magnetism caused by Ga irradiation. This result is in good agreement with a preliminary work realized by Castán-Guerrero and co-workers in antidot arrays patterned by FIB etching on a cobalt thin film grown on silicon [15], where they have demonstrated that the Ga irradiation deteriorates *Regions* (*ii*) and (*iii*), inhibiting the magnetism and forming an effective non-magnetic diameter higher than the physical antidot.

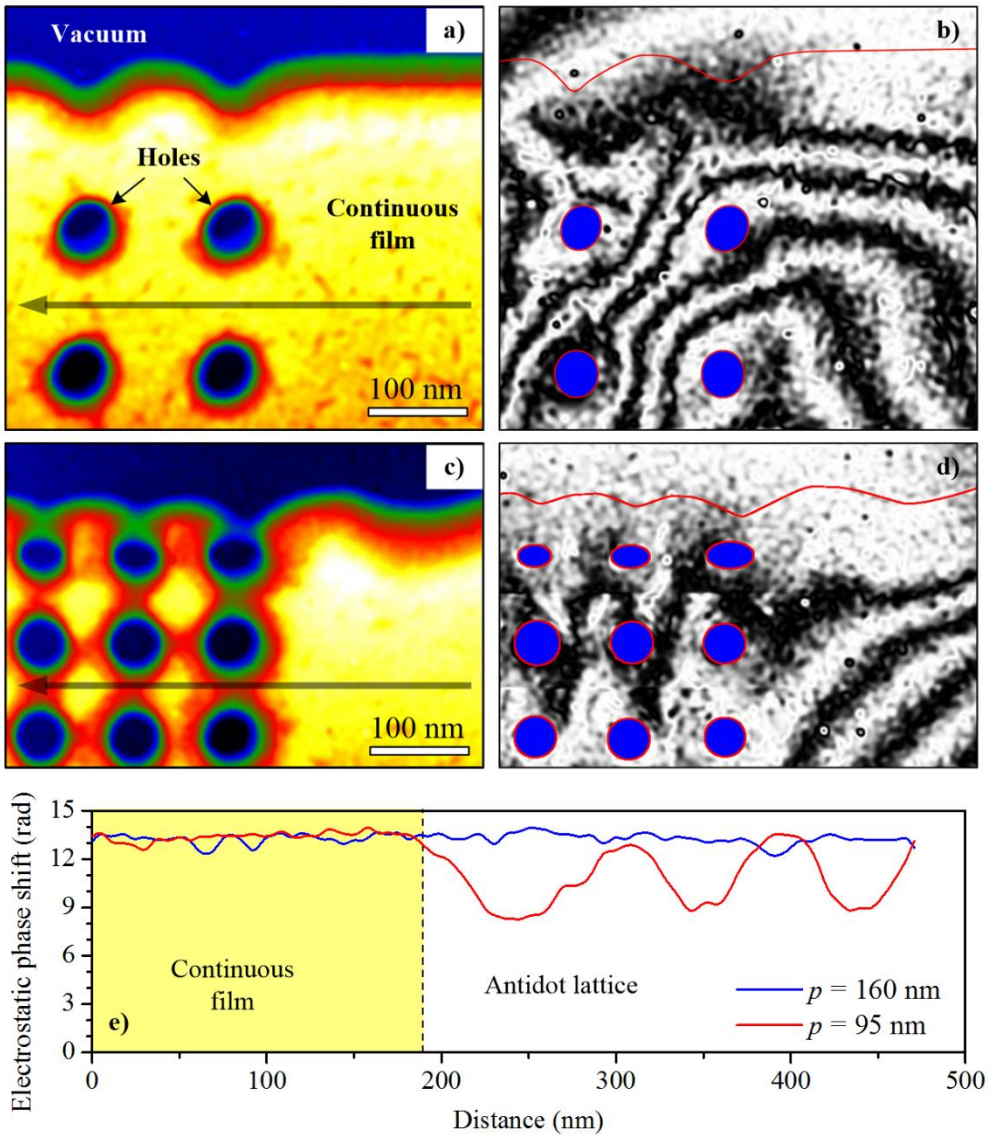

Figure 5.3. EH experiments in antidot arrays with (a-b) p = 160 and (c-d) p = 95 nm. Figures (a) and (c) display the electrostatic phase image, while figures (b) and (d) exhibit the magnetic flux lines as the cosine of the magnetic phase image. The effect of Ga irradiation is illustrated in (e), where line profiles of the electrostatic phase shift along the arrows plotted in (a) and (c) show the comparative effect of Ga irradiation on the areas between the antidots for p = 160 nm and p = 95 nm with respect to the continuous film.

5.4. Magnetic imaging at remanence

5.4.1 A qualitative description: defocused Lorentz microscopy images

A preliminary exploration of the remanent magnetic configuration of the antidot arrays was carried out by LM in Fresnel mode. As commented in *Chapter 2*, Fresnel mode allows a direct visualization of magnetic structures by imaging in a defocus condition magnetic contrasts produced by DWs. Before imaging the remanent magnetic states, a demagnetization protocol was performed also *in situ* by applying an oscillating magnetic field cycle along the *x*-direction, where the amplitude of the field was progressively reduced from saturation to zero while wobbling the sample tilt.

Series of in- and out-of-focus LM images for four representative antidot arrays (p = 524, 327, 160 and 116 nm) are depicted in Figure 5.4. Bright and dark lines only observed in the defocused LM images correspond to DWs. These magnetic lines are present in the continuous cobalt film that surrounds the arrays, and inside the antidot arrays of largest periodicities, p = 524 and 327 nm, see Figures 5.4(e) and (f). In these arrays, DWs are randomly distributed with a clear tendency to run across two antidot positions. Furthermore, we observe that the reduction of the periodicity increases the density of DWs nucleated inside the antidot lattice, as a direct consequence of the growing number of pinning centers.

The geometry of the magnetic contrasts for antidot arrays with smaller periodicities, p = 160 and 116 nm, changes drastically. Defocused LM images of Figures 5.4(g) and (h) do not reveal the typical bright/dark magnetic contrasts observed in the continuous film; only straight lines of weak contrast variations are observed along the horizontal and vertical antidot rows. In addition to the bright/dark DW contrast, Fresnel fringes arising from the interference between the electrons passing through a hole and those interacting with the film [49] form a series of concentric rings around each hole in defocused LM images, as illustrated in Figure 5.4(i). For large p, these concentric rings do not interfere with the DW contrast, but for small p, the Fresnel fringes from neighboring antidots overlap, masking the magnetic

contrasts produced inside the array, as can be seen in Figure 5.4(j). In the case of the antidot array with p = 116 nm in Figure 5.4(h), the holes are even hardly observable. Thus, Fresnel fringes arising from holes present a serious obstacle that limits the capability to study the magnetism of high-density antidot arrays by LM.

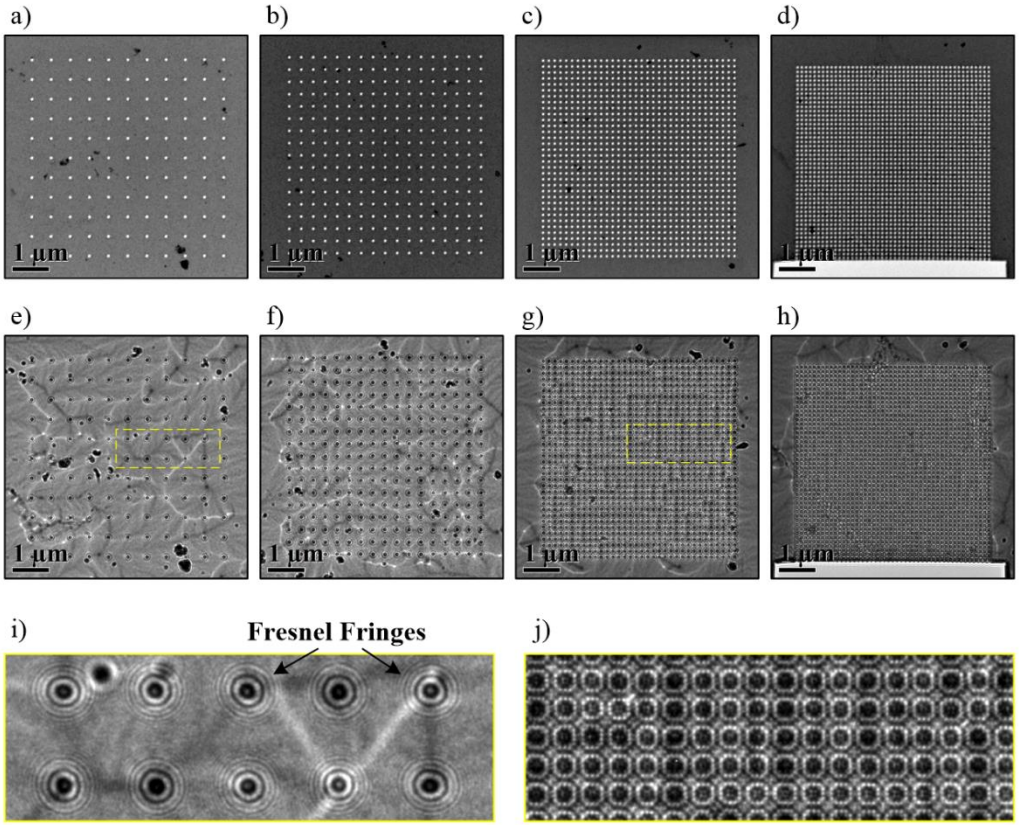

Figure 5.4. In-focus LM images of antidot arrays with different periodicities: (a) 524 nm, (b) 327 nm, (c) 160 nm and (d) 116 nm. Panels (e)-(h) show their corresponding over-focus LM images. (i) and (j) represent magnified regions (yellow boxes) of the defocused LM images for p = 327 and 160 nm, respectively.

To overcome this difficulty, we have used a filtering method to separate the magnetic contrast in antidot arrays with small periodicity from the Fresnel fringes of the physical holes by taking advantage of the periodic ordering of the antidots. The

maximum electron beam deflection caused by a 10 nm-thick pure cobalt film is approximately 0.086 mrad, which is equivalent to a periodicity in real space of about 230 nm. Thus, the magnetic information is confined in the low frequency region of the reciprocal space (corresponding to large spatial distances). Consequently, in the range of array periodicities most studied here ($p \leq 160$ nm), the magnetic information can be filtered using a low frequency band filter and separated from the smaller periodicity coming from the antidot lattice. We then use a filtering process in the Fourier space. When calculating the fast Fourier transform (FFT) of the LM images, we obtain a square pattern of spots in the Fourier space related to the periodicity of the antidot array in the real space. If we mask those spots in the Fourier space and only select the low frequency regions to calculate the inverse Fourier transform (FFT^{-1}), the effect of the Fresnel fringes is minimized and the resulting image only shows the low-frequency information arising from the magnetic contrasts. An example of this low-frequency Fourier filtering method to analyze the antidot array with p = 160 nm is illustrated in Figure 5.5. The in-, over-, and under-focus LM images are reported in Figure 5.5(a)-(c) and the FFT of the over-focus image in Figure 5.5(d). A circular mask is used to select the low frequencies information located around the central spot of the power spectrum of the FFT, which encloses the magnetic information, setting its radius smaller than the closest diffraction spot, see Figure 5.5(d). Calculating the inverse of the masked FFT, we obtain the new filtered LM images in Figures 5.5(e)-(g), where the contrast arising from the hole array is suppressed and the magnetic contrast enhanced. From Fourier filtered LM images, we find that the weak contrast variations along the horizontal and vertical antidot rows correspond to pairs of bright and dark lines, confirming a change of the DW structure with respect to the arrays with the largest periodicity.

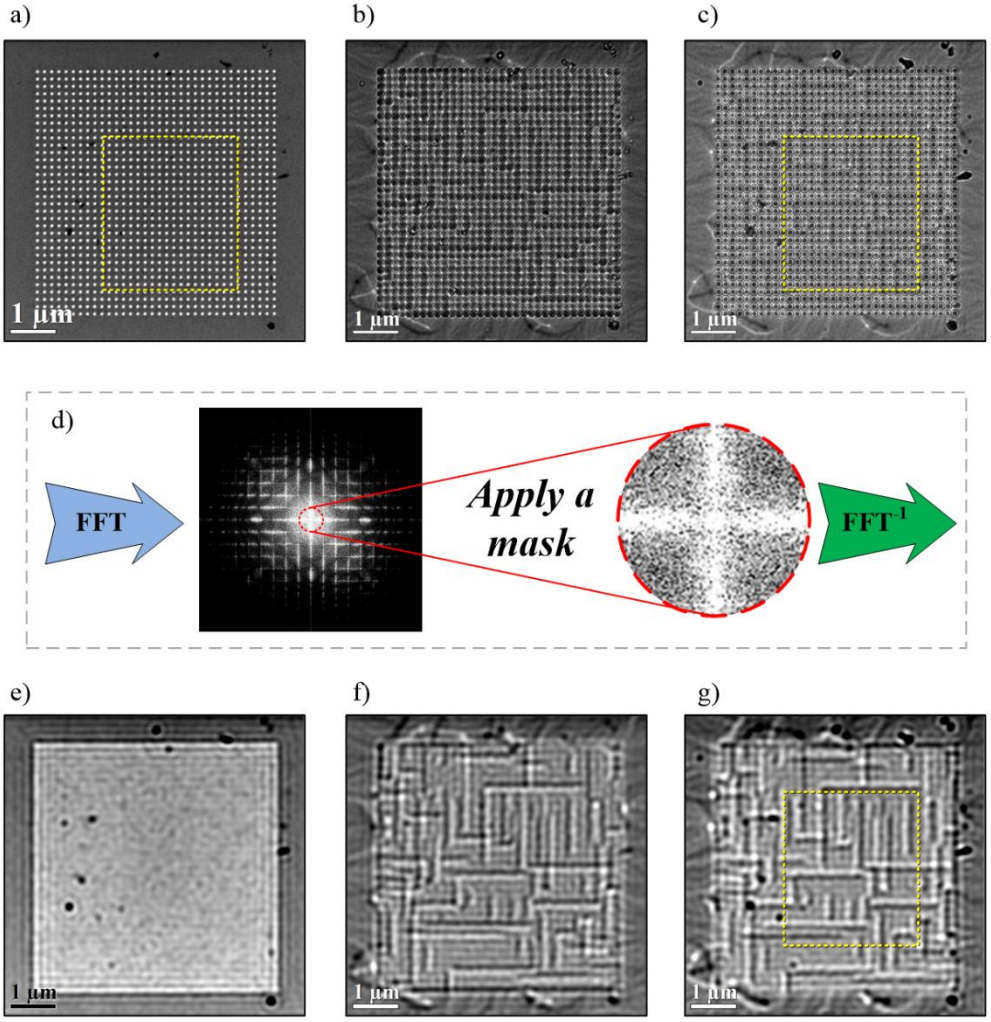

Figure 5.5. Focal series of LM images of the cobalt antidot array with p = 160 nm: (a) in-focus, (b) over-focus, and (c) under-focus. (d) Schematic illustration of the method used to improve the visualization of the magnetic contrast. (e)-(g) Filtered focal series of LM images extracted from (a)-(c), respectively. The yellow dashed lines delimit the region, displayed in Figure 5.8, used to perform the TIE reconstruction.

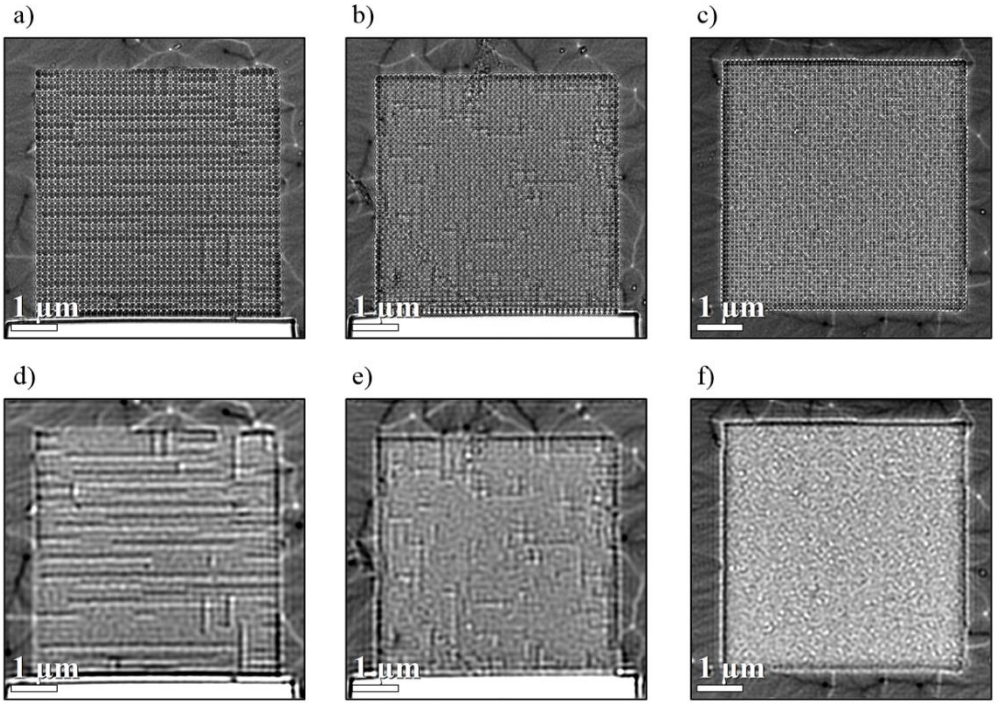

Figure 5.6. (a)-(c) Raw and (d)-(f) filtered defocused LM images of antidot arrays with (a), (d) p =138 nm, (b), (e) p = 116 nm, and (c), (f) p = 95 nm array periodicity.

This procedure was also applied in antidot arrays with p = 138, 116 and 95 nm, as reported in Figure 5.6. Antidot arrays with p = 138 and 116 nm present the same magnetic contrast structure observed in the array of p = 160 nm, whereas no magnetic contrast is seen for p = 95 nm, as shown in Figures 5.6(c) and (f). Arrays with smaller periodicities were also observed by LM (not shown here), and likewise no magnetic contrast was found. Two factors could have contributed to the absence of magnetic contrast:

(1) The reduction of the hole spacing increases the overlapping of the Fresnel fringes, further degrading the quality of the LM.

(2) The reduction of the periodicity, which increases the extent of the damaged area, as reported in Figure 5.2(c), could have depressed further the magnetism of the array.

The significance of the latter can be also deduced from the comparison of the magnetic contrast of Figures 5.6(d-e), where the intensity of the magnetic contrast gradually decrease with p.

The results presented until now for cobalt antidot arrays have demonstrated the capability of LM to evaluate qualitatively the magnetic configuration of these systems by the direct visualization of magnetic contrasts in defocused LM images. The Fourier filtering procedure not only improves the visualization of magnetic contrasts, but also reveals a magnetic transition in the type of magnetic domain formed inside the arrays of small periodicities ($p \leq 160$ nm). Moreover, further quantitative information can be extracted by mapping the magnetization by means of TIE reconstructions.

5.4.2 A quantitative description: TIE reconstructions

The remanent state of cobalt antidot arrays has been quantitatively studied by solving the Transport-Intensity-Equation (TIE), which permits mapping the local in-plane magnetic induction inside the arrays, see *Chapter 3*. A color map of the magnetic induction of the antidot array of largest periodicity ($p = 524$ nm) is shown in Figure 5.7(a), as well as a vector-color map of a magnified area in the center of the array in Figure 5.7(b). The remanent magnetic configuration of the array is composed by magnetic domains of different sizes and magnetization orientations. In Figure 5.7(b) the arrows representing the magnetization directions indicate that the magnetic domains are separated by 90° or 180° DWs, similar to those observed at remanence in continuous cobalt thin films [50–52]. In such array, the holes affect the magnetic configuration working as pinning centers for DWs. Only in some cases we observed the magnetization turning around a single antidot to achieve the flux closure. This occurs thanks to the local anisotropy modifications around of the holes.

TIE reconstructions have been also performed in antidot arrays with $p = 160$ nm using both raw and filtered focal series of LM images displayed in Figure 5.5, and only considering the region delimited by the yellow rectangle. Color maps of the in-plane magnetic induction for this particular array are shown in Figure 5.8. A

qualitative comparison between the TIE reconstructions of unfiltered (Figure 5.8 (a)) and Fourier filtered (Figure 5.8 (b)) focal series images demonstrates the efficiency of the Fourier filtering method in enhancing the magnetic contrast. This allows a clear and smooth visualization of the DWs and resolving more efficiently the local magnetization orientation. The comparison between the filtered defocused LM image in Figure 5.5(g) and the magnetic induction reconstruction of Figure 5.8(b) leads to conclude that the pairs of bright and dark straight magnetic lines correspond to a stripe-shaped magnetic domains formed between two parallel neighboring hole rows. These stripe-shaped magnetic domain are oriented along horizontal or vertical directions of the array, similar to those imaged by MFM and XPEEM in square antidot arrays with sub-micron antidot spacing [9,15,22,38]. For this particular remanent state, the magnetization color scale indicates that the greater part of the magnetic stripes has an average magnetization direction pointing up (green stripes) and left (red stripes). Between these magnetic stripes, regions with less clear magnetization directions are evidenced (in violet, blue and cyan). Therefore, micromagnetic simulations of this specific remanent state have been carried out using GPMagnet in order to interpret the whole reconstructed remanent magnetic state. For such calculations, we used the exact physical geometry of the corresponding region, i.e. the yellow box in Figure 5.5(a), using the in-focus LM image as reference. The initial configuration of the remanent state was defined by taking the average magnetization direction of the magnetic stripes from the TIE reconstruction of Figure 5.8(b) as initial state, and assuming that the magnetization direction in the regions between the stripes points transversally to the hole rows, at 225° with respect to the *x*-axis. For the micromagnetic simulations, a cell size of $5 \times 5 \times 10$ nm was defined and we used the following magnetic parameters of Co: saturation magnetization = 1400×10^3 A m^{-1} and exchange constant = 30×10^{-12} J m^{-1} [53]. The magnetocrystalline anisotropy constant assigned was 0 because of the polycrystalline nature of the cobalt film with small grain size and the dominance of the shape anisotropy due to the small thickness of the film with respect to the in-plane distance between the antidots.

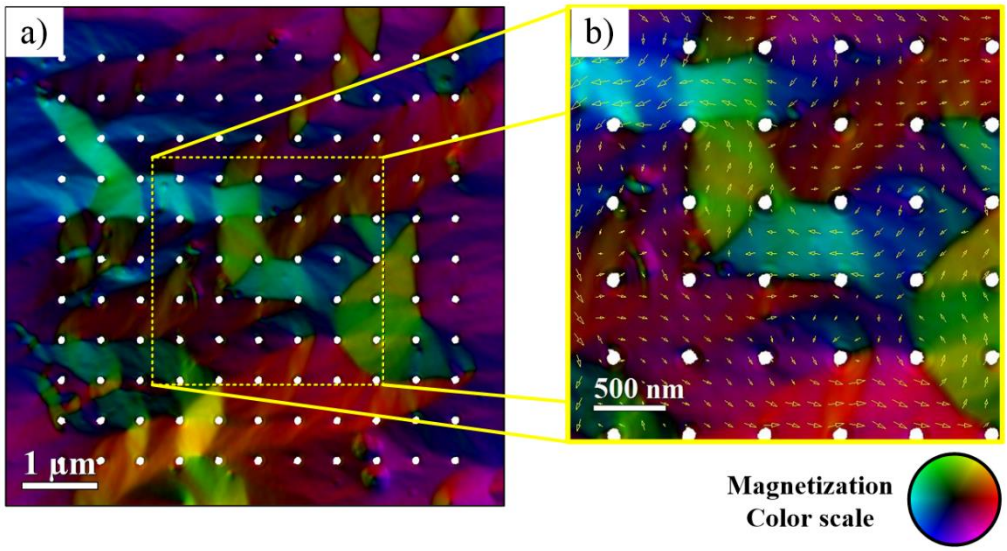

Figure 5.7. (a) Color map of the remanent magnetic state of the antidot array with p = 524 nm obtained by TIE reconstruction. (b) Vector-color map of the magnetization for the small region of (a) delimited by the yellow dashed square. The arrows and colors indicate the magnetization direction. A magnetization color scale is shown below (b). For the sake of clarity, the array of antidots has been superimposed with the reconstruction as white circles.

After running the micromagnetic simulations until the minimization of the total magnetic energy, we found that the simulated magnetization state of the array depicted in Figure 5.8(c) is significantly similar to the experimental one, even though small differences occur. Indeed small color variations along the magnetic stripes show up in the simulation that were not clearly evidenced in the TIE reconstructions, see Figure 5.8(a) and (b). Thus, such micromagnetic simulation can be used as a complementary tool for analyzing in more detail the local magnetization around the holes. However, it is still possible to enhance the details of the experimental magnetic induction maps by performing a TIE reconstruction of a smaller area (1.0 × 0.9 µm^2). The resulting magnetic map and the simulated vector-color map of the same region are depicted in Figure 5.9. At this scale, both experimental and simulated results show the same complex remanent state, where the local magnetization direction is changing slightly inside each domain.

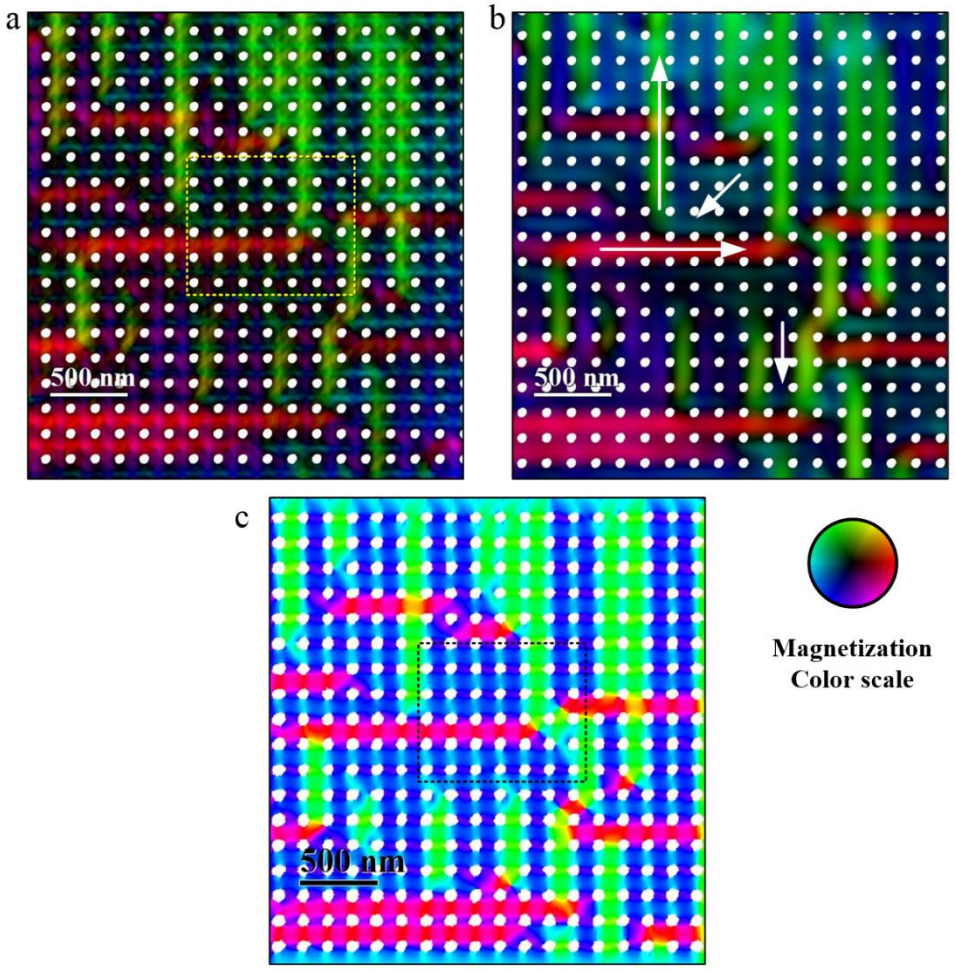

Figure 5.8. Color maps of the remanent magnetization state of a reduced region (yellow dashed box of Figures 5.5) of the antidot array with p = 160 nm obtained by TIE reconstruction using (a) raw and (b) filtered focal series LM images, and (c) performing a micromagnetic simulation. In (b) white arrows indicate the estimated direction of the average direction of magnetization in each magnetic domain. Dashed rectangles delimit the regions represented in Figure 5.9 as vector-color maps. For the sake of clarity, the array of antidots has been superimposed with the reconstruction as white circles.

A schematic drawing of the magnetic configurations observed inside the antidot array is shown in Figure 5.9(c). In the regions between the two nearest neighboring holes (Regions of *Type 1*), the magnetization is aligned tangentially to the holes, i.e. horizontal or vertical, to avoid magnetic charges at the edge of the holes, and therefore

to decrease the demagnetizing energy. In the larger regions enclosed by the four nearest neighboring holes (Regions of *Type 2*), the magnetization direction of the four neighboring *Type 1* regions forces the magnetization to align diagonally with respect to the lattice. The specific diagonal orientation depends on the magnetization direction in the four *Type 1* regions to achieve the continuity of the magnetic flux. These magnetic configurations are comparable to those reported in previous works on magnetic square antidot arrays with hole periodicities down to 400 nm [9,11,18,22].

Similarly to Ref. [18], we assumed that each magnetic unit cell is composed of five domains, four *Type 1* and one *Type 2*, whose integration results in a mean magnetization vector. Regions composed by consecutive magnetic unit cell with the same average magnetization vector constitute a magnetic domain inside the array, the so-called magnetic *Superdomains* (SDs), which are separated by *Superdomain Walls* (SDWs) [22]. The SDWs separate two neighboring cells with different average magnetization orientations, where the in-plane magnetization rotates progressively through the *Type 1* region that connects them. SDs and SDWs have already been observed in cobalt antidot arrays [9,20,38]. At remanence, the square antidot array induces head-to-tail or tail-to-head 90° SDWs, which have been referred as *Low-Energy Superdomain Walls* (LE-SDWs) because they create lower stray fields and minimize the exchange energy [22]. As for the magnetic domain walls observed in Fresnel LM, two SDWs surrounding a SD produce a pair of bright and dark straight lines that depend on both the magnetization orientation on each side of the SDWs and the sign of the defocus (*in the last section of this Chapter we will present in detail the process of SDW magnetic contrast formation*). Our experimental results also indicate that between large SDs, magnetic stripes appear along single rows of magnetic cells with the same average magnetization vector. These unit-cell-wide SDs are called *Magnetic Chains* (MCs) [38] and are limited by two parallel head-to-tail SDWs of different Lorentz force (LF) orientations (one tail-to-tail LF and another one head-to-head LF orientation). In the defocused LM images, MCs produce exotic magnetic contrasts composed by pairs of bright and dark straight lines. As we will see later, the

nucleation and propagation of MCs are the most favorable mechanisms for magnetization switching in these high-density antidot arrays.

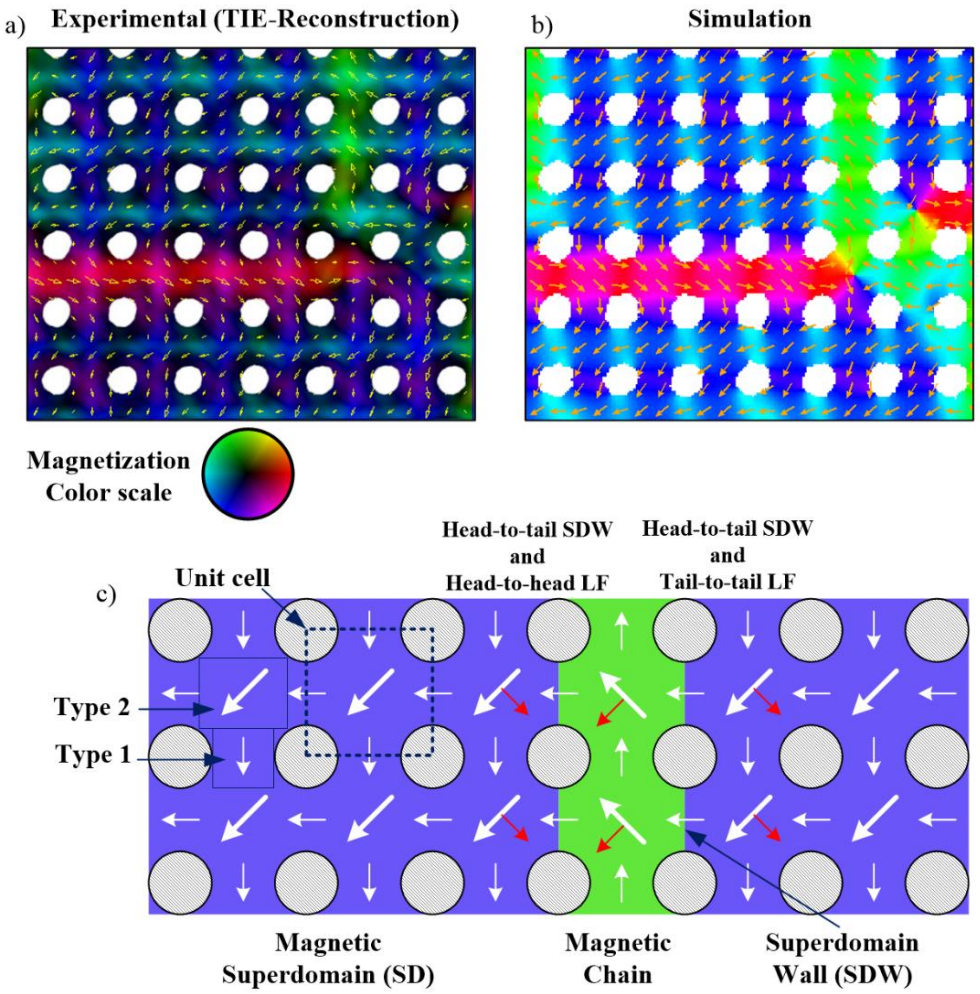

Figure 5.9. Vector-color maps of the region delimited in Figure 5.8(c) for (a) the experimental and (b) the simulated remanent magnetic state. (c) Schematic illustration of the remanent spin configuration across a magnetic chain. White and red arrows indicate the magnetization direction and LF orientation, respectively. For the sake of clarity, the array of antidots (white circle) has been superimposed with the reconstruction.

5.5. Magnetization reversal processes

The magnetization reversal process of the antidot arrays with periodicities higher than 320 nm does not differ much from that of a continuous film; the magnetization switching occurs by the nucleation and propagation of 90° and 180° DWs through the film, until the saturation is reached. Due to the holes acting as pinning center, the DWs propagation occurs by a sequence of pinning and depinning steps between different sets of antidots. This sequential process hinders the propagation of DWs and requires the application of a higher magnetic field to achieve the complete switching of the magnetization. Therefore, antidot arrays exhibit much larger coercive fields than continuous thin films.

More complex and interesting magnetization switching mechanisms are observed in antidot arrays with periodicities equal or less than 160 nm. As for magnetic data storage, the smaller the periodicity of the array, the higher the storage capacity. Thus, it is of great importance to understand the magnetic configuration and the reversal process in antidot arrays of reduced periodicity. Therefore, we have focused our work on the analysis of arrays with periodicity p = 160 nm by *in situ* LM experiments. Even if this array is not of the smallest periodicity, its magnetic configuration is similar to those of arrays with a smaller periodicity (down to 116 nm) and the results we obtained can be extrapolated to array of smaller periodicities. We have already showed that in such arrays the confinement of the magnetization changes dramatically the micromagnetic configuration, leading to the appearance of horizontal and vertical MCs located between extended SDs. We have studied the magnetization reversal by performing *in situ* half hysteresis loops with the in-plane component of the applied magnetic field horizontal (parallel to the antidot rows) and diagonal (at 45° with respect to the antidot array). For square antidot arrays, these directions correspond to the magnetization hard axis (HA) and easy axis (EA), respectively, [18,20]. For this experiment, the sample was tilted 16.7° with respect to the zero-tilt holder plane, so the ratio between the in-plane and out-of-plane components was k = 0.3, and the magnitude of the in-plane magnetic field was swept between -800 to 800 Oe. Several defocused LM images were recorded during the magnetization reversal process and

allowed studying the evolution of the SDWs in detail. Videos of the switching processes were composed by means of these series of defocused LM images (*Such videos in the supplementary data of the article: L. A. Rodríguez et. al., Nanotechnology, 25 (2014) 385703*).

Two series of defocused LM images highlighting the most relevant behavior of the reversal processes along the HA (horizontal) and EA (diagonal) are reported in Figures 5.10 and 5.11, respectively. In both cases, the magnetization switching occurs by the nucleation and propagation of SDWs, with the predominant formation of MCs. However, the SDW nucleation and propagation mechanisms are considerably different in each case. When the magnetic field is applied along the EA, the magnetization switching begins by the simultaneous nucleation of horizontal and vertical MCs at the edges of the array (see Figure 5.10 at H = -132 Oe). Both types of MCs then propagate toward the center of the array with equal probability (see Figure 5.10 at H = -227 Oe). At H = -320 Oe, just before saturation, small magnetic domains remain in the lattice as a result of the collapse of long MCs into single-cell MCs where magnetic flux closes around single antidots. When the magnetic field is applied along the HA, the magnetization switching begins by the nucleation and propagation of horizontal MCs, which are parallel to in-plane magnetic field (see Figure 5.11 at H = -110 Oe) and then occurs the nucleation and propagation of vertical MCs (see Figure 5.11 at H = -194 Oe). At H = 0, while some vertical MCs are nucleated in the HA hysteresis loop (see Figure 5.11), no SDW is formed in the EA hysteresis loop, thus the system remains saturated at remanence (see Figure 5.10 at H = 0). This confirms that the direction parallel to the antidot rows is the HA while the diagonal is the EA.

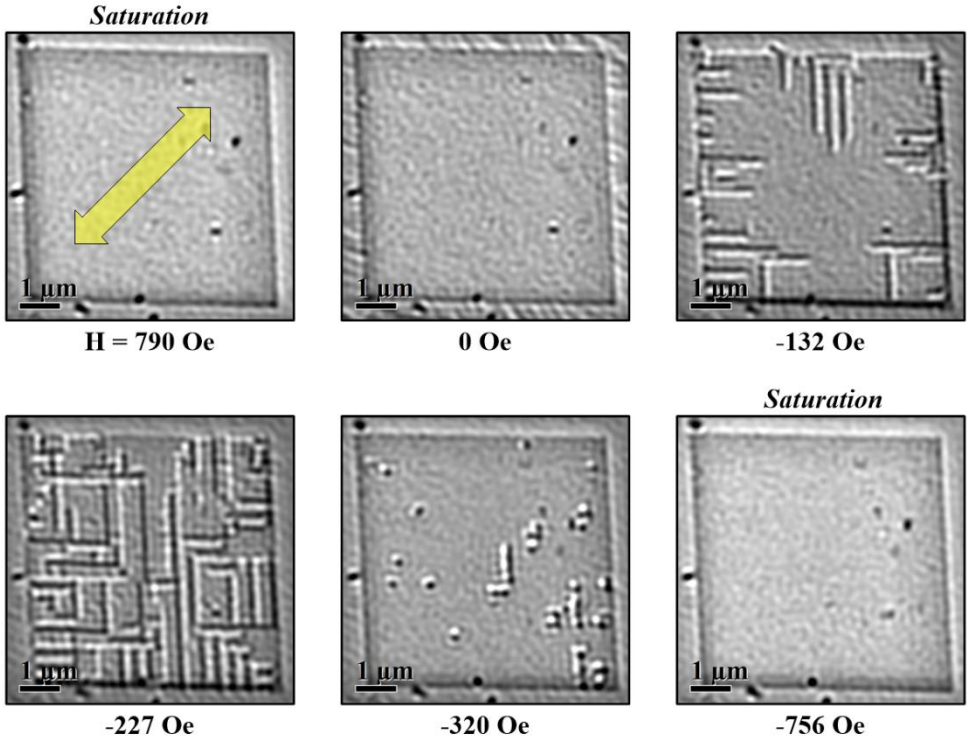

Figure 5.10. Series of filtered defocused LM images that highlight the magnetization reversal process upon application of transversal magnetic fields, along the EA, for the antidot array with p = 160 nm. The yellow arrow indicates the orientation of the in-plane magnetic field.

Quasi-static micromagnetic simulations following the same experimental setup (k = 0.3) have been performed to simulate the magnetization switching observed when the field is applied along both EA and HA, although our following discussion will be mainly focused on the HA hysteresis field. To reduce the computation time, we simulated a square antidot lattice of 3.0 × 2.7 μm, which is approximately 60% smaller that the real one. In addition, the antidot array was constructed in the middle of a continuous thin film of 5.0 × 4.5 μm to take into account the effect of the continuous magnetic region surrounding the antidot array. The compared experimental and simulated results are displayed in Figure 5.11, where filtered defocused LM images obtained on the whole array for different magnetic fields (H = 0, -110, -194 and -314 Oe) are reported on the left panel, and next to them on the right panel the

simulated images obtained for the same fields. For easy viewing of horizontal/vertical MCs, simulated images of the *x*- and *y*-component of the magnetic induction are depicted independently. Even though specific details may differ between the simulation and the experimental results, the simulated magnetization switching shows qualitatively the same behavior as observed in the *in situ* LM experiments. In particular, the simulation reproduces the three-step magnetization reversal: first, as the magnetic field decreases from saturation to $H = 0$ Oe, few MCs oriented along *y*-axis appear (stage 1 in Figure 5.11); secondly, at negative fields the simulation shows the nucleation and propagation of SDWs parallel to the applied field (stage 2 in Figure 5.11), and subsequently the nucleation and propagation of SDWs in a perpendicular direction (Stage 3 in Figure 5.11). The simulations also reveal the remaining of small magnetic domains just before the complete saturation of the array. Similar micromagnetic simulations were carried out for the EA hysteresis loop (*not shown here*) and agree with the experimental observations of the reversal process. The corresponding simulated EA and HA hysteresis loop calculated to the *x*-component of the magnetic induction is displayed in Figure 5.12(b).

To analyze in more detail the simulated magnetization switching, we have depicted vector-color maps extracted from a small region delimited by the black dashed lines in the simulation of Figure 5.11. Starting from positive saturation ($H_x/H_s = +1.0$, where $H_s = 770$ Oe), the entire magnetization is completely saturated along the *x*-direction. When the magnitude of the magnetic field is reduced progressively to zero ($H_x/H_s = 0$), the demagnetizing field of the array controls the magnetization orientation, forcing a rotation of 45° with respect to the positive *x*-axis in the *Type 2* regions. The square symmetry of the array offers two possible orientations for the magnetization either at +45 or -45° with respect to the *x*-axis. Both experimental and simulation results demonstrate that there is a preferential magnetization direction (for example, +45°) that allows the creation of extended SDs where all regions of *Type 2* present the same direction of magnetization (+45° in this example) and the appearance of few MCs where the magnetization in the regions of *Type 2* is oriented in the non-preferential direction (-45°). This explains why some vertical MCs are observed at

remanence for the HA hysteresis loops while for the EA hysteresis, the external magnetic field tends to align the magnetization at 45° with respect to *x*-axis, so that the demagnetizing field of the array maintains such orientation in the *Type 2* regions. At H_x/H_s = -0.1, we observe that the magnetization switching occurs inside the extended SDs through the nucleation, and then the propagation of horizontal MCs, while the initially formed vertical MCs remain almost unaltered. At H_x/H_s = -0.6, the mean magnetization within the large SDs have switched toward a negative orientation respect to *x*-axis, nearly parallel to the applied field. However, the competition between the demagnetization and Zeeman energies forces the magnetization orientation in the *Type 2* regions to tilt slightly up or down with respect to the negative *x*-axis, favoring the formation of vertical MCs. On the other hand, in the vertical MCs nucleated at remanence, this energy competition makes the average magnetization direction point vertically. This highly stable magnetic configuration induces 180° SDWs, as observed in Figure 5.12 at H_x/H_s = -0.6. When increasing the negative applied field even more (H_x/H_s = -0.7), the vertical MCs finally collapse and the magnetization turns parallel to the applied magnetic field. In some cases, the vertical MC may result in the creation of a single-unit-cell magnetic domain. These very last magnetic domains finally switch at saturation (H_x/H_s = -1) where the applied magnetic field forces the magnetization orientation to lie along the *x*-axis. It is worth noting that each stage of the magnetization reversal process gives a particular behavior of the HA hysteresis loop plotted in Figure 5.12(b): (1) the formation of vertical MCs slightly reduces the M_x value at H = 0; (2) the magnetization switching of horizontal MCs produces an abrupt drop in M_x across the coercive field; (3) the formation and switching of vertical MCs causes a slight and continuous increase of M_x and (4) single-unit-cell magnetic domains are still present at high magnetic fields, just before saturation.

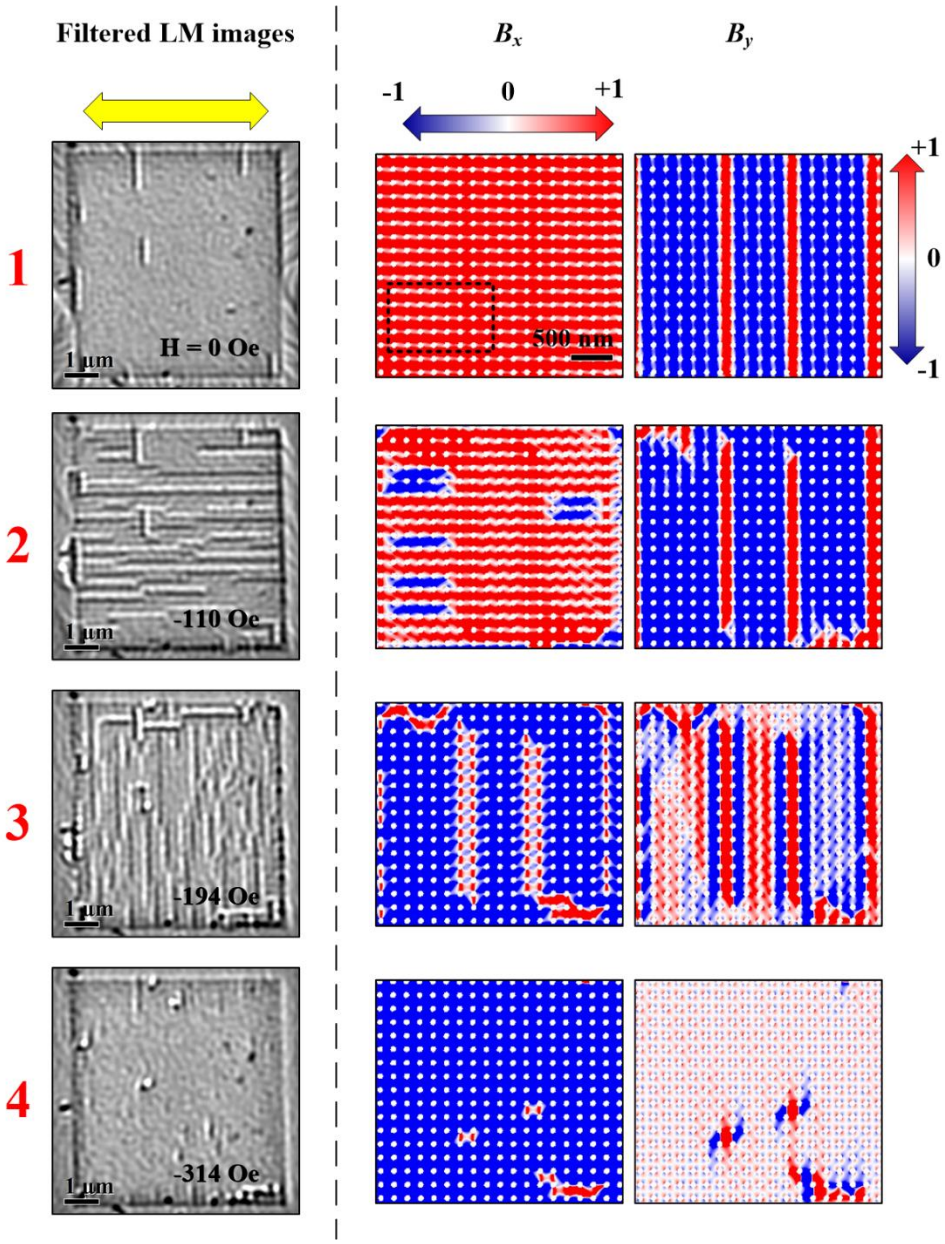

Figure 5.11. Filtered LM images (*left*) and micromagnetic simulations (*right*) summarizing the relevant stages of the magnetization reversal mechanisms along the HA direction of the antidot array with p = 160 nm. The yellow arrow indicates the direction of the in-plane applied magnetic field. The numbers label each stage of the magnetization switching to compare them with the hysteresis loop plotted in Figure 5.12. B_x and B_y are the x and y components of the magnetic induction. The black dashed rectangle in the B_x component at stage 1 delimits the region used to compose the vector-color maps in Figure 5.12

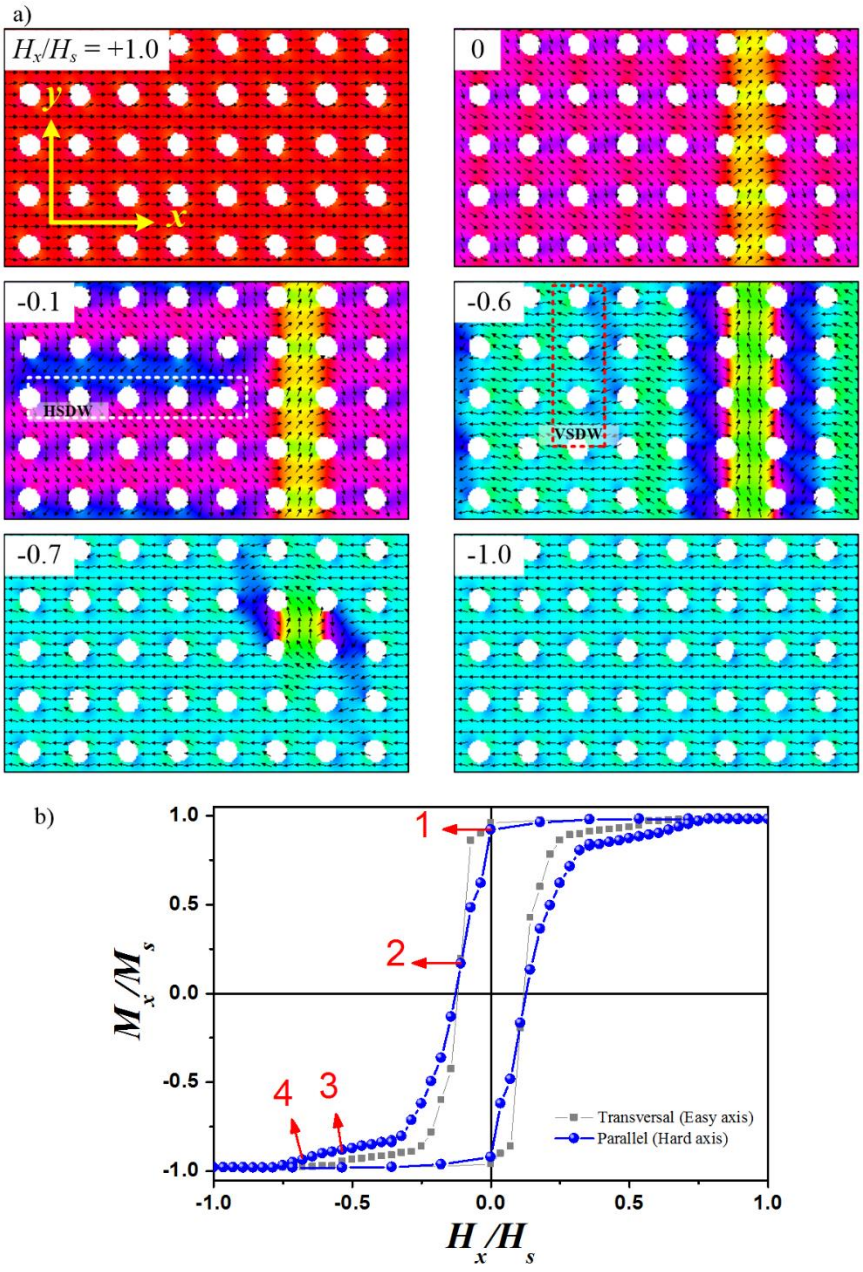

Figure 5.12. (a) Simulated vector-color maps of different stages of the magnetization reversal process by application of magnetic fields in the HA direction. They have been extracted from the area enclosed in the dashed rectangle in Figure 5.11. The black arrows represent the local magnetization orientation. The white and red dashed rectangles indicate the formation of horizontal and vertical SDWs, HSDW and VSDW, respectively. (b) Hysteresis loop calculated from the simulations for EA (gray dots) and HA (blue dots) hysteresis loops.

A careful analysis of the hysteresis loop along the EA and HA magnetization axes (*see videos*) indicates that, whereas the MCs tend to propagate easily along the extended SDs when the magnetic field increases, the eventual crossing of chain ends belonging to orthogonal MCs causes a very energetically stable pinning center. Although MCs with free ends propagates in a continuous way, orthogonal magnetic chains with their ends pinned together are only depinned at high magnetic field close to saturation. Heyderman *et. al*. have already reported this phenomenon in EBL antidot arrays with higher period (p > 200 nm) [9]. These authors also report the tendency of the MCs to align their chain ends, which was not observed in our LM experiments. Along these lines, it is noteworthy that, in addition to the smaller period of our system, the Ga irradiation effect produces large effective hole diameters. Thus the magnetic regions between the holes are further reduced, and significant differences are expected from systems fabricated by EBL.

5.6. Fresnel contrast formation of superdomain walls

We have noticed the following specific features in the bright-dark straight lines of magnetic contrasts produced by MCs at remanence and during the magnetization reversal processes in the antidot array with p = 160 nm:

a) While horizontal and vertical MCs observed at remanence (Figure 5.5(g)) and at H = -227 Oe of the EA hysteresis loop (Figure 5.10) present a similar contrast, horizontal MCs formed at H = -110 Oe exhibit sharper contrast than the vertical MCs formed at H = -194 Oe of the HA hysteresis (Figure 5.11).
b) In the HA hysteresis loop, at H = -194 Oe, vertical MCs formed at remanence have higher contrast than those formed during the magnetization switching (Figure 5.11).

To understand these features, we have to analyze in detail the origin of these magnetic contrasts. As discussed in the *Chapter 2*, Fresnel contrasts in Lorentz mode arise from the LF acting on the electron beam when it interacts with the magnetic

fields within and around the specimen. For a given defocus condition and depending on the relative magnetization direction at each side of the DW, the electron deflection either induces an overlap of the beams passing by each side of the DW, leading to a line of high intensity with possible interference fringes running parallel to the DW, or a divergence of the beams reducing the electron density and leading to a lower intensity line. According to the Lorentz force (see Equation 2.16), the bright (respectively dark) magnetic contrast of a head-to-tail SDW observed in an under-focus condition is formed by the electron interference produced by a head-to-head (respectively tail-to-tail) LF configuration schematized in Figure 5.9(c). Changing the defocus sign reverses the contrast.

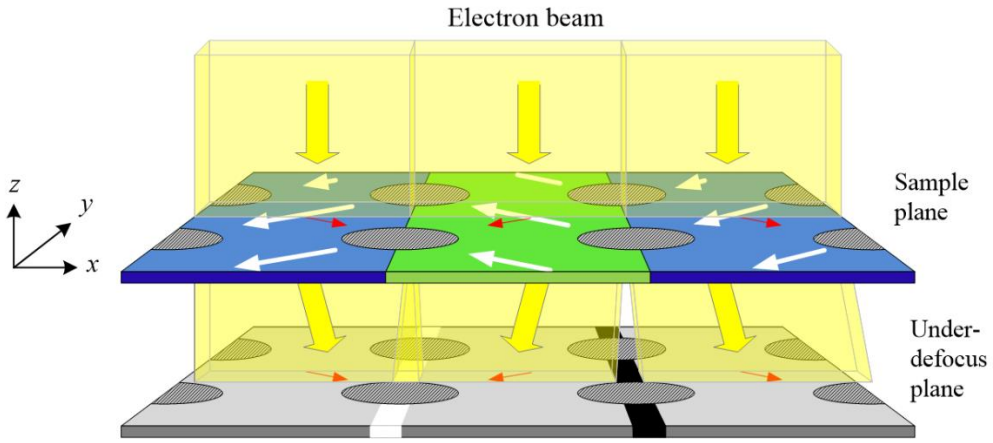

Figure 5.13. Schematic illustration showing how the magnetic contrast are formed in a defocused LM image around a MC. Yellow arrows represent the trajectories of the electrons. White and red arrows represent the magnetization and Lorentz Force direction, respectively.

The schematic illustration shown in Figure 5.13 gives a simple image of the process of magnetic contrast formation by two SDWs forming a vertical MC (oriented along *y*-axis). In this cartoon we also note that the magnetization orientation along the *x*-direction, which is perpendicular to the length of the MC, is rotating 90° between magnetic unit-cells following a zigzag type ordering of the local magnetization

orientation. Therefore, the right-side SDW of the vertical MC will produce a dark contrast by the tail-to-tail LF configuration around it, while the left-side SDW will produce a bright contrast by the head-to-head LF configuration. Thus, the vertical MC is composed by a pair of bright and dark lines of magnetic contrast.

Now, to understand why some magnetic contrasts are shaper than others, we have to express in detail how these magnetic contrasts are formed. The phase shift of the electron beam due to its interaction with magnetic induction may be expressed as:

$$\varphi(\mathbf{r}) = -\frac{e\mu_0}{2\pi h r} \otimes \int (\nabla \times \mathbf{M}(\mathbf{r})) \cdot d\mathbf{l} \qquad \text{(Eq. 5.1)}$$

where $\otimes$ denotes a convolution in 2D, the coordinates $\mathbf{r} = (x, y)$ and $r = |\mathbf{r}$. This expression can be introduced in the TIE (Equation 2.23), leading to the following normalized expression for the intensity of a Fresnel image at small defocus [54]:

$$I(x, y, \Delta_z) = 1 - \frac{e\mu_0 \lambda \Delta_z t}{h} (\nabla \times \mathbf{M}(\mathbf{r})) \cdot \hat{\mathbf{z}} = 1 - \Delta I \qquad \text{(Eq. 5.2)}$$

Equation 5.2 is applicable to thin films where the magnetization does not vary with the thickness. As we see in the Equation 5.2, magnetic contrast (ΔI) is only visible out of focus ($\Delta_z \neq 0$), and in regions where a spatial variation of the magnetization occurs, such as DWs. Equation 5.2 can be rewritten if we know how $\mathbf{M}(\mathbf{r})$ varies with respect to $\mathbf{r} = (x, y)$. There are different mathematical models to describe the magnetization rotation through the wall [55], but for the sake of simplicity, we consider a one-dimension (1D) DW model where the magnetization rotation is linear:

$$M_y = \frac{2M}{\delta} \sin\left(\frac{\theta_{DW}}{2}\right) x - M \sin\left(\frac{\theta_{DW}}{2}\right) \quad for \;\; 0 < x < \delta \qquad \text{(Eq. 5.3)}$$

where δ is the DW width and M is the saturation magnetization. In Equation 5.3, θ_{DW} corresponds to the total rotation of the magnetization through the 1D DW, ranging

between -180° < θ_{DW} < 180°. The sign of θ_{DW} is positive or negative if the rotation is counterclockwise or clockwise, respectively. In addition, Equation 5.3 assumes that the progressive reorientation of the magnetization occurs toward the positive *x* direction. For the opposite direction, the signs of Equation 5.3 have to be changed. A graphical representation of this simple 1D DW is shown in Figure 5.14.

For such variation of **M**(**r**) across a DW, the Equation 5.2 can be transformed into

$$I(x,y,\Delta_z) = 1 - \Delta I(\theta_{DW}) = 1 \mp C \sin\left(\frac{\theta_{DW}}{2}\right) \qquad \text{(Eq. 5.4)}$$

where $C = 2M_e\mu_0\lambda\Delta_z t/h\delta$, and the sign depends on the sense of rotation of the magnetization across the DW: a minus sign for positive *x* direction and a positive sign for negative *x* direction.

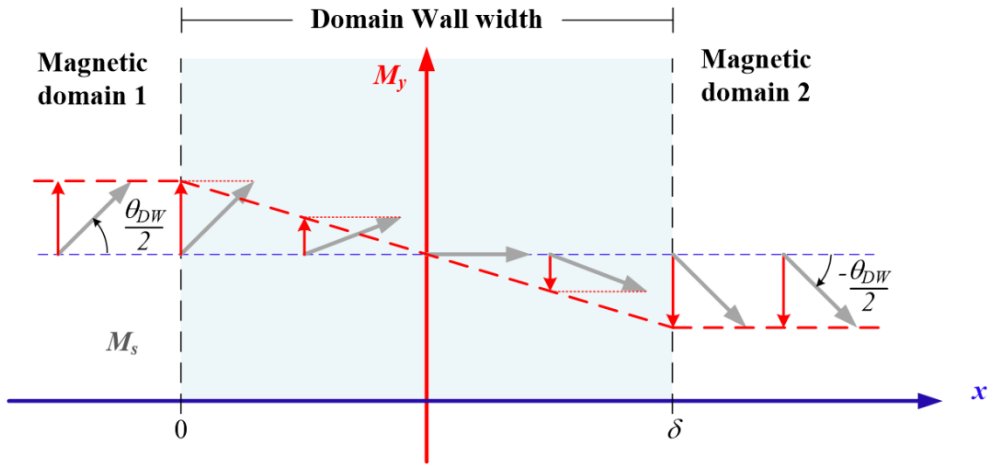

Figure 5.14. Schematic illustration of the magnetization rotation in a 1D DW. Gray and red arrows represent the two-dimensional magnetization vector and the *y*-component of the magnetization, respectively, through the wall.

A plot of the Equation 5.4 is shown in Figure 5.15. Assuming a constant DW width, Equation 5.4 reveals that the intensity of the magnetic contrasts only depends on the total magnetization rotation through the wall. As we see in Figure 5.14, the highest magnetic contrast, ΔI_{max}, occurs for a 180° DWs. This DW configuration has been observed at H_x/H_s = -0.6 in the vertical MCs initially nucleated at remanence for the HA hysteresis loop. For the experimental ones, the same DW configuration would be present in the sharpest vertical MCs at H = -194 Oe (see stage 3 of Figure 5.11). At remanence, horizontal and vertical MCs are composed by pairs of 90° SDWs which produce a magnetic contrast of I (90°) = $0.7 \cdot \Delta I_{max}$. Such 90° SDWs are also been observed in the horizontal MCs formed at H_x/H_s = -0.1 of the HA hysteresis loop. However, according to Figure 5.12, at H_x/H_s = -0.6 the micromagnetic simulation shows that vertical MCs nucleated as a consequence of the magnetization switching process are composed by 45° DWs. These DWs will produce a magnetic contrast of $I(45°) = 0.38 \cdot \Delta I_{max}$, almost twice smaller than the SDWs for the horizontal MCs.

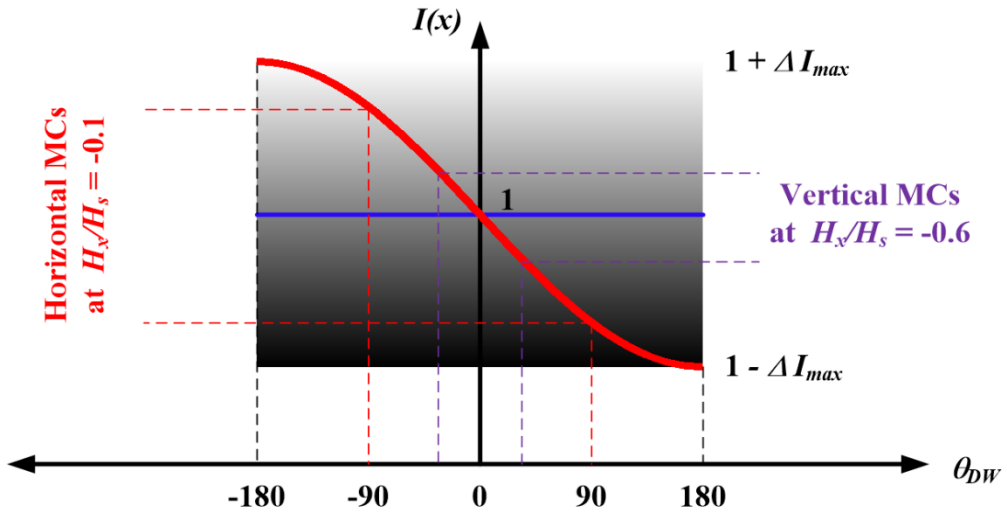

Figure 5.15. Plot of the variation of the Fresnel image in a DW with respect to the total magnetization, according to Equation 5.4. A degraded black-to-white background in the plot indicates the brightness of the magnetic contrast.

5.7. Conclusions

High-resolution *in situ* LM has provided a clear description of the magnetization states of Co square antidot arrays with periodicities down to 116 nm with unprecedented detail. One of the main drawbacks of LM in Fresnel mode for the study of these kinds of structures, i.e. the formation of Fresnel fringes in the border of the holes, has been successfully overcome by applying a low-frequency Fourier filter. This filtering procedure has enabled the visualization and quantitative analysis of the lineal magnetic contrast produced by SDWs in antidot arrays with periodicities between 160 and 116 nm. The magnetization states of antidot arrays with hole periodicities lower than 116 nm could not be studied due to the proximity of the antidots and the increasing proportion of the regions damaged by FIB etching around the holes, both factors preventing the detection of a magnetic signal inside the array.

A qualitative analysis of the remanent magnetic states by the direct visualization of magnetic contrast in defocused LM images has allowed detecting a transition in the magnetic structure: for antidot arrays with large periodicities ($p \geq 327$ nm), the remanent magnetic configuration inside the array was similar to that observed in continuous cobalt films, composed by bright and dark lines randomly distributed and running across the hole positions. For antidot arrays with $160 \leq p \leq 116$ nm, pairs of bright and dark lines of magnetic contrast oriented in horizontal and vertical directions were detected. A quantitative analysis by TIE reconstruction in the antidot array with $p = 160$ nm demonstrated that these remanent magnetic states were formed by MCs embedded in extended magnetic SDs. The formation of these exotic magnetic structures is caused by the induced magnetic shape anisotropy of the holes that, when the periodicity is reduced, control the orientation of the magnetization.

A study of the magnetization reversal process was carried in one of the antidot arrays with presence of SDWs ($p = 160$ nm) by applying magnetic fields along the easy (parallel to the hole rows) and hard (transversal to the hole rows) magnetic axis of the array. In both cases, we found that the magnetization reversal occurred by means of nucleation and propagation of SDWs, with a predominant tendency to form

MCs. However, the reversal process differed depending on the orientation of the applied magnetic field. Magnetic fields applied diagonally to the array produced a simultaneous nucleation and propagation of vertical and horizontal SDWs, preferentially forming MCs at the edge of the lattice, and then propagating and collapsing toward the center of the array. Vertical and horizontal MCs collapsed into small magnetic domains of single-unit-cell size just before magnetic saturation. On the other hand, magnetic fields applied parallel to the array switched the magnetization in two stages, beginning by the nucleation and propagation of horizontal MCs, and then approaching saturation through vertical MCs. Similar to the previous case, MCs eventually collapsed into single-cell domains before complete saturation.

This work highlights the potential of LM, as well as EH, to characterize magnetic antidot structures with reduced hole distance. As discussed in the motivation of this Chapter, an exhaustive analysis of the local magnetic states at this scale contributes to determine their potential in applications for data storage in magnetic media or magnonic crystals for applications in spin wave filters or guides. On the other hand, the novel low-frequency Fourier filtering method opens new opportunities for a versatile and straightforward quantitative imaging of magnetization process in low-periodicity arrays of nanomagnets.

Reference

[1] Xu Y and Thompson S 2006 *Spintronic Materials and Technology* (Taylor & Francis)

[2] Utke I, Moshkalev S and Russell P 2012 *Nanofabrication Using Focused Ion and Electron Beams: Principles and Applications* (Oxford University Press, USA)

[3] Adeyeye A O, Bland J A C and Daboo C 1997 Magnetic properties of arrays of "holes" in $Ni_{80}Fe_{20}$ films *Appl. Phys. Lett.* **70** 3164

[4] García-Sánchez F, Paz E, Pigazo F, Chubykalo-Fesenko O, Palomares F J, González J M, Cebollada F, Bartolomé J and García L M 2008 Coercivity mechanisms in lithographed antidot arrays *EPL Europhysics Lett.* **84** 67002

[5] Torres L, Lopez-Diaz L and Iñiguez J 1998 Micromagnetic tailoring of periodic antidot permalloy arrays for high density storage *Appl. Phys. Lett.* **73** 3766

[6] Ruiz-Feal I, Lopez-Diaz L, Hirohata A, Rothman J, Guertler C ., Bland J A, Garcia L, Torres J, Bartolome J, Bartolome F, Natali M, Decanini D and Chen Y 2002 Geometric coercivity scaling in magnetic thin film antidot arrays *J. Magn. Magn. Mater.* **242-245** 597–600

[7] Jalil A B A, Phoa S L A, Tan S L and Adeyeye A O 2002 Magnetic properties of lateral "antidot" arrays *IEEE Trans. Magn.* **38** 2556–8

[8] Jalil M B A 2003 Bit isolation in periodic antidot arrays using transverse applied fields *J. Appl. Phys.* **93** 7053

[9] Heyderman L, Nolting F, Backes D, Czekaj S, Lopez-Diaz L, Kläui M, Rüdiger U, Vaz C, Bland J, Matelon R, Volkmann U and Fischer P 2006 Magnetization reversal in cobalt antidot arrays *Phys. Rev. B* **73** 214429

[10] Vázquez M, Pirota K R, Navas D, Asenjo A, Hernández-Vélez M, Prieto P and Sanz J M 2008 Ordered magnetic nanohole and antidot arrays prepared through replication from anodic alumina templates *J. Magn. Magn. Mater.* **320** 1978–83

[11] Van de Wiele B, Manzin A, Vansteenkiste A, Bottauscio O, Dupré L and De Zutter D 2012 A micromagnetic study of the reversal mechanism in permalloy antidot arrays *J. Appl. Phys.* **111** 053915

[12] Castán-Guerrero C, Sesé J, Bartolomé J, Bartolomé F, Herrero-Albillos J, Kronast F, Strichovanec P, Merazzo K J, Vázquez M, Vavassori P and García L M 2012 Fabrication and Magnetic Characterization of Cobalt Antidot Arrays: Effect of the Surrounding Continuous Film *J. Nanosci. Nanotechnol.* **12** 7437–41

[13] Gawroński P, Merazzo K J, Chubykalo-Fesenko O, Asenjo A, del Real R P and Vázquez M 2012 Micromagnetism of dense permalloy antidot lattices from anodic alumina templates *EPL Europhysics Lett.* **100** 17007

[14] Paz E, Cebollada F, Palomares F J, González J M, Im M-Y and Fischer P 2012 Scaling of the coercivity with the geometrical parameters in epitaxial Fe antidot arrays *J. Appl. Phys.* **111** 073908

[15] Castán-Guerrero C, Herrero-Albillos J, Bartolomé J, Bartolomé F, Rodríguez L A, Magén C, Kronast F, Gawronski P, Chubykalo-Fesenko O, Merazzo K J, Vavassori P, Strichovanec P, Sesé J and García L M 2014 Magnetic antidot to dot crossover in Co and Py nanopatterned thin films *Phys. Rev. B* **89** 144405

[16] Wang C, Adeyeye A and Lin C 2004 Magnetic properties of lithographically defined rectangular antidot permalloy arrays *J. Magn. Magn. Mater.* **272-276** E1299–E1300

[17] Castaño F J, Nielsch K, Ross C A, Robinson J W A and Krishnan R 2004 Anisotropy and magnetotransport in ordered magnetic antidot arrays *Appl. Phys. Lett.* **85** 2872

[18] Wang C C, Adeyeye A O and Singh N 2006 Magnetic antidot nanostructures: effect of lattice geometry *Nanotechnology* **17** 1629–36

[19] Tiberto P, Boarino L, Celegato F, Coïsson M, De Leo N, Vinai F and Allia P 2010 Magnetic and magnetotransport properties of arrays of nanostructured antidots obtained by self-assembling polystyrene nanosphere lithography *J. Appl. Phys.* **107** 09B502

[20] Mengotti E, Heyderman L J, Nolting F, Craig B R, Chapman J N, Lopez-Diaz L, Matelon R J, Volkmann U G, Kläui M, Rüdiger U, Vaz C A F and Bland J A C 2008 Easy axis magnetization reversal in cobalt antidot arrays *J. Appl. Phys.* **103** 07D509

[21] Chuang V P, Jung W, Ross C A, Cheng J Y, Park O-H and Kim H-C 2008 Multilayer magnetic antidot arrays from block copolymer templates *J. Appl. Phys.* **103** 074307

[22] Hu X K, Sievers S, Müller A, Janke V and Schumacher H W 2011 Classification of super domains and super domain walls in permalloy antidot lattices *Phys. Rev. B* **84** 024404

[23] Hu X K, Sievers S, Müller A and Schumacher H W 2013 The influence of individual lattice defects on the domain structure in magnetic antidot lattices *J. Appl. Phys.* **113** 103907

[24] Torres L, López-Díaz L, Alejos O and Iñiguez J 1999 Remanent states in periodic antidot permalloy arrays *J. Appl. Phys.* **85** 6208

[25] Torres L, Lopez-Diaz L, Alejos O and Iñiguez J 2000 Micromagnetic study of lithographically defined non-magnetic periodic nanostructures in magnetic thin films *Phys. B Condens. Matter* **275** 59–64

[26] Xiao Z L, Han C Y, Welp U, Wang H H, Willing G A, Vlasko-Vlasov V K, Kwok W K, Miller D J, Hiller J M, Cook R E and Crabtree G W 2003 Magnetic Antidot Arrays with a Storage Density of 10 Gbits/cm2 *Nanotech* **3** 357–60

[27] Kruglyak V V, Demokritov S O and Grundler D 2010 Magnonics *J. Phys. D. Appl. Phys.* **43** 264001

[28] Lenk B, Ulrichs H, Garbs F and Münzenberg M 2011 The building blocks of magnonics *Phys. Rep.* **507** 107–36

[29] Kłos J W, Kumar D, Romero-Vivas J, Fangohr H, Franchin M, Krawczyk M and Barman A 2012 Effect of magnetization pinning on the spectrum of spin waves in magnonic antidot waveguides *Phys. Rev. B* **86** 184433

[30] Lenk B, Abeling N, Panke J and Münzenberg M 2012 Spin-wave modes and band structure of rectangular CoFeB antidot lattices 4

[31] Schwarze T and Grundler D 2013 Magnonic crystal wave guide with large spin-wave propagation velocity in CoFeB *Appl. Phys. Lett.* **102** 222412

[32] Kłos J W, Kumar D, Krawczyk M and Barman A 2014 Influence of structural changes in a periodic antidot waveguide on the spin-wave spectra *Phys. Rev. B* **89** 014406

[33] Cowburn R P, Adeyeye A O and Bland J A C 1997 Magnetic domain formation in lithographically defined antidot Permalloy arrays *Appl. Phys. Lett.* **70** 2309

[34] Torres L, Lopez-Diaz L and Alejos O 2000 Micromagnetic analysis of recording processes in periodic antidot arrays: Interaction between adjacent bits *J. Appl. Phys.* **87** 5645

[35] Xiao Z L, Han C Y, Welp U, Wang H H, Vlasko-Vlasov V K, Kwok W K, Miller D J, Hiller J M, Cook R E, Willing G A and Crabtree G W 2002 Nickel antidot arrays on anodic alumina substrates *Appl. Phys. Lett.* **81** 2869

[36] Owen N and Petford-Long A 2002 Patterning magnetic antidot-type arrays by Ga/sup +/ implantation *IEEE Trans. Magn.* **38** 2553–5

[37] Zhukov A A, Goncharov A V, de Groot P A J, Bartlett P N and Ghanem M A 2003 Magnetic antidot arrays from self-assembly template methods *J. Appl. Phys.* **93** 7322

[38] Heyderman L J, Nolting F and Quitmann C 2003 X-ray photoemission electron microscopy investigation of magnetic thin film antidot arrays *Appl. Phys. Lett.* **83** 1797

[39] Qing-Fang L, Chang-Jun J, Xiao-Long F, Jian-Bo W and De-Sheng X 2006 Low-Temperature Magnetic Properties of Co Antidot Array *Chinese Phys. Lett.* **23** 1592–5

[40] Martyanov O, Yudanov V, Lee R, Nepijko S, Elmers H, Hertel R, Schneider C and Schönhense G 2007 Ferromagnetic resonance study of thin film antidot arrays: Experiment and micromagnetic simulations *Phys. Rev. B* **75** 174429

[41] Jiang C, Liu Q, Liu R, Wang J and Xue D 2007 Magnetic moment distribution study of Fe antidot arrays *Thin Solid Films* **515** 6967–70

[42] Yu M, Malkinski L, Spinu L, Zhou W and Whittenburg S 2007 Size dependence of static and dynamic magnetic properties in nanoscale square Permalloy antidot arrays *J. Appl. Phys.* **101** 09F501

[43] Phuoc N N, Lim S L, Xu F, Ma Y G and Ong C K 2008 Enhancement of exchange bias and ferromagnetic resonance frequency by using multilayer antidot arrays *J. Appl. Phys.* **104** 093708

[44] Tse D, Steinmuller S, Trypiniotis T, Anderson D, Jones G, Bland J and Barnes C 2009 Static and dynamic magnetic properties of Ni80Fe20 square antidot arrays *Phys. Rev. B* **79** 054426

[45] Rahman M T, Shams N N, Lai C H, Fidler J and Suess D 2010 Co/Pt perpendicular antidot arrays with engineered feature size and magnetic properties fabricated on anodic aluminum oxide templates *Phys. Rev. B* **81** 014418

[46] Ho C-C, Hsieh T-W, Kung H-H, Juan W-T, Lin K-H and Lee W-L 2010 Reduced saturation magnetization in cobalt antidot thin films prepared by polyethylene oxide-assisted self-assembly of polystyrene nanospheres *Appl. Phys. Lett.* **96** 122504

[47] Vázquez M, Asenjo A, Rosa W O, Mínguez I, Im M and Fischer P 2012 Studies of the Magnetization Reversal Processes in Co Dot and Antidot Arrays on a Microscopic Scale *Open Surf. Sci. J.* **4** 65–70

[48] Toporov A Y, Langford R M and Petford-Long A K 2000 Lorentz transmission electron microscopy of focused ion beam patterned magnetic antidot arrays *Appl. Phys. Lett.* **77** 3063

[49] Ramberg E G 1949 Phase Contrast in Electron Microscope Images *J. Appl. Phys.* **20** 441

[50] Oepen H P, Benning M, Ibach H, Schneider C M and Kirschner J 1990 Magnetic domain structure in ultrathin cobalt films *J. Magn. Magn. Mater.* **86** L137–L142

[51] Berger A and Oepen H P 1993 Magnetic domain walls in ultrathin fcc-cobalt films *J. Magn. Magn. Mater.* **121** 102–4

[52] Li S, Samad A, Lew W, Xu Y and Bland J 2000 Magnetic domain reversal in ultrathin Co(001) films probed by giant magnetoresistance measurements *Phys. Rev. B* **61** 6871–5

[53] Donahue M J and Porter D G http://math.nist.gov/oommf/ **87**

[54] McVitie S and Cushley M 2006 Quantitative Fresnel Lorentz microscopy and the transport of intensity equation. *Ultramicroscopy* **106** 423–31

[55] García-Cervera C J 2004 One-dimensional magnetic domain walls *Eur. J. Appl. Math.* **15** 451–86

Chapter 6

Strain-induced effects on the magnetic properties of epitaxial $La_{2/3}Ca_{1/3}MnO_3$ thin films

6.1. Motivation

The previous works carried out in ferromagnetic NWs and antidot arrays are two practical examples that demonstrate how the potential of nanometer scale magnetic characterization by LM and EH techniques can be greatly enhanced with the use of *in situ* external stimuli. Both the manipulation of single DWs in NWs and the magnetization switching of antidot arrays by nucleating and propagating SDWs were only possible due to the *in situ* capability to apply controlled in-plane magnetic field. Another very powerful application of LM and EH is the capability to perform experiments at low temperatures to perform magnetic studies on materials such as high-temperature superconductors or ferromagnets with T_C below room temperature. This is possible using commercial TEM cryo-holders cooled with liquid nitrogen or even helium.

An exciting group of ferromagnetic materials with low T_C are the perovskite-type manganese oxides $(R_{1-x}A_x)MnO_3$ (R = rare-earth cation; A = alkali or alkaline earth cation) [1,2]. The strong correlation between the structural, magnetic and transport properties in these complex oxides originates fascinating physical phenomena such as colossal magnetoresistance (CMR) at metal-insulator (FM-PM) transitions [1,3–6],

charge and orbital ordering [7–9], ferroelectricity [9–11] and large spin polarization [12–14] among others, with potential applications in a large variety of spintronic devices [13,15,16]. Even though experimental and theoretical phase diagrams reveal that half-doped manganites present a rich variety of electronic and magnetic phases [17–19], most of them exhibit optimal properties, such as the maximal T_C, the highest CMR near to TMI, half metallicity and the lowest resistivity, in intermediate compositions with $0.2 < x < 0.4$ [1–3,8,18,20]. As we see in Figure 6.1, for a particular composition $x = 0.3$ most of the bulk polycrystalline $R_{0.7}A_{0.3}MnO_3$ compounds order ferromagnetically with T_C in the range between room temperature and 100 K, so the local exploration of the magnetism by EH and LM can be performed using a liquid nitrogen cooling holder.

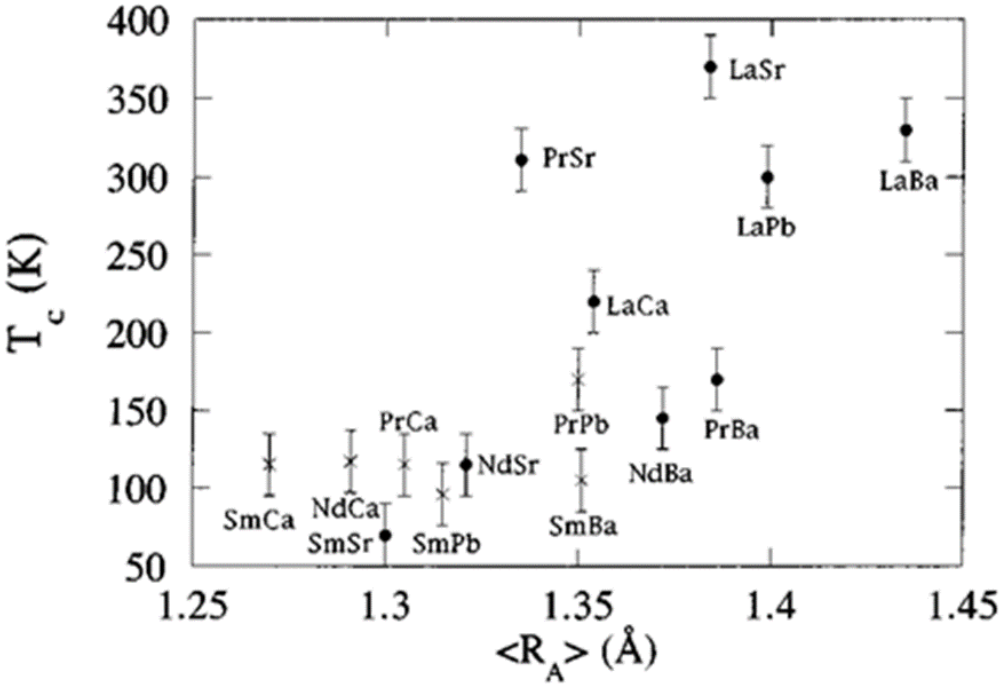

Figure 6.1. Curie temperature (T_C) as a function of ionic radius of the A cation for a series of bulk polycrystalline $(R_{0.7}A_{0.3})MnO_3$ compounds (R = La, Pr, Nd and Sm; A = Ca, Sr, Ba and P). Extracted from Ref. [21].

The design of Spintronic devices requires the synthesis of these mixed valence manganites in the form of thin films grown on a particular substrate, while improving or at least preserving their bulk properties. The best results are usually obtained in the case of epitaxial growth on single crystal substrates, where there is direct relationship between the crystal orientations of the substrate and the film. Unfortunately, it is common that some of their physical properties are deteriorated. For instance, the saturation magnetization (M_S), conductivity (σ) and magnetic/electric transition temperature (T_C/T_{MI}) are often lower in films than in their bulk counterparts [22–25]. In addition to other growth parameters such as temperature, atmosphere, growth rate or annealing, the substrate structure and particularly the substrate/film interface plane is one of the main constraints that determines the degradation, improvement or even the onset of new physical properties in high-quality epitaxial thin film, since it plays an important role in the resulting crystalline structure of the film. In the epitaxial growth on single crystal substrates, the lattice mismatch (e.g., the difference between the substrate and manganite lattice constant) can induce a deformation of the crystal lattice of the film, either producing a uniform biaxial strain (for small lattice mismatch) or leading to the appearance of misfit dislocations to release the epitaxial strain (for large lattice mismatch). Great efforts have been focused on the investigation of effect of the substrate-induced strain on the physical properties of the manganite thin films by numerous experimental and theoretical works [4,22–36]. Regarding the local study of magnetization distributions, in the last decade several works have been reported using advanced nanocharacterization techniques. Among them LM and EH were used to investigate the magnetic microstructure of manganites taking advantage their high spatial resolution to visualize "simple" phenomena as magnetic domain configurations or understand "complex" phenomena as the phase separation which is responsible for the CMR [37–47].

In this work, we have exploited the high spatial resolution of EH to locally investigate the substrate-induced strain effects in the magnetic properties of $La_{2/3}Ca_{1/3}MnO_3$ (LCMO) thin films grown in three different (100)-oriented substrates: $SrTiO_3$ (STO), $(LaAlO_3)_{0.29}$-$(Sr_{0.5}Al_{0.5}TaO_3)_{0.71}$ (LSAT) and $LaAlO_3$ (LAO). As

LCMO films order ferromagnetically at T_C ~ 180 K, EH experiments were carried out at low temperature (100 K)..

6.2. Experimental details

The growth of epitaxial LCMO thin films was carried out by Lorena Marín at the Thin Film Growth Laboratory of INA. LCMO films with thicknesses between 43 and 60 nm were grown by Pulse Laser Deposition (PLD) on (100)-oriented LSAT, STO and LAO substrates using a KrF excimer laser (λ = 248 nm), with high oxygen pressure of 400 mTorr and a substrate temperature of 820 °C. After deposition, full oxygen pressure of 700 Torr was used during the cooling process to ensure the correct oxygen stoichiometry of the films. Different batches of LCMO films were grown varying the pulse frequency (2, 10 and 20 Hz), and with/without annealing the sample at 1000 °C to evaluate their influence on the magnetic properties.

X-ray diffraction (XRD) studies were performed using a Bruker HRXRD diffractometer belonging to the INA. θ-2θ diffraction patterns taken around the (002) reflection of the substrate were acquired to determine the crystallinity and the out-of-plane lattice parameter of the films. Magnetization measurements were performed at the *Servicio de Medidas Magnéticas* of the University of Zaragoza in a Superconducting Quantum Interference Device (SQUID) from Quantum Design, applying magnetic fields up to 5 T. For Zero-Field-Cooling (ZFC) and Field-Cooling (FC) experiments, the samples were cooled at a rate of 1 K/min down to 10 K. Once the temperature is stabilized, hysteresis cycles were carried out by sweeping the magnetic field between -50 to 50 kOe, applying the magnetic field parallel to the film surface. FC ramps were realized fixing a magnetic field of 100, 1000 or 1500 Oe during the cooling process from the room temperature paramagnetic state of LCMO. Both x-ray diffraction studies and magnetization measurements were also carried out by Lorena Marín.

For TEM experiments, thin lamellae of representative LCMO films were extracted by FIB in the FEI Helios Nanolab 650 DualBeam of the LMA. Local structural and chemical characterization was performed by STEM combining high angle annular dark field (HAADF) and EELS techniques in a probe-corrected FEI Titan 60-300 microscope operated at 300 kV. This microscope is equipped with a high brightness gun (XFEG), a Wien filter monochromator, a CETCOR probe corrector and a Gatan Tridiem 866 ERS spectrometer/image filter. The relative deformations of the film with respect to the substrate along (100) and (001) directions were determined on HAADF-STEM images by Geometry Phase Analysis (GPA) [48,49]. Imaging of the local magnetic state of the LCMO films was carried out by EH experiments at low temperature (100 K) using a single-tilt liquid nitrogen TEM cryo-holder in the FEI Titan Cube 60-300 microscope of the LMA, also operated at 300 kV.

Experimental results were correlated with first-principles calculations in collaboration with Dr. Remi Arras (CEMES-CNRS) based on the Density Functional Theory + *U* (DFT + *U*) method. We used the full-potential linearized augmented plane wave code Wien2K [50] with the Perdew-Burke-Ernzerhof parametrization of the Generalized Gradient Approximation (GGA-PBE) [51]. The fully-localized and rotationally invariant U_{eff} dependent ($U_{eff} = U - J$) correction [52,53] was applied on the 3*d* orbitals of Mn atoms and 4*f* orbitals of La atoms, with the respective values of U_{eff}(Mn, 3d) = 2 eV and U_{eff}(La, 4*f*) = 7 eV. We used a $2\sqrt{2} \times 2\sqrt{2} \times 2\sqrt{2}$ supercell containing 16 formula units of $La_{0.375}Ca_{0.625}MnO_3$. We chose a distribution of La and Ca cations leading to the space group 6-*Pm* (according to the Bilbao crystallographic server [54]). Calculations were performed fixing the in-plane lattice parameter to two values 3.8 Å and 3.9 Å close to the experimental lattice parameters of LAO (3.791 Å) and STO (3.905 Å), respectively, and a series of calculations were carried out for different out-of-plane lattice parameters. Four magnetic orderings have been envisaged as proposed by Colizzi *et al*. in a similar study on LSMO [55]: FM, and A_x-type, A_z-type and C-type AFM. In each case, we performed a full relaxation of internal atomic coordinates. The irreducible part of the first Brillouin zone was sampled with 8 *k*-points. A_x- and C-type AFM ordering correspond to in-plane AFM ordering,

respectively along the [100] and [110] directions; A_z-type AFM ordering modeled is oriented along the out-of-plane [001] direction.

6.3. Structural properties of LCMO thin films

The XRD study of the (002) reflection shown in Figure 6.2 gives a first view of the structural properties of a first batch of LCMO thin films grown by PLD on (100)-oriented STO, LSAT and LAO substrates, with a pulse frequency of 10 Hz. The presence of a single LCMO peak with clearly defined Laue oscillations evidences the very good crystalline quality of the films. As the θ-2θ XRD scans were performed in the plane of the sample, the positions of the peaks determine the out-of-plane lattice parameter (c) of each crystalline phase (substrate and film). This lattice parameter can be determined thanks to the Bragg's law [56] through the following equation:

$$c = \frac{\lambda}{\sin(\theta_{002}/2)} \qquad \text{(Eq. 6.1)}$$

where λ and θ_{002} are the wavelength of the incident x-ray beam, in our case, λ(Cu k_α) = 1.541 Å, and the angle of incidence corresponding to the (002) reflection plane, respectively. Thus, the different peak positions of the LCMO film reveal a variation of the out-of-plane lattice parameter, c_{LCMO}, as a function of the substrate. Compared with the bulk LCMO c_{LCMO} value (c = 3.867 Å), we find that c_{LCMO} hardly changes when LCMO grows in LSAT because the lattice mismatch is very small (+0.05%), while it is elongated and compressed when LCMO is grown in LAO and STO, respectively (see reported values in Figure 6.2).

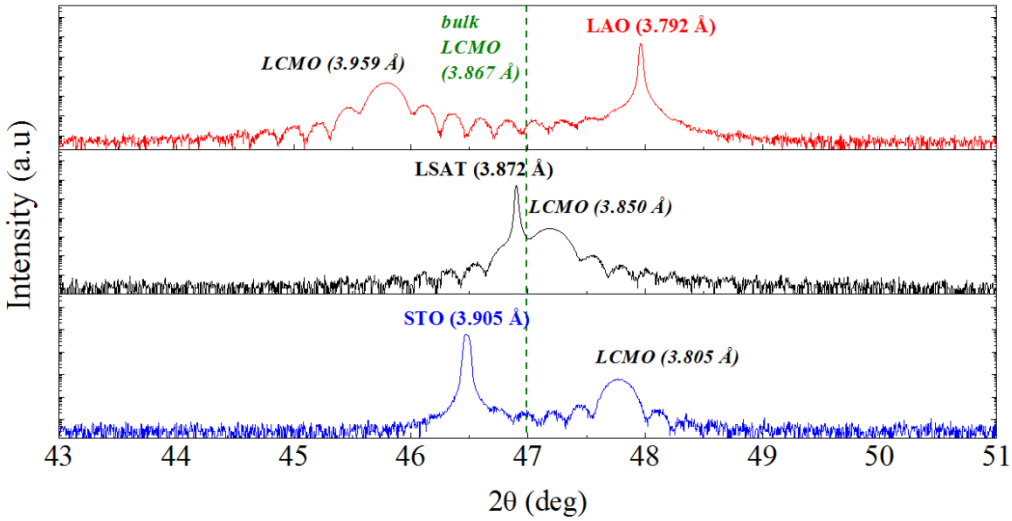

Figure 6.2. XRD patterns around the (002) reflection of epitaxial LCMO thin films grown on (*top*) LAO, (*center*) LSAT and (*bottom*) STO substrates. In front of each label, the calculated out-of-plane lattice parameter is presented.

Detailed local information about the crystal deformation of the LCMO films were extracted by applying GPA to HAADF-STEM images, as depicted in Figure 6.3. This method allows mapping the 2D strain fields of the LCMO films, that describe the local lattice deformations along the (100) and (001) directions, corresponding to the in-plane (a_{LCMO}) and out-of- plane (c_{LCMO}) lattice parameters, respectively, taking as reference the lattice parameters of the substrate. Thus, the relative strain (in %) for a_{LCMO} (ε_{xx}) and c_{LCMO} (ε_{zz}) is calculated as [48,49]

$$\varepsilon_{xx} = 100 \times \frac{(a_{LCMO} - a_{subs})}{a_{subs}} \qquad \text{(Eq. 6.2)}$$

$$\varepsilon_{zz} = 100 \times \frac{(c_{LCMO} - c_{subs})}{c_{subs}} \qquad \text{(Eq. 6.3)}$$

where subscript "*subs*" refers to the substrate lattice parameters. Making a qualitative description of the strain maps around the substrate/LCMO interfaces, we note that ε_{xx}

and ε_{zz} for LSAT/LCMO system are almost uniform across the film/substrate interface (see Figures 6.3(b), (c), (e) and (h)), while a sharp jump is observed just at the interface in the ε_{zz} strain field in the other STO and LAO cases. The color codes indicate a negative deformation (compressive) of the LCMO film (relative to the substrate out-of-plane lattice parameter) in the STO/LCMO system, and a positive one (tensile) in the LAO/LCMO system (see Figures 6.3(f) and (i), respectively). Furthermore, a particular discontinuous color variation in a punctual region inside the LCMO film is observed in the ε_{xx} strain field of the LAO/LCMO system. A zoom of the STEM image around this region, as well as a Bragg filtered image for the (100) planes, reveals that such discontinuity is associated to an edge on dislocation where one atomic plane along 001 direction disappears above the defect (see Figure 6.4).

The continuous ε_{xx} strain fields around the substrate/LCMO interfaces for the 3 systems indicate that the film grows epitaxial and fully strained, adapting its in-plane lattice parameter with that of the substrate. Lines profiles traced perpendicular to the substrate/LCMO interfaces show in Figure 6.5 that ε_{xx} is negligible along the whole film thickness in the LSAT/LCMO and STO/LCMO systems. In the case of LAO/LCMO system, a line profile traced far to the dislocation shows that a_{LCMO} remains fully strained (ε_{xx} = 0.05 ± 0.05 %) for the initial 34 nm of film near the substrate, and then it is relaxed to a value of 0.6 %, close to the surface of the film (see Figure 6.5(c)). Across the dislocation we found that a_{LCMO} remains strained below the crystal defect (ε_{xx} = 0.05 ± 0.05 %), while ε_{xx} abruptly increases up to a mean value of 0.7 ± 0.1 % above the dislocation, indicating that the defect causes the rapid relaxation of a_{LCMO} (see Figure 6.5(d)).

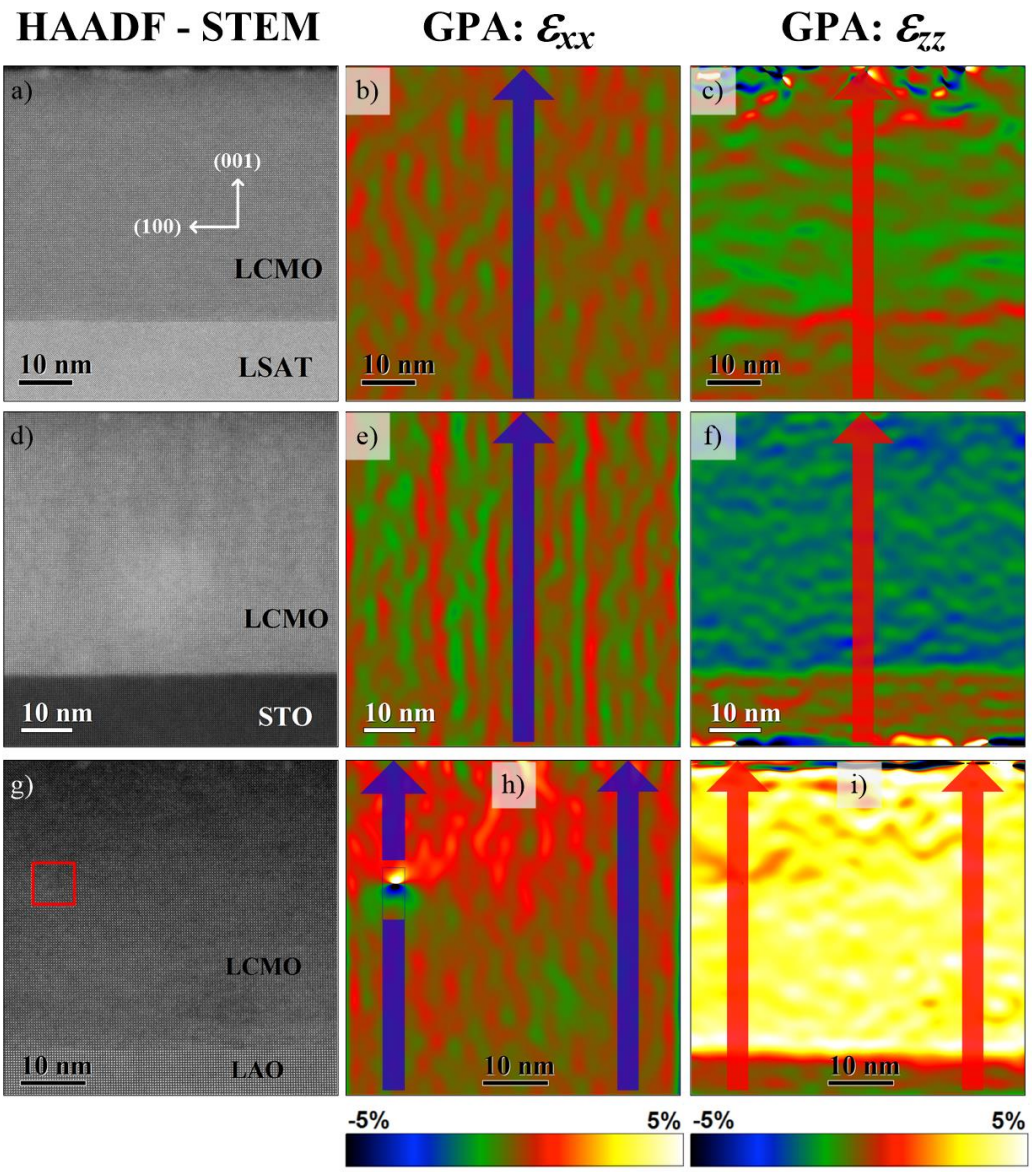

Figure 6.3. (*Left column*) HAADF-STEM images of as-grown LCMO films on (a) LSAT, (d) STO and (g) LAO substrates. Next to each STEM image, strain color maps obtained by GPA for (*center*) in-plane (ε_{xx}) and (*right side*) out-of-plane (ε_{zz}) deformations.

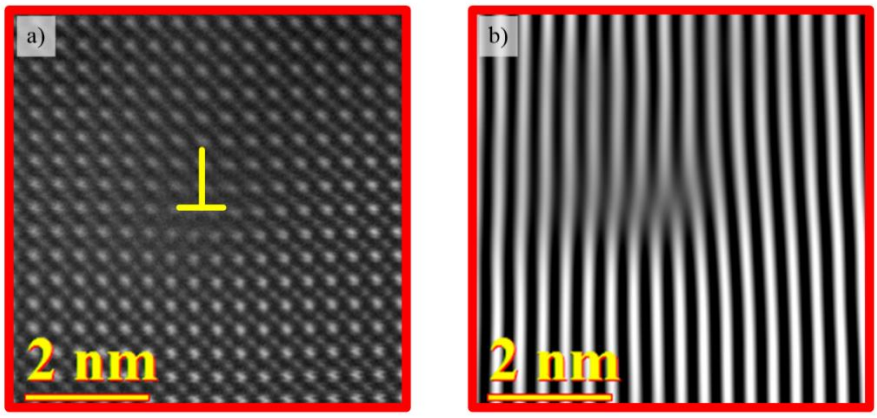

Figure 6.4. (a) A filtered zoom of the HAADF-STEM image around the dislocation (red box in the Figure 6.3 (g)). (b) Filtered Bragg image of the (100) reflection reconstructed from (a).

On the other hand, the abrupt change at the substrate/LCMO interface observed in the ε_{zz} strain fields evidences that the LCMO films grow with an out-of-plane lattice parameter significantly different to the substrate, being $\varepsilon_{zz} < 0$ ($c_{LCMO} < c_{subs}$) in the LCMO film grown on STO and $\varepsilon_{zz} > 0$ ($c_{LCMO} > c_{subs}$) in the LCMO film grown on LAO, similarly to that found in the XRD spectra of Figure 6.2. Within the experimental error, lines profiles plotted in Figure 6.5 show that ε_{zz} seems to be constant throughout all thickness when the film is fully strained (LCMO on STO, and on LAO far to the dislocation), with mean values of ε_{zz} = -1.7 ± 0.2% and +3.5 ± 0.7% for LCMO films grown in STO and LAO, respectively. These mean relative strains of c_{LCMO} are however considerably lower than those calculated through XRD patterns (for LCMO film on STO: -2.53 ± 0.05 %; for LCMO film on LAO: +4.40 ± 0.02 %). These discrepancies could be associated to different factors such a strain relaxation at the surface of the thin TEM specimen or different sample drift when the beam irradiates the film (conductor) and the substrate (insulator) [57,58]. In the case of LSAT/LCMO system, a visual inspection of the ε_{zz} strain field (Figure 6.3 (c)) indicates that c_{LCMO} is very close to c_{LSAT}. However, the line profile plotted in Figure 6.5 (a) shows that c_{LCMO} is slightly compressed, with a mean value of ε_{zz} = -0.6 ± 0.2 %, which is similar to that calculated through XRD pattern (ε_{zz} = -0.56 ± 0.07 %).

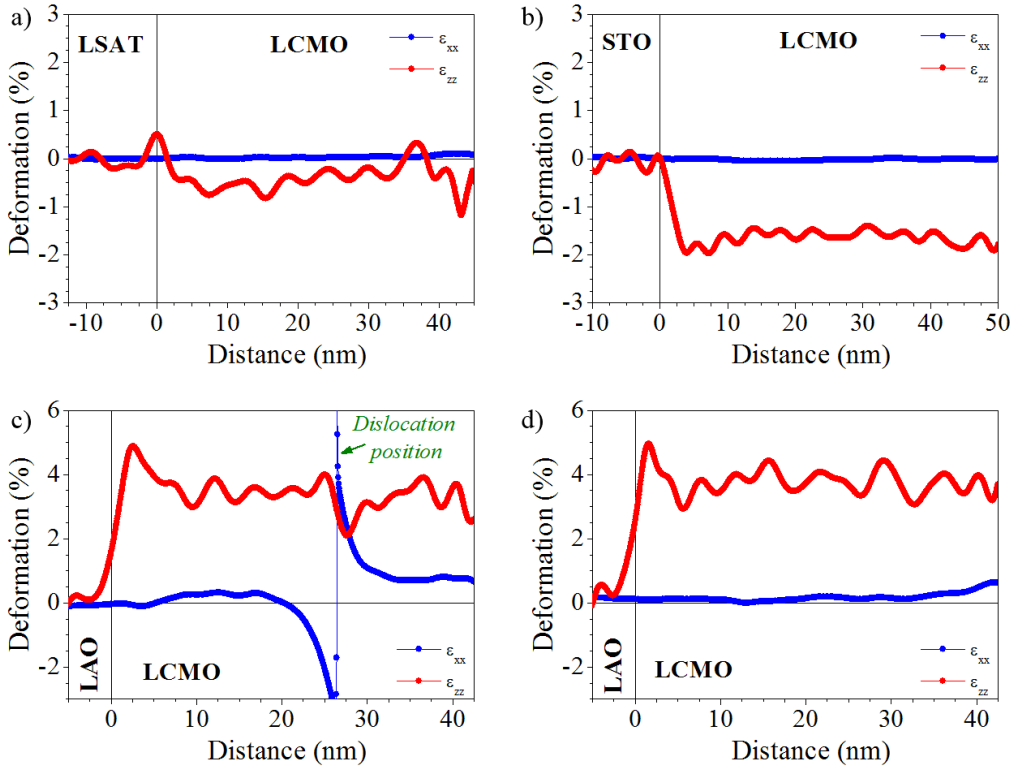

Figure 6.5. Lines profiles of the strain color maps for the (a) LSAT/LCMO, (b) STO/LCMO, and LAO/LCMO (c) across and (d) far to the crystal dislocation traced perpendicular to the substrate/LCMO interface. Red and blue lines correspond to the relative deformation along the (001) and (100) directions, respectively. The profiles for LSAT/LCMO and STO/LCMO have been obtained by the integration of 500 pixels along the substrate plane direction, while for LAO/LCMO they have been obtained by integration of 100 pixels.

The local structural results obtained by GPA therefore reveal the strained LCMO films present a typical substrate-induced biaxial strain [25,59], where a_{LCMO} tends to adapt to that of the substrate while c_{LCMO} is deformed depending on the type of strain suffered by a_{LCMO}, roughly following the Poisson's effect [60,61]: a tensile strain in a_{LCMO} induces a compressive strain in c_{LCMO} (LCMO on STO substrate), while a compressive strain in a_{LCMO} induces a tensile strain in c_{LCMO} (LCMO on LAO substrate). A schematic illustration of the type of crystal distortions induced by the substrates is shown in Figure 6.6. Such biaxial strain is uniform throughout whole

thickness of LCMO film grown on STO, while the formation of crystal dislocation at intermediate thickness of the LCMO film grown on LAO allows the partial relaxation of the crystal structure above the defect.

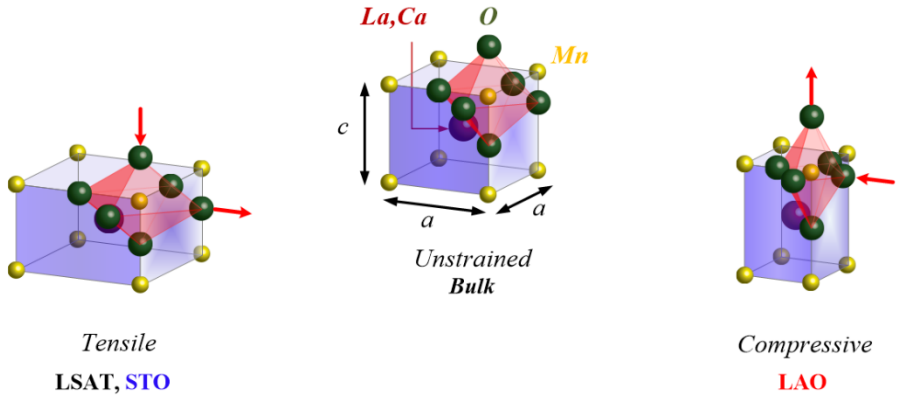

Figure 6.6. Sketch of the type of crystal distortions induced by the different substrates.

Considering that a_{LCMO} is equal to a_{subs}, the induced in-plane strain in the LCMO film can be directly estimated by the calculation of the lattice mismatch between the bulk LCMO (a_{LCMO}(bulk) = 3.867 Å) and the substrate (a_{STO} = 3.905 Å, a_{LSAT} = 3.868 Å, and a_{LAO} = 0.3792 Å), define as

$$f_{subs} = 100 \times \frac{(a_{subs} - a_{LCMO(bulk)})}{a_{subs}} \qquad \text{(Eq. 6.4)}$$

where subscript "subs" is referred to the lattice parameters of the substrate. Thus, we have that the STO substrate induces a tensile strain of f_{STO} = +0.93 %, the LAO substrate a compressive strain of f_{LAO} = -2.01 %, and LSAT a very weak tensile strain of f_{LSAT} = +0.03 % on the in-plane lattice parameter of LCMO film. The high lattice mismatch of LCMO with LAO, which is a factor by 2 respect to that produced by STO substrate, makes that the LCMO film cannot grow fully strained, forming misfit dislocations at an intermediate thickness of between 18-33 nm to relax the strain, as evidenced from the GPA images of ε_{xx} strain fields calculated from HAADF-STEM

images recorded in different positions along the TEM lamella, see Figure 6.7. This results is in a good agreement with those previously reported in LCMO thin films grown on LAO, where reciprocal space mapping reveals structural relaxation and mosaicity when increasing the thickness [62–65]. As we will see later, the strain relaxation induced by these dislocations at the intermediate thickness of the LCMO film produces an exotic magnetic state at remanence.

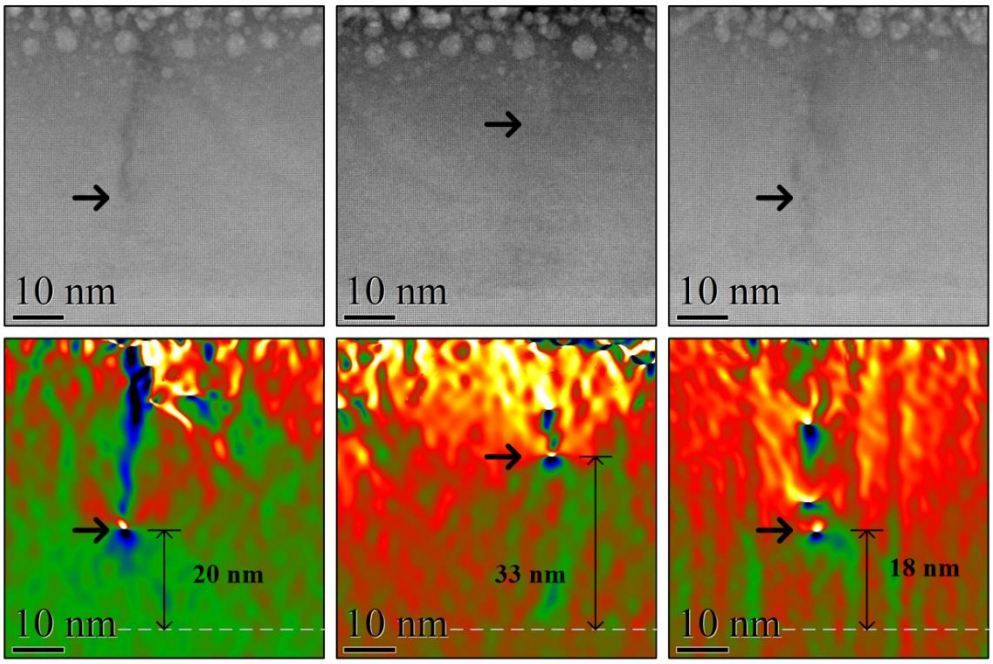

Figure 6.7. (*Up*) HAADF-STEM images taken in different regions of the LCMO thin film grown on LAO. (*Down*) Below each STEM image, GPA color maps obtained for the in-plane (ε_{xx}) strain reveal the position of the misfit dislocations (red arrows).

6.4. Strain effect dependence of the magnetic properties of LCMO thin films

An interesting correlation between the crystal distortion and the magnetism in the LCMO films is found after analyzing low-temperature magnetization hysteresis loops measured along the [100] direction at 10 K (see Figure 6.8). While the virtually

unstrained LCMO film grown on LSAT presents a high saturation magnetization, close to that measured in the polycrystalline bulk LCMO used as target (M_s = 650 emu/cm^3), the strained LCMO films grown on STO and LAO substrates exhibit reduced values of saturation magnetization of M_s = 440 and 175 emu/cm^3, respectively (see Figure 6.8(a) and (c)).

The tetragonality of the LCMO film is defined as

$$\tau = \frac{\left|c_{LCMO} - a_{LCMO}\right|}{a_{LCMO}}, \qquad \text{(Eq. 6.5)}$$

so the values calculated it for each system are τ = 0.005 (LSAT/LCMO), τ = 0.025 (STO/LCMO) and τ = 0.044 (LAO/LCMO). We observe that the saturation magnetization is reduced when the tetragonality increases. This tendency is similar to what has been previously observed in other ferromagnetic manganite thin films, where large lattice mismatch (e.g., induction of large tetragonal distortion) produces a suppression of the saturation magnetization [24]. An opposite relation is observed between the coercivity and the tetragonality where H_c increases with the tetragonality: H_c = 109 Oe (LSAT/LCMO), H_c = 433 Oe (STO/LCMO) and H_c = 507 Oe (LAO/LCMO). Besides having a reduced M_s and a high H_c, LCMO films grown on LAO substrate present a very small remanent field and a progressive magnetic reversal process, following the typical shape of a hysteresis loop measured along an unfavorable magnetization direction. This behavior has been previously reported in LCMO films grown on LAO [62,64,66–68], where the compressive substrate-induced strain modifies the magnetocrystalline anisotropy to produce the easy magnetization direction perpendicular to the film plane. However, a magnetization hysteresis loop performed along [001] direction (perpendicular to the film plane) showed a similar behavior to that observed in the [100] direction indicating that, in our LCMO film grown on LAO, the perpendicular direction is also an unfavorable magnetization direction, see Figure 6.8(e).

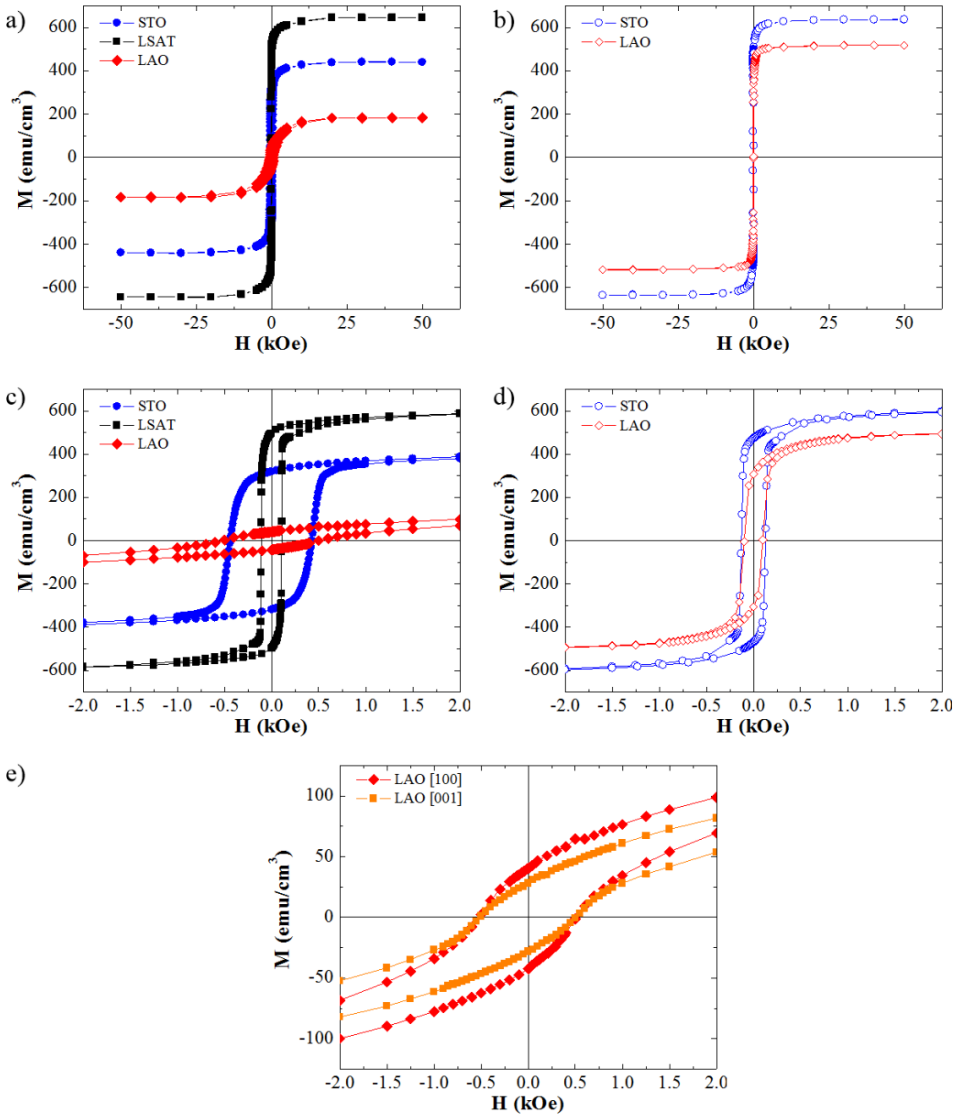

Figure 6.8. (a) and (c) Magnetization hysteresis loops along the [100] direction for the first batch of samples early characterized by XDR spectra and GPA method. (b) and (d) Magnetization hysteresis loops along the [100] direction for the second batch of samples where the magnetic properties were optimized by adjusting the laser frequency during the growth process (in STO), or annealing the sample after the growth (in LAO). (c) and (d) Zooms of the hysteresis cycles of (a) and (b), respectively. (e) Comparative plot between magnetization hysteresis loops along the [100] and [001] for the LAO/LCMO system belonging to the first batch of samples.

The previous analysis suggests that both the reduction of M_s and the increase of H_c are caused by the substrate-induced strain of the LCMO films. However, we have found that such magnetic parameters can be optimized either by tuning one of the growth parameters (laser frequency, temperature, oxygen pressure) or performing an annealing treatment after the film growth. For instance, we have found that reducing the pulse frequency from 10 to 2 Hz leads to grow a LCMO film on STO with M_s = 635 emu/cm^3 and H_c = 127 Oe, very similar to those obtained in the unstrained LCMO film, as shown in the hysteresis loops of LCMO/STO system plotted in Figures 6.8(b) and (d). In the case of strained LCMO films grown on LAO, an annealing treatment at 1000 °C for 5 hours allowed increasing M_s up to 517 emu/cm^3, which is almost three times higher than the value measured before the thermal treatment, and reducing H_c down to 99 Oe. XRD patterns obtained around the (002) reflection for the second batch of samples show that both optimization processes allowed obtaining strained LCMO films with a lower tetragonal distortion.

This effect can be directly visualized in Figure 6.9, where XRD spectra for the first and second batch of samples are plotted together. If we consider as a rough approximation that $a_{LCMO} = a_{subs} = c_{subs}$, the lower the tetragonality, the smaller the distance between the two peak positions of the spectrum. In this second batch of the sample, the LCMO tetragonality is reduced down to 0.020 (on STO) and 0.022 (on LAO). The annealing process in the LCMO film grown in LAO also modifies the shape of the hysteresis cycle, becoming more similar to those grown on STO or LSAT. These results therefore confirm how the magnetic parameters of the film are strongly affected by the distortion of the LCMO lattice. A reduction of the tetragonality by growing films with out-of-plane lattice parameters closer to those of unstrained films leads to a magnetic behavior approaching to that of bulk or unstrained LCMO.

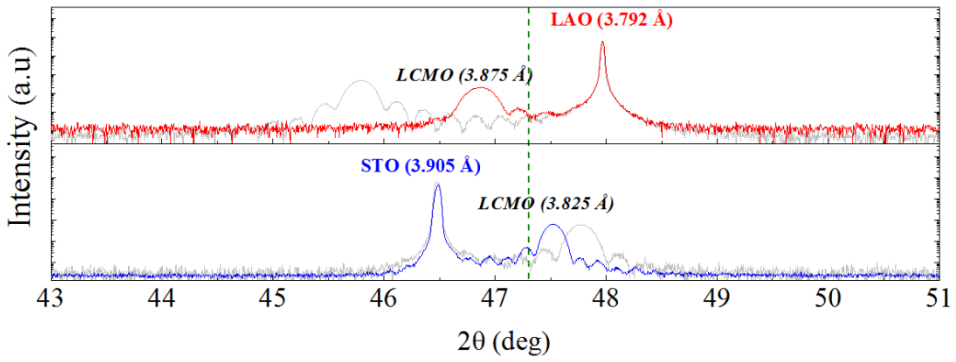

Figure 6.9. XRD patterns for the second batch of STO/LCMO and LAO/LCMO systems (red and blue lines) after annealing. Gray lines are XRD patterns of the first batch of samples plotted in Figure 6.2 and the vertical dashed line marks the value corresponding to the bulk LCMO lattice parameter.

To perform a more detailed analysis of the influence of the tetragonality in M_s and H_c, we have grown a large number of LCMO thin films where the tetragonality was modulated by using different substrates (LSAT, STO and LAO), slightly tuning the growth conditions and/or annealing the samples up to 1000 °C. Plots of M_s and H_c as a function of τ displayed in the Figure 6.10 summarize the strain-induced effect on the magnetic properties of LCMO films. We observe that for tetragonality values below a certain critical value of $\tau_c \sim 0.024$, the saturation magnetization remains close to the bulk value. Above τ_c, the magnetization decreases sharply reaching values down to 190 emu/cm^3 for $\tau = 0.049$ (in LAO substrates). Around τ_c, the tetragonality variation is mainly produced by the variation of c_{LCMO} in LCMO films grown on STO, where the saturation magnetization suffers a dramatic reduction within a small range of τ, from 657 Oe ($\tau = 0.022$) to 392 Oe ($\tau = 0.027$). Large tetragonality is found in the LCMO films grown on LAO and produces very low values of M_s, between 264 and 190 emu/cm^3. The coercive field dependence of the tetragonality follows an opposite behavior, where low coercive field values between 25 and 130 Oe are found at $\tau < \tau_c$. Above τ_c, the coercivity suddenly increase up value between 430 and 550 Oe.

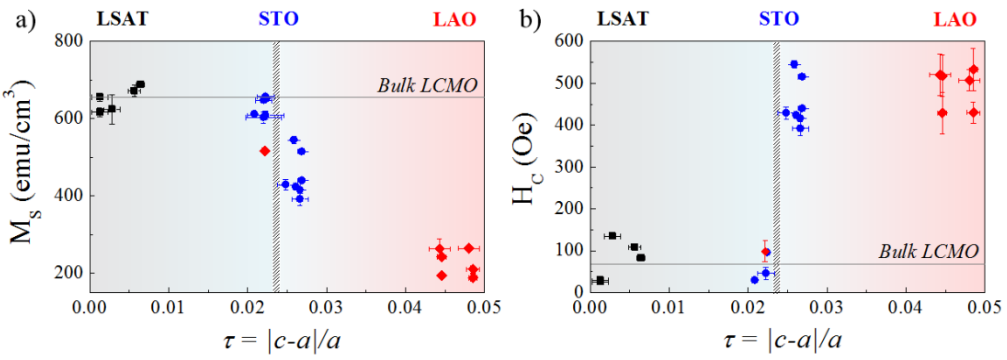

Figure 6.10. Plots of the (a) saturation magnetization and (b) coercive field as a function of the tetragonality for different batches of LCMO films on LSAT (black squares), STO (blue circles) and LAO (red diamonds).

Thus, the macroscopic magnetic characterization of strained LCMO films reveals a critical value of tetragonality where M_s and H_c abruptly change. Below τ_c, the magnetic properties are hardly modified by the tetragonality, exhibiting similar values to the bulk LCMO. Above τ_c, the films are magnetically harder (high H_c) and the magnetization is strongly depressed. Even though a high lattice mismatch contributes to the degradation of the magnetic properties, we have found that they can be improved by the optimization of the growth conditions (laser frequency and/or annealing treatment) to obtain an epitaxial tetragonal structure with $\tau < \tau_c$. However, macroscopic characterization does not permit understanding the origin of the anomalous behavior of the magnetic properties as a function of the tetragonality. For this reason, we have studied the substrate-induced strain effect on the magnetic properties of LCMO thin film by low temperature EH. As we will see next, EH gives the key evidence of the microscopic origin of this phenomenology.

6.5. Direct visualization of the remanent state of LCMO thin films

For the local study of the remanent magnetic states of strained LCMO films by EH experiments at low temperature, we have chosen three sets of representative samples:

1) High-tetragonality LCMO films, where $\tau > \tau_c$. These samples are strained LCMO films grown on STO and LAO belonging to the first batch of samples.

2) Low-tetragonality LCMO films, where $\tau < \tau_c$. The samples of this second batch are strained LCMO films grown on STO and LAO belonging to the second batch of samples.

3) The last samples are pseudocubic unstrained LCMO film, where $\tau \rightarrow 0$, grown on LSAT.

EH images of the electron wave amplitude, magnetic phase shift (φ_{MAG}) and magnetic flux (**B**) for the unstrained LCMO film grown on LSAT are shown in Figure 6.11(a), whereas high-tetragonality LCMO films are displayed in Figure 6.11(b) (on STO) and Figure 6.12 (on LAO). Magnetic phase shift images inside the LCMO films grown on LSAT and STO present a color gradient (e.g., phase shift gradient) perpendicular to the substrate/LCMO interface, see φ_{MAG} image of Figures 6.11(a) and (b). According to Equation 2.37 of *Chapter 2*, a perpendicular phase shift gradient indicates that the magnetization is oriented parallel to the interface, along the [100] direction. This is confirmed by the magnetic flux images plotted in the right side of Figures 6.11(a) and (b), which represent the cosines of 11 times the magnetic phase shift ($\cos(n\varphi_{MAG})$). At remanence, this magnetization orientation is favored by the magnetocrystalline anisotropy of the film with the easy axis oriented along the (100) direction and the shape anisotropy induced by the geometry of the TEM lamella that tend to align the magnetization parallel to the interface along the plane of the specimen. Lines profiles traced in the magnetic phase shift images perpendicular to the substrate/LCMO interface reveal an anomalous magnetization distribution in the

high-tetragonality LCMO film grown on STO: we note that the first 30 nm of the film near the substrate exhibits a strong lineal variation of φ_{MAG}, while the next 29 nm in thickness presents a very weak φ_{MAG} variation, see plot of Figure 6.11(d). In agreement with the magnetic flux image of Figure 6.11(c), this phase shift variation indicates that the film only present a clear ferromagnetic phase in a sub-layer of about 30 nm next to the substrate/LCMO interface, while the surface layer is not ferromagnetic. This is not the case in the unstrained LCMO film, where such strong lineal variation of φ_{MAG} occurs along the whole thickness of the film, see plot of Figure 6.11(b). Consequently the magnetic flux image of the unstrained LCMO shown in Figure 6.11(a) corresponds to a fully magnetized film.

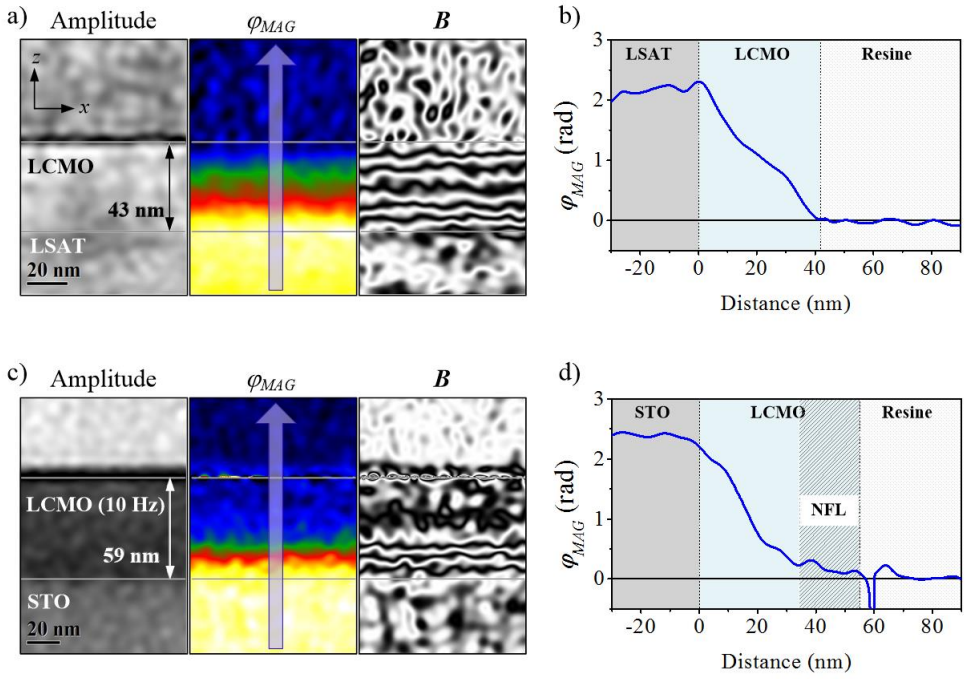

Figure 6.11. *Left*. Amplitude, magnetic phase shift (φ_{MAG}) and magnetic flux (**B**) images of the remanent state of (a) unstrained and (c) high-tetragonality LCMO films grown on LSAT and STO, respectively. *Right*. Lines profiles traced on φ_{MAG} (blue arrows) for (b) unstrained LCMO on LSAT and (d) highly tetragonal LCMO on STO.

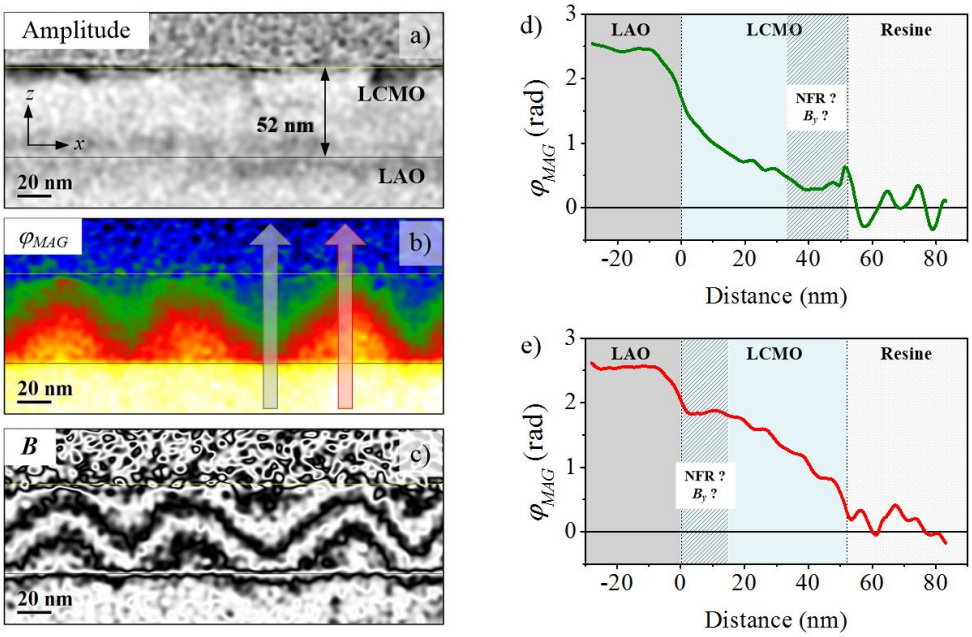

Figure 6.12. (a) Amplitude, (b) magnetic phase shift (φ_{MAG}) and (c) magnetic flux (**B**) images of the remanent state for a high-tetragonality LCMO film grown on LAO. (d) and (e) Line profiles traced on φ_{MAG} (blue and green arrows).

On the other hand, EH images in the high-tetragonality LCMO film grown on LAO show a complex remanent magnetic configuration. The transversal orientation of the phase shift gradient as well as the magnetic flux image reveal a zigzag shape configuration of the magnetization. Similar to high-tetragonality LCMO film grown on STO, perpendicular lines profiles traced in the magnetic phase shift image across the valleys and peaks of the zigzag allow detecting small regions close to either the substrate/LCMO or surface of the film with very weak, or no phase shift gradient (see green and red lines profiles plotted in Figure 6.12). Thus, these areas do not present a clear ferromagnetic response.

Summarizing the most relevant results obtained by low temperature EH experiments on high-tetragonality LCMO films, we have found:

a) The formation of non-ferromagnetic layer (NFL) in the surface of the LCMO film grown on STO and apparent non-ferromagnetic regions (NFRs) both in the surface and substrate/LCMO interface of the LCMO film grown on LAO.

b) A zigzag shaped remanent magnetic state in the LCMO film grown on LAO, where the magnetization is tilted almost 45° out to the plane of the film.

Thus, the local exploration of the magnetism in high-tetragonality LCMO film gives us the key information to understand the anomalous behavior observed in the macroscopic measurements. The existence of a NFL inside the high-tetragonality LCMO film explains the depression of the saturation magnetization detected in the low-temperature magnetization hysteresis cycles of Figure 6.8(a). Such hysteresis cycle is normalized to the total volume of the film, both ferromagnetic and non-ferromagnetic regions, so the value of M_s of the ferromagnetic sublayer is underestimated. The same analysis is not straightforward in the LCMO film grown on LAO, as the complex magnetization configuration prevents a clear interpretation of the formation of NFR. Magnetic domains oriented parallel to the electron beam, i.e. with a unique magnetic component along the *y*-axis (B_y), could also causes such apparent non-ferromagnetic state. Such magnetization orientation is however unlikely, as both the shape anisotropy and the tendency of magnetocrystalline anisotropy in compressively strained LCMO to favor easy magnetization axis pointing out of the substrate plane impose the magnetization to lie in the plane which corresponds to the image plane. On the other hand, as supposed previously, the zigzag remanent magnetization configuration in the high-tetragonality LCMO film grown on LAO explains why neither [100] nor [001] direction presented a hysteresis loop shape similar to that could be obtained along an easy axis direction, revealing that the compressive strain induces an magnetocrystalline anisotropy out-of-the plane of the surface film, probably with easy axes along the [101] and [10-1] directions.

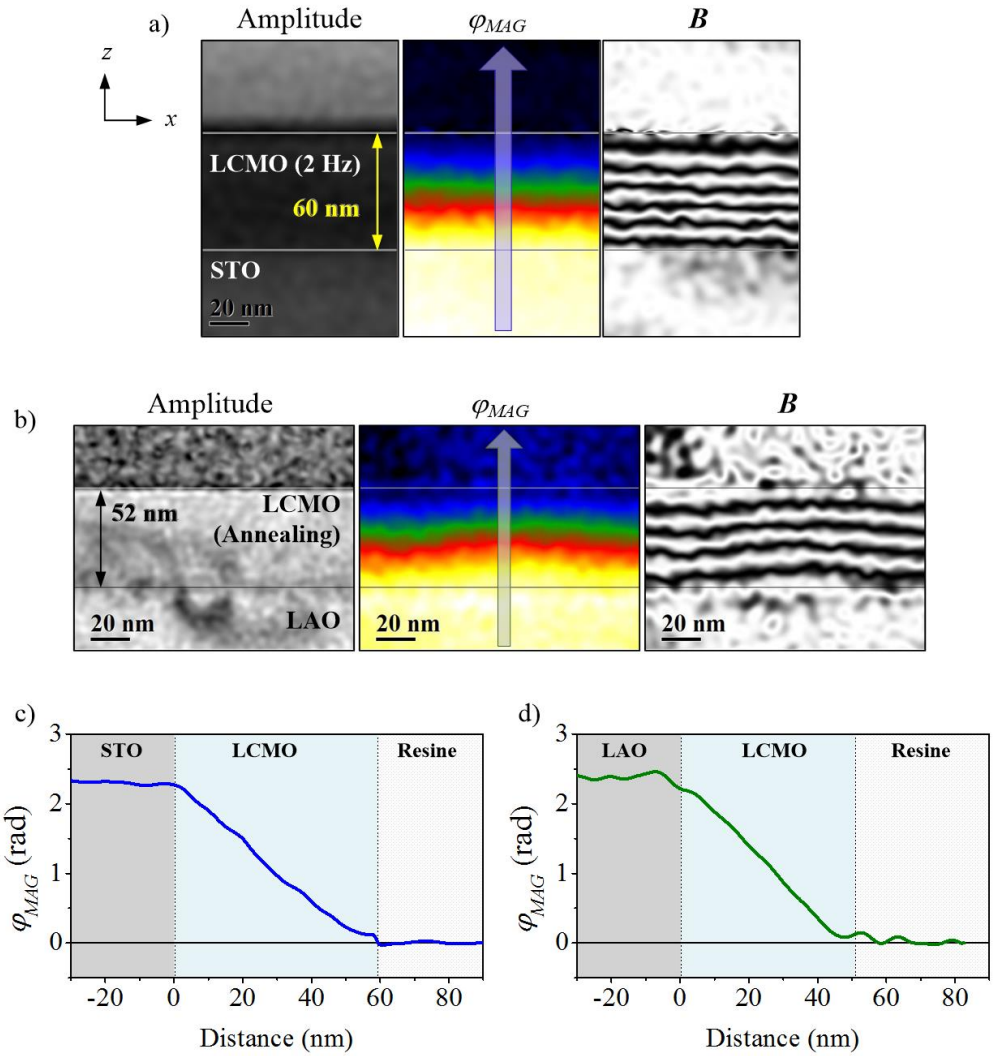

Figure 6.13. Amplitude, magnetic phase shift (φ_{MAG}) and magnetic flux (**B**) images of the remanent state for low-tetragonality LCMO film grown on (a) STO and (b) LAO. (c) and (d) are plots of line profiles traced on φ_{MAG} along the blue and green arrows, respectively.

These exotic behaviors found in high-tetragonality films have not been observed in low-tetragonality LCMO films grown on STO and LAO after fine-tuning the growth conditions to recover a bulk-like magnetic behavior. As we see in EH image displayed in Figure 6.13, the magnetization configuration of both LCMO films are very similar to that found in the unstrained LCMO film. Magnetic phase line profiles

and magnetic flux images reveal that the films are fully ferromagnetic, with the magnetization oriented parallel to the substrate/LCMO interface. In the case of low-tetragonality LCMO films grown on LAO, GPA studies of a HAADF-STEM image of this film demonstrate that the annealing treatment causes the complete relaxation of the LCMO crystal structure (see Figure 6.14). In the recrystallization process induced by the annealing, the misfit dislocations migrate toward the substrate/LCMO interface to release the epitaxial strain of the whole LCMO film. Plots of line profiles traced from the ε_{xx} and ε_{zz} strain fields of the annealed sample in Figure 6.14(d) show that beyond the first 2 nm of the film next to the substrate, the lattice parameter of the LCMO film is similar to that the bulk LCMO. This clearly indicates that the annealing induces the relaxation of the biaxial compressive strain and that LCMO recovers its pseudocubic structure.

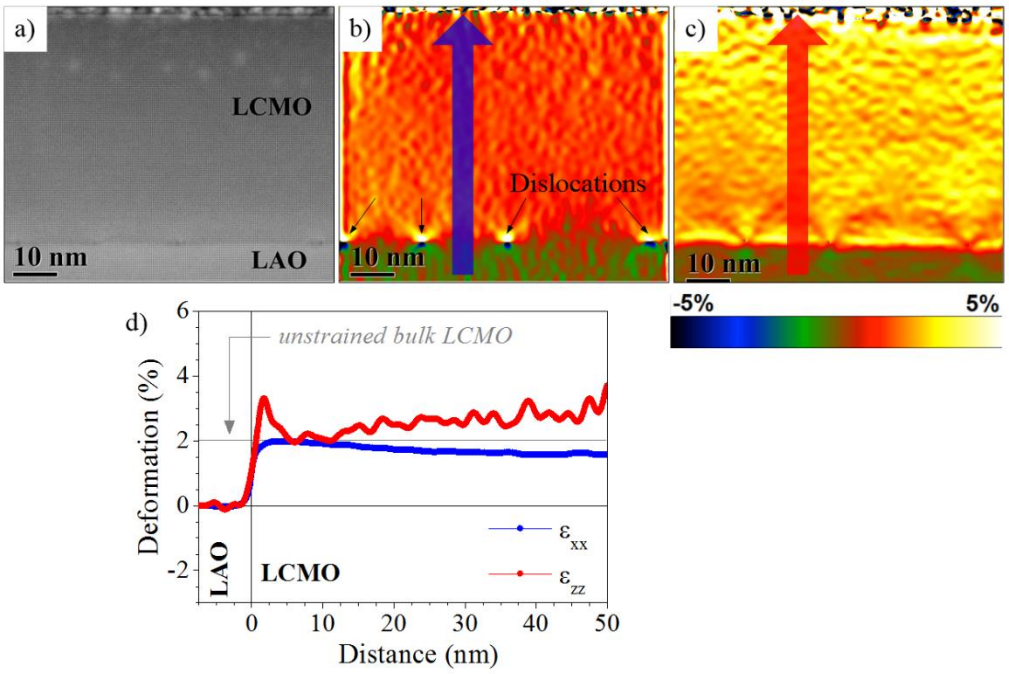

Figure 6.14. (a) HAADF-STEM images of the low-tetragonality LCMO film grown on LAO (annealed film). Strain maps obtained by GPA for (b) in-plane (ε_{xx}) and (c) out-of-plane (ε_{zz}) deformations. (d) Plots of line profiles traced perpendicular to the substrate/LCMO interface on the strain maps.

EH experiments reveal that the substrate-induced strain produces a magnetic phase separation, where a ferromagnetic phase and a non-ferromagnetic phase coexist. The nature of the NFL in LCMO, commonly referred as magnetically dead layer, has been widely discussed in previous work [68–80]. Unfortunately, EH does not provide further information about the magnetic nature of the NFL. For this reason, additional characterization was performed to understand the type of magnetic phase and its origin.

6.6. Origin of the non-ferromagnetic layer

The phenomenology associated with this loss of ferromagnetism could have different origins, some of them are of *chemical nature* such as oxygen vacancies that expand the lattice unit cell volume [78], Mn valence instabilities at the surface of LCMO grown on LAO due to the formation of Mn^{2+} by air exposure [68], cation segregation [74,75] or interface chemical diffusion [76]. The evaluation of the chemical composition and the local Mn oxidation state were done by careful spectroscopic analysis by STEM-EELS experiments on the high-tetragonality LCMO film grown on STO presenting the NFL in order to detect possible chemical inhomogeneities or differences in the chemical composition between the ferromagnetic and non-ferromagnetic sublayers. Figure 6.15(a) depicts a profile of the relative compositions in La, Ca, Mn and O obtained along a direction perpendicular to the substrate/LCMO interface. These chemical line profiles were obtained from spectrum lines collected with an energy dispersion of 0.5 eV, an acquisition time of 0.1 s, a collection angle of 60 mrads, a beam current of ~ 350 pA and calculated following the standard procedure of background subtraction and intensity integration implemented in the DigitalMicrograph™ software package. Within the experimental accuracy of the technique, we determine that there is not significant change of composition along the film thickness. The discrepancy in the absolute quantification of the different elements is related to the presence of plural scattering and non-optimal signal-to-background ratio in the spectra due to the relatively large thickness (50-60

nm) of the EH specimens. Additional tests performed in thinner specimens (*not shown here*) gives a stoichiometry close to the nominal.

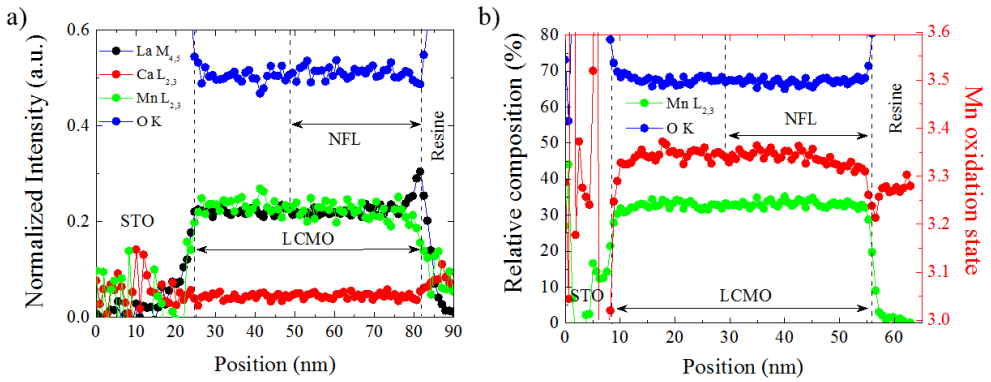

Figure 6.15. (a) Chemical profile determined from STEM-EELS spectrum lines of the high-tetragonality LCMO film grown on STO substrate. (b) Line profiles of the Mn oxidation estimated from the O K edge acquired from STEM-EELS spectrum lines in the same sample.

On the other hand, Mn oxidation state has been determined in spectrum lines at a dispersion of 0.1 eV, an acquisition time of 1 s, a collection angle of 47 mrad and a beam current of ~ 250 pA. The procedure developed by Varela *et. al.* for the $La_xCa_{1-x}MnO_3$ has been followed [81], based on the energy difference between the main peak and the pre-peak of the O K edge, which is related to the hybridization of Mn and O orbitals. A change in the Mn oxidation state would be the signature of lack of stoichiometry of the sample due to either the presence of oxygen vacancies or deficiency of some of the metallic cations. Figure 6.15(b) shows a comparison of the estimated Mn oxidation state with the relative composition of Mn and O extracted from the O K and the Mn $L_{2,3}$ edges from the same spectrum line. Similar to the composition profiles, the oxidation state is very uniform along the whole layer. Moreover, the coincidence of the estimated oxidation state and the nominal one is remarkably good, with a value of +3.34 ± 0.01, where the error bar is the standard deviation upon integration of the value along the whole layer. Thus, this is a strong indication that not only the chemical composition is uniform along the layer, but also the whole stoichiometry is very close to nominal, confirming that the discrepancy in

the quantification of the composition of the Figure 6.15(a) is due to artifacts related to specimen thickness.

The ferromagnetic ordering could also be suppressed by structural modifications related to the film growth modifying the magnetic ordering. Tiny perturbations caused by biaxial strain may break the degeneracy of Mn 3*d* e_g and t_{2g} orbitals due to the tetragonal distortion [82,83]. This orbital reconstruction causes a selective orbital occupancy that suppresses the ferromagnetic order (FM). Furthermore, symmetry breaking at the surface leads to the weakening or suppression of double exchange interaction, which would favor an antiferromagnetic (AFM) ordering at the surface as demonstrated in different theoretical works [84,85]. Inspired by these predictions, macroscopic magnetic measurements were carried out to detect a possible AFM state of the NFL. An indirect method to elucidate this is to perform hysteresis cycles at low temperature (10 K), after ZFC and FC processes in order to detect the existence of exchange bias effect due to exchange coupling between the FM and AFM layers [86,87]. ZFC and FC hysteresis cycles for the unstrained LCMO film grown on LSAT, low-tetragonality LCMO film grown on STO and high-tetragonality LCMO films grown on STO and LAO substrates are displayed in Figure 6.16. As expected, the ZFC and FC hysteresis loops for unstrained and low-tetragonality films do not show any significant difference, contrary to that found in the high-tetragonality films where both FC hysteresis cycles present a remarkable shift toward negative fields. This behavior is typically found in FM-AFM bilayers that are exchange coupled after field cooling through the Néel temperature of the AFM layer. For our LCMO films, this antiferromagnetic phase that produces exchange bias fields of 35 Oe (high-tetragonality LCMO film on STO) and 122 Oe (high-tetragonality LCMO film on LAO) would be the NFL (or NFR in the LCMO film grown on LAO) detected by EH. Furthermore, the increase of H_c agrees with the presence of an AFM layer that is exchange-coupled with the FM layer, see Figure 6.8(c).

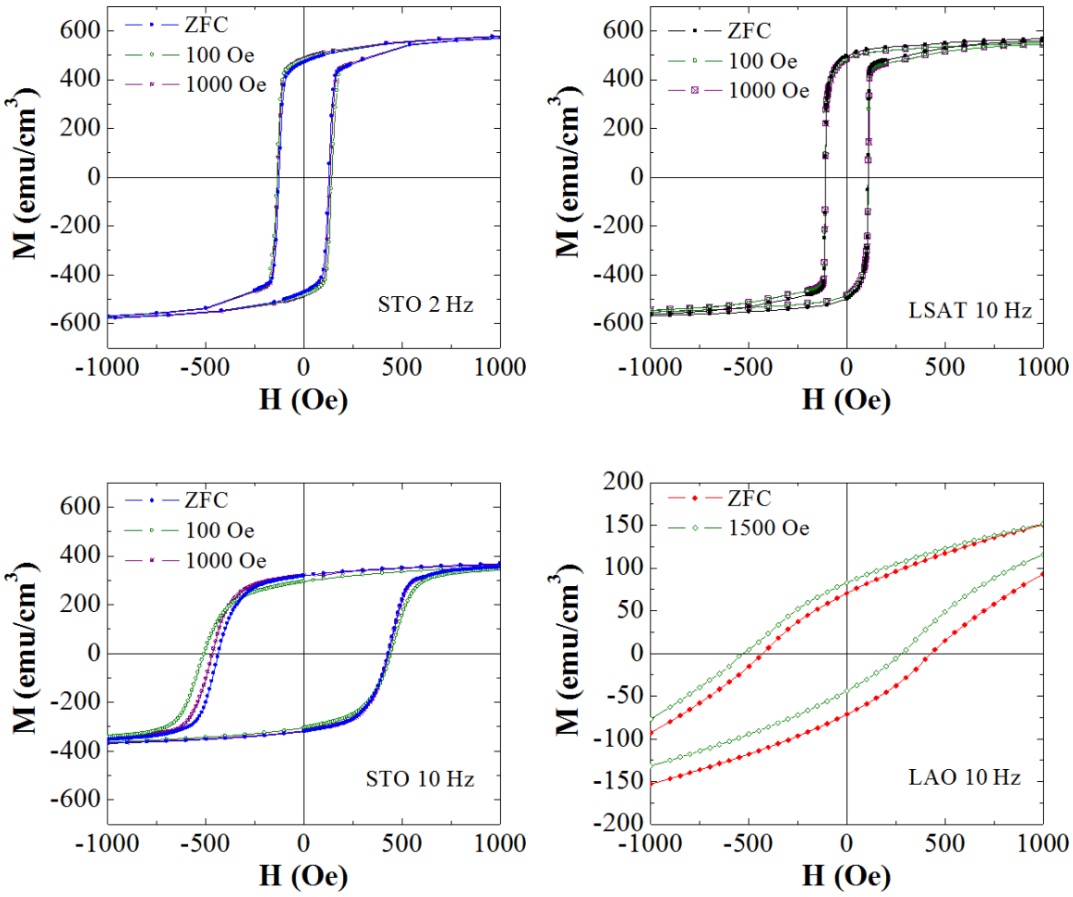

Figure 6.16. ZFC and FC magnetization hysteresis cycles at 10 K of: (a) highly tetragonal LCMO grown on STO (at 10 Hz), (b) unstrained LCMO on LSAT (at 10 Hz), (c) low-tetragonality LCMO on STO (at 2 Hz). The set of samples at 10 Hz were grown simultaneously.

The strain induced crystal distortion itself can be the physical mechanism that explains, for instance, the segregation of a top AFM layer in the high-tetragonality LCMO film grown on STO. This deformation can induce tilts and distortions of the MnO_6 octahedral, modifying the Mn-O bond distance and the Mn-O-Mn angles [88]. This structural modifications cause radical changes in the magnetic and transport properties in manganites. Theoretical and experimental results predict that a coupling between the orbital ordering of the e_g states and the Jahn-Teller distortions of the

MnO_6 octahedron lead to a magnetic transition from a FM state in unstrained films to a C-type antiferromagnetic state (C-AFM) at large compressive strains or an A-type antiferromagnetic state (A-AFM) under large tensile strains [82]. Other physical mechanism is an orbital glass insulator [59,89], insomuch as the exchange bias effect indicates a coupling between phases with different spin orders and different interactions could be considered [87].

To get a deeper insight on the origin of FM and AFM orders in strained LCMO films, DFT+*U* calculations were performed on LCMO structures with an in-plane lattice parameter determined by STO (a = 3.9 Å) and LAO substrates (a = 3.8 Å) as a function of the out-of-plane lattice parameter for 4 magnetic ordering as proposed by Colizzi *et al*. in LSMO [55]. According to these calculations, whose results are plotted in Figure 6.17, for $\tau = 0$ the FM ordering is always the most stable, independently of the in-plane lattice parameter. For a = 3.9 Å, the *c* axis is reduced by the in-plane tensile strain and our calculations predict a magnetic transition from a FM to an A_z-AFM ordering for $\tau > 0.06$. Between $\tau = 0$ and $\tau = 0.025$, the energy of both FM and A_z-AFM states increase but the energy difference between the two ordering is reduced by approximately 40%. For $\tau = 0.025$, the experimental critical value of tetragonality defined in Figure 6.10, the energy difference is then 37.9 meV/f.u., and only 6.3 meV/f.u. if τ increase up to 0.05. Thus, such small energy differences suggest that the coexistence of the two ordering is possible considering the thermal energy and additional local perturbations not taken into account in the present calculations. As already discussed, these perturbations can result from the presence of a free top surface and an interface with the substrate, or small deviations from the nominal stoichiometry undetected by our experimental techniques. Eventually it becomes clearer for $\tau \sim 0.06$, where a crossover take place after which the AFM ordering is favored energetically.

On the other hand, for $a = 3.8$ Å, equivalent to the in-plane compressive strained induced by LAO, the ferromagnetic ordering remains the most stable for tetragonality values as high as 0.125. Above $\tau = 0.075$, the total energy difference between the FM

and the A_x-AFM ordering is lower than 11.6 meV/f.u., which also suggests that both phase can also coexist. Our results also confirm that such tendencies are accompanied by a change in the e_g-bands occupation due to the tetragonal distortion, favoring the occupation of the dx^2-y^2 bands for $c/a < 1$, with an increase by 12.5% of the d-e_g orbitals averaged occupation to the detriment of the $d3z^2$-r^2 bands (for $\tau = 0.1$) and the reverse for $c/a > 1$. It is worth noting that, for a lattice parameter ratio $c/a > 1$, the transition is generally considered in the literature to occur between FM and C-type AFM ordering, whereas our calculations suggests that the A_x-AFM ordering is the most stable. This is however in agreement with the results of Colizzi *et al*. [55], who also found a strong competition between these three orderings in LSMO. A direct comparison with previous works on the other manganites is however complicated for several reasons. The different magnetic transitions certainly depend closely on atomic structure distortions (i.e. oxygen octahedral tilts) which can be affected by the nature and the distribution of the cations on the A position of the perovskites. The calculation parameters used for GGA+U methods can also result in slight quantitative differences compared to the experimental measurements [90]. Supposing that the suitable c/a ratio can be obtained, the coexistence of FM and AFM phases is plausible for sufficiently high tetragonality for both c/a <1 or > 1 and may be observed experimentally for both a = 3.8 Å and 3.9 Å, as indeed we have evidenced in this study. The tetragonality at which one of these transition will appear can be non-universal and would also certainly depend on the lattice mismatch with the substrate.

Our findings evidence both experimental and theoretically that the substrate-induced strain effect in chemically homogeneous LCMO film can produce two type of spatially separated magnetic orderings, where the non-ferromagnetic regions present an AFM ordering. We also see that, even though the evidence of NFR of AFM nature is not straightforward from the EH results in the high-tetragonality LCMO grown on LAO, both FC hysteresis loop and theoretical calculation point to their existence.

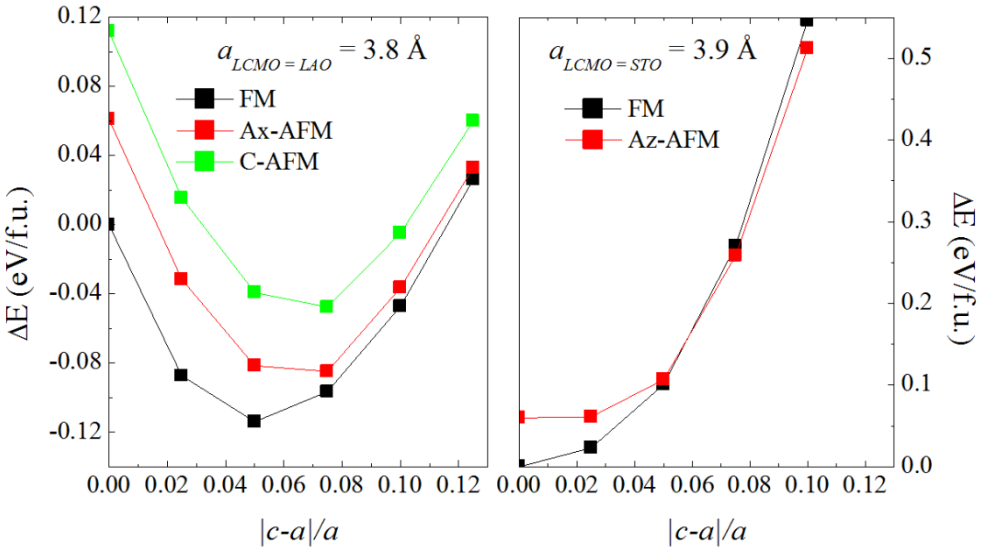

Figure 6.17. Energy variation of the FM and A_z-AFM orders in LCMO as a function of the tetragonality for an in-plane lattice parameter fixed by (a) LAO and (b) STO substrates.

6.7 Conclusions

This work evidences the potential of EH combined with the use of a TEM cryo-holder cooled with liquid nitrogen to probe magnetism at low temperatures. This has enabled us to explore locally the effect of the substrate-induced strain on the magnetic properties of epitaxial LCMO thin films with T_C well below room temperature. With this study, we take a step forward in the understanding of the origin of some of exotic physical phenomena that give manganites their unique properties.

EH experiments at low temperature demonstrated that the high-tetragonality distortion of the LCMO films, resulting from the epitaxial strain induced by the substrate, gives rise to two important changes in the magnetic properties of LCMO: (1) a magnetic phase separation upon tensile strain where both ferromagnetic and antiferromagnetic orders coexist, and (2) a magnetocrystalline anisotropy variation for a compressively stressed film. The first phenomenon was clearly detected in strained

LCMO films grown on STO substrates showing a superficial NFL. The second magnetic change was observed in strained LCMO films grown on LAO substrate, where the compressive strain led to complex remanent state where the magnetization followed a zigzag-shape structure oscillating along the [101] and [10-1] directions intermixed with what appears to be NFRs.

The origin of the NFL was exhaustively studied by using additional characterization techniques. A local chemical analysis by STEM-EELS showed that the high-tetragonality LCMO film grown on STO presented a homogeneous chemical composition throughout the thickness of the film. This result allowed us discarding that the NFL has an origin of *chemical nature* (oxygen vacancies, cation segregation, Mn valence instabilities or interface chemical diffusion). However, structural analysis and theoretical calculation of first principles showed that the crystal deformation may cause the segregation of the surface NFL. For high degree of strain, the crystal distortion produces an orbital reconstruction where a ferromagnetic ordering is suppressed and an antiferromagnetic ordering can emerge. An antiferromagnetic state in the NFL also explained the apparent reduction of the saturation magnetization, the high values of coercive fields and the observation of exchange bias.

The anomalous magnetic properties of strained LCMO film could be however recovered by either tuning the growth conditions (for instance, reducing the deposition frequency) or performing an annealing treatment. Both procedures allowed growing strained LCMO film with a lower tetragonality distortion and recovered saturation magnetization. These results demonstrate once more that, firstly, the magnetic changes are associated to the degree of strain of the film and, secondly, it is possible to engineer such phenomena with smart growth conditions.

Reference

[1] Coey J M D, Viret M and von Molnár S 1999 Mixed-valence manganites *Adv. Phys.* **48** 167–293

[2] Gorkov L and Kresin V 2004 Mixed-valence manganites: fundamentals and main properties *Phys. Rep.* **400** 149–208

[3] Tokura Y and Tomioka Y 1999 Colossal magnetoresistive manganites *J. Magn. Magn. Mater.* **200** 1–23

[4] Prellier W, Lecoeur P and Mercey B 2001 Colossal-magnetoresistive manganite thin films *J. Phys. Condens. Matter* **13** R915–R944

[5] Haghiri-Gosnet A-M and Renard J 2003 CMR manganites: physics, thin films and devices *J. Phys. D. Appl. Phys.* **36** R127–R150

[6] Chatterji T 2004 *Colossal Magnetoresistive Manganites* (Dordrecht: Springer Netherlands)

[7] Van den Brink J, Khaliullin G and Khomskii D 1999 Charge and Orbital Order in Half-Doped Manganites *Phys. Rev. Lett.* **83** 5118–21

[8] Tomioka Y, Okuda T, Okimoto Y, Asamitsu A, Kuwahara H and Tokura Y 2001 Charge/orbital ordering in perovskite manganites *J. Alloys Compd.* **326** 27–35

[9] Yamauchi K and Picozzi S 2013 Mechanism of Ferroelectricity in Half-Doped Manganites with Pseudocubic and Bilayer Structure *J. Phys. Soc. Japan* **82** 113703

[10] Efremov D V, Brink J van den and Khomskii D I 2003 Charge order versus Zener polarons: ferroelectricity in manganites *arXiv:cond-mat/0306651*

[11] Goto T, Kimura T, Lawes G, Ramirez A P and Tokura Y 2004 Ferroelectricity and Giant Magnetocapacitance in Perovskite Rare-Earth Manganites *Phys. Rev. Lett.* **92** 257201

[12] Dörr K 2006 Ferromagnetic manganites: spin-polarized conduction versus competing interactions *J. Phys. D. Appl. Phys.* **39** R125–R150

[13] Bibes M and Barthelemy A 2007 Oxide Spintronics *IEEE Trans. Electron Devices* **54** 1003–23

[14] Chopdekar R, Arenholz E and Suzuki Y 2009 Orientation and thickness dependence of magnetization at the interfaces of highly spin-polarized manganite thin films *Phys. Rev. B* **79** 104417

[15] Cibert J, Bobo J-F and Lüders U 2005 Development of new materials for spintronics *Comptes Rendus Phys.* **6** 977–96

[16] Volkov N V 2012 Spintronics: manganite-based magnetic tunnel structures *Physics-Uspekhi* **55** 250–69

[17] Shu Z, Dong J and Xing D 2001 Phase diagram of half-doped manganites *Phys. Rev. B* **63** 224409

[18] Dunaevskii S M 2004 Magnetic phase diagrams of manganites in the electron doping region *Phys. Solid State* **46** 193–212

[19] Mochizuki M and Furukawa N 2009 Microscopic model and phase diagrams of the multiferroic perovskite manganites *Phys. Rev. B* **80** 134416

[20] Siwach P K, Singh H K and Srivastava O N 2008 Low field magnetotransport in manganites. *J. Phys. Condens. Matter* **20** 273201

[21] Thomas R M, Ranno L and Coey J M D 1997 Transport properties of ($Sm_{0.7}A_{0.3}MnO_3$) ($A=Ca^{2+},Sr^{2+},Ba^{2+},Pb^{2+}$) *J. Appl. Phys.* **81** 5763

[22] Tsui F, Smoak M C, Nath T K and Eom C B 2000 Strain-dependent magnetic phase diagram of epitaxial $La_{0.67}Sr_{0.33}MnO_3$ thin films *Appl. Phys. Lett.* **76** 2421

[23] Lu Y, Klein J, Herbstritt F, Philipp J, Marx A and Gross R 2006 Effect of strain and tetragonal lattice distortions in doped perovskite manganites *Phys. Rev. B* **73** 184406

[24] Adamo C, Ke X, Wang H Q, Xin H L, Heeg T, Hawley M E, Zander W, Schubert J, Schiffer P, Muller D A, Maritato L and Schlom D G 2009 Effect of biaxial strain on the electrical and magnetic properties of (001) $La_{0.7}Sr_{0.3}MnO_3$ thin films *Appl. Phys. Lett.* **95** 112504

[25] Helali S, Daoudi K, Fouzri A, Oumezzine M, Oueslati M and Tsuchiya T 2012 Effects of substrate-induced-strain on the structural and transport properties of $La_{0.7}Ca_{0.3}MnO_3$ thin films *Appl. Phys. A* **108** 379–84

[26] Koo T Y, Park S H, Lee K-B and Jeong Y H 1997 Anisotropic strains and magnetoresistance of $La_{0.7}Ca_{0.3}MnO_3$ *Appl. Phys. Lett.* **71** 977

[27] Suzuki Y, Hwang H Y, Cheong S-W and van Dover R B 1997 The role of strain in magnetic anisotropy of manganite thin films *Appl. Phys. Lett.* **71** 140

[28] Ju H L, Krishnan K M and Lederman D 1998 Evolution of strain-dependent transport properties in ultrathin $La_{0.67}Sr_{0.33}MnO_3$ films *J. Appl. Phys.* **83** 7073

[29] Paranjape M, Raychaudhuri A, Mathur N and Blamire M 2003 Effect of strain on the electrical conduction in epitaxial films of $La_{0.7}Ca_{0.3}MnO_3$ *Phys. Rev. B* **67** 214415

[30] Souza-Neto N M, Ramos A Y, Tolentino H C N, Favre-Nicolin E and Ranno L 2004 Local effects in strained manganite thin films *J. Alloys Compd.* **369** 205–8

[31] SouzaNeto N M, Ramos a. Y, Tolentino H C N, FavreNicolin E and Ranno L 2005 Local Structure in Strained Manganite thin Films *Phys. Scr.* **589** 589

[32] Souza-Neto N M, Ramos A Y and Tolentino H C N 2005 Strain effect on the tilt angle in manganite thin films *Nucl. Instruments Methods Phys. Res. Sect. B Beam Interact. with Mater. Atoms* **238** 259–63

[33] Dhakal T, Tosado J and Biswas A 2007 Effect of strain and electric field on the electronic soft matter in manganite thin films *Phys. Rev. B* **75** 092404

[34] Baena A, Brey L and Calderón M J 2011 Effect of strain on the orbital and magnetic ordering of manganite thin films and their interface with an insulator *Phys. Rev. B* **83** 064424

[35] Demidov V V., Borisenko I V., Klimov A A, Ovsyannikov G A, Petrzhik A M and Nikitov S A 2011 Magnetic anisotropy of strained epitaxial manganite films *J. Exp. Theor. Phys.* **112** 825–32

[36] Ranno L, Llobet A, Tiron R and Favre-Nicolin E 2002 Strain-induced magnetic anisotropy in epitaxial manganite films *Appl. Surf. Sci.* **188** 170–5

[37] Mori S 2002 Observation of magnetic domain structure in phase-separated manganites by Lorentz electron microscopy *J. Electron Microsc. (Tokyo).* **51** 225–9

[38] Murakami Y, Yoo J H, Shindo D, Atou T and Kikuchi M 2003 Magnetization distribution in the mixed-phase state of hole-doped manganites. *Nature* **423** 965–8

[39] Loudon J, Mathur N . and Midgley P . 2004 Direct evidence of phase coexistence in La0.5Ca0.5MnO3 *J. Magn. Magn. Mater.* **272-276** 13–4

[40] He J, Asaka T, Volkov V, Chaudhuri S, Budhani R and Zhu Y 2007 Ferromagnetic Domains and Phase Separation in $La_{5/8-y}PryCa_{3/8}MnO_3$ Manganites: Observations by Lorentz Electron Microscopy *Microsc. Microanal.* **13** 2002–3

[41] Mori S, Horibe Y, Asaka T, Matsui Y, Chen C H and Cheong S W 2007 Nanoscale ferromagnetism in phase-separated manganites *J. Magn. Magn. Mater.* **310** 870–2

[42] Asaka T, Mori S, Horibe Y, Takenaka K, Ishizuka K, Kimoto K and Matsui Y 2007 Observation of magnetic domain structures in *J. Magn. Magn. Mater.* **310** 782–4

[43] He J Q, Volkov V V., Asaka T, Chaudhuri S, Budhani R C and Zhu Y 2010 Competing two-phase coexistence in doped manganites: Direct observations by in situ Lorentz electron microscopy *Phys. Rev. B* **82** 224404

[44] He J Q, Volkov V V, Beleggia M, Asaka T, Tao J, Schofield M a. and Zhu Y 2010 Ferromagnetic domain structures and spin configurations measured in doped manganite *Phys. Rev. B* **81** 094427

[45] Mamishin S, Kasai H, Xia W, Murakami Y, Shindo D, Mori S and Tonomura A 2010 Lorentz Microscopy Study on Magnetization Reversal Process in Single-Domain State in Perovskite-Type Manganite *Jpn. J. Appl. Phys.* **49** 063003

[46] Nagai T, Nagao M, Kurashima K, Asaka T, Zhang W and Kimoto K 2012 Formation of nanoscale magnetic bubbles in ferromagnetic insulating manganite $La_{7/8}Sr_{1/8}MnO_3$ *Appl. Phys. Lett.* **101** 162401

[47] Horibe Y, Mori S, Asaka T, Matsui Y, Sharma P a., Koo T Y, Guha S, Chen C H and Cheong S-W 2012 Preformed nanoscale ferromagnetism in manganites *EPL Europhysics Lett.* **100** 67007

[48] Hÿtch M J 1997 Geometric phase analysis of high resolution electron microscope images *Scanning Microsc.* **11** 53–66

[49] Hÿtch M J, Snoeck E and Kilaas R 1998 Quantitative measurement of displacement and strain fields from HREM micrographs *Ultramicroscopy* **74** 131–46

[50] Blaha P, Schwarz K, Madsen G, Kvasnicka D and Luitz J 2013 *WIEN2k: An Aufmented Plane Wave Plus Local Orbtails Program for Calculating Crystal Properties* vol 1

[51] Perdew J P, Burke K and Ernzerhof M 1996 Generalized Gradient Approximation Made Simple *Phys. Rev. Lett.* **77** 3865–8

[52] Anisimov V I, Solovyev I V and Korotin M A 1993 Density-functional theory and NiO photoemission spectra *Phys. Rev. B* **48** 16929–34

[53] Liechtenstein A I and Zaanen J 1995 Density-functional theory and strong interactions: Orbital ordering in Mott-Hubbard insulators *Phys. Rev. B* **52** R5467–R5470

[54] Aroyo M I, Kirov A, Capillas C, Perez-Mato J M and Wondratschek H 2006 Bilbao Crystallographic Server. II. Representations of crystallographic point groups and space groups. *Acta Crystallogr. A.* **62** 115–28

[55] Colizzi G, Filippetti A, Cossu F and Fiorentini V 2008 Interplay of strain and magnetism in $La_{1-x}Sr_xMnO_3$ from first principles *Phys. Rev. B* **78** 235122

[56] Bragg W H and Bragg L 1933 *The Crystalline State. Volume I: A General Survey* (London: London: Bell & Sons 1933)

[57] Lubk A, Javon E, Cherkashin N, Reboh S, Gatel C and Hÿtch M 2014 Dynamic scattering theory for dark-field electron holography of 3D strain fields. *Ultramicroscopy* **136** 42–9

[58] Javon E, Lubk A, Cours R, Reboh S, Cherkashin N, Houdellier F, Gatel C and Hÿtch M J 2014 Dynamical effects in strain measurements by dark-field electron holography. *Ultramicroscopy* **147C** 70–85

[59] Abad L, Laukhin V, Valencia S, Gaup A, Gudat W, Balcells L and Martínez B 2007 Interfacial Strain: The Driving Force for Selective Orbital Occupancy in Manganite Thin Films *Adv. Funct. Mater.* **17** 3918–25

[60] Greaves G N, Greer A L, Lakes R S and Rouxel T 2011 Poisson's ratio and modern materials. *Nat. Mater.* **10** 823–37

[61] Liu X, Pan D, Hong Y and Guo W 2014 Bending Poisson Effect in Two-Dimensional Crystals *Phys. Rev. Lett.* **112** 205502

[62] Lu C J, Wang Z L, Kwon C and Jia Q X 2000 Microstructure of epitaxial $La_{0.7}Ca_{0.3}MnO_3$ thin films grown on $LaAlO_3$ and $SrTiO_3$ *J. Appl. Phys.* **88** 4032

[63] Moskvin A S, Zenkov E V, Sukhorukov Y P, Mostovshchikova E V, Loshkareva N N, Kaul A R and Gorbenko O Y 2003 Nanoscale phase separation in $La_{0.7}Ca_{0.3}MnO_3$ films: evidence for texture-driven optical anisotropy *J. Phys. Condens. Matter* **15** 2635–43

[64] Valencia S, Balcells L, Martínez B and Fontcuberta J 2003 Thickness dependence of the magnetic anisotropy in $La_{2/3}Ca_{1/3}MnO_3$ thin films grown on $LaAlO_3$ substrates *J. Appl. Phys.* **93** 8059

[65] Estradé S, Arbiol J, Peiró F, Abad L, Laukhin V, Balcells L and Martínez B 2007 Cationic diffusion in $La_{2/3}Ca_{1/3}MnO_3$ thin films grown on $LaAlO_3$ (001) substrates *Appl. Phys. Lett.* **91** 252503

[66] Chang-Min X, Ji-Rong S, Deng-Jing W, Guan-Juan L, Hong-Wei Z and Bao-Gen S 2005 Dependence of the coercivity of $La_{0.67}Ca_{0.33}MnO_3$ films on substrate and thickness *Chinese Phys.* **14** 604–9

[67] Xiong C M, Sun J R and Shen B G 2005 Dependence of magnetic anisotropy of the $La_{0.67}Ca_{0.33}MnO_3$ films on substrate and film thickness *Solid State Commun.* **134** 465–9

[68] Valencia S, Gaupp a., Gudat W, Abad L, Balcells L, Cavallaro A, Martínez B and Palomares F 2006 Mn valence instability in $La_{2/3}Ca_{1/3}MnO_3$ thin films *Phys. Rev. B* **73** 104402

[69] Borges R P, Guichard W, Lunney J G, Coey J M D and Ott F 2001 Magnetic and electric "dead" layers in $(La_{0.7}Sr_{0.3})MnO_3$ thin films *J. Appl. Phys.* **89** 3868

[70] Perroni C, Cataudella V, De Filippis G, Iadonisi G, Marigliano Ramaglia V and Ventriglia F 2003 Modeling of strain effects in manganite films *Phys. Rev. B* **68** 224424

[71] Freeland J W, Kavich J J, Gray K E, Ozyuzer L, Zheng H, Mitchell J F, Warusawithana M P, Ryan P, Zhai X, Kodama R H and Eckstein J N 2007 Suppressed magnetization at the surfaces and interfaces of ferromagnetic metallic manganites. *J. Phys. Condens. Matter* **19** 315210

[72] Huijben M, Martin L W, Chu Y-H, Holcomb M B, Yu P, Rijnders G, Blank D H A and Ramesh R 2008 Critical thickness and orbital ordering in ultrathin $La_{0.7}Sr_{0.3}MnO_3$ films *Phys. Rev. B* **78** 094413

[73] Sun Y, Zhao Y, Tian H, Xiong C, Xie B, Zhu M, Park S, Wu W, Li J and Li Q 2008 Electric and magnetic modulation of fully strained dead layers in $La_{0.67}Sr_{0.33}MnO_3$ films *Phys. Rev. B* **78** 024412

[74] Song J H, Susaki T and Hwang H Y 2008 Enhanced Thermodynamic Stability of Epitaxial Oxide Thin Films *Adv. Mater.* **20** 2528–32

[75] Estradé S, Rebled J M, Arbiol J, Peiró F, Infante I C, Herranz G, Sánchez F, Fontcuberta J, Córdoba R, Mendis B G and Bleloch A L 2009 Effects of thickness on the cation segregation in epitaxial (001) and (110) $La_{2/3}Ca_{1/3}MnO_3$ thin films *Appl. Phys. Lett.* **95** 072507

[76] Kourkoutis L F, Song J H, Hwang H Y and Muller D A 2010 Microscopic origins for stabilizing room-temperature ferromagnetism in ultrathin manganite layers. *Proc. Natl. Acad. Sci. U. S. A.* **107** 11682–5

[77] Pesquera D, Herranz G, Barla A, Pellegrin E, Bondino F, Magnano E, Sánchez F and Fontcuberta J 2012 Surface symmetry-breaking and strain effects on orbital occupancy in transition metal perovskite epitaxial films. *Nat. Commun.* **3** 1189

[78] Schumacher D, Steffen A, Voigt J, Schubert J, Brückel T, Ambaye H and Lauter V 2013 Inducing exchange bias in $La_{0.67}Sr_{0.33}MnO_{3-\delta}/SrTiO_3$ thin films by strain and oxygen deficiency *Phys. Rev. B* **88** 144427

[79] Xie Q Y, Wu X S, Li J, Lv B and Gao J 2013 Probing the dead layer thickness and its effect on the structure and magnetic properties in $La_{2/3}Ca_{1/3}$MnO3 thin films *Thin Solid Films* **545** 89–93

[80] Valencia S, Peña L, Konstantinovic Z, Balcells L, Galceran R, Schmitz D, Sandiumenge F, Casanove M and Martínez B 2014 Intrinsic antiferromagnetic/insulating phase at manganite surfaces and interfaces. *J. Phys. Condens. Matter* **26** 166001

[81] Varela M, Oxley M, Luo W, Tao J, Watanabe M, Lupini A, Pantelides S and Pennycook S 2009 Atomic-resolution imaging of oxidation states in manganites *Phys. Rev. B* **79** 085117

[82] Tokura Y and Nagaosa N 2000 Orbital Physics in Transition-Metal Oxides *Science (80-.).* **288** 462–8

[83] Fang Z, Solovyev I and Terakura K 2000 Phase Diagram of Tetragonal Manganites *Phys. Rev. Lett.* **84** 3169–72

[84] Calderón M, Brey L and Guinea F 1999 Surface electronic structure and magnetic properties of doped manganites *Phys. Rev. B* **60** 6698–704

[85] Cossu F, Schwingenschlögl U, Colizzi G, Filippetti A and Fiorentini V 2013 Surface antiferromagnetism and incipient metal-insulator transition in strained manganite films *Phys. Rev. B* **87** 214420

[86] Nogués J and Schuller I K 1999 Exchange bias *J. Magn. Magn. Mater.* **192** 203–32

[87] Kiwi M 2001 Exchange bias theory *J. Magn. Magn. Mater.* **234** 584–95

[88] He J, Borisevich A, Kalinin S V., Pennycook S J and Pantelides S T 2010 Control of Octahedral Tilts and Magnetic Properties of Perovskite Oxide Heterostructures by Substrate Symmetry *Phys. Rev. Lett.* **105** 227203

[89] Cui B, Song C, Wang G Y, Mao H J, Zeng F and Pan F 2013 Strain engineering induced interfacial self-assembly and intrinsic exchange bias in a manganite perovskite film. *Sci. Rep.* **3** 2542

[90] Chen H and Ismail-Beigi S 2012 Ferroelectric control of magnetization in $La_{1-x}Sr_xMnO_3$ manganites: A first-principles study *Phys. Rev. B* **86** 024433

Chapter 7

Conclusions and outlooks

The scope of this Thesis is to exploit the high spatial resolution and *in situ* capability of LM and EH to perform local magnetic characterization of nanostructures. The *in situ* experiments allow performing reversal magnetization studies and direct observations of the magnetic configuration of ferromagnetic systems with a Curie temperature higher than 100 K. In this Chapter, we present the conclusions of this Thesis followed by the outlook on possible future research in this field.

7.1. Optimization of *in situ* TEM characterization under external magnetic field

An accurate method to control the component in the plane of the sample of the magnetic field produced by the OL has been developed through a precise sample orientation with a conventional double-tilt rotation TEM holder. Such control is achieved by a combination of linear rotation transformations in two orthogonal axis. This procedure was validated by manipulating DWs in a Co nanoring. We also evidenced the influence of the unavoidable out-of-plane component of the magnetic field in the quantitative measurement of magnetic parameters such as the determination of H_c in elongated nanostructures. The potential of this method was widely exploited in the works presented in *Chapter 4* and *5*, where we investigated the intensity and direction of the in-plane magnetic field component to manipulate DW in L-shape nanowires. There, we quantified the DW conduit parameters such as the nucleation, propagation, pinning and depinning fields. In *Chapter 5* we evaluated the mechanisms that govern the reversal magnetization processes in high-density cobalt antidot arrays for different applied magnetic field orientations. Thus, most of the future *in situ* TEM

experiments in magnetic nanostructures that require well-oriented in-plane magnetic fields could be carried out, always having in mind that an out-of-plane magnetic field component more intense that the in-plane one cannot be avoided and, in some cases, cannot be neglected.

7.2. DW manipulation in magnetic Co FEBID and notched $Co_{50}Fe_{50}$ nanowires

We have studied the DW nucleation processes of Co FEBID nanowires of various thicknesses and width by implementing an *in situ* method to nucleate and propagate small DW structures by applying magnetic fields in the plane of the sample. One of the most remarkable results was been found in the series of Co nanowires of 500 nm width, where an unusual variation of the DW nucleation field with the thickness was correlated with the DW magnetic structure. We evidenced that as the nanowire increases in thickness, the magnetic structure of the nucleated DW transforms itself from a Transverse Wall (TW), for the thinnest NW (t < 10 nm) to Asymmetric Transverse Wall (ATW), then to Asymmetric Vortex Wall (AVW) to reach a complex two Vortex Wall (2VW) structure (t = 30 nm). Close to the crossover between ATW and AVW (t = 13 nm), the nanowires presented the best DW conduit performance, with the largest different between DW nucleation and propagation field for such DW configuration. In addition we also performed pinning/depinning studies of single DW through notched $Co_{50}Fe_{50}$ nanowires fabricated by EBL with different size and geometries. This allowed us determining the most suitable configuration of notches to manipulate a single DW.

Until we know, the results presented in this Chapter are the first application of *in situ* LM under external magnetic fields for the study of Co nanostructures grown by FEBID. Additional work could be carried out or is currently underway in such nanostructures, as for example:

(1) One of the "unsolved mystery" in the Co FEBID nanowires is the increasing behaviour of the H_N with the width, for low values of widths. As we briefly shown in the discussion of the *Chapter 2*, micromagnetic simulations revealed that this fact could be associated to the shape of the profile of the NWs. In

previous work have been demonstrated that Co NWs grown by FEBID has a bell-type shape profile [1,2]. Thus, the next step is to perform an exhaustive magnetic analysis of the influence of the non-uniform profile in the magnetization reversal processes. At present, a similar work is performing in Fe NWs grown on FEBID, and we have found that the bell-shape profile play an important role in the magnetization switching (*a manuscript is in the process of submission*).

(2) The studies of the gallium irradiation effect on the magnetism in Co nanowires by the local exploration of the magnetic configuration using EH. A preliminary work has been published in Reference [2] demonstrating by nanoMOKE that a moderate irradiation increases the gap between nucleation and propagation fields, further optimizing the DW conduit properties of Co FEBID nanowires. Magnetic characterization by EH is currently in progress to locally investigate how the Ga irradiation affects the ferromagnetic character of the Co.

(3) In a close collaboration with several groups participating in ESTEEM2 project (the Institute of Structural Physics of the Technique Universität Dresden, Germany; EMAT at University of Antwerp, Belgium; CEMES-CNRS in Toulouse, France, and the LMA-INA in Zaragoza) we are exploring the 3D distribution magnetic induction of nanometer-scale Co FEBID nanopillars (100 – 130 nm of diameter) by the tomography reconstruction of the phase shift determined from holographic tilt series. At the moment of writing this Thesis, the reconstruction of the 3D magnetic induction of the Co nanopillar in a remanent magnetic state has been achieved (*a manuscript is in the process of submission*). The next step will be to reconstruct the 3D magnetic structure of a nucleated DW.

(4) Observation of the magnetic frustration in complex magnetic structures such as Kagome or Penrose-like structure (see Figure 7.1). Such magnetic frustration could be explored either after following a smart demagnetization protocols or during a reversal magnetization process. Even though the nanomagnets of the

Penrose structure of Figure 7.1 are connected, we also studied this phenomenology in unconnected tiles.

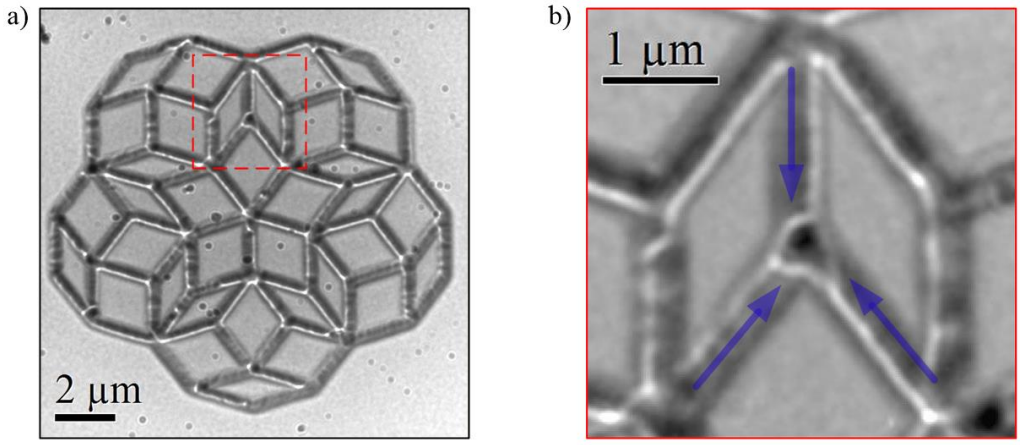

Figure 7.1. (a) Defocused LM image for a Co-FEBID Penrose-like tile nanostructure. (b) A zoom of the image (b) around a vertex where the magnetization of the nanowires (blue arrows) is pointed in the vortex (magnetic-like monopole).

7.3. Studies of the remanent and reversal magnetization states in Co antidot arrays

We have developed an image analysis procedure to highlight the magnetic contrasts in defocused LM images and qualitatively analyse of the periodicity dependence of the remanent magnetic states in high-density square Co antidot arrays. We evidenced, as a function of the hole periodicity *"p"*, a transition from magnetic domains with 90° and 180° DWs (large periodicities, $p \geq 300$ nm) to extended magnetic superdomains and magnetic chains separated by superdomain walls (small periodicities, $116 \leq p \leq 160$ nm). Reversal magnetization studies of the antidot array ($p = 160$ nm) with a magnetic configuration composed by SD structures at remanence were performed by applying magnetic field parallel and transversal to the antidot rows. Although the magnetization switching mechanisms are similar in both cases, with the nucleation and propagation of horizontal and vertical SDWs, the way it occurs is clearly different: (*i*) a transversal magnetic field switched the magnetization by simultaneous nucleation and propagation

of vertical and horizontal SDWs, (*ii*) a parallel magnetic field switched the magnetization in two steps: nucleating and propagating firstly (1) horizontal SDWs (SDWs parallel to the magnetic field) and then (2) vertical SDWs (SDWs perpendicular to the magnetic field). For the visualization of magnetic contrast in high-density antidot arrays (in our study, periodicities of 116 nm < p < 160 nm), a low-frequency Fourier filtering method was implemented to allow a quantitative analysis of the LM images via TIE method. The results of this work demonstrated the huge potential of LM and EH to characterize the local magnetic configuration of magnetic antidot arrays. Both techniques, but specially EH, could be useful to explore the magnetism in arrays with $p < 100$ *nm*. As a continuation of this work, we are resolved to explore the "dot regime", where each region *Type 2* (regions enclosed by four nearest-neighbouring holes) behaves as an individual magnetic entity, ideal to be used as magnetic bits of information for high density storage. To do that, firstly we need to optimize the nanofabrication process of ferromagnetic antidot arrays on support Si_3N_4 membranes by minimizing the damage induced by the Ga-irradiation. Several strategies to solve this problem could be evaluate such as the deposition of a non-magnetic thin layer on the top of the magnetic layer that would act as a protect layer, fine tune the etching conditions for this membrane, and/or employing cryogenic conditions.

Furthermore, although LM technique allowed us achieving a unprecedented resolution to explore the local magnetic configuration of high-density antidot arrays with periodicities down to 116 nm, future studies with a higher spatial resolution and sensibility could be made through an optimized EH setting, where split illumination setup allowed exploring magnetic states far away of vacuum edge, overcoming one of the limitation of EH: the exploration of magnetic configuration with a plane of view of few hundreds of nanometers close to an vacuum edge. This experiment can be performed in a dedicated LM microscope such as the I2TEM installed in the CEMES-CNRS lab.

7.4. Studies of the substrate-induced strain effect on the magnetic properties of strained LCMO thin films

The alterations of the magnetic properties of epitaxial LCMO thin films have been explored by EH at low temperature (100 K). The high-tetragonality distortion of the LCMO films structure resulting of the epitaxial stress induced by the lattice mismatch between the substrate and the film induces a magnetic phase separation where both ferromagnetic and antiferromagnetic orders coexist. This effect was clearly observed in strained LCMO films grown on STO substrate, where a tensile-induced strain induced a superficial non-ferromagnetic layer. On the other hand, the compressive-induced strain in strained LCMO films grown on LAO substrate altered the magnetocrystalline anisotropy inducing an out-of-plane magnetization. First principle calculations by DFT-*U* method demonstrated that an antiferromagnetic order in stoichiometry LCMO films is attributed to a high deformation of the crystalline structure only. Although the substrate-induced strain effect in the magnetic properties of manganites thin film have been widely studied in the past, this work has been pioneer in the use of EH to analyse the strain induced modifications of the magnetic structure by low temperature EH our work therefore being unique. As a next step to the work presented in this chapter, we have proposed to investigate the complex magnetic configuration of high-tetragonality LCMO films grown on LAO. The macroscopic magnetization measures, as well as the theoretical calculation indicate that a non-ferromagnetic layer (o region) should exist. Thus, a clear understanding of this magnetic states allowed elucidating where is located the non-ferromagnetic regions. The EH capabilities to work at low temperature can be extended to study other complex magnetic oxides that present similar behaviour like, for instance, $La_xSr_{1-x}MnO_3$. Moreover, a further work to be carried out would be to explore the artificial induction of the superficial non-ferromagnetic layer by an external mechanical strain. This experiment can be performed using a nano-indenter TEM holder, where a micro-tip is used to impose a local uniaxial stress by pressing the surface of the TEM lamella. For this experiment, LSMO would be a more suitable specimen, as it is ferromagnetic at room temperature. From a material science point of view, it would be interesting to explore if we can fine tune the size and properties of the NFL (so-called

dead layer). As have been proposed by S Valencia *et al* [3], if we achieve controlling the dimensions of the dead layer, we can use it as an MTJ barrier to grow later another electrode on the top. EH will be the key tool to evaluate such control, but the optimization of the dead layer will require the manpower of thin film "growers".

The work developed in this Thesis perfectly exemplify how EH and LM together with *in situ* process will emerge as a powerful magnetic characterization tool to explore the magnetism of the matter at nanoscale, and in different scenarios. Over the years, the magnetism community increasingly accepted their use as a complementary technique, and the expansion of new *in situ* scenarios are limited by the restrictions imposed by the microscope itself. For this reason, the new generation of microscopes are designed considering the best condition that increase the numbers of different *in situ* process.

References

[1] Fernández-Pacheco A, De Teresa J M, Szkudlarek A, Córdoba R, Ibarra M R, Petit D, O'Brien L, Zeng H T, Lewis E R, Read D E and Cowburn R P 2009 Magnetization reversal in individual cobalt micro- and nanowires grown by focused-electron-beam-induced-deposition. *Nanotechnology* **20** 475704

[2] Serrano-Ramón L, Fernández-Pacheco A, Córdoba R, Magén C, Rodríguez L A, Petit D, Cowburn R P, Ibarra M R and De Teresa J M 2013 Improvement of domain wall conduit properties in cobalt nanowires by global gallium irradiation. *Nanotechnology* **24** 345703

[3] Valencia S, Peña L, Konstantinovic Z, Balcells L, Galceran R, Schmitz D, Sandiumenge F, Casanove M and Martínez B 2014 Intrinsic antiferromagnetic/insulating phase at manganite surfaces and interfaces. *J. Phys. Condens. Matter* **26** 166001

List of publications

Along my Ph.D. studies, I have co-authored 11 publications in peer-reviewed journals: 7 are published. In addition, 1 manuscript is submitted and 3 are in preparation. The results of this Thesis are contained in 4 of these articles:

1. ***Optimized cobalt nanowires for domain Wall manipulation imaged by in situ Lorentz Microscopy***
   L A Rodríguez, C Magén, E Snoeck, L Serrano-Ramón, C Gatel, R Córdoba, E Martínez-Vecino, L Torres, J M De Teresa and M R Ibarra.
   Applied Physics Letters **102** (2013) 022418.
   (Chapter 4 of the thesis)

2. ***Quantitative in situ magnetization reversal studies in Lorentz microscopy and electron holography***
   L A Rodríguez, C Magén, E Snoeck, C Gatel, L Marín, L Serrano-Ramón, J L Prieto, M Muñoz, P A Algarabel, L Morellón, J M De Teresa and M R Ibarra.
   Ultramicroscopy **134** (2013) 144-154.
   (Chapter 3 and 4 of the thesis)

3. ***High-resolution imaging of remanent state and magnetization reversal state of superdomain structures in high-density cobalt antidot arrays***
   L A Rodriguez, C Magén, E Snoeck, C Gatel, C Castán-Guerrero, J Sesé, L M García, J Herrero-Albillos, J Bartolomé, F Bartolomé and M R Ibarra.
   Nanotechnology **23** (2014) 385703.
   (Chapter 5 of the thesis)
   An image of this publication was selected as Cover image of Nanotechnology Volumen 23, Issue 38 (2014).

4. ***Observation of the strain induced magnetic phase segregation in manganite thin films***
   L Marín, L A Rodríguez, C Magén, E Snoeck, A Rémi, I Lucas, L Morellón, P A Algarabel, J M De Teresa and M R Ibarra.
   Nano Letters (2014) submitted
   (Chapter 6 of the Thesis)

In the rest of the published articles, I have participated as collaborator author contributing with my expertise different TEM techniques:

5. ***Ultrasmall Functional Ferromagnetic Nanostructures Grown by Focused-Electron-Beam-Induced Deposition***
   L Serrano-Ramón, R Córdoba, L A Rodríguez, C Magén, E Snoeck, C Gatel, I Serrano, M R Ibarra and J M De Teresa.
   ACS Nano **5** (2011) 7781-7787.

6. ***Improvement of domain wall conduit properties in cobalt nanowires by global gallium irradiation***
   L Serrano-Ramón, A Fernández-Pacheco, R Córdoba, C Magén, L A Rodríguez, D Petit, R P Cowburn, M R Ibarra and J M De Teresa.
   Nanotechnology **24** (2013) 345703.

7. ***Enhanced Magnetotransport in Nanopatterned Manganite Nanowires***
   L Marín, L Morellón, P A Algarabel, L A Rodríguez, C Magén, J M De Teresa and M R Ibarra.
   Nano Letters **14** (2014) 423-428.

8. ***Magnetic antidot to dot crossover in Co and Py nanopatterned thin films***
   C Castán-Guerrero, J Herrero-Albillos, J Bartolomé, F Bartolomé, L A Rodríguez, C Magén, F Kronast, P Gawronski, O Chubykalo-Fesenko, K J Merazzo, P Vavassori, P Strichovanec, J Sesé and L M García.
   Physical Review B **39** (2014) 144405.

This is the list of works in preparation with their tentative titles and the journals where they will be submitted:

9. ***Electron beam induced deposition of high-purity and high aspect ratio three dimensional cobalt structures***
   L Serrano-Ramón, A Fernández-Pacheco, L A Rodríguez, C Magén, C Gatel, E Snoeck, M R Ibarra and J M De Teresa
   Small.

10. ***Influence of the shape and surface oxidation in the magnetization reversal of thin iron nanowires grown by focused-electron-beam-induced deposition***
    L A Rodríguez, L Deen, R Córdoba, C Magén, E Snoeck, B Koopmans and J M De Teresa
    Beilstein Journal of Nanotechnology.

11. ***Retrieving the 3D magnetic field of nanostructures by electron holography-tomography***
    D Wolf, L A Rodríguez, A Béche, E Javon, L Serrano-Ramon, C Magén, C Gatel, A Lubk, H Lichte, S Bals, G Van Tendeloo and E Snoeck
    Nature Materials

Résumé étendu de la Thèse

ETUDES *IN-SITU* PAR MICROSCOPIE DE LORENTZ ET HOLOGRAPHIE ELECTRONIQUE DE NANOSTRUCTURES MAGNETIQUES

Directeurs de Thèse : Dr. César MAGEN (INA – Université de Saragosse).

Dr. Etienne SNOECK (CEMES - Toulouse)

L'objectif général de la thèse vise à développer des mesures quantitatives des configurations magnétiques locales dans des matériaux nanostructurés par des études *in-situ* en microscopie de Lorentz (LM) et holographie électronique (EH) sous l'application de champs magnétiques extérieurs et à basse température (100 K). Ce travail fait partie d'une collaboration entre les deux groupes de recherche du LMA-INA et du CEMES–CNRS notamment dans le cadre du LIA « TALEM ». Une partie des objets étudiés ont été élaborés à l'INA, d'autres de *l'Instituto de Ciencia de Materiales de Aragó*n (ICMA) de Saragosse ou encore de *l'Instituto de Sistemas Optoelectrónicos y Microtecnología* (ISOM) de Madrid.

La thèse débute par une Introduction générale (*Chap. 1*) qui situe le contexte général et donne les objectifs du travail. Un chapitre (*Chap. 2*) détaille ensuite les outils expérimentaux utilisés au cours de cette thèse. La suite du manuscrit est ensuite divisée

en 4 chapitres (*Chapitre 3 à 6*) qui détaillent les différents sujets abordés. Successivement ils concernent:

- Le développement des études in-situ quantitatives sous l'application de champs magnétiques (*Chap. 3*).
- La caractérisation et manipulation des parois de domaines magnétique (DWs) dans des nanofils magnétiques (*Chap. 4*).
- l'imagerie haute résolution de l'état magnétique à la rémanence et des modes de renversement d'aimantation dans des réseaux magnétiques d'antidots de cobalt de haute densité (*Chap. 5*).
- les effets de contrainte sur les propriétés magnétiques de couches minces épitaxiales de $La_{2/3}Ca_{1/3}MnO_3$ à basse température (*Chap. 6*).

Le manuscrit se termine par une conclusion générale qui résume les principaux résultats obtenus au cours de ce travail et ouvre sur des développements futurs.

Chapitre 2 : Techniques Expérimentales

Après une description des différentes techniques utilisées pour l'imagerie magnétique, ce premier chapitre décrit en détail les moyens expérimentaux mis en œuvre dans ce travail. Il y est présenté le fonctionnement d'un microscope électronique à transmission (MET) et les principes des techniques classiques d'imagerie en microscopie. Vient ensuite une présentation détaillée de la microscopie de Lorentz (LM) et des techniques de reconstruction d'images de l'induction magnétique par la méthode TIE (Transport Intensity Equation - TIE) appliquée sur des série d'images défocalisées. Le paragraphe suivant concerne l'Holographie Electronique (EH) tant dans sa présentation théorique détaillée, sa mise en œuvre pratique que dans les méthodes d'analyse des hologrammes permettant de cartographier le potentiel électrostatique et l'induction magnétique. Les paragraphes suivant concernent les techniques associées à

l'instrument « Focused Ion Beam » (FIB) et notamment la méthode de nanostructuration « Focused Electron Beam Induced Deposition (FEBID) » utilisé dans ce travail pour déposer des nanostructures magnétiques de cobalt.

Chapitre 3: Caractérisation *in-situ* en MET de nanostructures magnétiques sous l'application d'un champ magnétique externe

Nous avons mis au point une méthode précise permettant de contrôler le champ magnétique appliqué dans le plan de l'échantillon à partir du champ produit par la lentille objectif du microscope. Les lentilles objectifs des microscope créent un champ aligné le long de l'axe optique du MET (selon « *z* ») qui peut atteindre des valeurs de l'ordre de 2 Tesla dans un MET fonctionnant à 200-300 kV. En ajustant l'orientation de l'échantillon à l'aide d'un porte objet à double inclinaison il est possible de contrôler la composante dans le plan de l'objet de ce champ « extérieur ». Ce contrôle est réalisé par la combinaison des rotations α et β autour de deux axes orthogonaux du porte-objet double rotation (Fig. 1). Ce travail a permis de pouvoir ajuster ces tilts et l'intensité du champ appliqué par la lentille de façon à piloter l'intensité et la direction des champs planaires appliqués sur l'échantillon.

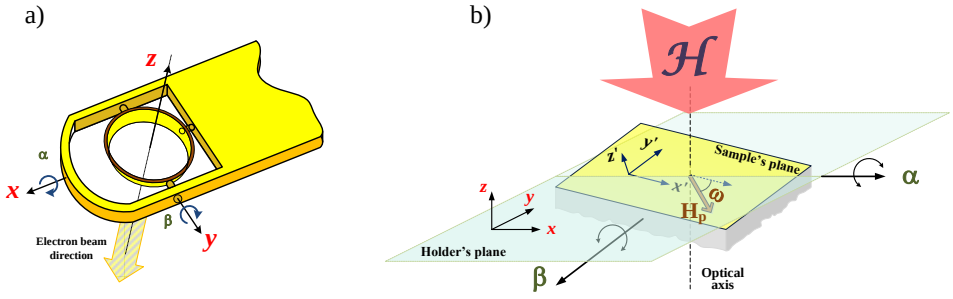

Figure 1: (a) Porte-objet MET à double inclinaison. (b) Représentation schématique des axes dans les coordonnées cartésiennes associées au MET (*x*, *y*, *z*) et à l'échantillon (*x'*, *y'*, *z'*).

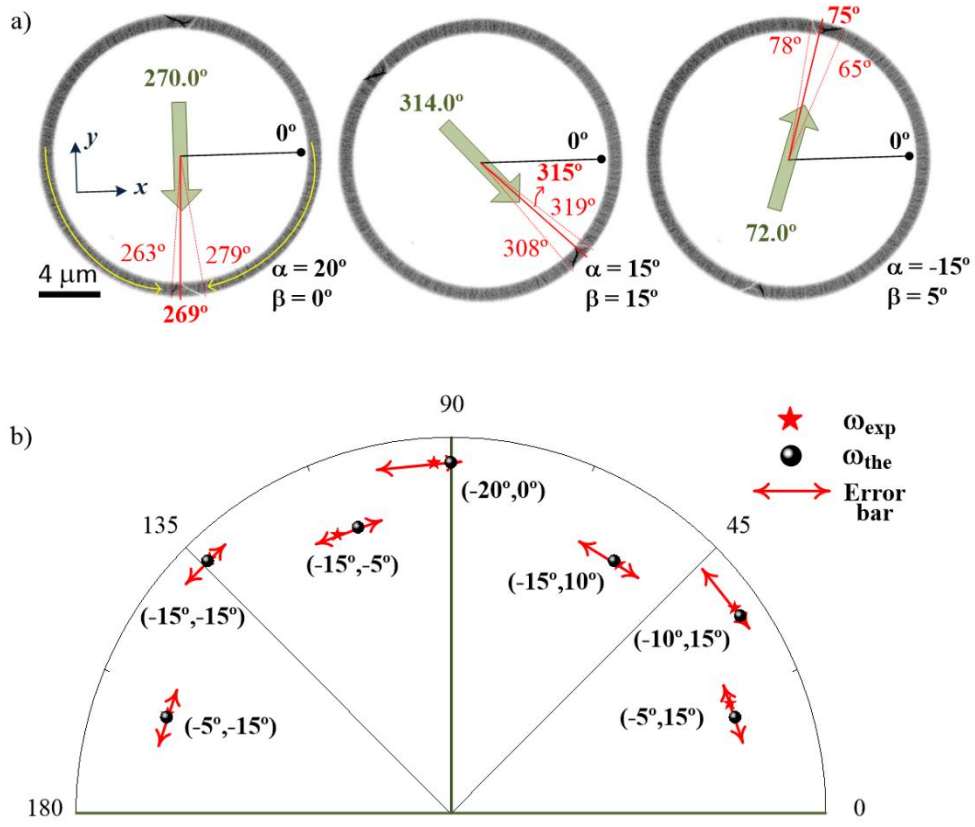

Figure 2: (a) Série d'images obtenue en LM sur un nanoring de Co après l'application d'un champ magnétique dans le plan selon trois directions différentes. Le contraste clair et sombre à l'intérieur de l'anneau correspond aux deux parois de domaine (DWs) nucléées. Les flèches jaunes et vertes indiquent respectivement l'orientation de l'aimantation et la direction théorique de la composante dans le plan du champ magnétique appliqué. Les valeurs en rouges indiquent la position angulaire du DW mesuré expérimentale. (b) représentation polaire du résultat expérimental (étoiles rouges) et théorique (points noirs).

Les composantes du champ dans le plan de l'échantillon *(x', y', z')* s'écrivent en fonction des rotations α et β

$$H_{x'} = -H[\cos(\beta)\sin(\beta_0) - \sin(\alpha)\sin(\beta)\sin(\alpha_0)\cos(\beta_0) - \cos(\alpha)\sin(\beta)\sin(\alpha_0)\cos(\beta_0)] \quad \text{(Eq. 1)}$$

$$H_{y'} = -H[-\cos(\alpha)\sin(\alpha_0)\cos(\beta_0) + \sin(\alpha)\cos(\alpha_0)\cos(\beta_0)] \quad \text{(Eq. 2)}$$

$$H_{z'} = H[-\sin(\beta)\sin(\beta_0) - \sin(\alpha)\cos(\beta)\sin(\alpha_0)\cos(\beta_0) - \cos(\alpha)\cos(\beta)\cos(\alpha_0)\cos(\beta_0)] \quad \text{(Eq. 3)}$$

Cette procédure a été validée expérimentalement par la manipulation d'un DW dans un nanoring de Co magnétique comme illustré sur la Figure 2.

Nous avons également mis en évidence l'influence de la composante du champ magnétique hors-plan dans la mesure quantitative des paramètres magnétiques, tels que la détermination du champ coercitif H_c dans des nanostructures anisotropes (nanofils de Co obtenus par FEBID) pour différentes valeurs du champ perpendiculaire (Fig. 3).

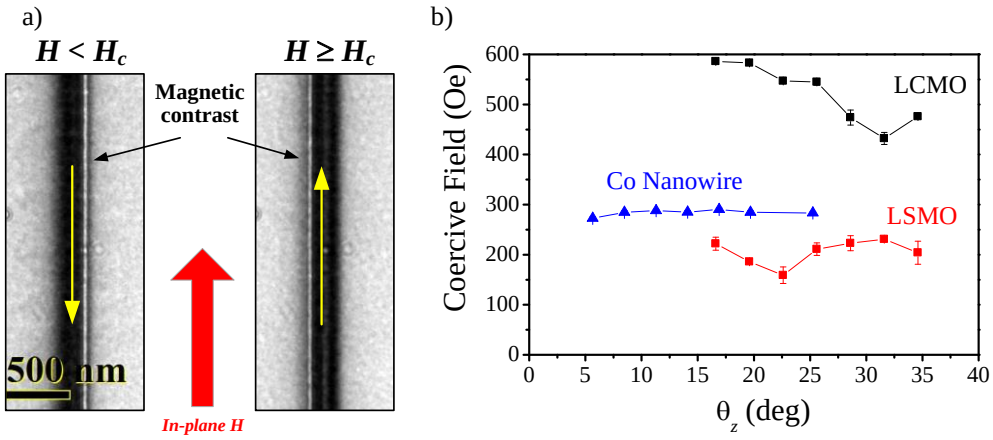

Figure 3: a) Images LM défocalisées d'un nanofils de Co obtenus pour un champ appliqué $H < H_c$ et $H > H_c$ montrant l'inversion du contrast de Fresnel brillant d'un bord du fil à l'autre et permettant de mesurer le champ de renversement de l'aimantation (champ coercitif: H_c). (b) Dépendance du champ coercitif en fonction de la composante de champ magnétique hors du plan (représenté par θ_z) pour les trois systèmes ferromagnétiques différents analysés.

Les performances de cette méthode quantitative permettant d'appliquer un champ contrôlé in-situ dans un MET ont été largement exploitées dans les travaux présentés dans les *Chapitres 4* et *5*, où nous avons utilisé l'intensité et la direction de la composante de champ magnétique dans le plan pour manipuler des parois de domaines magnétiques (DWs) dans des nanofils en forme de « *L* ». Grace à ces développements méthodologiques, nous avons pu également quantifier les paramètres permettant le déplacement de ces DWs tels que: le champ de nucléation des parois de domaine, le champ de propagation de ces parois et les champs de piégeage et de dépiégeage de celles-ci. Dans le *Chapitre 5*, nous avons pu évaluer les mécanismes qui régissent les processus renversement d'aimantation dans des réseaux d'antidots de cobalt de haute densité et ce, pour différentes orientations du champ magnétique appliqué.

Chapitre 4: Caractérisation et manipulation des parois de domaines magnétique dans des nanofils magnétiques de Co et de $Co_{50}Fe_{50}$

Dans cette partie, nous avons étudié les processus de nucléation de DWs dans des nanofils de Co déposés dans un FIB par une méthode originale: *Focused Electron Beam Induced Deposition* (FEBID) développée à l'INA dans le groupe du Prof. Jose Maria de Teresa. Plusieurs nanofils en forme de « L » et de différentes épaisseurs et largeurs ont été réalisés puis étudié en mettant en œuvre le procédé décris dans le chapitre précédent pour quantifier la nucléation et la propagation des DW par application de champs magnétiques contrôlés dans le plan de l'échantillon. Un des résultats les plus remarquables a été trouvé dans la série de nanofils Co de 500 nm de large. Nous avons mis en évidence une variation inattendue du champ de nucléation des DWs avec l'épaisseur. Nous avons observé que la structure des DW évolue avec l'épaisseur et se transforme d'une paroi transverse (TW) pour des épaisseurs $t < 10$ nm (les fils les plus minces) à une structure de paroi asymétrique transversale (ATW), puis à une structure de vortex asymétrique, (AVW) pour atteindre une structure plus complexe encore formée de deux parois vortex (2VW) structure ($t = 30$ nm) (Fig. 3).

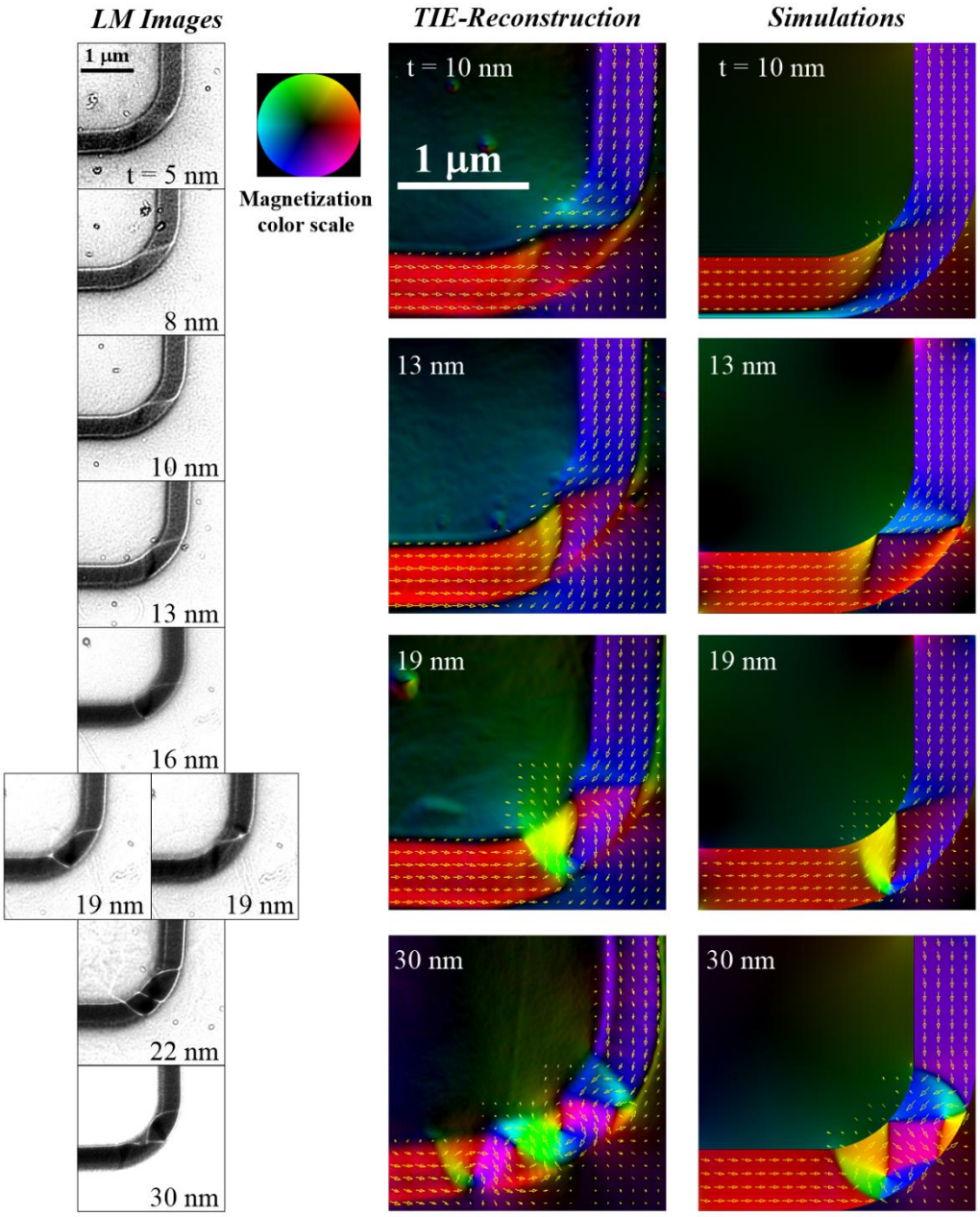

Figure 3: Observation par LM des configurations de DW pour différentes épaisseurs de nanofils de Co. *Gauche*: Images de LM, *Centre*: Reconstructions TIE, *Droite*: simulations micromagnétiques. Nous observons une configuration TW (pour t = 10 nm), ATW (pour t = 13 nm), AVW (pour t = 19 de nm) et 2VW (pour t = 30 nm) avec un état intermédiaire entre TW et VW (pour t = 19 nm).

Nous avons pu simuler par des calculs de micromagnétisme les diverses configurations observées expérimentalement.

Près de la transition entre ATW et AVW (t = 13 nm), les nanofils présentent des qualités tout à fait remarquables pour le déplacement des DW. Pour cette épaisseur le champ de nucléation et le champ de propagation présentent la plus grande différence (140 Oe) (Fig. 4d) qui permet de nucléer et déplacer les DWs de façon indépendante. Nous avons reliée cette particularité à la structure spécifique des parois de domaine pour cette valeur de l'épaisseur des nanofils.

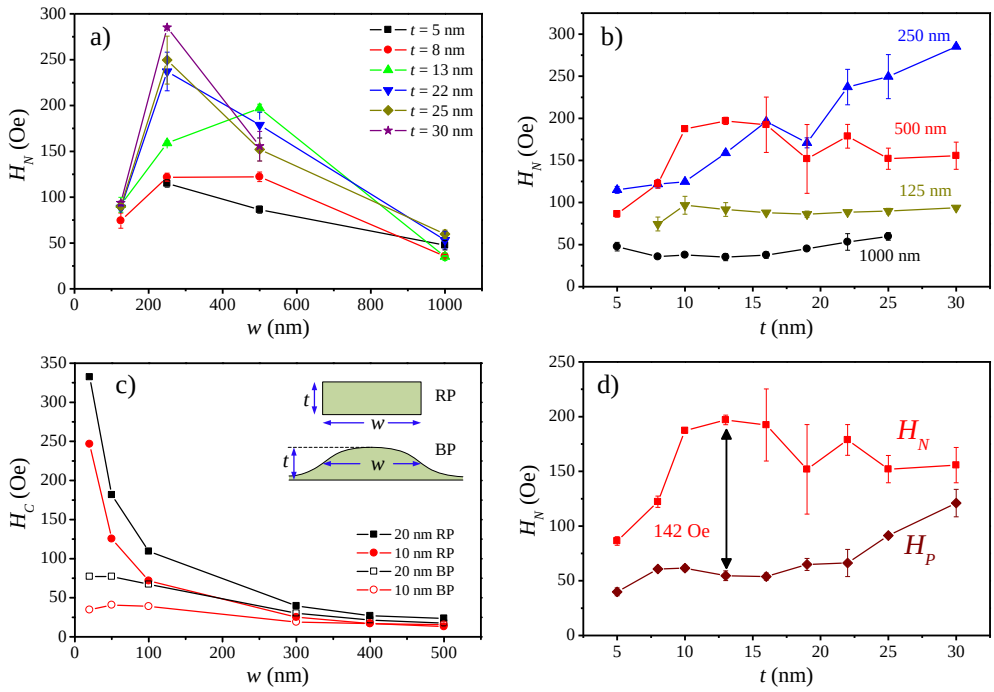

Figure 4: Dépendance des champs de nucléation en fonction de (a) la largeur (b) l'épaisseur des nanofils de cobalt. (c) Simulation micromagnétique du champ coercitif en fonction de la largeur dans les nanofils d'épaisseur 10 et 20 nm avec des profils différents: rectangulaire (RP) et en forme de cloche (BP). (d) Comparaison entre les champs de nucléation et de propagation pour les nanofils de cobalt de 500 nm en fonction de l'épaisseur.

Nous avons ensuite effectué des études similaires sur le piégeage/dépiégeage de un seul DW dans des nanofils de $Co_{50}Fe_{50}$ fabriqués par lithographie électronique et sur lesquels des encoches (nanoconstrictions) de taille et de géométrie différentes ont été réalisées comme autant de centres de piégeage des DWs (Fig.5). Les mesures de champs de nucléation, propagation et transmission/depiégeage nous a permis de déterminer la configuration la plus adaptée de nanoconstriction permettant de manipuler un unique DW.

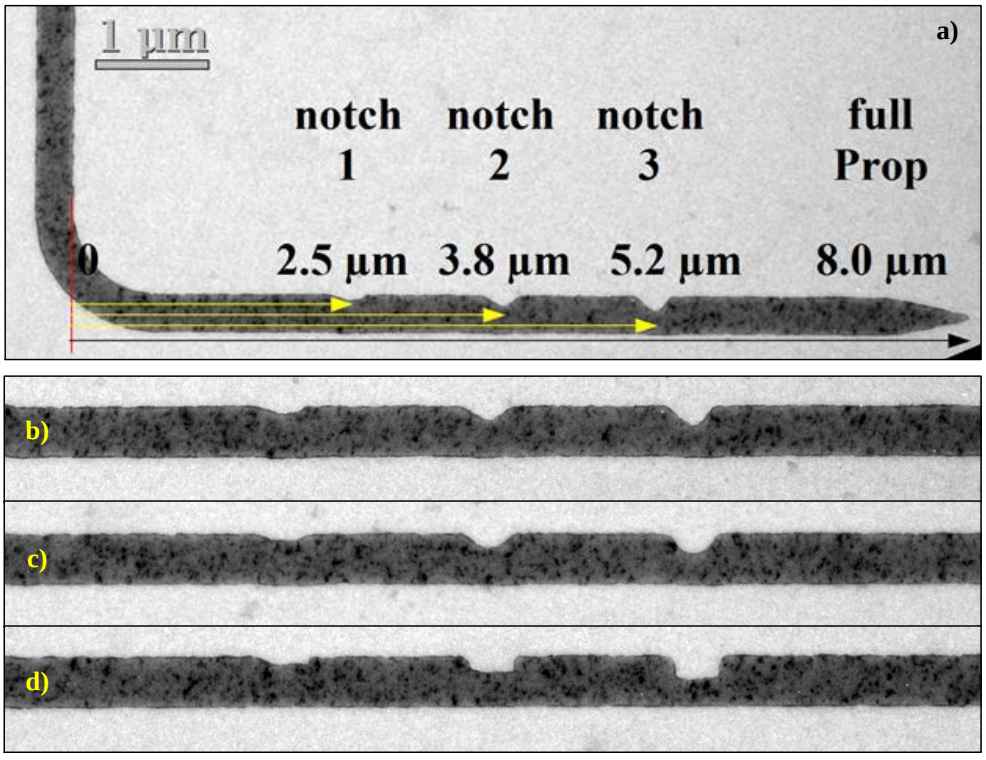

Figure 5: (a) Image TEM d'un ensemble de nanoconstrictions distribuées le long des fils de $Co_{50}Fe_{50}$ de forme (b) triangulaire, (c) courbe (d) à encoche rectangulaire.

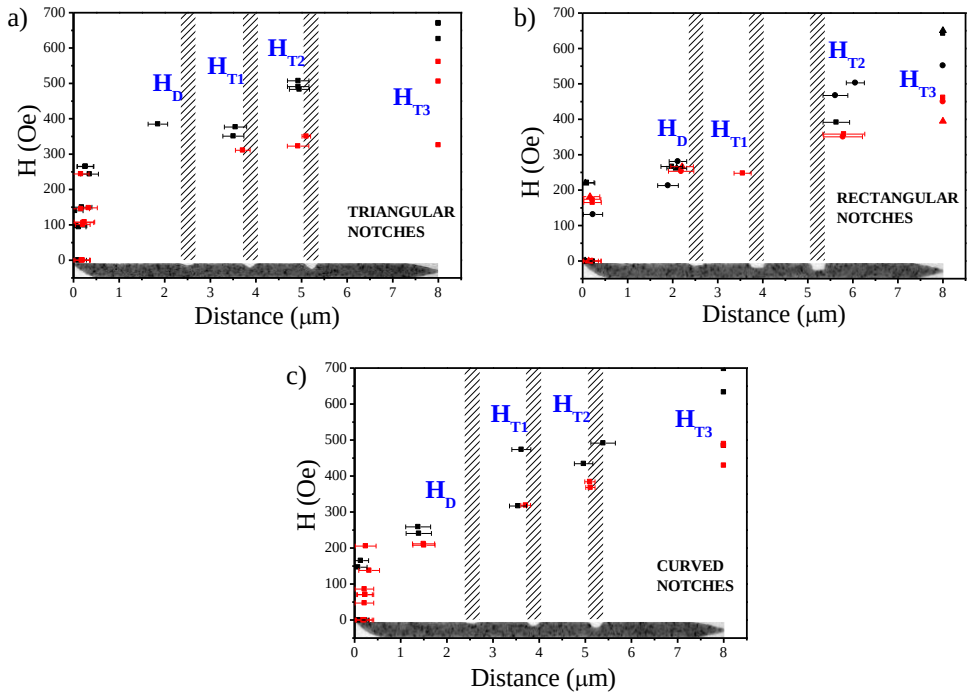

Figure 6: Variation des champs de dépiegeage de parois de domaine magnétique dans des nanofils de $Co_{50}Fe_{50}$ pour différentes morphologie de centre de piegeage.

Chapitre 5: Imagerie haute résolution de l'état magnétique à la rémanence et des mode de renversement d'aimantation dans des réseaux magnétiques d'antidot de Co de haute densité

Les réseaux d'antidot magnétiques sont constitués d'une couche magnétique continue dans laquelle ont été réalisé un reseau des « trous » par des méthodes de lithographie. Ces réseaux sont potentiellement très prometteurs pour des réaliser des mémoires magnétiques à haute densité car les domaines magnétiques y sont de taille réduite et dépendent du pas du réseau. Le travail ici vise à étudier les configurations des domaines dans ces réseaux d'antidots et à étudier les modes de renversement d'aimantation spécifiques à ceux-ci.

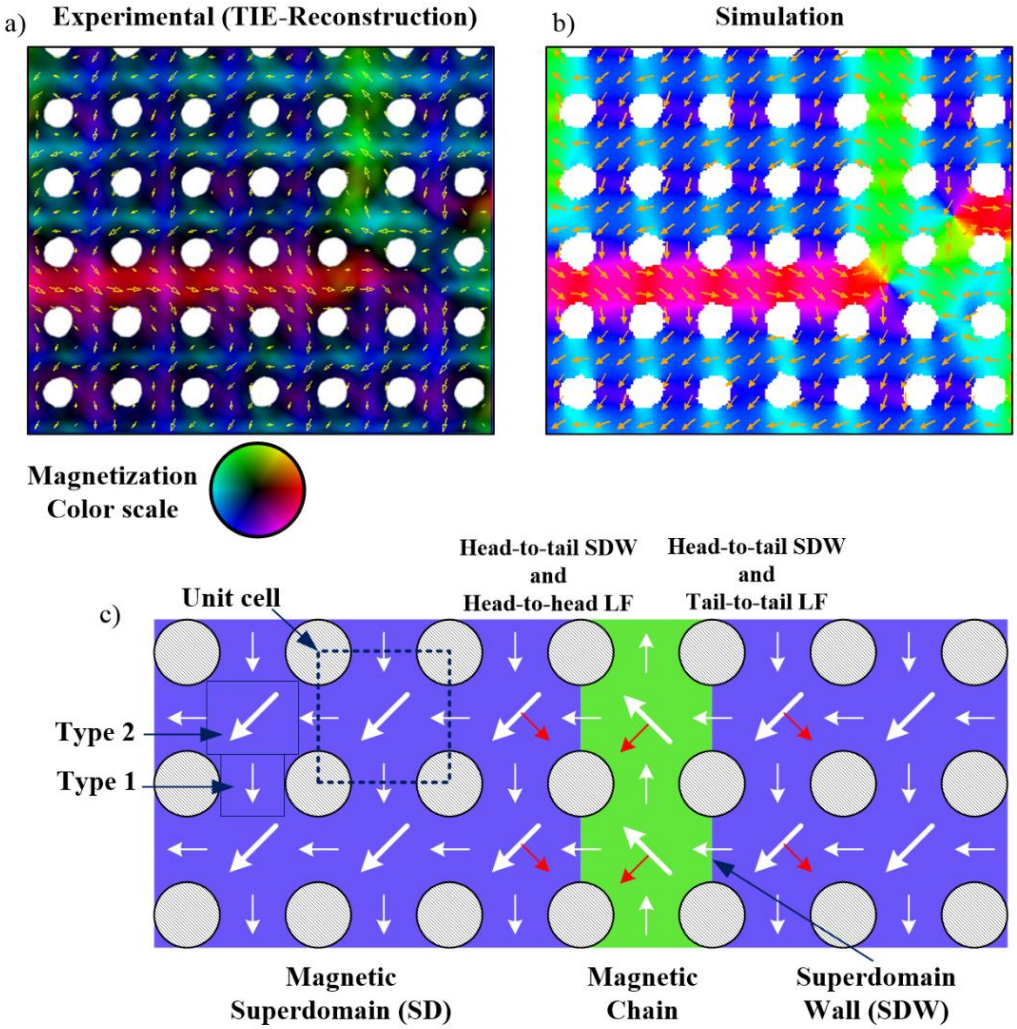

Figure 7: Cartographie vectorielle de l'aimantation obtenue à la remanence expérimentalement (a) et simulée (b). (c) Illustration schématique de la configuration de spin rémanente issue de (b). Les flèches blanches indiquent la direction de l'aimantation et les rouges la force de Lorentz. Par souci de clarté, le réseau d'Antidots (cercle blanc) a été superposé à la reconstruction.

Pour mener à bien l'étude des configurations magnétiques et des processus de renversement d'aimantation nous avons développé une procédure d'analyse d'image spécifique. Celle-ci permet de mettre en évidence les contrastes magnétiques obtenus en mode Lorentz (LM) défocalisé en éliminant les contrastes de Fresnel parasite apparaissant au bord des trous. Cette méthode permet une analyse qualitative de

l'évolution de la structure des états magnétiques rémanents dans les réseaux d'antidot carrés très denses. Nous avons mis en évidence, en fonction de la périodicité "p" des trous des réseaux, une transition entre la présence de domaines magnétiques à 90° et 180° pour de grandes périodicités, ($p \geq 300$ nm) à l'apparition de longs super-domaines magnétiques et de chaînes magnétiques séparées par des parois de super-domaine pour de petites périodicités ($116 \leq p \leq 160$ nm). Une image des configurations magnétique obtenue comparées aux simulations micromagnétiques que nous avons menées est reportée Fig. 7.

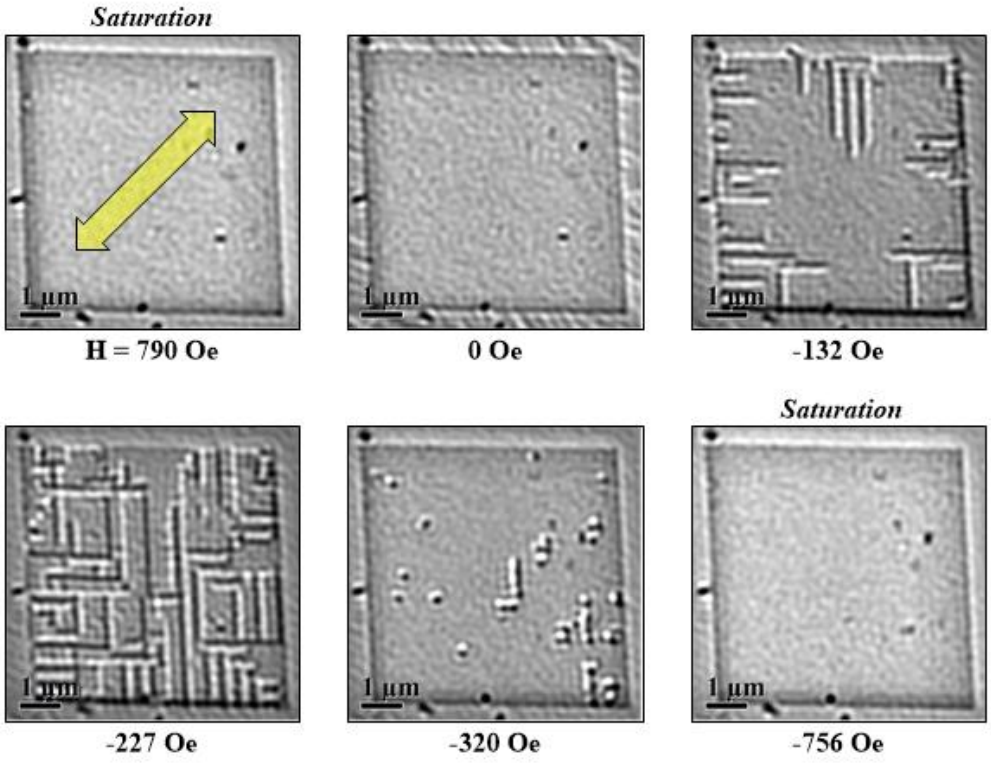

Figure 8: Série d'images LM défocalisées et filtrées qui mettent en évidence le processus de retournement de l'aimantation quand le champ est appliqué transversalement au réseau de trous de périodité p = 160 nm. La flèche jaune indique l'orientation du champ magnétique dans le plan.

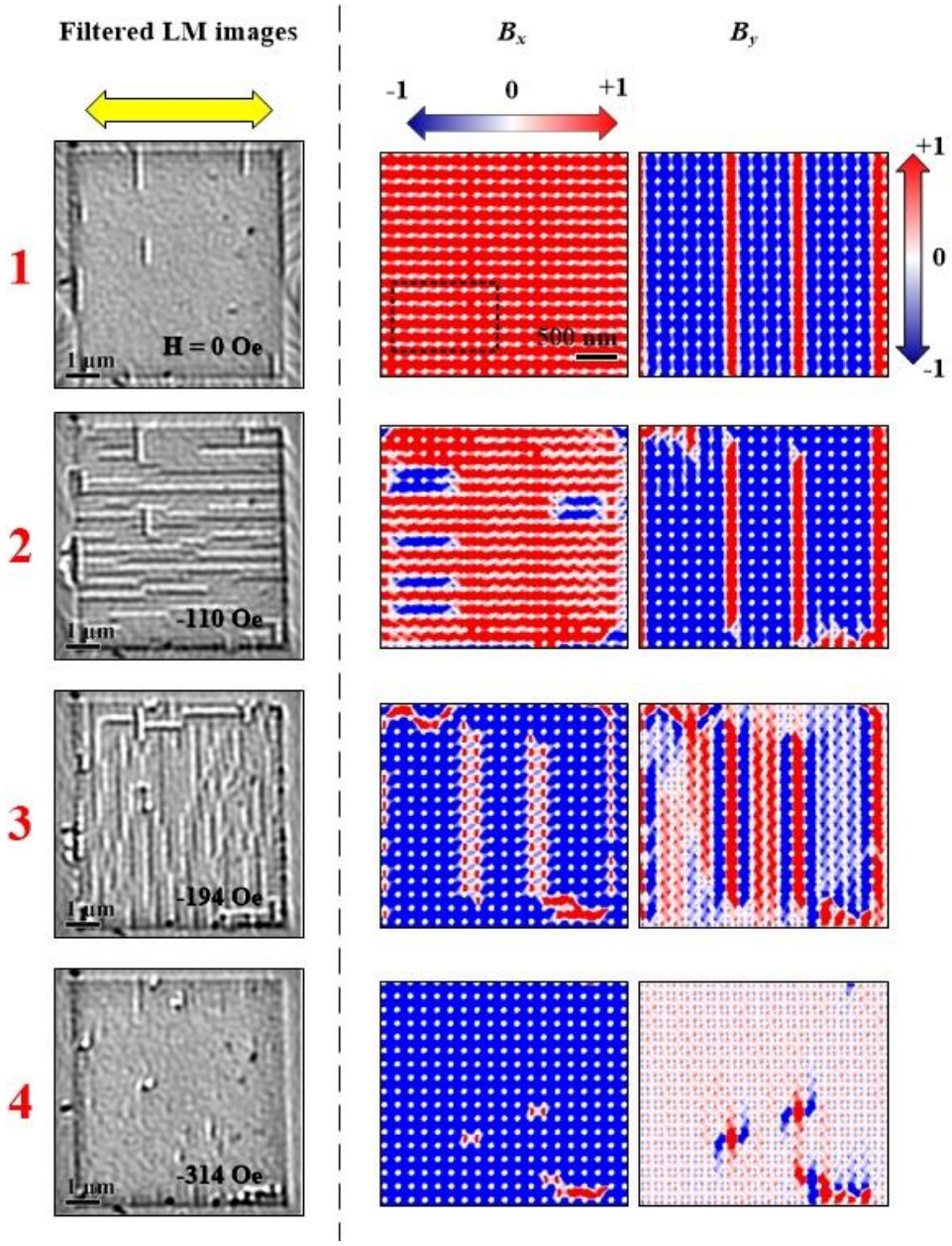

Figure 9: Images LM défocalisées et filtrées (*à gauche*) et simulations micromagnétiques (*à droite*) des images résumant les étapes caractéristiques du mécanisme de retournement de l'aimantation quand le champ est appliqué le long de la direction des trous de périodité p = 160 nm. La flèche jaune indique la direction de l'induction magnétique dans le plan. B_x et B_y sont les composantes x et y de l'induction magnétique résultante.

L'étude du retournement de l'aimantation des réseaux d'antidot de périodicité p = 160 nm (dans une configuration magnétique à rémanence constituée par les structures en superdomaines) a été réalisée en appliquant le champ magnétique parallèlement puis transversalement aux rangées d'antidot. Bien que les mécanismes de renversement de l'aimantation sont similaires dans les deux cas, avec la nucléation et la propagation de parois de super domaines (SDWs) horizontales et verticales, la façon dont ils se produisent est très différente: un champ magnétique transversal retourne l'aimantation par nucléation et propagation de SDWs horizontalement et verticalement simultanément (Fig. 8) alors qu'un champ magnétique parallèle renverse l'aimantation en deux étapes: (1) la nucléation et la propagation d'abord de SDWs horizontalement (parallèlement au champ magnétique) et ensuite (2) la propagation de SDWs verticalement (i.e. perpendiculaire au champ magnétique) (Fig. 9) .

Les résultats de ces travaux ont démontré l'énorme potentiel de la LM et EH pour caractériser la configuration magnétique local de réseaux d'antidots magnétiques.

Chapitre 6: Effet de contrainte sur les propriétés magnétiques de couches minces épitaxiales de $La_{2/3}Ca_{1/3}MnO_3$

Les modifications des propriétés magnétiques des films minces de $La_{2/3}Ca_{1/3}MnO_3$ épitaxiales ont été explorées par EH à basse température (100 K). Nous nous sommes intéressés à différentes couches de $La_{2/3}Ca_{1/3}MnO_3$ épitaxiées sur divers substrats : $LaAlO_3$, $LaSrTiO_3$, $SrTiO_3$ par croissance PLD. Ces trois substrats induisent respectivement une contrainte épitaxiale en compression, quasi nulle et en tension. Nous avons étudié l'état de déformation du dépôt résultant de la croissance contrainte par des techniques de diffraction des rayons X (Fig. 10) et pour différentes conditions de croissance, i.e. essentiellement la fréquence du laser de la PLD et les températures et temps de recuits.

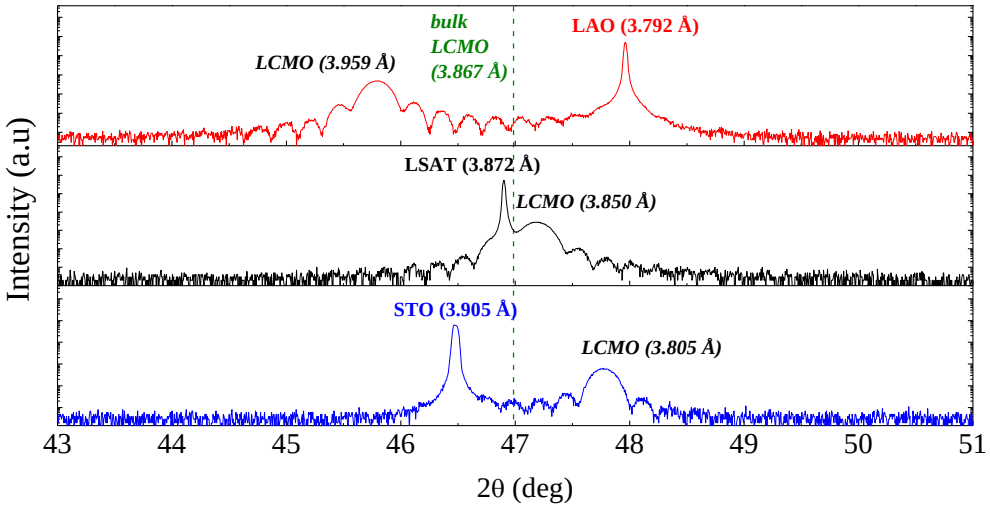

Figure 10: Spectre de diffraction des rayons X autour de la réflexion (002) pour des couches minces de LCMO épitaxiales sur des substrats de LAO (*en haut*), LSAT (*au centre*) et STP (*en bas*). Est repéré sur chaque diffraction la mesure du paramètre hors-plan de la couche et du substrat considéré.

Nous avons étudié les propriétés magnétiques macroscopiques des couches contraintes ainsi réalisées et corrélé ces résultats à l'état de déformation de celles-ci. Les principaux résultats sont rassemblés dans la Fig. 12, sur laquelle on observe une diminution de l'aimantation dans les couches contraintes, quelles soient en tension ou en compression (Fig. 12a) et une augmentation du champ coercitifs dans les deux cas (Fig. 12c). Une modification des paramètres de croissance que ce soit une réduction de la fréquence laser ou une augmentation de la température de recuit permet de retrouver les propriétés magnétiques de la couche non contrainte (Fig. 12b et 12d) ainsi que les paramètres cristallins de la couche de LCMO relaxée.

Nous avons alors étudié à basse température les configurations magnétiques des divers dépôts par EH. Nous avons montré que la déformation tétragonale de la structure des films $La_{2/3}Ca_{1/3}MnO_3$ résultant de la contrainte épitaxiale induite par le désaccord de maille entre le substrat et le film provoque l'apparition d'une couche non magnétique située sur la partie supérieure de la couche mince contrainte.

Cet effet a été clairement observé dans les films de $La_{2/3}Ca_{1/3}MnO_3$ contraints en tension déposés sur un substrat de $SrTiO_3$. La contrainte biaxiale induite par la croissance résulte en l'apparition d'une couche superficielle non ferromagnétique (Fig. 13).

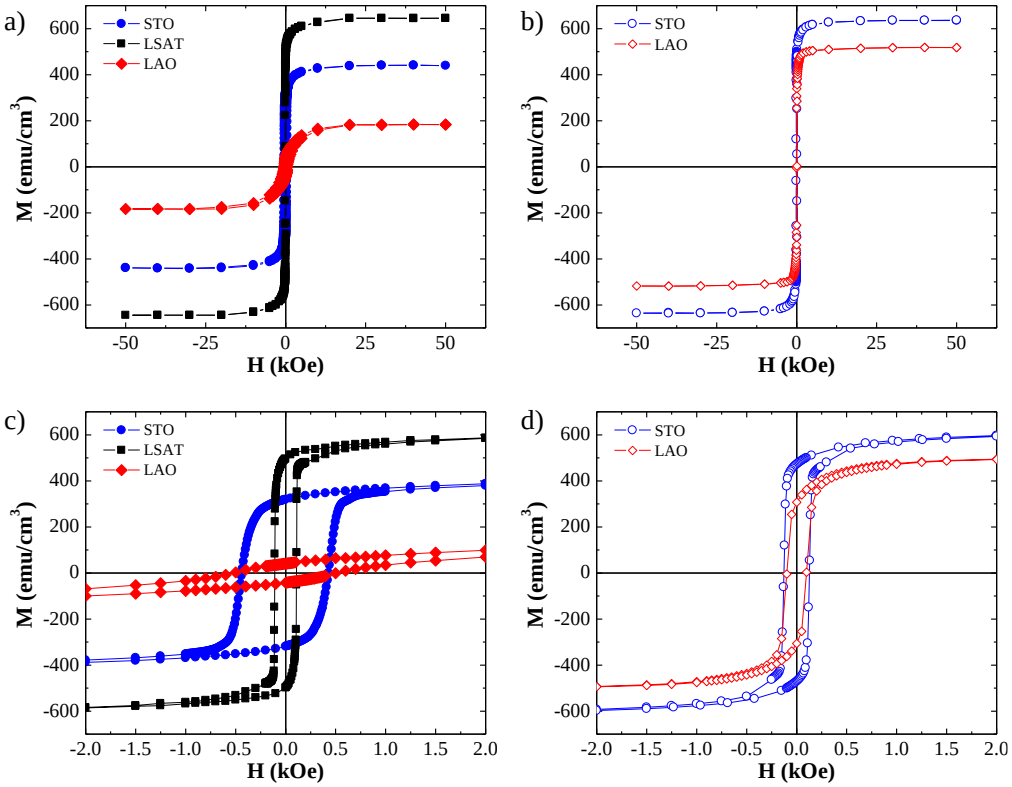

Figure 12: (a) et (c) Mesure d'aimantation et cycle d'hystéresis obtenus pour des champs appliqués le long de la direction [100] dans des couches minces de LCMO contraintes sur les trois substrats et caractérisés par des spectres XDR (Fig. 11). (b) et (d) Mesure d'aimantation et cycle d'hystérésis obtenus pour des champs appliqués le long de la direction [100] dans des couches minces de LCMO dont les propriétés magnétiques ont été optimisées en ajustant la fréquence du laser pendant le processus de croissance (pour le dépôts sur STO), ou en augmentant le temps recuit de l'échantillon après la croissance (pour le dépôts sur LAO). (c) et (d) zooms des cycles d'hystérésis de (a) et (b), respectivement.

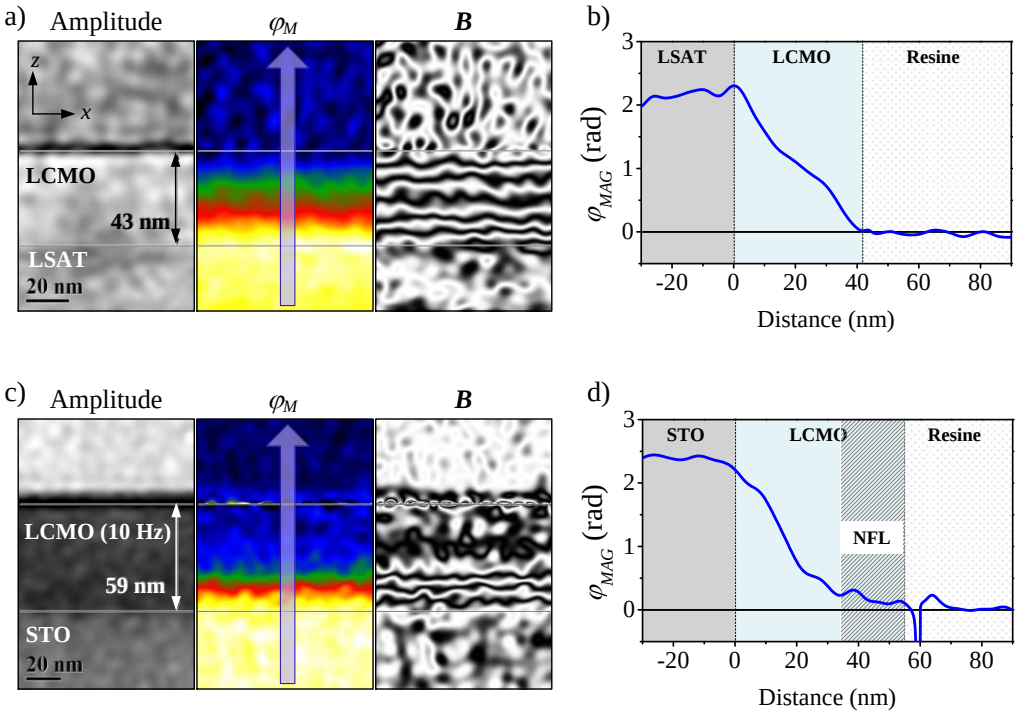

Figure 13: Image d'amplitude, du déphasage magnétique (φ_{MAG}) et du flux magnétique (B) dans l'état remanent pour des couches de LCMO à l'état rémanent sans contrainte sur LSAT (a) et fortement contrainte sur STO (c). A droite sont reportés les profils obtenus dans la direction de croissance sur les images de φ_{MAG} (flèches bleues) pour LCMO sans contrainte sur LSAT (b) et de LCMO très quadratique sur STO (d).

D'autre part, lorsque $La_{2/3}Ca_{1/3}MnO_3$ est déposé sur $LaAlO_3$ de plus petit paramètre, il est alors contraint en compression dans le plan du film et la tension dans la direction perpendiculaire modifie l'anisotropie magnétocristalline provoquant le passage de l'aimantation hors du plan. La configuration magnétique résultante est alors très différente comme reportée sur la Fig. 14.

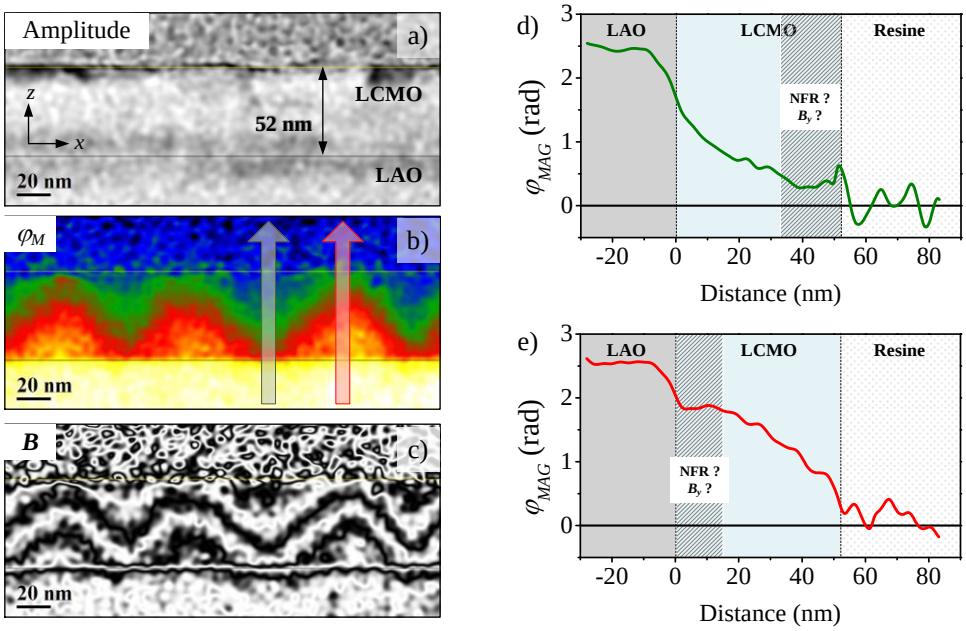

Figure 14: Images d'amplitude (a), de déphasage magnétique (φ_{MAG}) (b) et du flux magnétique "*B*" (c) obtenues par EH dans l'état rémanent sur un film de LCMO très contraint déposé sur LAO. (d) et (e) profils de ligne extrait de φ_{MAG} (bleu et flèches vertes).

Les mesures macroscopiques indiquent que la phase non ferromagnétique est en fait antiferromagnétique et que nous observons donc une séparation de phase magnétique où les deux ordres ferromagnétique et antiferromagnétique coexistent. Les premiers calculs par la méthode DFT principe-U ont confirmé que l'ordre antiferromagnétique peut apparaître dans des films de $La_{2/3}Ca_{1/3}MnO_3$ stochiométrique pour certaines valeurs de déformation de la structure cristalline. Bien que l'effet des déformations induites par le substrat sur les propriétés magnétiques des manganites en couches minces a été largement étudiés dans le passé, ce travail a été pionnier dans l'utilisation de l'HE pour analyser localement les modifications induite par la contrainte de la structure magnétique à basse température.

Chapitre 7: Conclusions générales et prospectives

Une conclusion générale reprend les principaux résultats obtenus sur les sujets présentés ci-dessus en y précisant pour chacun d'entre eux les nouvelles perspectives que ces travaux permettent d'entrevoir et les développements futurs qu'il faudrait entreprendre pour développer plus encore ces sujets.

De manière général, les travaux développés dans cette thèse illustrent parfaitement les performances de l'Holographie Electronique et la Microscopie de Lorentz associées aux expériences *in-situ* en TEM comme puissantes techniques de caractérisation magnétique permettant d'explorer le magnétisme de la matière à l'échelle nanométrique. Cet outil est devenu incontournable dans la communauté du magnétisme qui l'a intégré comme une technique complémentaire de mesure locale et d'imagerie. Les nouvelles générations de microscope devront permettre d'étendre plus encore les expérimentations *in-situ* par EH et LM dans des conditions d'environnement plus étendues.

Ce travail de thèse a donné lieu aux 8 publications ci-dessous et 15 présentations dans des conférences (8 oraux, 7 posters)

Observation of the strain induced magnetic phase segregation in manganite thin films
L Marín, L A Rodríguez, C Magén, E Snoeck, A Rémi, I Lucas, L Morellón, P A Algarabel, J M De Teresa and M R Ibarra.
Nano Letters (2014) submitted

High-resolution imaging of remanent state and magnetization reversal state of superdomain structures in high-density cobalt antidot arrays
L A Rodriguez, C Magén, E Snoeck, C Gatel, C Castán-Guerrero, J Sesé, L M García, J Herrero-Albillos, J Bartolomé, F Bartolomé and M R Ibarra.
Nanotechnology **23** (2014) 385703

Magnetic antidot to dot crossover in Co and Py nanopatterned thin films

C Castán-Guerrero, J Herrero-Albillos, J Bartolomé, F Bartolomé, L A Rodríguez, C Magén, F Kronast, P Gawronski, O Chubykalo-Fesenko, K J Merazzo, P Vavassori, P Strichovanec, J Sesé and L M García.

Physical Review B **39** (2014) 144405

Enhanced Magnetotransport in Nanopatterned Manganite Nanowires

L Marín, L Morellón, P A Algarabel, L A Rodríguez, C Magén, J M De Teresa and M R Ibarra.

Nano Letters **14** (2014) 423-428

Improvement of domain wall conduit properties in cobalt nanowires by global gallium irradiation

L Serrano-Ramón, A Fernández-Pacheco, R Córdoba, C Magén, L A Rodríguez, D Petit, R P Cowburn, M R Ibarra and J M De Teresa.

Nanotechnology **24** (2013) 345703

Quantitative in situ magnetization reversal studies in Lorentz microscopy and electron holography

L A Rodríguez, C Magén, E Snoeck, C Gatel, L Marín, L Serrano-Ramón, J L Prieto, M Muñoz, P A Algarabel, L Morellón, J M De Teresa and M R Ibarra.

Ultramicroscopy **134** (2013) 144-154

Optimized cobalt nanowires for domain Wall manipulation imaged by in situ Lorentz Microscopy

L A Rodríguez, C Magén, E Snoeck, L Serrano-Ramón, C Gatel, R Córdoba, E Martínez-Vecino, L Torres, J M De Teresa and M R Ibarra.

Applied Physics Letter **102** (2013) 022418

Ultrasmall Functional Ferromagnetic Nanostructures Grown by Focused-Electron-Beam-Induced Deposition

L Serrano-Ramón, R Córdoba, L A Rodríguez, C Magén, E Snoeck, C Gatel, I Serrano, M R Ibarra and J M De Teresa.

ACS Nano **5** (2011) 7781-7787